Mesoporous oxides as efficient catalysts for the electrocatalytic oxygen evolution reaction (OER)

vorgelegt von

Diplom-Chemiker Michael Bernicke

geb. in Berlin

Von der Fakultät II - Mathematik und Naturwissenschaften

der Technischen Universität Berlin

zur Erlangung des akademischen Grades

Doktor der Naturwissenschaften

Dr. rer. nat.

genehmigte Dissertation

Promotionsausschuss:

Vorsitzender:	Prof. Dr. Thomas Friedrich
Gutachter:	Dr.-Ing. Ralph Krähnert
Gutachter:	Prof. Dr. Peter Strasser
Gutachter:	Prof. Dr. Michael Bron

Tag der wissenschaftlichen Aussprache: 7. September 2016

Berlin 2016

Wir sind gleichsam Zwerge, die auf den Schultern von Riesen sitzen, um mehr und Entfernteres als diese sehen zu können - freilich nicht dank eigener scharfer Sehkraft oder Körpergröße, sondern weil die Größe der Riesen uns zu Hilfe kommt und uns emporhebt.

- Bernhard von Chartres

Danksagung

Ich danke Dr.-Ing. Ralph Krähnert für die Aufnahme in den Arbeitskreis und die Möglichkeit der Promotion. Durch anregende und strukturierte wissenschaftliche Diskussionen war immer ein effizientes Arbeiten im Laufe meiner Promotion möglich. Für die unzähligen Ratschläge und die fruchtbare Zusammenarbeit möchte ich mich bedanken.

Bei Herrn Professor Thomas Friedrich bedanke ich mich für die bereitwillige Übernahme der Funktion des Vorsitzenden und bei den Herren Professoren Peter Strasser und Michael Bron bedanke ich mich für die Erstellung des Gutachtens.

Mein weiterer Dank gilt Erik Ortel für die freundliche Einweisung in die Künste eines Doktoranden. Bei Tobias Reier, Arno Bergmann und Nadine Menzel möchte ich mich für die vielen Ratschläge zu Beginn und während meiner Promotion bedanken. Mein besonderer Dank gilt hierbei Tobias Reier, der unzählige Stunden damit verbracht hat, mich in die Geheimnisse der Elektrokatalyse einzuweihen. Des Weiteren bedanke ich mich bei Andreas Lippitz für XPS- und Eicke Gericke für SAXS-Messungen. Besonders möchte ich Kornelia Weh für zahlreiche ICP-Messungen danken. Bei Denis Bernsmeier bedanke ich mich für bereitwilliges Messen von SAXS und BET. Björn Eckhardt und Katrin Schulz danke ich für viele XRD-Messungen. Ich danke Jorge Araujo für DEMS-Messungen. Des Weiteren möchte ich mich bei Erik Ortel, Benjamin Paul, Roman Schmack und allen Mitarbeitern des ZELMI für unzählige elektronenmikroskopische Bilder bedanken. Nicolas Chaoui, Jérôme Roeser, Nathaniel Leonard und vor allem Ebru Özer danke ich für sorgfältiges Korrekturlesen.

Bei meinen Kollegen Denis Bernsmeier, Björn Eckhardt, Roman Schmack, Katrin Schulz, Benjamin Paul, Huan Wang und René Sachse möchte ich mich für ein angenehmes Arbeitsklima und die gemeinsamen Abende mit viel Spaß bedanken.

Der Arbeitsgruppe von Herrn Professor Strasser danke ich für die angenehme Arbeitsatmosphäre und die stundenlangen Freuden am Kickertisch. Besonders hervorheben möchte ich hierbei Ebru Özer, Camillo Spöri, Hong Nhan, Tobias Reier, Vera Beermann, Henrike Schmieß, Julian Steinberg, Malte Klingenhof, Thomas Merzdorf, Henner Heyen und Elisabeth Hornberger.

Zu guter Letzt möchte ich mich bei meinen Eltern und meiner restlichen Familie für die ständige Unterstützung in meinem Leben bedanken. Ihr wart immer an meiner Seite und habt mich unterstützt, wo ihr nur konntet, dafür möchte ich euch von ganzem Herzen danken!

Zusammenfassung

Wasserstoff ist ein wichtiger Energieträger der Zukunft und findet Verwendung in einer Vielzahl industrieller Prozesse. Die elektrokatalytische Wasserspaltung stellt eine wichtige Möglichkeit der Wasserstoffgewinnung dar und wird durch einen komplexen Mechanismus an der sauerstofferzeugenden Anode limitiert. Die Erhöhung der Massenaktivität eingesetzter Katalysatoren führt zur Verringerung der Investitionskosten von Elektrolyseuren.

Die vorliegende Doktorarbeit zeigt die Synthese mesoporöser Oxidfilme als saure oder alkalische OER-Elektrokatalysatoren. Die Katalysatoren basieren auf unterschiedlichen Metalloxiden, wie NiO, IrO_2 und IrO_2/TiO_2. Die Herstellung oxidischer Filme erfolgte mittels Tauchbeschichtung und basiert auf einer verdampfungsinduzierten Selbstanordnung eines PEO-*b*-PB-*b*-PEO Blockcopolymers als Porentemplat und eines geeigneten Metalloxidpräkursors sowie einer anschließenden thermischen Behandlung. Die jeweiligen Synthesen und physikochemischen Charakterisierungen der einzelnen Verbindungen werden im Diskussionsteil beschrieben.

Die Korrelation von Struktur und OER-Aktivität erlaubte das Ableiten von Struktur-Aktivitäts-Beziehungen. Diese Beziehungen konnten genutzt werden, um OER-Einflussparameter zu identifizieren. Die Verwendung verschiedener Systeme mit spezifischen Eigenschaften erlaubte die gezielte Untersuchung der wichtigsten OER-Einflussparameter. Durch Zusammenfassen der wichtigsten OER-Einflussparameter wurde ein mögliches OER-Model vorgeschlagen. Das OER-Model beschreibt, bei welchen strukturellen Eigenschaften hohe OER-Aktivitäten erwartet werden können. Zusätzlich wurde der Einfluss auf kinetische Kenngrößen, wie etwa dem Tafelanstieg, berücksichtigt. Hohe OER-Aktivitäten und geringe Tafelanstiege werden vor allem für Materialien mit geringer Kristallitgröße, hoher aktiver Oberfläche, hoher Leitfähigkeit sowie bei elektrokatalytischen Messungen mit moderaten Überspannungen (ca. $\eta < 0.35$ V) beobachtet.

Katalysatoren, welche nach dem postulierten OER-Model, hohe OER-Aktivitäten zeigen, wurden mit kommerziellen Referenzsystemen verglichen. Es konnte gezeigt werden, dass die in dieser Arbeit hergestellten Oxidfilme über eine 11- bis 24- fach höhere OER-Aktivität bezogen auf die eingesetzte Masse an Iridium Metall im Vergleich zu kommerziell verfügbaren Katalysatorpulvern verfügen.

Abstract

Hydrogen is considered an important energy carrier and feedstock for industrial applications. The generation of hydrogen can be realised by electrocatalytic water splitting. However, the efficiency of water electrolysers is limited by the slow kinetics of oxygen evolution reaction (OER). An increase in mass based OER activity is mandatory for a lower capital cost of electrolyser cells.

In this thesis, synthesis routes are presented for new mesoporous metal oxide films used as catalytic layers for OER in alkaline or acidic media. The catalytic layers contain different metal oxides, such as NiO, IrO_2 and IrO_2/TiO_2. The synthesis of metal oxide coatings with high accessible ordered mesopore structure was achieved via evaporation induced self assembly. The synthesis succeeds by utilizing PEO-*b*-PB-*b*-PEO triblock copolymers as a pore template, a suitable metal oxide precursor, and a final heat treatment under air. The synthesis conditions and corresponding physicochemical characterisations are shown in the discussion.

Correlation of structure and OER activity was used to deduce structure-activity relationships. These relationships were then used to identify the most significant OER-controlling parameters. All identified OER-controlling parameters were combined in order to develop an OER-model describing which structural properties benefit OER activity the most. Furthermore, the influence on kinetic parameters such as Tafel slope was investigated. High OER-activities and low Tafel slopes were found for materials with low crystallinity, high surface area, high conductivity and electrocatalytic measurements conducted at moderate overpotentials (ca. $\eta < 0{,}35$ V).

In order to demonstrate the commercial relevance of the catalytic layers synthesised in this work, their OER activity was compared with commercial reference catalysts. It was shown that oxide layers of this work exhibit a 11 to 24 times higher iridium mass based OER activity compared to commercial reference catalysts.

Published work

Note that parts of this thesis were already published and that reuse solely for this document was permitted by John Wiley and Sons.

M. Bernicke, B. Eckhardt, A. Lippitz, E. Ortel, D. Bernsmeier, R. Schmack, R. Kraehnert, *ChemistrySelect* **2016**, *3*, 1-9. http://dx.doi.org/10.1002/slct.201600110

M. Bernicke, E. Ortel, T. Reier, A. Bergmann, J. Ferreira de Araujo, P. Strasser, R. Kraehnert, *ChemSusChem* **2015**, *8*, 1908-1915. http://dx.doi.org/10.1002/cssc.201402988

Contents

1 Motivation

Modern society consumes huge amounts of energy relying on the combustion of fossil resources. The amount of fossil resources such as coal and oil is limited. Therefore, new routes of energy conversion and storage have to be developed.

Molecular hydrogen (H_2) has the highest mass specific energy density of all chemical fuels[1] and thus appears to be a very attractive candidate for energy storage. The stored energy can be regained as electrical energy in fuel cells[2] with water as a byproduct. However, depletion of fossil resources[3] and competition with other industrial applications (e. g. Haber-Bosch-process,[4] HCl-synthesis,[5] metal oxide reduction[6] and Fischer-Tropsch-Synthesis[7]) require efficient and sustainable routes for hydrogen generation.

Many routes for generating molecular H_2 are available, i.e. it is commonly generated by the reaction of zinc and hydrochloric acid[8] for laboratory scale purposes. The reaction is considered as uneconomic thus industrial generation of hydrogen relies on steam reforming[9] and partial oxidation of methane[10] accompanied by the production of unwanted greenhouse gases, i.e. CO_2.

Several approaches for water splitting are available, such as photocatalysis,[11] thermal water splitting[12] or water electrolysis.[13] Due to nonpolluting operation conditions and fairly high efficiencies of 93 % ($\varepsilon_{\Delta H}$),[14] electrocatalytic water splitting is considered a promising candidate for establishing a sustainable hydrogen economy. Clean energy economy without indirect CO_2 formation is established only when feeding the required energy for electrolysis from renewable energy sources, such as solar or wind energy.

The efficiency and competiveness of water electrolysis is limited by a complex reaction mechanism of the oxygen evolution reaction (OER) causing a high anodic overpotential. The development and improvement of novel electrocatalysts is considered as the major task to overcome these roadblocks in energy conversion.

2 State of the Art

The following chapter (2) introduces general aspects that are most relevant for the present thesis. Chapter 2.1 presents principles of electrocatalytic water splitting in alkaline and acidic electrolyte solutions. Moreover, the chapter contains literature reports of electrocatalysts used for the oxygen evolution reaction in both media. The reported electrocatalysts usually contain metal oxides. An increase in surface area is often used to enhance activity which can be achieved by the introduction of porosity. Chapter 2.2 presents general synthesis concepts for the preparation of oxides with templated porosity such as evaporation induced self assembly (EISA). Chapter 2.3 introduces reports from literature exploiting EISA and polymer template based synthesis routes for the preparation of different mesoporous metal oxides, i.e. oxides of Al, Mg, Co, Zn, Ti and Ir. The presented synthesis routes are of particular interest to achieve the specified goals in this thesis (chapter 2.4). A roadmap for the successful realisation of the aims is presented in chapter 2.5.

2.1 Electrocatalytic water splitting and electric properties

The history of water electrolysis began in the beginning of the 19th century with the discovery by Nicholson and Carlisle of electrocatalytic water splitting.[15] A century later more than 400 industrial water electrolysis devices were in operation. The first large water electrolysis plant was deployed in 1939 and provided hydrogen production rates of 10 000 Nm³H$_2$/h. The first industrial electrolyser capable to work under pressurized conditions was developed in 1948 by Zdansky/Lonza. The development of water electrolysers was continued with the construction of the first solid polymer electrolyte system by General Electric in 1966. In 1972 the first solid oxide water electrolysis units were introduced.

The following chapter 2.1 deduces the thermodynamic standard potential required for the electrocatalytic water splitting (2.1.1). Advantages, disadvantages and typical OER catalysts used for water splitting in alkaline (chapters 2.1.2 - 2.1.3) and acidic media (chapters 2.1.4 - 2.1.5) are presented. Finally, basic investigations reported in literature on structure-activity relationships are shown for state of the art catalysts used in acidic water splitting, i.e. iridium oxide. The presented publications underline effects on OER activity and electron transport mechanism, i.e. layer thickness (chapter 2.1.6), calcination temperature (chapter 2.1.7) and electrical conductivity (chapter 2.1.8).

2.1.1 Thermodynamic standard potential of water splitting

The net balance for electrochemical water splitting is:

$$H_2O \rightarrow \tfrac{1}{2} O_2 + H_2 \quad | \Delta H^0 = 285.8 \text{ kJ/mol}$$

The minimal required voltage E^0 that has to be applied under standard conditions (p,T = constant) in order to carry out electrolysis of water is expressed as:

$$E^0 = \frac{-\Delta G^0}{n \cdot F}$$

Wherein ΔG^0 is referred to as the change in Gibbs free energy under standard conditions, F is related to the Faraday constant (96 485 C/mol) and n expresses the number of electrons transferred during reaction (in this case n=2).

The fundamental Gibbs-Helmholtz equation is expressed as followed:

$$\Delta G^0 = \Delta H^0 - T\Delta S^0$$

For water electrolysis under standard conditions the standard reaction enthalpy ΔH^0 amounts to 285.8 kJ/mol, whereas the standard molar entropies ΔS^0 are found to be:

$$\Delta S^0(H_2) = 130.7 \frac{J}{K \cdot mol}; \ \Delta S^0(O_2) = 205.1 \frac{J}{K \cdot mol}; \ \Delta S^0(H_2O) = 70 \frac{J}{K \cdot mol}$$

The total change of molar entropy for the electrolysis of water is expressed as:

$$\Delta S^0_{total} = \Delta S^0(H_2) + 0.5 \cdot \Delta S^0(O_2) - \Delta S^0(H_2O)$$

And amounts to the following value:

$$\Delta S^0_{total} = (130.6 + 0.5 \cdot 205.1 - 70)\frac{J}{K \cdot mol} = \boldsymbol{163.15} \frac{\boldsymbol{J}}{\boldsymbol{K \cdot mol}}$$

Inserting ΔS^0 and ΔH^0 in the Gibbs-Helmholtz equation allows the determination of Gibbs free energy ΔG^0 under standard conditions (298 K, 1 bar):

$$\Delta G^0 = \Delta H^0 - T\Delta S^0 = 285.8 \frac{kJ}{mol} - 298 \, K \cdot 163.15 \frac{J}{K \cdot mol} = \boldsymbol{236.88} \frac{\boldsymbol{kJ}}{\boldsymbol{mol}}$$

Moreover the minimum required potential for the beginning of water electrolysis in an open cell can be determined:

$$E_{cell}^0 = \frac{-\Delta G^0}{n \cdot F} = \frac{-236.88 \; \frac{kJ}{mol}}{2 \cdot 96485 \; \frac{C}{mol}} = -1.23 \; \frac{J}{C} = -1.23 \; V$$

The negative value indicates that the reaction does not occur spontaneously thus requiring energy to proceed. In conclusion, the determined voltage as high as 1.23 V is considered as the thermodynamic minimum potential required for water electrolysis under standard conditions (25 °C, 1 bar).

Water splitting usually is conducted in either acidic or alkaline media. The advantages and disadvantages for electrolysers operating in various media are discussed in chapters 2.1.2 - 2.1.5.

2.1.2 General aspects of alkaline water splitting

Alkaline water splitting is characterized by two electrodes immersed in a solution typically containing 20 % - 30 % KOH. Both electrodes are separated from each other by a diaphragm ensuring physical segregation of evolving O_2 and H_2 at the anode and cathode, respectively. The separation of both gases is necessary for the sake of safety and efficiency. The utilized diaphragm is permeable for hydroxide and water molecules in order to provide transport of reactants between both reaction chambers.[13]
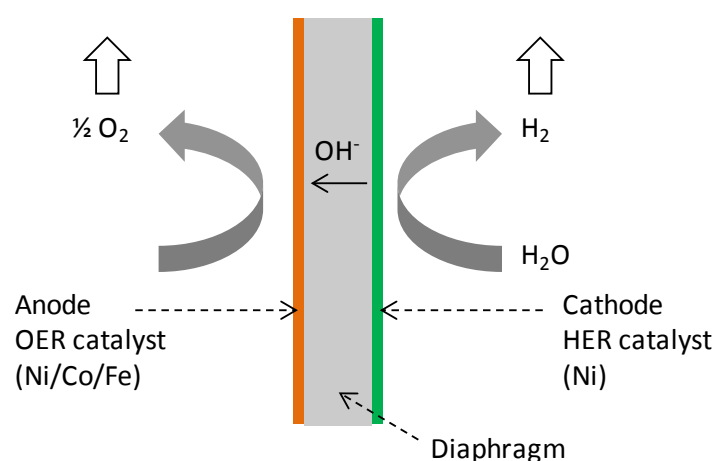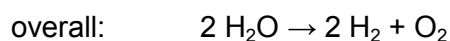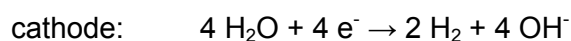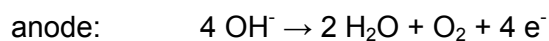

Figure 1: Schematic illustration of an alkaline electro-catalytic water splitting cell. Anode and Cathode are separated by a diaphragm to inhibit cross diffusion.

The half-cell reactions for water splitting in alkaline media are:

anode: $4\ OH^- \rightarrow 2\ H_2O + O_2 + 4\ e^-$
cathode: $4\ H_2O + 4\ e^- \rightarrow 2\ H_2 + 4\ OH^-$

overall: $2\ H_2O \rightarrow 2\ H_2 + O_2$

A closer look at alkaline electro-catalytic water splitting cells reveals several disadvantages. First, the diaphragm does not fully separate the evolving gases. As a result, evolving O_2 diffuses from the anode to the cathode and H_2 diffuses from the cathode to the anode. This cross-diffusion leads to decreased efficiency by the reduction of enriched O_2 at the cathode and can be potentially dangerous due to the formation of a hazardous mixture of O_2 and H_2 in the anode chamber. A shutdown and subsequent purge of the chamber with inert gas is required in order to prevent damage.[13]

The cross diffusion rate is independent of current density. The contamination of both cell chambers caused by crosss diffusion thus proceeds rather quickly at low production rates and low current densities. As a result, hazardous working conditions are reached fast and should be avoided by using high production rates in order to flush the contaminants from the system.[13]

Many other problems are associated with the use of liquid electrolyte and diaphragms. Notably, high ohmic losses occur throughout the liquid electrolyte and diaphragm which limits the maximum achievable current density. Moreover, operation at high pressures is not possible which results in a clunky stack design.[13]

2.1.3 OER catalysts used in alkaline media

Catalysts used for oxygen evolution in alkaline media are typically based on the oxides, oxyhydroxides or hydroxides of metals such as CoO_x,[16-19] $CoFeO_x$,[16, 20-21] NiO_x,[22-27] $NiCeO_x$,[22] $NiCoO_x$,[28] $NiCuO_x$,[28] $NiFeO_x$,[16, 29-33] $NiLaO_x$,[22] MnO_x,[34-35] $MnCoO_x$.[36]

Several reports in the literature show investigations on the electrocatalytic activity of nickel based water splitting catalysts. The overpotential can be used as a measure of catalytic activity. Yu et al.[23] prepared a nickel-based thin film (NiO_x) on multi walled carbon nanotubes deposited on ITO and observed an OER overpotential of 523 mV. Singh et al.[24] electrodeposited layers of nickel oxide from $[Ni(en)_3]Cl_2$ (en= 1,2-diaminoethane) on glassy carbon and reported 510 mV overpotential. Nardi et al.[25] deposited thin films of NiO $Ni(Cp)_2$ (cp=cyclopentadienyl) on fluorine doped tin oxide (FTO) via atomic layer deposition and achieved an overpotential of 400 mV. Lyons et al.[37] investigated the electrocatalytic activity

of polycrystalline nickel foils and reported an overpotential of 379 mV. Fominykh et al.[26] prepared NiO nanoparticles using a solvothermal reaction in *tert*-butanol. Subsequently, NiO nanoparticles were deposited on Au-coated QCM electrodes in order to access the OER overpotential (280 mV). Trotochaud et al.[27] obtained a thin film of NiO_x by spincoating a solution containing $Ni(NO_3)_2 \cdot 6H_2O$ on Au-coated QCM electrodes. Subsequent electrocatalytic investigation in the OER regime revealed an overpotential of 279 mV.

McCrory et al.[38] published a comprehensive review on the electrocatalytic activity for different metal oxide catalysts finding that the activity of NiO_x catalysts can be further enhanced by the addition of Fe. Gorlin et al.[30] synthesized Ni-Fe (62:38 at. %) catalysts with a solvothermal approach and subsequently deposited them on carbon. Oxygen evolution reaction activity was investigated in 0.1 M KOH revealing an overpotential of 0.25 V (1 mA/cm²). Gong et al.[32] prepared a nickel-iron layered double hydroxide carbon nanotube complex by a solvothermal method and showed an OER overpotential of 0.23 V (1 mA/cm², 0.1 M KOH). Trotochaud et al.[33] electrodeposited thin films of Ni-Fe onto substrates and subsequently investigated the OER activity revealing an overpotential of 0.27 V at 1 mA/cm² (1 M KOH). A similar synthesis was conducted by Lu et al.[39] who electrodeposited Ni-Fe on GC substrate and observed an OER overpotential of 0.31 V at 1 mA/cm² in 0.1 M KOH.

2.1.4 General aspects of acidic water splitting

Many problems arising for electrolysers working in alkaline media can be avoided when operating under acidic conditions. For instance, the replacement of diaphragms with Nafion® allows achieving higher current densities and better separation of product gases.[13] Developed in the late 1960's by Walter Grot of DuPont.[40-41] Nafion® is described as a teflon derivate consisting of sulfonated tetrafluoroethylene polymer (PTFE) groups (Figure 2).
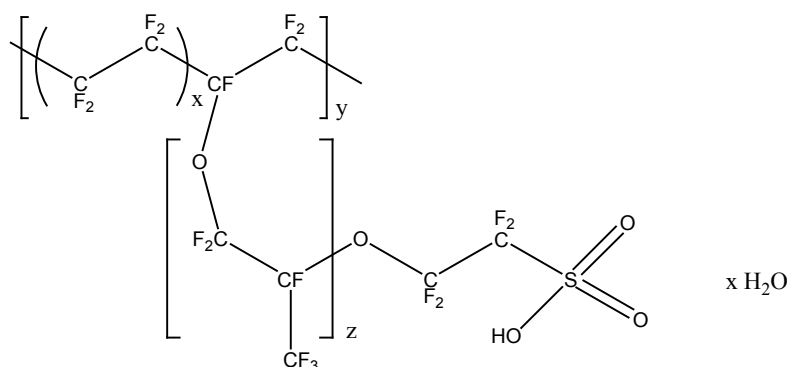

Figure 2: Nafion® was invented by Walter Grot of DuPont in the late 1960's and is described as a polymer typically deployed in electrolyser cells as a Proton Exchange Membrane (PEM). The polymer overcomes typical problems observed for alkaline electrolysers, such as low pressure output, low partial load range and low electric current densities.

Nafion® is applicable in two major fields of electro-catalysis. It can be dissolved in lower aliphatic alcohols and subsequently used as a binder for attaching a catalyst powder on substrates or used as a Proton Exchange Membrane (PEM) in acidic electrolyser cells (Figure 3)
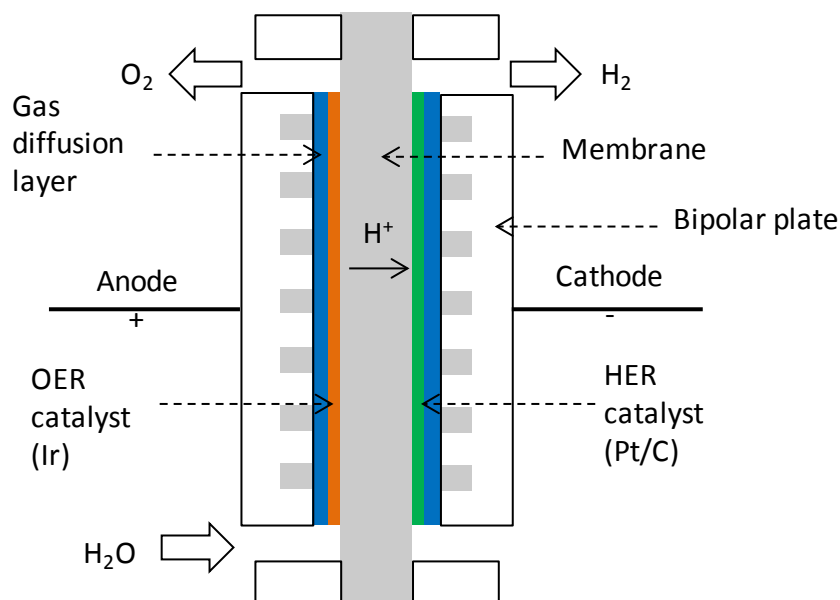
Figure 3: Proton exchange membrane (PEM) electrolyser cell usually consist of OER and HER catalysts separated by a proton conducting membrane (e.g. Nafion®) embedded in gas diffusion layers and bipolar plates. Water is fed at the anode side, whereas evolving O_2 and H_2 is released of the compartment at the anode and cathode side, respectively.

The following half reactions are observed for a PEM electrolyser cell:

anode: $2 H_2O \rightarrow O_2 + 4 e^- + 4 H^+$

cathode: $4 H^+ + 4 e^- \rightarrow 2 H_2$

overall: $2 H_2O \rightarrow 2 H_2 + O_2$
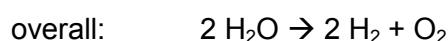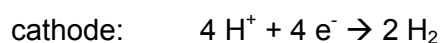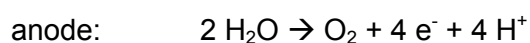
In general, PEM electrolyzer cells provide several advantages compared to alkaline electrolysers. First of all, the Nafion membrane is as thin as 20 - 300 µm (commercially available) and provides high proton conductivity between 0.083 and 0.16 S/cm.[42] This leads to lower potential drop between the anode and cathode than for alkaline electrolysers. Hence, current densities above 2 A/cm² can be achieved resulting lower operational costs. Furthermore proton transport across the membrane responds very fast to the applied power input, thus lowering the gas crossover rate and consequently increasing H_2 purity in the cathode chamber. In addition, no hazardous condition at low power input is reached in the

anode chamber. As a result, the operational range appears to be wider than for alkaline electrolyser cells, whereby the nominal power density ranges between 10 - 100 %. Electrolyser cells with a solid electrolyte allow a compact system architecture featuring resistant structural properties allowing operation at high pressure.[43-44] This grants an important benefit to the end user, who does not have to apply an additional amount of energy in order to compress the evolved H_2 gas. Furthermore, working under high pressure lowers the specific volume of produced gas thus providing better gas removal.[13]

Even though acidic electrolyser cell provide plenty of advantages, some negative aspects must be considered. Cross-diffusion of evolved gas in the respective opposite reaction chambers is still present. Working pressures exceeding values higher than 100 bar further enhance cross diffusion and usually requires the use of thicker membranes and internal gas recombiners in order to prevent formation of hazardous gas mixtures. Furthermore, deployed catalysts, current collectors and separator plates must withstand harsh working environment characterized by low pH values, high applied potentials (>2 V) and high current densities. Only a few materials can be applied to operate under such working conditions, e.g. noble metal as catalysts as well as current collectors and separator plates based on titanium.

Water electrolysis is characterised by the Oxygen Evolution Reaction (OER) occuring at the anode and the Hydrogen Evolution Reaction (HER) proceeding at the cathode. Typical electrolysers are limited by the OER due to the fact that four electrons are needed to produce one molecule of oxygen and that the OER proceeds by a complex reaction mechanism. [13, 45-47] Active and stable catalysts with high accessible surface area can minimize the overpotential required for both reactions[47] and potentially lower the amount of noble metal thus decreasing investment cost of PEM electrolyser cells.

2.1.5 OER catalysts used in acidic media

A wide range of materials are used for the OER reaction, such as mixtures of IrO_2/SnO_2,[48] IrO_2/Ta_2O_5,[49] IrO_2/Nb_2O_5,[50] IrO_2/RuO_2.[51] However, oxides of ruthenium and iridium show the lowest OER overpotential in acidic media.[13, 52-53] Although ruthenium oxide shows higher activity,[54] it typically corrodes during OER potential cycles.[55-56] Attempts were made in order to stabilize RuO_2, such as implementing 20 % IrO_2 within RuO_2. The corrosion rate of the compound was successfully reduced to 4 % of the original value.[53] Iridium oxide is therefore the best compromise for an active and stable OER catalyst.[13] Iridium oxide catalysts can be prepared in different ways. Johnson et al.[57] dropcasted a solution containing iridium acetate and isopropanol onto a titanium cylinder, followed by heat treatment at 480 °C. Electrochemical testing in 0.1 M $HClO_4$ indicated overpotentials of about 0.24 V_{RHE} at a

8

current density of 1 mA/cm². Hu et al.[58] synthesized macroporous IrO_2 utilizing colloidal SiO_2 as pore template. Electrochemical testing in 0.5 M H_2SO_4 indicated 0.25 V_{RHE} overpotential at a current density of 1 mA/cm². Kushner-Lenhoff et al.[59] synthesized iridium oxide layers by electrodepositing organic precursors $Cp^*Ir(H_2O)_3]^{2+}$ (Cp^* = pentamethylcyclopentadienyl). OER yielded overpotentials of about 0.267 V at 0.5 mA/cm². A similar synthesis by Blakemore et al.[60] obtained a catalyst with approximately 0.270 V overpotential (at 0.5 mA/cm²). Oh et al.[61] prepared antimony doped tin oxide (ATO) with a sol-gel and hydrothermal method. A solution containing $H_2IrCl_6 \cdot xH_2O$, TTAB, water and NaOH was heated to 70 °C and $NaBH_4$ was added. The solution was cooled down and centrifuged in order to obtain colloidal iridium nanodendrites. The as prepared colloids were washed, dispersed in an ethanolic solution and finally deposited on an ATO support. Electrocatalytic investigations were performed in 0.05 M H_2SO_4 observing an OER overpotential of 0.27 V at 1 mA/cm². A different approach was pursued by Nong et al.[62] who dealloyed a bimetallic $IrNi_x$ alloy precursor. The obtained $IrNi_x@IrO_x$ nanoparticles showed a core-shell architecture and were deposited on mesoporous ATO. Electrochemical investigations were performed in 0.05 M H_2SO_4 showing an OER overpotential of 0.26 V at 1 mA/cm². Films of iridium oxide and nickel oxide were synthesized by Reier et al.[63] via spincoating a solution containing iridium acetate and nickel acetate tetrahydrate on titanium substrates. The as prepared samples were heat treated at 450 °C and electrochemically investigated in 0.1 M $HClO_4$. The catalytic testing revealed an overpotential in the OER of 0.258 V at 1 mA/cm².

In general, iridium oxide catalysts with i) low crystallinity[64] and ii) high surface area[65] are suggested to be more active for oxygen evolution. These characteristics can either be adjusted by applying a moderate calcination temperature or by introduction of porosity into the catalyst.

However, limited abundance and competition with other applications such as supercapacitors,[66-67] stimulating neural electrodes[68-69] and microelectrodes for pH sensing[70-71] require the most efficient utilization of IrO_2 possible.[47] Many studies were conducted on determine optimal synthesis conditions for iridium based OER catalysts. Some of the most important findings are discussed in the chapters 2.1.6 - 2.1.8.

2.1.6 Basic investigations on iridium oxide - role of layer thickness

Johnson et al.[57] investigated the influence of layer thickness on electrochemical active surface area and OER activity. They prepared, a solution containing $Ir(OAc)_3$ and isopropyl alcohol. Subsequently, a thin layer was prepared on a titanium substrate by spincoating, whereas a thick layer was obtained by a dropcasting procedure. Afterwards, the samples were heat treated at 480 °C in air. Catalyst layers were 17 -19 nm on silicon and even thinner on titanium. An exact value for the titanium supported layer was not reported. However, the layer thickness of dropcasted samples was not measured. XRD measurements were conducted for thin and thick IrO_x layers on titanium substrates. The thin IrO_x layer showed significant oxidation of the titanium susbtrate to TiO_2, whereas no oxidized titanium was observed for the thick layer. The authors conclude that, the IrO_x layer is shielding the underlying titanium susbtrate thus preventing oxidation. Investigations of the electrocatalytic properties showed a 50-60 times higher electrochemical active surface area as well as higher OER activity for the thicker IrO_x layer. Furthermore, normalisation of the OER activity with respect to the electrochemical active surface area showed a higher intrinsic OER activity for the thicker IrO_x layer related to the absence of an insulating TiO_2 interlayer.

The work from Johnson et al. depicts two major advantages for thick IrO_x layer on titanium substrate. At first, they provide higher electrochemical surface area thus higher OER activity. Furthermore, thick IrO_x layers sufficiently prohibit oxidation from underlying titanium susbtrate to TiO_2 consequently providing a higher intrinsic OER activity.

2.1.7 Basic investigations on iridium oxide - role of calcination temperature

The impact of calcination temperature on structural properties of IrO_x and electrocatalytic OER activity was investigated by Reier et al.[64]. Similar to Johnson, a solution containing $Ir(OAc)_3$ and EtOH was spincoated on titanium coated silicon substrates. Subsequently, heat treatment was conducted at temperatures ranging from 250 to 550 °C in air. Afterwards, morphology, crystallinity and chemical state of IrO_x was investigated as a function of calcination temperature. A layer thickness of ~55 nm was found for samples calcined between 250 and 450 °C, whereas calcination at 550 °C leads to thicker layers indicating migration from titanium into the IrO_x layer. Furthermore, XRD measurements were conducted and showed higher IrO_x crystallite size for samples calcined at higher temperaure. Samples calcined at 350 °C exhibit the highest OER activity and electrochemical active surface area. Calcination at 550 °C leads to oxidation of the underlying titanium substrate and enhances diffusion of TiO_x into the IrO_x layer consequently leading to higher electrical resistivity throughout the film volume and to reduced electrocatalytic OER activity.

The work from Reier et al. is of fundamental importance. It showed higher OER activity for IrO_x with smaller crystallite size. Furthermore, negative aspects of insulating TiO_2 are

underlined and in good agreement with the observations made by Johnson et al. However, the impact of TiO_2 on electrical conductivity was not investigated in detail.

2.1.8 Basic investigations on iridium oxide - role of electrical conductivity

The influence of electrical conductivity on electrocatalytic activity was investigated by Marshall et al.[72], by preparing a colloidal dispersion from metal precursors (i.e. $H_2IrCl_6 \cdot 4H_2O$ and $SnCl_2 \cdot 2H_2O$) in ethylene glycol. After heating under reflux at a constant pH value of 2.5 the dispersion was centrifuged in order to obtain colloids. The colloids were then dried and calcined in air at 500 °C. Subsequently, X-ray diffraction measurements revealed a rutile structure with altering lattice parameters as a function of tin content indicating the formation of a solid solution of iridium oxide and tin oxide. Electrical resistivity of the powder was investigated and showed an increase of resistivity depending on the Sn content. Finally, the electrochemical activity of the powder was investigated in a PEM electrolyser cell. The activity normalized to the electrochemical active surface area remains high until a tin content of 50 - 60 mol %, whereas a higher tin content leads to a remarkable drop of intrinsic activity. The work from Marshall[72] thus underlines that highly active electrocatalysts are obtained solely by providing a sufficient degree of conductivity.

Furthermore, Chen et al.[73] claims that high electrical conductivity is necessary in order to provide a stable Ir-based catalyst on titanium substrate. Usually, low electrical conductivity results in high electric fields throughout the coating causing quick migration of O^{2-} species through the substrate. Migrating O^{2-} may then have a severe impact on the oxidation of the underlying titanium substrate. Oxidized titanium leads to an additional ohmic loss thus lowering the electro catalytic activity. The catalysts further lose activity with ongoing passivation.

Comninellis et al.[74] studied the impact of electrical conductivity on electrocatalytic OER activity. A metal salt solution containing at least one of the following compounds H_2IrCl_6, $RuCl_3$, $TaCl_5$ or $ZrOCl_2$ was coated on titanium and subsequently heat treated in air at temperatures below 560 °C. The resulting microstructures of IrO_x-TiO_2, IrO_x-ZrO_2 and IrO_x-Ta_2O_5 were analyzed in terms of crystallinity, conductivity as well as OER activity. It was found, that the obtained oxides showed low miscibility indicating a distribution of the respective metal oxide clusters. Taking into account that TiO_2, ZrO_2 and Ta_2O_5 possess poor electrical conductivity, whereas IrO_2 shows metallic conductivity[54, 75-76] it was concluded that electric conductivity is established by chains of conducting IrO_2 clusters (percolation theory). An insufficient amount of IrO_2 in the catalyst leads to interruption of conducting chains, causing a drop of electric conductivity as well as OER activity. Therefore, a significant

amount of metallically conductive metal oxide (i.e. IrO_2) must be added in order to provide a sufficient degree of conductivity that is beneficial for retaining highly active OER catalysts.

Another study investigated the mechanism of electron transport through a catalytic layer. Oakton et al.[77] synthesized mixed metal oxides of IrO_2/TiO_2 by a simple one-pot Adams method route. $TiOSO_4 \cdot 0.6H_2SO_4 \cdot 1.3H_2O$ was dissolved in water along with H_2SO_4 and $IrCl_3 \cdot 3H_2O$. Afterwards, $NaNO_3$ was added to the solution. The solution was dried in a rotary evaporator and subsequently heat treated at 150 °C for 2h and 350 °C for 1 h. The obtained powder was washed with water, dried and used for physicochemical and electrochemical characterization. X-ray diffraction patterns of 40 % IrO_2 - 60 % TiO_2 revealed the presence of three different oxides, i.e. TiO_2 anatase, TiO_2 rutile and IrO_2 rutile. TEM images of the corresponding sample in bright field mode showed IrO_2 nanoparticles with 1 nm in diameter deposited on TiO_2 particles with a diameter of ca. 5 nm. The observed electrical conductivity exponentially increased as a function of iridium content (TiO_2: $2.3 \cdot 10^{-8}$ S/cm, IrO_2: 3.9 S/cm). Percolation theory is a well known model to describe the electrical conductivity of randomly packed particles with high and low electrical conductivity. The so called percolation limit describes the minimal volume percentage that is required to form a conductive network. Oakton determined a percolation limit of 35 % and observed an onset of electrical conductivity for samples with iridium loadings higher than 35 mol % Ir (0.2 S/cm).

Further quantification of conductivity can be achieved by measuring sheet resistivity of catalyst layers coated on insulating substrates such as glass. Furthermore, electrochemical methods can be used in order to elucidate electron transport through bulk materials. Stoerzinger et al.[78] deposited $LaCoO_3$ on three substrates (with different conductivity) by pulsed laser epitaxy in order to study the impact of conductivity on electron transport through the layer by analyzing the peak positions of the $[Fe(CN)_6]^{3-/4-}$ redox couple. They observed enlarged distances of redoxpeaks spreading away from the equilibrium potential for samples with low conductivity. Hence, samples with high resistivity cause a large voltage drop over the layer leading to a lower voltage which promotes catalysis.

The literature survey from the chapters 2.1.6 - 2.1.8 underlines the influence of critical reaction parameters that control the OER activity of iridium based catalysts. It can be concluded that, the iridium based catalytic layer should preferentially be thick, amorphous, electrically conductive and possess a high electrochemical active surface area in order to operate as a highly active OER catalyst.

2.2 Oxides with templated porosity

Porous materials are used for different applications in industry and everyday life. Zeolites are one of the most popular materials and used in washing powder. The properties of mesoporous materials are presented in a very general manner in chapter 2.2.1. Different synthesis approaches for the preparation of mesoporous materials are introduced in chapter 2.2.2 and the utilization of amphiphilic surfactants (chapter 2.2.3) i.e. amphiphilic block copolymers (chapter 2.2.4) will be discussed in more detail. The synthesis of mesoporous metal oxides with high pore ordering through self assembly of block copolymers (chapter 2.2.5) surrounded by suitable metal oxide precursors (chapter 2.2.6) will be described. The self assembly of polymer templates can be triggered by exceeding the critical micelle concentration achieved by ongoing solvent evaporation (EISA, chapter 2.2.7). A final treatment decomposes the polymer template and converts the precursor into a mesoporous metal oxide with a nanocrystalline structure (chapter 2.2.8).

2.2.1 Properties of mesoporous materials

Mesoporous systems are described as solid phase materials fully composed of pores. In the case of connected pores the materials are considered as open porous materials providing higher inner surface areas than bulk materials. This paves the way for different applications in the field of catalysis and sorption. Zeolithes are the most prominent porous materials first used by Henkel in 1977 for water softening. IUPAC classifies porous materials into 3 different categories[79] according to their pore size.

microporous: < 2 nm
mesoporous: 2 - 50 nm
macroporous: > 50 nm

Microporous and mesoporous systems usually provide sufficient high surface areas for catalytic processes. A major drawback for microporous and small mesoporous materials is the occurrence of transport limitation processes during catalysis. Therefore, larger pore diameters must be incorporated in order to provide sufficient product removal.[80] Mesoporous systems are distinguished in unordered and ordered materials, both derived by different synthesis approaches. The most relevant approaches for the introduction of mesoporosity in materials are discussed in chapter 2.2.2.

2.2.2 Synthesis approaches for mesoporous oxides

Two different synthesis approaches are available in order to obtain mesoporous templated materials. Endotemplating usually is characterized by a preliminary stage material that is

later surrounded by the mesoporous material precursor, whereas exotemplating first requires a solid compound with cavities that can be later filled with precursor solution. A subsequent template removal by etching or thermal treatment obtains the final porous material with a high surface area (Figure 4).
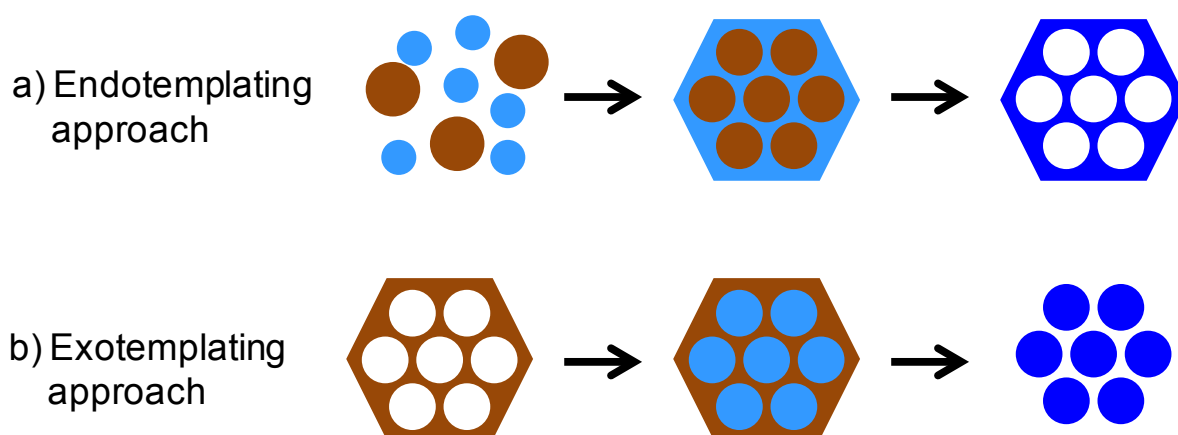

Figure 4: The a) endo- and b) exotemplating approaches are characterized by the utilizaton of a template (brown), the occurrence of intermediates (light blue) and the synthesis of a porous material (blue). a) Endotemplating features the introduction of template in an arising solid material, whereas b) exotemplating is characterised by the infiltration of a solid template with precursor solution. Independently of the approach, both routes provide porous materials as a product. (Scheme based on the work of Ortel[81])

The endotemplating approach is usually used for the synthesis of mesoporous oxides. Within the approach, the preliminary stage material is a polymer that forms micelles within the metal oxide precursor solution. After the condensation of the precursors into a "mesophase", a thermal treatment will remove the micelles and transform the precursor into a porous metal oxide. The prior enclosed micelles provide an accessible pore system leading to a porous metal oxide with high surface area.[82] The characteristics of the pore system such as pore diameter and pore ordering can be easily tuned by an appropriate choice and concentration of surfactant. Chapter 2.2.3 introduces the most common class of polymers (i.e. amphiphilic block copolymers) used for the preparation of mesoporous metal oxides via endotemplating.

2.2.3 Amphiphilic surfactants

Amphiphilic surfactants exhibit a hydrophobic and hydrophilic part leading to versatile reaction behaviours. The hydrophobic part consists of a large uncharged hydrocarbon moiety, such as $CH_3(CH_2)_n$ with n > 4 and potentially contains alcohols or ethers, whereas the hydrophilic part can be either ionic or non ionic. Ionic surfactants are subcategorised into anionic (e.g. RCO_2^-) and cationic surfactants (e.g. RNH_3^+), where R presents the hydrophobic part of the surfactant. Non ionic or uncharged surfactants usually contain alcohols with large R groups. Amphiphilic surfactants contain a variety of subcategories, wherein the amphiphilic

block copolymers are from particular interest. Therefore, chapter 2.2.4 presents important aspects related to amphiphilic block copolymers

2.2.4 Amphiphilic block copolymers

Amphiphilic block copolymers are the main building blocks for the preliminary stage materials of the endotemplating approach. They are defined as an arrangement of covalent connected polymers with different composition[83] and are divided in different types, such as diblock copolymer and triblock copolymer. Figure 5 schematically shows the bonding characteristics of diblock and triblock copolymers.

Figure 5: "Typical block copolymers" - Diblock and triblock copolymer with the main building block "A" and "B". Exemplarily, "A" might consist of a water soluble polymer such as polyethylene oxide (PEO), whereas "B" is potentially composed of a water insoluble polymer like polypropylene oxide (PPO). BASF developed such polymers in the 1950's and still sell them under the tradename Pluronic®. For instance, Pluronic® F127 is described as PEO_{106}-PPO_{70}-PEO_{106}.

The amphiphilic block copolymers that are used for generating ordered mesoporous materials mostly contain polyethylene oxide (PEO) as a hydrophilic part. Furthermore, a vast amount of block copolymers are known in literature:
PS-*b*-PEO,[84-88] PI-*b*-PEO,[89-91] PMMA-*b*-PEO,[92] PHB-*b*-PEO (KLE),[93-95] PIB-*b*-PEO,[96-97] PEO-*b*-PB)[97] and PEO-*b*-PB-*b*-PEO,[98] as well as commercially available block copolymers like Pluronic® P123 (PEO_{20}-PPO_{70}-PEO_{20}; M_w = 5800 g/mol) and Pluronic® F127 (PEO_{106}-PPO_{70}-PEO_{106}; M_w = 12600 g/mol).

All these amphiphilic block copolymers possess a variety of properties in solution according to their structure and concentration, which directly influence the architecture of the synthesized material. The most important characteristics of amphiphilic block copolymers used for the synthesis of mesoporous materials will be highlighted in chapter 2.2.5.

2.2.5 Critical micelle concentration and self assembly of block copolymers

Block copolymers in solution with a concentration below it's critical micelle concentration (CMC) are dissolved and randomly distributed. Exceeding the CMC significantly changes the properties of the isotropic solution. The dissolved block copolymers form aggregates in order to minimize their free energy. These aggregates usually shield the hydrophobic part in the inside of the micelle, whereas the hydrophilic part keeps contact with the solution. A further increase of polymer concentration caused by lower amounts of solvent between the micelles results in rearrangement and various mesophases.[99] Figure 6 exemplarily shows different mesophases potentially formed by amphiphilic block copolymers.
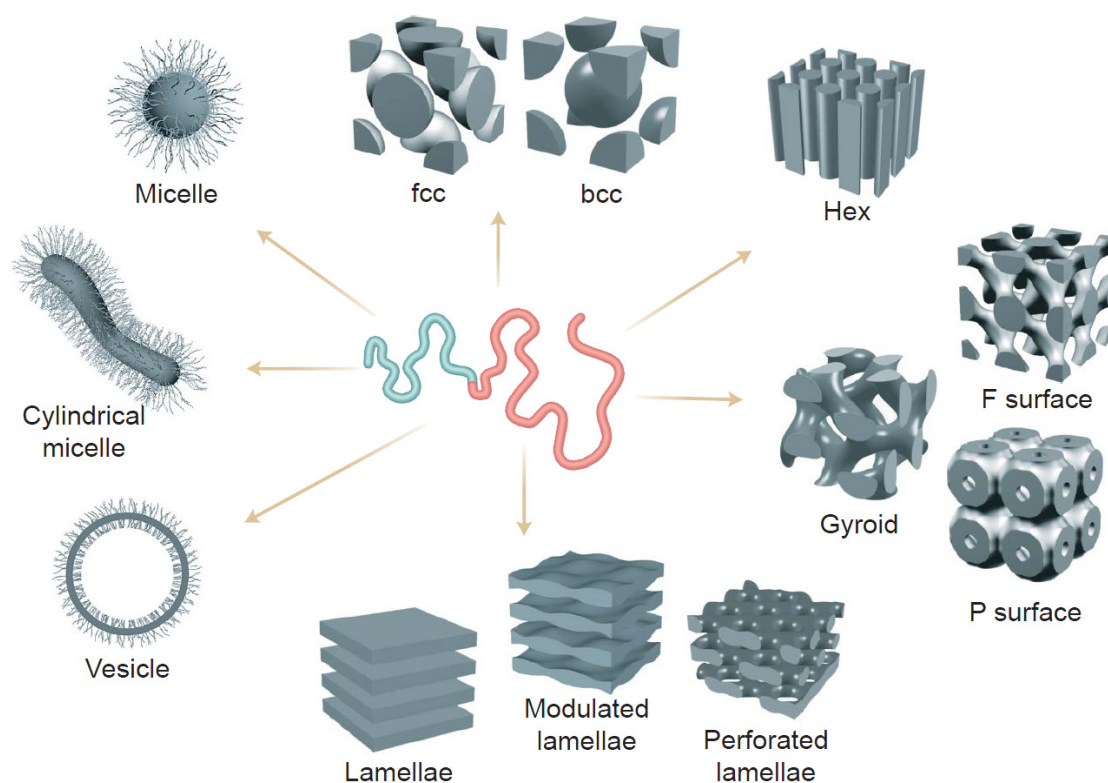
Figure 6: "Self assembly of block copolymers" - A large variety of different phases are formed by block copolymers, e.g. spherical, cylindrical micelles with face centered cubic (fcc) and body centered cubic packing (bcc). Image taken from Bucknall[100] with granted permission from The American Association for the Advancement of Science.

Figure 6 shows the self organization of block copolymers possessing the capability to form spherical and cylindrical micelles, vesicles, spheres with face-centered (fcc) cubic and body centered cubic (bcc) packing, hexagonally packed cylinders, minimal surfaces (gyroid, F surface, and P surface), simple lamellae, and modulated and perforated lamellae.[100]

The self organization is further exploited in the endotemplating approach by using polymers as the preliminary stage material along with metal oxide precursor (see Figure 4). The combination of a metal oxide precursor, and a polymer exhibiting the capability to form an

ordered mesophase is a well known technique in literature[94, 101-103] for the preparation of mesoporous oxides. Chapter 2.2.6 describes fundamental aspects of one popular metal oxide precursors, i.e. $TiCl_4$. The rearrangement of polymers to highly ordered mesophases is often achieved by exceeding the critical micelle concentration triggered by ongoing solvent evaporation. The so called evaporation induced self assembly is an important tool for the simple preparation of mesoporous metal oxides and explained in detail in chapter 2.2.7

2.2.6 Hydrolysis and condensation of metal oxide precursors

Suitable precursors must be utilized in order to obtain mesoporous templated compounds. The metal oxide precursor usually is dissolved and subsequently interacts with solvent molecules. A general reaction scheme is described as followed:

Hydrolysis: $M\text{-}X + H_2O \rightarrow M\text{-}OH + HX$

Condensation: $M\text{-}OH + M\text{-}OH \rightarrow M\text{-}O\text{-}M + H_2O$
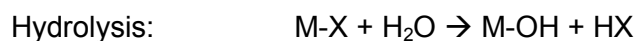
Where M = metal centre and X = halide

First, hydrolysis takes place wherein the metal halide reacts with water to form a hydroxide species under the release of a halide acid. Afterwards, the obtained metal hydroxide species reacts with itself forming a metal oxide bridged network. Reports in literature describe $TiCl_4$ as a suitable precursor for the synthesis of mesoporous templated TiO_2.[99, 102, 104-105] A general reaction scheme for $TiCl_4$ performing hydrolysis in a solution of ethanol and water was published for instance by Pan.[99]

$TiCl_4 + x\ EtOH + y\ H_2O \rightarrow TiCl_{4\text{-}x\text{-}y}(OEt)_x(OH)_y + (x+y)\ HCl$

Hydrolysis of $TiCl_4$ takes place under the release of HCl triggering hydrolysis. Moreover, the hydrolysed titanium species can undergo condensation reaction thus forming an oxygen bridged metal network under the release of EtOH. The release of HCl during hydrolysis of $TiCl_4$ in solution of $EtOH/H_2O$ induces strong acidic environments. As a result, further hydrolysis of $TiCl_4$ or even polycondensation of partially oxygen bridged titanium species is suppressed. The obtained species exhibit small molecular mass and are present as inorganic oligomers in the sol dispersion. Titanium oligomers[106-107] under acidic conditions are stabilized and terminated by hydroxide groups. They are referred to as nano building blocks (NBB) due to the interaction of the hydroxide groups with the hydrophilic part of the block copolymer micelles through hydrogen bonding.[99, 102, 108]

The last chapters pointed out typical characteristics of polymers (chapters 2.2.3 - 2.2.5) and metal oxide precursors in solution (chapter 2.2.6). Moreover, the interaction between both reactants was introduced (chapter 2.2.6). The following chapter (2.2.7) depicts the combination of both reactants in an endotemplating approach for the preparation of a mesoporous templated metal oxide.

2.2.7 Evaporation Induced Self Assembly (EISA) exemplarily explained with TiO$_2$

The so called evaporation induced self assembly (EISA) requires a solution containing block copolymers (e.g. PEO-PB-PEO[98, 109]) and metal oxide precursors (e.g. TiCl$_4$,[98] TALH[109]). The EISA process is described as a combination of the i) cooperative liquid crystal template (CLCT) mechanism[99, 110] and the ii) true liquid crystal template (TLCT) mechanism[99, 110] taking place at two different stages during film preparation i) initial sol solution preparation and ii) film deposition and aging. Therefore, EISA is divided into two stages according to the present mechanism.[99, 110]

i) Preparation of sol solution (cooperative liquid crystal template mechanism, CLCT)

A homogenous dispersion of block copolymer and inorganic precursor (e.g. TiCl$_4$) is prepared in a volatile solution (e.g. EtOH/H$_2$O). In general, the inorganic precursor immediately reacts in terms of hydrolysis and condensation.[99] Thus, leading to the formation of HCl and small inorganic oligomers terminated by hydroxide groups referred to as nano building blocks (NBBs, chapter 2.2.6).[106-107] The HCl formation causes an acidic environment consequently suppressing further polycondensation of NBBs. Subsequently, the partially hydrolyzed titanium species interact with hydrolytic regions of the block copolymers through hydrogen bonding.[99, 102, 108] This cooperative liquid crystal template (CLCT) mechanism leads to the formation of titanium oligomers attached to the block copolymers.

ii) Film deposition and ageing (true liquid crystal template mechanism, TLCT)

The as prepared solution is characterised by a dissolved polymer interacting with dissolved metal oxide precursors through hydrogen bonding. The solution is now used for film deposition on suitable substrates such as silicon or titanium. Dipcoating appears to be a convenient method due to control of temperature, humidity and withdrawal rate.[111] Immersion and consecutive dragging out of the substrate from the solution triggers several processes. The continuous evaporation of the solvent induces an increase of polymer- and metal oxide precursor concentration. At first, the enrichment of the block copolymer induces phase segregation between the hydrophilic and hydrophobic part. After exceeding the critical micelle concentration the block copolymers self assemble to micelles (TLCT).[99, 110] At

18

second, other volatile compounds besides EtOH evaporate (e.g. HCl). Thus, leading to an increase of pH-value and consequently triggering the thermodynamically favourable condensation and polycondensation reactions of the hydrolysed metal oxide precursor (sol-gel process). Finally, a connected amorphous metal oxide network is formed around the highly ordered self assembled micelles.[99]

Figure 7 schematically illustrates the evaporation induced self assembly of block copolymers and metal oxide precursors during dipcoating.
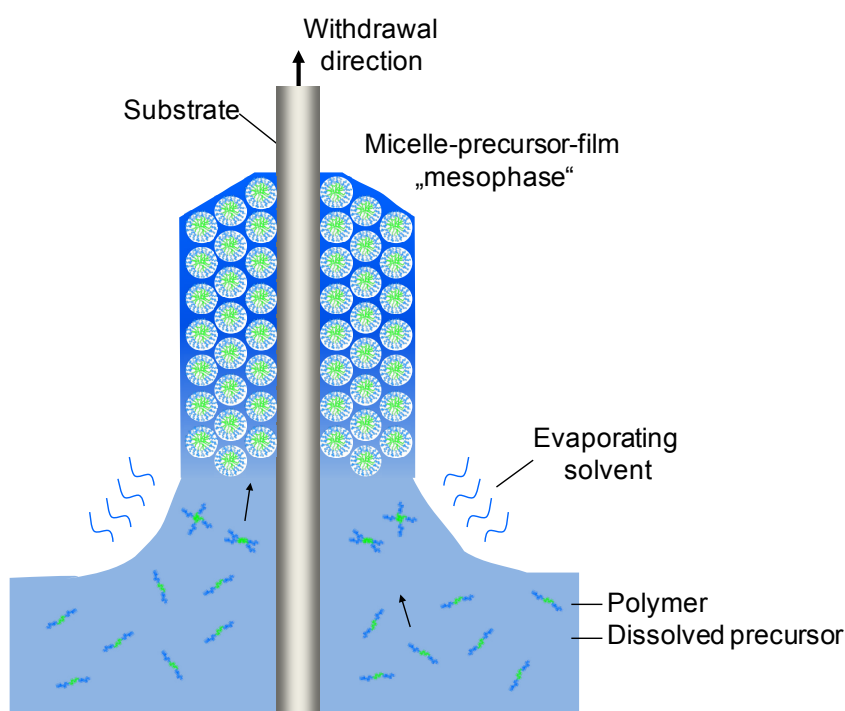
Figure 7: Schematic illustration of the Evaporation Induced Self Assembly (EISA). A volatile solution containing a block copolymer and metal oxide precursor is prepared. The substrate is immersed in solution and consequently dragged out. Evaporation of solvent and HCl (in case of TiCl$_4$) leads to enrichment of the polymer and precursor concentration inducing self assembly of the polymers and polycondensation of the oxide precursor. In the end, a connected amorphous metal oxide network is formed around the ordered micelles.

A variety of different porous metal oxide compositions have been prepared by the evaporation induced self assembly process. Chapter 2.2.8 presents the transformation of the arranged spherical micelles surrounded by metal oxide precursor into a mesoporous templated material.

2.2.8 Transformation of ordered mesophases to mesoporous oxides

The micelle-precursor films prepared according to the procedure described in chapter 2.2.7 are subsequently dried at temperatures between 60 - 200 °C[99] in order to grant full polycondensation of nano building blocks leading to a more stable mesophase. Afterwards, heat treatment at higher temperatures is performed to transform micelle-precursors into a mesoporous templated metal oxide with nanocrystalline structure. In case of Pluronic F127 (PEO_{106}-PPO_{70}-PEO_{106}; M_w = 12600 g/mol) the decomposition temperature was found to be 340 °C,[112] whereas Pluronic P123 (PEO_{20}-PPO_{70}-PEO_{20}; M_w = 5800 g/mol) decomposes around 220 °C.[113] Thermally induced crystal growth of pore walls composed of TiO_2 is observed for calcination at 350 °C.[114] Decomposition of pore template and transformation of amorphous pore wall into a crystalline material typically is accompanied by film shrinkage perpendicular to the substrate. Due to strong attachment of metal oxide precursor on the substrate surface the occurring contraction of the film is only present perpendicular to the substrate thus prevent cracking of the layer.[81, 99] In case of TiO_2, a lower crystallization temperature accompanied by less film contraction was observed for slow heating ramps of 0.5 - 2 °C/min.[115] Figure 8 illustrates the heat treatment process of a micelle-precursor-film mesophase into a crystalline oxide with an accessible porous system.
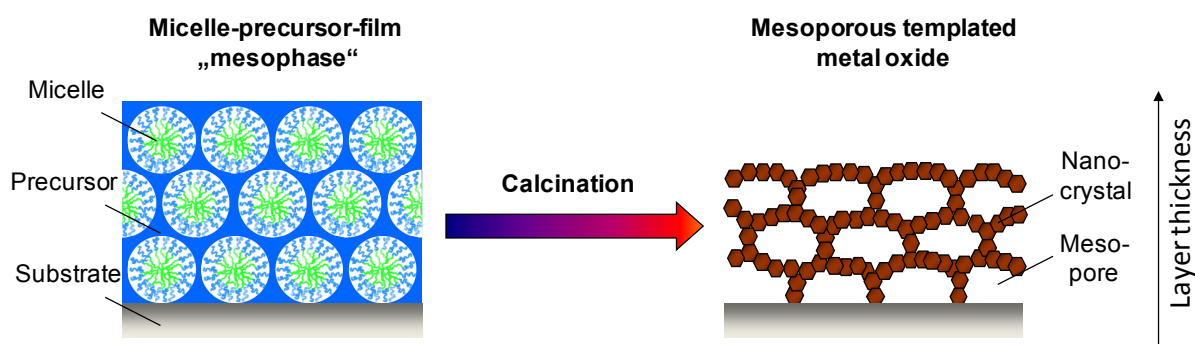
Figure 8: General scheme for the synthesis of mesoporous templated metal oxides. The micelle-precursor-film obtained by dipcoating (described in chapter 2.2.7) is thermally treated in air. Thus, decomposition of micelles and transformation of the precursor into a metal oxide with nanocrystalline structures takes place. Furthermore, template removal is accompanied by film shrinkage perpendicular to the substrate.

Polymer templating is a powerful route to introduce mesoporosity in various metal oxides, i.e. TiO_2,[98, 116] IrO_2,[65] NiO,[117] RuO_2,[118] SnO_2,[105] Nb_2O_5,[105] MgO.[103] Thus, the next chapters describe different synthesis approaches for the preparation of Al_2O_3, MgO, Co_3O_4, ZnO (all chapter 2.3.1), TiO_2 (chapter 2.3.2), and IrO_2 (chapter 2.3.3).

2.3 Synthesis routes for metal oxides

The following chapter (2.3) introduces synthesis concepts based on different metal oxide precursor systems for the preparation of mesoporous metal oxides such as Al, Mg, Co, Zn, Ti and Ir. Chapter 2.3.1 presents a very simple and versatile approach for the successful preparation of metal oxides from aluminum, magnesium, cobalt and zinc. The synthesis succeeds by employing a metal complex formed from citric acid and metal nitrate along with a triblock copolymer PEO_{213}-PB_{184}-PEO_{213} employed as a mesopore template. Chapter 2.3.2 introduces exemplarily different precursor concepts reported in literature to obtain mesoporous templated titania. Finally, chapter 2.3.3 shows to the best of our knowledge, the only synthesis concepts based on polymer templating for the preparation of mesoporous iridium oxide.

2.3.1 Synthesis concepts for mesoporous Al$_2$O$_3$, MgO, Co$_3$O$_4$, ZnO - The "citrate route"

Eckhardt et al.[103, 119] presented a synthesis route which combines three different strategies such as i) complexing the metal ion (Pechini method), ii) decomposing the carbonate and iii) pore templating with polymer micelles. The approach tackle typical problems associated with the building mechanism of mesoporous oxides, thus granting access to various metal oxide and even carbonate compounds of Al,[119] Mg,[103] Co,[119] and Zn.[119]
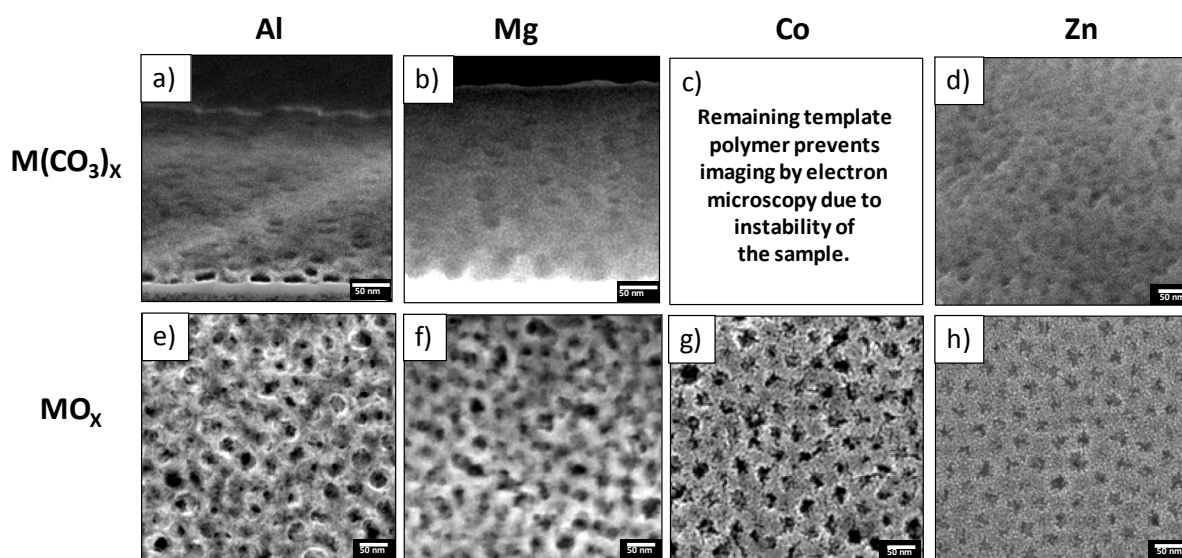
Figure 9: Scanning electron microscopy (SEM) images of accessible mesoporous templated metal carbonates and oxides of aluminium, magnesium, cobalt and zinc. All compounds were synthesized via citrate route. (SEM images taken from Eckhardt et al.[103, 119] and reprinted with permission from the American Chemical Society)

Five different boundary conditions must be fulfilled in order to provide a generalized synthesis approach for metal oxides. Figure 10 illustrates the different requirements usually associated with the synthesis strategy:

1) Metal salts have to form a chemical complex with ligands containing carboxylic acid functionality (e.g. citric acid). Moreover, chelating ligands are favored due to their higher chemical stability.

2) The solution is coated onto a substrate leading to solvent evaporation. The containing polymer should possess the capability of evaporation induced self assembly. Self assembly is required for the successful formation of an ordered micelle-precursor-film mesophase.

3) The metal complex should show the ability to transfer into a carbonate at temperatures below the descomposition temperature of the polymer template. Transformation of the metal complex into a carbonate prior template removal is epecially important for preventing pore structure collapsing thus providing stabilization of the micelle-precursor-film mesophase.

4) The pore template must be removed prior to metal carbonate decomposition in order to obtain a mesoporous metal carbonate. Otherwise, the mesoporous structure of the metal carbonate is not accessible due to the presence of pore template.

5) Finally, a calcination step is applied to decompose the metal carbonate consequently leading to formation of nanocrystalline metal oxides with preserved pore structure.
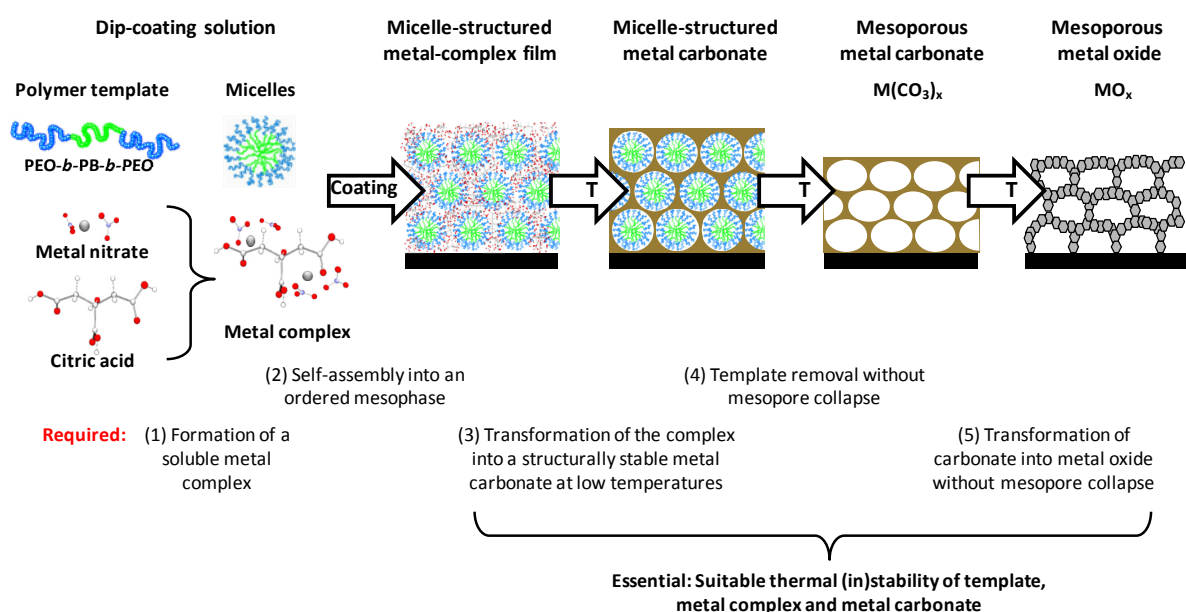
Figure 10: The citric acid complexed metal nitrate synthesis route is shown together with the deduced requirements (1-5). Necessary requirements for the successful preparation of mesoporous templated metal oxides are as followed: 1) Formation of a soluble metal complex (i.e. metal nitrate and citric acid). 2) Film deposition to induce self assembly of polymer template and obtain an ordered mesophase. 3) Precursor decomposition and transformation of the complex into a structurally stable carbonate at low temperatures under retaining the ordered mesophase. 4) Heat treatment in air to decompose polymer template and generate mesoporous metal carbonate with accessible mesoporosity. 5) Heat treatment at higher temperatures to transfer amorphous metal carbonates into nanocrystalline metal oxides under the release of CO_2 and preservation of the mesoporous system. Image taken from Eckhardt et al.[119] and reused with the permission of the American Chemical Society.

In case of MgO[103] the metal complex is formed in solution by treating magnesium nitrate with citric acid. The as prepared metal complex is transferred into a stable $MgCO_3$ phase by thermal treatment. Subsequently, a second calcination step at higher temperature leads to decomposition of the carbonate and finally results in the formation of a mesoporous templated MgO phase. The synthesis was conducted in ethanolic solution containing PEO-PB-PEO triblock copolymer employed as a polymer template and a metal complex as an oxide precursor. Dipcoating was performed on silicon substrate followed by calcination at 400 and 600 °C to obtain a mesoporous magesium carbonate and oxide. Another publication of Eckhardt et al.[119] demonstrate the versatility of the citric acid approach by showing the successful synthesis of micelle-templated oxides and carbonates of zinc, cobalt and aluminium (see Figure 9 for corresponding SEM images).

2.3.2 Synthesis concepts for mesoporous TiO_2

Several synthesis routes are available for the preparation of mesoporous templated TiO_2. Figure 11 exemplarily shows a selection of electron microscopy images of TiO_2 obtained by different metal oxide precursors such as a) $Ti(^iPrO)_4$, b) $TiCl_4$, c) preformed TiO_2 nanocrystals and d) TALH.

$Ti(^iPrO)_4$ + stabilizer $TiCl_4$ TiO_2 nanocrystals   TALH
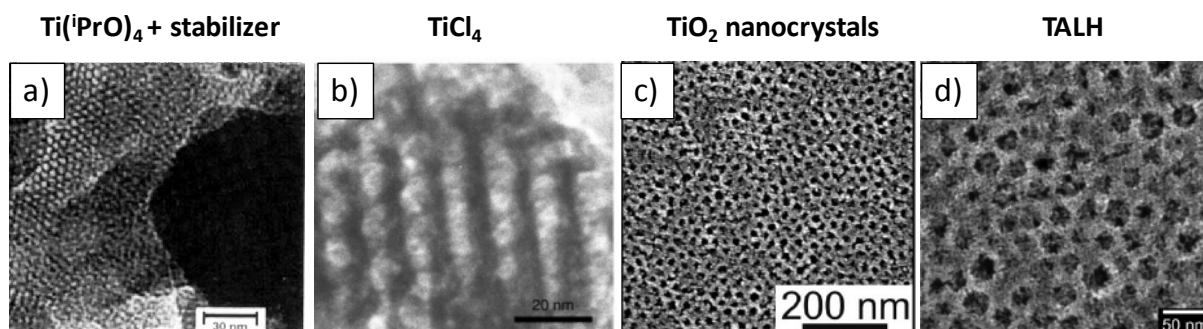
Figure 11: SEM micrographs of mesoporous templated TiO_2 synthesized from different precursors. a) Antonelli et al.[120] prepared pre-stabilized titanium isopropylate with acetylacetonate and subsequently introduced pore templating polymers. b) Yang et al.[105] achieved self-stabilization of titanium species by providing intrinsically acidic environments through HCl, which is released by the reaction of $TiCl_4$ in water ethanol-rich solutions. c) Brezesinski et al.[95] first prepared TiO_2 nanocrystals and subsequently added KLE as a pore template. d) Ortel et al.[109] worked in non acidic conditions by employing lactic acid complexed titanium (TALH) as a titania source and PEO-PB-PEO triblock copolymer as a mesopore template. All pictures have been taken from the respective publications.

a) One of the first synthesis approaches to obtain mesoporous TiO_2 was published by Antonelli et al.[120] The authors prepared acetylacetonate stabilized titanium alkoxides such as $Ti(^iPrO)_4$. The exclusion of the stabilizing agent (acetylacetonate) immediately led to excessive hydrolysis and condensation reaction, thus precipitation of the oxide-alkoxide aggregates. However, the stabilized titanium alkoxide was added to a solution containing a

polymer template (e.g. tetradecylphosphate). After several synthesis steps including a final heat treatment under air preserved the first hexagonally packed mesoporous TiO_2 with a surface area of 200 m²/g and a pore opening with 3.2 nm in diameter.

b) No stabilizing agent is necessary in the case of $TiCl_4$ being utilized as a TiO_2 source as it provides self stabilization. The route was published by Yang et al.[105] and exploits the formation of HCl during hydrolysis of $TiCl_4$ in a water ethanol-rich solution. The formation of HCl induces strong acidic environments thus suppressing further polycondensation of the oxide-alkoxide aggregates. The stabilized titanium alkoxides are subsequently mixed with suitable polymers (e.g. P123) and heat treated in air to obtain mesoporous templated TiO_2 in anatase phase with a crystallite size of 2.4 nm. Further physicochemical analysis revealed a pore size of 6.5 nm and a BET surface area of 205 m²/g.

c) Brezesinski et al.[95] sythesized pre-formed TiO_2 nanocrystals from $TiCl_4$, EtOH and benzyl alcohol. Afterwards, the obtained nanoparticles were redispersed in ethanol and subsequently mixed with KLE as a pore template. Dipcoating and heat treatment in air at 600 °C leads to the formation of mesoporous templated TiO_2 layers. The derived layers show bimodal porosity with 1 - 4 and 20 - 25 nm diameter pores. Further physicochemical analysis revealed a body centered cubic packing of the pore system and a BET surface area in the range between 180 - 200 m²/g.

d) Moreover, Ortel et al.[109] prepared a solution of lactic acid complexed titanium (titanium(IV) bis(ammonium lactato)dihydroxide abbreviated as TALH), polymer template (e.g PEO-PB-PEO, F127), water and ethanol. Due to the high chemical stability of the metal complex no hydrolysis and condensation reaction occur under non acidic conditions. Subsequently, the solution was dipcoated on different substrates and heat treated in air. The prepared mesoporous templated TiO_2 showed high surface area, exhibited an anatase structure and showed locally ordered mesopores with an opening of 13.5 nm (F127) and 29.4 nm (PEO-PB-PEO) in diameter.

2.3.3 Synthesis concepts for mesoporous IrO_2

Only a few precursor concepts for the preparation of polymer templated IrO_2 is reported in literature. Figure 12 shows different iridium oxide precursors used along with amphiphilic block copolymers to obtain mesoporous IrO_2.
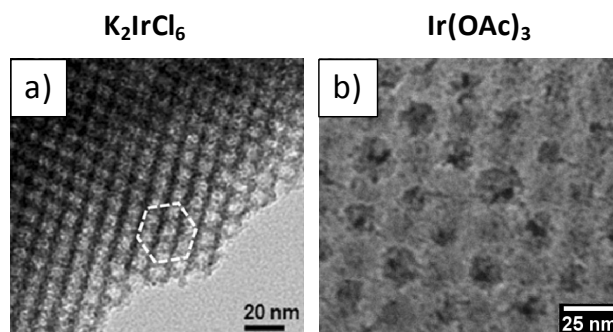
Figure 12: SEM images of polymer templated IrO_2 obtained by a) F127, K_2IrCl_6 and alkaline hydrolysis[121] and b) PEO-PB-PEO and $Ir(OAc)_3$. [65] Images were taken from the respective publications.

a) Chandra et al.[121] used PEO-PPO-PEO (F127) block copolymer as a pore template and a monomeric $[Ir(OH)_6]^{2-}$ complex obtained by alkaline hydrolysis of K_2IrCl_6 as an oxide precursor. The solution was spincoated onto FTO substrate dried at 80 °C, annealed at 150 °C and finally heat treated at temperatures between 400 - 500 °C, respectively. Thicker layers were obtained by multi spincoating with intermediate drying (80 °C) and annealing (150 °C). Physicochemical analysis revealed a pore diameter of 7 nm, layer thickness of ca. 70 nm and BET surface areas between 65 m²/g ($T_{calc.}$ = 400 °C) and 105 m²/g ($T_{calc.}$ = 500 °C).

b) Ortel et al.[65] prepared an ethanol rich solution containing iridium acetate as a metal oxide precursor and employed PEO-PB-PEO polymer as a pore template. The solution was dipcoated on different substrates and consequently heat treated under air. The authors reported a pore diameter of ~16 nm, rutile type structure, a locally ordered pore arrangement and BET surface areas between 140 ($T_{calc.}$ = 300 °C) and 20 ($T_{calc.}$ = 700 °C) m² per m² of geometric surface area.

2.4 Deduced thesis aim and approaches

The aim of this thesis is to obtain catalysts with higher electrocatalytic oxygen evolution reaction activity compared to commercially available catalyst powders and to understand the factors that control OER activity.

To achieve this goal the synthesis route presented for oxides of Al, Mg, Co, Zn (see chapter 2.3.1) is extended to Ni for electrochemical testing in alkaline media. The synthesis approaches for IrO_2 by $Ir(OAc)_3$ (chapter 2.3.3) and TiO_2 from $TiCl_4$ and TALH (chapter 2.3.2) are combined in order to obtain mesoporous templated layers of IrO_2 and mixed metal oxides IrO_2/TiO_2 with higher catalytic activity in acidic media compared to a commercial reference.

A controlled variation of synthesis parameters during the preparation of mesoporous templated catalytic layers, i.e. NiO, IrO_2, IrO_2/TiO_2 was performed. An extensive analysis for the impact of synthesis parameters on structural properties and electrochemical activity was performed. The obtained data were then evaluated in order to identify the optimal synthesis conditions for the generation of highly active electrocatalysts. The varied parameters were: i) calcination temperature, ii) iridium loading and iii) withdrawal rate.

i) Heat treatment conducted at different temperatures was used in order to study the effect of crystallinity on intrinsic and overall OER activity. ii) A different amount of iridium oxide was dispersed within TiO_2 to obtain samples with different electrical conductivity. The different electrical conductivity was then used to identify changes in electron transport mechanisms. iii) By varying the withdrawal rate electrocatalytic coatings with different layer thicknesses were obtained. The catalysts were used as a model type system to identify potential gas removal limitation at high electrical current densities and potentials.

A comprehensive investigation and comparison of physicochemical and electrochemical properties revealed that the overall OER activity is affected by several parameters such as crystallinity, electrical conductivity and active surface area. However, no signs of transport limitations were detected for systems with high layer thicknesses at high gas production rates.

2.5 Thesis outline

Chapter 3 illustrates experimental data by offering information about the synthesis of mesoporous templated catalytic coatings on different substrates (chapter 3.1). Moreover, the applied physicochemical techniques (chapter 3.2) to determine structural properties and electrocatalytic testing procedures (chapter 3.3) for quantifying the oxygen evolution reaction activity and electrochemical accessible surface area are explained.

The results and discussion are presented in chapter 4. Chapter 4.1 describes a new approach for the synthesis of NiO coatings with narrow pore size distribution and tunable mesopore size. The synthesis is based on micelles of amphiphilic block copolymers employed as a pore template and citric acid complexed metal compounds. The versatility of the citrate based synthesis approach is confirmed by showing the accessibility of homogeneous NiO coatings with templated and locally ordered mesoporous structure. The electrochemical OER activity is investigated in alkaline media to deduce structure activity relationships. Moreover, a comparison of OER activity with reports from literature is provided.[122]

Chapter 4.2 exploits the potential of pore templating with polymer micelles in order to produce model-type porous catalysts for the investigation of structure-activity relationships in gas evolution reactions and for the optimization of the performance of IrO_2-based OER catalysts. The developed synthesis from Ortel[65] based on pore templating with micelles of amphiphilic block copolymers PEO-PB-PEO[65, 98] is further improved to produce iridium oxide films with controlled pore size, film thickness and crystallinity. The model systems are used to study the influence of porosity and crystallinity on electrochemically accessible surface area (ECSA), OER performance and gas transport. A controlled variation in thickness of the porous catalysts explores, which parts of the catalyst can be utilized without transport limitations during high-current OER. The combined knowledge is used to design a multilayer-IrO_2 catalyst that shows the lowest overpotential reported so far for monometallic oxide compounds of Ir.[47]

Chapter 4.3 and 4.4 investigate two different synthesis routes for the preparation of mixed Ir and Ti metal oxides. Both routes are based on a soft templating approach with PEO_{213}-PB_{184}-PEO_{213} as a pore template, iridium acetate as an IrO_2 source and either $TiCl_4$ (chapter 4.3) or TALH (chapter 4.4) as a titania precursor. The chemical properties of $TiCl_4$ and TALH vary from each other leading to different interaction with the dissolved polymer template thus providing different morphological properties such as metal oxide distribution. The influence of calcination temperature and iridium content for both synthesis routes is investigated in terms

of surface area, crystallinity, conductivity, morphology and OER activity. Correlations of the obtained data are used to identify OER-controlling parameters for the successful preparation of highly active OER electrocatalysts.

Chapter 4.5 illustrates the electrocatalytic performance of commercially available catalyst powders. The purchased powders were deposited on the working electrode by a typical "Nafion-ink" based synthesis approach. Electrocatalytic investigations were conducted in order to identify the most active commercial powder. Moreover, the reproducibility of the ink-based synthesis approach is shown by applying different iridium loadings on the working electrode. The obtained data are used to determine the iridium mass based OER activity for commercial reference catalyst powders.

Chapter 5 presents combined observations of systems used for electrochemical testing under acidic condition, i.e. IrO_2 and IrO_2/TiO_2. This general discussion is used to identify general trends and deduce potential structure-activity relationships. Synthesis parameters such as calcination temperature, crystallinity, electrical conductivity, electrochemical active surface area (ECSA) and layer thickness were identified as the most relevant OER-controlling parameters. Furthermore, the applied overpotential during electrocatalytic investigation showed to possess an impact on kinetical aspects, i.e. Tafel slope. A comprehensive study on observed structure-activity relations revealed high OER activities for samples exhibiting low crystallinity, high electrical conductivity and large ECSA. Synthesized catalytic coatings of IrO_2 (chapter 4.2) and IrO_2/TiO_2 (chapter 4.3 ($Ir(OAc)_3$ + $TiCl_4$) and chapter 4.4 ($Ir(OAc)_3$ + TALH)) fulfilling the observed criteria are then used for comparison with commercial catalytic powders (from chapter 4.5) in terms of iridium mass based OER activity. The observed iridium mass normalized OER activity of polymer templated IrO_2 and IrO_2/TiO_2 appear to be at least 10 times higher than for commercially available catalysts.

3 Experimental

The present chapter (3) contains information about the synthesis of micelle-templated films (chapter 3.1) and the applied analytical methods in order to determine morphology, crystallinity, phase composition, surface area, pore ordering, surface composition and electrical conductivity (chapter 3.2). Moreover, the electrocatalytic testing is described in detail (chapter 3.3) offering information about the investigation of oxygen evolution reaction (OER) activity and electrochemical active surface area (ECSA) in acidic and alkaline media, respectively.

3.1 Synthesis of micelle-templated films

Dipcoating (Coater 5 AC, IdLabs Vesely) was used in order to deposit thin metal oxide films on a suitable substrate. Different substrates were used for the investigation of certain structural and catalytical properties: Physicochemical analysis was conducted for samples coated on single side polished silicon wafers (SEM, XRD, TEM, SAED, XPS), double side polished silicon wafers (physisorption), microscope slides (electrical conductivity), titanium foil (SAXS) and titanium sheets/cylinders (SEM, XRD, TEM, SAED) Electrochemical investigations were solely performed for layers coated on titanium sheets and cylinders (OER, ECSA, DEMS). Prior to coating, silicon as well as titanium substrates passed through different cleaning procedures. Silicon wafers, titanium foil and microscope slides were washed with ethanol, whereas titanium substrates were firstly polished by SiO_2-polishing paste (Buehler, MasterMet 2, noncrystallizing colloidal silica suspension, 0.02 μm), then ultrasonicated in water and eventually rinsed with ethanol (VWR Chemicals, 99.98 % absolute).[122]

3.1.1 Mesoporous nickel oxide films

The solution for dipcoating was obtained by first dissolving 70 mg of a polymer template poly(ethylene oxide)-*b*-poly(butadiene)-*b*-poly(ethylene oxide) (PEO_{213}-PB_{184}-PEO_{213}, containing 18 700 g mol^{-1} PEO and 10 000 g mol^{-1} PB, from Polymer Service Merseburg GmbH)[65, 98] in 0.2 mL water (milliQ) and 2.8 mL ethanol. The solution was stirred for 12 h. Subsequently, 144.1 mg of citric acid (Carl Roth, 99.5 % p.a.) and 436.0 mg of $Ni(NO_3)_2 \cdot 6H_2O$ (NeoLab, 98 %) were added.

The obtained green solution was transferred to a cuvette inside a dipcoater, where a controlled atmosphere had been established with a temperature of 25 °C and a relative humidity of 40 %. Dipcoating was performed at a withdrawal rate of 200 mm/min. Freshly coated samples were dried for another 10 minutes under same conditions. Followed by two subsequent heat treatments, the freshly synthesized samples were first thermally treated for

1 hour in a prehated drying oven at 250 °C and then calcined for 1 hour in a preheated muffle furnace at 350, 400, 450 and 500 °C, respectively.

3.1.2 Mesoporous iridium oxide films synthesized from Ir(OAc)$_3$

Mesoporous IrO$_2$ films were synthesized on polished titanium cylinders following a procedure established by Ortel et al.[65] Dipcoating solutions for calcination studies were obtained by adding 225 mg Iridium(III) acetate (Heraeus, 48.76 % Ir content) and 45 mg of a polymer template poly(ethylene oxide)-*b*-poly(butadiene)-*b*-poly(ethylene oxide) (containing 18 700 g/mol PEO and 10 000 g/mol PB, from Polymer Service Merseburg GmbH)[98] to a volume of 1.5 mL ethanol. For thicker films and multilayers a volume of 1.3 mL EtOH and 0.1 mL H$_2$O was used.

Dipcoating of single layer catalysts was performed under controlled atmosphere at a relative humidity of 40 % and a temperature of 25 °C at a withdrawal rate of 100 mm/min in a dipcoater. Films were calcined subsequently placing the samples for 5 min in a hot muffle furnace with air atmosphere at temperatures between 325 and 625 °C, respectively. For the controlled variation of film thickness the substrates withdrawal rate was adjusted between 10 and 150 mm/min using the same calcination routine (5 min, 375 °C). Multilayer catalysts were obtained by repeated dipcoating (30 mm/min) and heat treating (30 min, 200 °C) of individual layers followed by a final calcination step (5 min, 375 °C).[47]

3.1.3 Mesoporous mixed oxide films of Ir and Ti synthesized from Ir(OAc)$_3$ and TiCl$_4$

The dipcoating solution for the preparation of 30 wt. % Ir in Ir/TiO$_2$ was obtained by dissolving 35 mg of a polymer template poly(ethylene oxide)-*b*-poly(butadiene)-*b*-poly(ethylene oxide) (PEO$_{213}$-PB$_{184}$-PEO$_{213}$, containing 18 700 g mol^{-1} PEO and 10 000 g mol^{-1} PB, from Polymer Service Merseburg GmbH)[65, 98] in 1.25 mL ethanol (99.9 %, Roth) and 0.21 mL milliQ water. Subsequently, a solution containing 1.25 mL EtOH and 93.3 µL of titanium(IV) chloride (TiCl$_4$, 99.9 %, Sigma Aldrich) was added dropwise under stirring. Finally, 55.8 mg Ir(III) acetate (Heraeus, 48.76 % Ir content) was added to the solution.

The obtained dark green solution was transferred to a cuvette inside a dipcoater, where a controlled atmosphere has been established with a temperature of 25 °C and a relative humidity of 40 %. Dipcoating was performed at a withdrawal rate of 200 mm/min on polished titanium substrate. Freshly coated samples were dried for another 10 minutes under the same conditions. Afterwards, the samples were calcined in a preheated muffle furnace for 10 minutes under air at temperatures between 200 to 600 °C, respectively.

3.1.4 Mesoporous mixed oxide films of Ir and Ti synthesized from Ir(OAc)$_3$ and TALH

Solution for dipcoating a layer of 30 wt. % Ir in Ir/TiO$_2$ was obtained by dissolving 35 mg of a polymer template poly(ethylene oxide)-*b*-poly(butadiene)-*b*-poly(ethylene oxide) (PEO$_{213}$-PB$_{184}$-PEO$_{213}$, containing 18 700 g mol^{-1} PEO and 10 000 g mol^{-1} PB, from Polymer Service Merseburg GmbH)[65, 98] and 55.8 mg Ir(III) acetate (Heraeus, 48.76 % Ir content) in 2.5 mL methanol (Sigma Aldrich). Subsequently, 408.6 µL of Titanium(IV) bis (ammonium lactate) dihydroxide solution (TALH, 50 wt. % in H$_2$O, Sigma Aldrich) was added dropwise under stirring.

Obtained dark green solution was transferred to a cuvette inside a dipcoater, where a controlled atmosphere has been established with a temperature of 25 °C and a relative humidity of 40 %. Dipcoating took place with a withdrawal rate of 200 mm/min on polished titanium substrate. Freshly coated samples were dried for another 10 minutes under the same conditions. Afterwards, the samples were calcined in a preheated muffle furnace for 10 minutes under air at temperatures between 200 to 600 °C, respectively.

3.1.5 Reference catalyst (IrO$_x$/TiO$_x$)

The dispersion for dropcasting a layer of commercial availabe IrO$_x$/TiO$_x$ was derived by suspending 5.4 mg of IrO$_x$/TiO$_x$ powder (73.9 wt. % Ir in TiO$_2$, "Elyst 750480", Umicore) in 2.49 mL water (milliQ), 2.49 mL iPrOH (> 99.5 %, Roth) and 20 µL Nafion perfluorinated resin solution (5 wt. % in lower aliphatic alcohols and water, contains 15-20 % H$_2$O, Sigma Aldrich). The dispersion was ultrasonicated for 15 minutes showing a black appearance ("ink"). Subsequently, 5 µL of the ink was pipeted onto a polished titanium cylinder (A = 0.1963 cm²) under room temperature. The titanium cylinder was transferred into a preheated furnace and dried at 60 °C for 5 minutes. The nominal loading of iridium metal on the titanium cylinder amounts to ca. 4 µg (~20 µg$_{Ir}$/cm²). Higher loadings were achieved by multi dropcasting (repeated pipeting of 5 µL several times) with intermediate drying steps at 60 °C for 5 minutes. The procedure was used to produce nominal loadings (iridium metal) between ca. 4 - 800 µg$_{Ir}$ (20 - 4075 µg$_{Ir}$/cm²).

3.1.6 Reference catalyst (IrO$_2$, Sigma Aldrich)

5 mg of commercially available IrO$_2$ powder (99.9 %, Sigma Aldrich) was dispersed in 2.49 mL water (milliQ), 2.49 mL iPrOH (> 99.5 %, Roth) and 20 µL Nafion perfluorinated resin solution (5 wt. % in lower aliphatic alcohols and water, contains 15-20 % H$_2$O, Sigma Aldrich). The suspension was ultrasonicated for 15 minutes showing black colour. Subsequently, 3 µL of the dispersion was dropcasted onto a titanium cylinder followed by a drying step in a preheated furnace at 60 °C for 5 minutes. The obtained IrO$_2$ catalyst on a titanium cylinder exhibit nominal loadings of 2.57 µg$_{Ir}$ (13.1 µg$_{Ir}$/cm²).

3.2 Analytical methods

The present chapter (3.2) offers information about the spectrum of physicochemical techniques used for determining the morphology (3.2.1: SEM, 3.2.2: TEM), crystallinity and phase composition (3.2.2: SAED, 3.2.3: XRD), surface area (3.2.4: Kr-physisorption), locally pore ordering (3.2.5: SAXS), surface composition (3.2.6: XPS), electrical conductivity (3.2.7), iridium content (3.2.8: ICP-OES) and faraday efficiency (3.2.9: DEMS).

3.2.1 Scanning electron microscopy (SEM)

SEM images were obtained using a JEOL 7401F instrument with an accelerating voltage of 10 kV. To determine film thickness of mesoporous iridium oxide films, a ceramic knife was used to scratch the layer followed by SEM imaging of tilted Ti cylinders. SEM images were analyzed with ImageJ v1.43u[123] to derive film thickness and pore diameter.[47]

3.2.2 Transmission electron micrographs (TEM) and selected area diffraction (SAED)

TEM and SAED images were obtained with a FEI Tecnai G² 20 S-Twin at an accelerating voltage of 200 kV. The film samples were scraped off from a titanium cylinder or sheet and then collected with a TEM-grid.[47] TEM micrographs were obtained in brightfield and high angle annular darkfield (HAADF, 3° tilt angle) mode. SAED images were recorded in diffraction mode at a sample area of ca. 200 nm in diameter. During TEM operation the electron dose was lowered by broadening the electron beam to prevent potential reduction of metal oxide compounds.

3.2.3 X-ray diffraction (XRD)

XRD patterns were recorded with a Bruker D8 Advance instrument using Cu K_α radiation, grazing incident for the incoming beam and a Goebel mirror. Scherrer equation was applied to certain reflections in order to determine crystallite size for phases of IrO_2 (110),[47] TiO_2 rutile (110), TiO_2 anatase (101) and NiO bunsenite (111) and (200).

3.2.4 Kr-physisorption

Surface area was measured with Kr physisorption at 77 K using the Autosorb-iQ automated gas adsorption station from Quantachrome and samples coated on double side polished silicon wafers. Prior to adsorption measurement the samples were degassed for 2 h at 150 °C in vacuum. The surface area was calculated via Brunauer-Emmett-Teller (BET) method.[122]

3.2.5 Small angle X-ray scattering (SAXS)

NiO 2D small angle X-ray diffraction (SAXS) measurements were performed at BESSY PCB beamline, using a wavelength of 1.5498 Å (8 keV), a 2D detector (981 x 1043 pixel) with a sample to detector distance of 1920 mm. Samples were mounted on a moveable sample holder, ensuring rotation of samples between 90° and 20° with respect to incident beam. Investigated oxide and carbonate films were coated on thin silicon wafers (50 µm) and analyzed in transmission mode at angles of β=90° or β=20° with respect to substrate normal.[122]

IrO$_2$ and IrO$_2$/TiO$_2$ 2D SAXS patterns (small angle X-ray scattering) were recorded on a Bruker Nanostar (three-pinhole collimation system) using a copper anode as X-ray source (CuK$_\alpha$ radiation), a 2D detector (2-D HI STAR 1024 x 1024 pixels) with a sample to detector distance of 670 mm and employing a sample holder that enabled rotation of the sample between 90° and 20° relative to incident beam. Respective oxide films were coated on thin titanium foil and analyzed in transmission mode with a beam incident angle of β = 90° and β = 20° with respect to the film surface.

3.2.6 X-ray photoelectron spectroscopy (XPS)

XPS measurements have been carried out with an ESCALab 200X photoelectron spectrometer (VG Scientific, U.K.) for all samples. XPS were recorded at an angle of emission of 0° using non-monochromatized Al K$_\alpha$ excitation. The Binding energy (BE) scale was calibrated using the C1s component of aliphatic hydrocarbon at BE = 285.0 eV.[122] Observed signals were finally associated with specific binding energies reported in literature and listed in NIST Chemistry WebBook, NIST Standard Reference Database

3.2.7 Electrical conductivity

Electrical conductivity was measured for catalytic coatings on microscope slides with a Keithley Model 6517B Electrometer employing a 8x8 pin probe head with an altering polarity sequence of the pins. Light induced enhancement of conductivity observed for semiconducting materials (e.g. TiO$_2$) was avoided by measuring under dark environment. Applied potential was varied between 1 V - 10 V and was increased by a factor of 1.2 for each step. The recorded current response was plotted as a function of potential. The observed slope corresponds to the electrical sheet conductivity and is expressed as (Ohm/sq)$^{-1}$. The volume conductivity of each catalytic layer can be derived by dividing sheet conductivity by layer thickness (expressed as (Ohm·m)$^{-1}$ or S·m^{-1}).

3.2.8 Inductively coupled plasma - optical emission spectrometry (ICP-OES)

The iridium loading on titanium substrates (diameters: cylinder 5 mm; sheets 6 mm) was determined by first suspending the sample in a mixture of 6 mL HCl (37 %, Roth), 2 mL HNO_3 (69 % Roth), 2 mL H_2SO_4 (96 %, Roth) and 40 mg $NaClO_3$ (99.0 %, Alfa Aesar). The obtained suspension was slowly stirred (130 rpm) for at least 3 hours under room temperature and subsequently transferred into a microwave (Discover, SP-D, CEM Corporation) for acid digestion at 180 °C (ramp 15 K/min, 40 min, 18 bar). 2 mL water (milliQ) was added to the solution after completion of a cooling down period. The as prepared solution was analyzed in a 715-ES-inductively coupled plasma system (ICP-OES, CCD detector, Varian) in order to determine the iridium content.

3.2.9 Differential electrochemical mass spectrometry (DEMS)

The amount of formed gas products was assessed in separate DEMS experiments utilizing mesoporous templated IrO_2 coated onto titanium cylinders. The DEMS apparatus is partly based on a design reported elsewhere[124] and consisted of an electrochemical flow cell (0.5 M H_2SO_4, flow rate: 5 µL/s) connected via separation PTFE membrane to a PrismaTM quadrupole mass spectrometer (QMS 200, Pfeiffer-Vacuum) equipped with two turbomolecular pumps HiPace 80 operating the MS chamber at 10^{-6} mbar. The MS was calibrated with a reference gas CO_2 in N_2/O_2 (Linde, 75.04 % N_2; 19.95 % O_2; 5.01 % CO_2). Cyclovoltammetric measurements were conducted in the OER regime by cycling the potential between 1.20 - 1.65 V_{RHE} (6 mV/s) while recording the ion current for O_2 (mass 32) and CO_2 (mass 44). The amount of evolved O_2 and CO_2 was calculated from the ion currents.[47]

3.3 Electrocatalytic testing

The following chapter contains detailed information about the electrochemical setup (chapter 3.3.1) and measuring procedures to determine the OER activity in alkaline (chapter 3.3.2) and acidic media (chapter 3.3.3), respectively. Moreover, the electrochemical active surface area (ECSA) was assessed for samples tested under acidic conditions (chapter 3.3.3).

3.3.1 Electrochemical setup

Electrocatalytic testing was performed in a three electrode disc setup using a Biologic SP 200 potentiostat, a reversible hydrogen electrode (Gaskatel, HydroFlex®) as a reference and a Pt-gauze (Chempur, 1024 mesh/cm², 0.06 mm wire diameter, 99.9 %) as a counter electrode. All potentials in this work are referred to the reversible hydrogen electrode and are iR corrected. The utilized electrochemical setup is schematically shown in Figure 13.
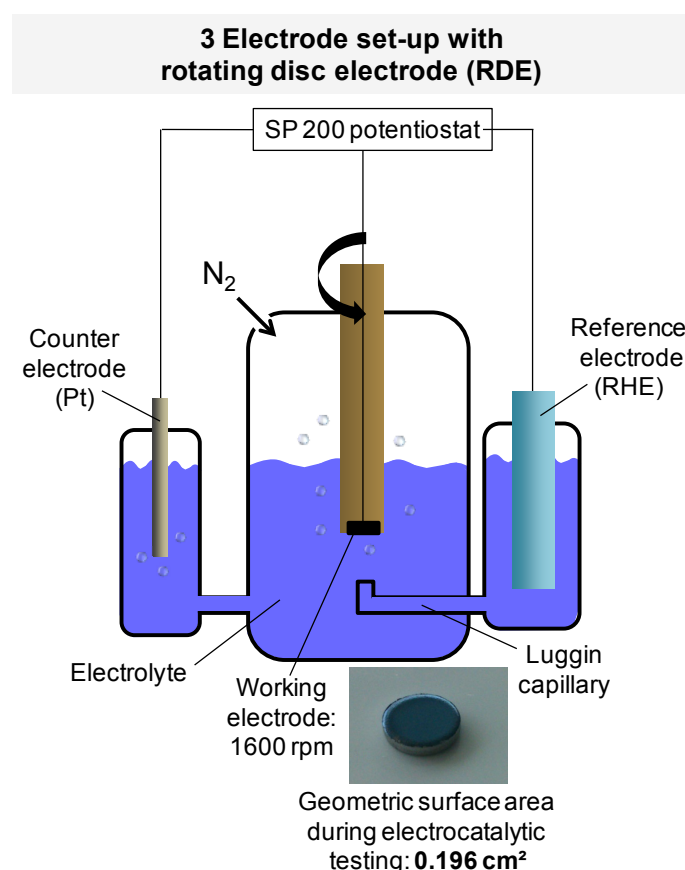

Figure 13: Electrochemical setup used for the determination of the oxygen evolution reaction (OER) activity and electrochemical accessible surface area (ECSA). Catalytic layers of NiO, IrO$_2$ and IrO$_2$/TiO$_2$ were deposited on titanium and served as the working electrode. Platinum gauze was used as a counter electrode. The applied potential is referred to a reversible hydrogen electrode and corrected for iR drop. Electrochemical testings were either performed with supporting electrolytes of KOH (alkaline, NiO) or H$_2$SO$_4$ (acidic, IrO$_2$, IrO$_2$/TiO$_2$).

All films coated on titanium cylinders or sheets (5 mm in diameter) were mounted on a rotating disk shaft and served as a working electrode (n = 1600 rpm) using H$_2$SO$_4$ (Fixanal,

Fluka Analytical) or KOH (Sigma Aldrich, pellets, ≥85 %) as supporting electrolyte. The electrolyte solution was purged with nitrogen prior to catalytic tests.

3.3.2 Alkaline procedure in KOH (NiO)

The OER activity was investigated by cyclic voltammetry in a potential window ranging between 1.20 - 1.95 V_{RHE} in 0.1 M KOH at a scan rate of 6 mV/s.[47, 122] Furthermore, NiO was electrochemically activated[27] in 1.0 M KOH at a static applied potential of 1.75 V_{RHE} for 5 hours. After every hour of chronoamperometric treatment an intermediated cyclic voltammogram was conducted at a scan rate of 20 mV/s in order to assess increasing oxygen evolution reaction performance as well as redox waves prior the OER onset. [47, 122]

3.3.3 Acidic procedure in H_2SO_4 (IrO$_2$ and IrO$_2$/TiO$_2$)

The OER activity of mesoporous templated catalytic coating, i.e. IrO_2 and IrO_2/TiO_2 was investigated by cyclic voltammetry in a potential window ranging between 1.20 - 1.65 V_{RHE} in 0.5 M H_2SO_4 at a scan rate of 6 mV/s.[47, 122] To analyze the electrochemically accessible surface area (ECSA) the potential was sweeped between 0.40 and 1.40 V_{RHE} at a scan rate of 50 mV/s. Placing hydrous IrO_2 in solution and alter the potential will change the valence state of surface metal atoms. TiO_2 shows no significant current response in the applied potential range. Furthermore, a reversible proton inclusion mechanism can take place as described by Trasatti et al.[125]:

$$IrO_x(OH)_y + \delta\ H^+ + \delta\ e^- \rightarrow IrO_{x-\delta}(OH)_{y+\delta}$$
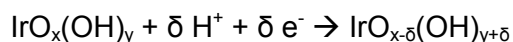
The ECSA of iridium oxide and mixed metal oxides of iridium and titanium was then quantified by determining the mean value of the integrated anodic and cathodic scan of the resulting cyclic voltammogram.[47, 55, 125-126]

4 Results and discussion

The following chapter (4) presents the synthesis approach for each mesoporous templated system, i.e. NiO, IrO_2 and mixed metal oxides of IrO_2/TiO_2. Subsequent to the film formation all samples were characterized physicochemical. The resulting data were evaluated and used for the creation of structure models containing detailed information on morphology, crystallinity, phase composition and surface area. Moreover, the catalytic coatings were electrochemically investigated to identify the performance in oxygen evolution reaction and quantify the electrochemical accessible surface area. The combined physicochemical and electrochemical data are then used to deduce structure-activity relationships. Exploiting this knowledge allows the design of highly active OER-electrocatalysts with iridium mass based OER-activities at least 10 times higher with respect to commercial available OER-catalysts.

Chapter 4.1 describes an approach for the synthesis of NiO by a citrate based synthesis approach. The electrochemical OER activity is investigated for NiO layers on titanium substrate in alkaline electrolyte solution to deduce structure activity relationships and conduct a comparison with OER activities reported in literature.

Chapter 4.2 presents the potential of pore templating with polymer micelles for the investigation of structure-activity relationships in gas evolution reactions and for the optimization of the performance of IrO_2-based OER catalysts. The chapter revealed that the OER performance of mesoporous IrO_2 is controlled by at least two independent factors, i.e. the accessible surface area and the intrinsic activity per accessible site.

Chapter 4.3 shows an extended approach for the preparation of mixed metal oxide layers with adjustable crystallinity and conductivity. The synthesis is based on micelles of triblock copolymers and two metal oxide precursors such as $Ir(OAc)_3$ and $TiCl_4$. Chapter 4.4 demonstrates a synthesis approach for designing an almost throughout mixed metal oxide comprising IrO_2 and TiO_2. The films were obtained by using a synthesis based on triblock copolymers and two metal oxide precursors with similar chemical properties, i.e. $Ir(OAc)_3$ and TALH. The obtained layers of both chapters (4.3 and 4.4) were characterized physicochemical and electrochemical. The obtained data were correlated to reveal structure-activity relations indicating that the overall OER activity and intrinsic reactivity is affected by the active surface area and electrical conductivity.

Chapter 4.5 illustrates a reproducible synthesis approach and the electrocatalytic performance of commercial available catalyst powders.

4.1 Mesoporous templated NiO synthesized from Ni(NO$_3$)$_2$ and citric acid

Chapter 4.1 demonstrates the synthesis of homogeneous NiO$_x$ coatings with a templated and locally ordered mesopore structure and their catalytic behaviour in alkaline OER. Mesoporous NiCO$_3$ and NiO films were obtained by deposition of Ni(NO$_3$)$_2$ in presence of citric acid and the mesopore template poly(ethylene oxide)-*b*-poly(butadiene)-*b*-poly(ethylene oxide) (PEO$_{213}$-PB$_{184}$-PEO$_{213}$). Chapter 4.1.1 shows the thermal stability of the polymer template and the nickel precursor investigated by thermogravimetric analysis (TGA) in order to derive suitable parameters for calcination of deposited films. The influence of calcination temperature on morphology, pore ordering and crystallinity of NiO and NiCO$_3$ layers were studied by scanning electron microscopy (SEM), transmission electron microscopy (TEM) small angle X-ray scattering (SAXS), selected area electron diffraction (SAED) and X-ray diffraction (XRD). The surface composition of the films was analyzed by X-ray photoelectron spectroscopy (XPS) (chapter 4.1.2). Differently calcined catalysts were tested in alkaline OER and studied by Kr-physisorption in order to deduce a direct relationship between OER activity and accessible surface area (chapter 4.1.3). Electrochemical activation studies similar to procedures reported in literature[27] resulted in further catalyst activation (chapter 4.1.4). Calcination at 350 °C produced NiO with low crystallinity yet high BET surface area and resulted after further electrochemical activation in the highest OER activity. The most active catalyst was further used for comparing the OER activity with reports from literature (chapter 4.1.5).

4.1.1 Thermal behavior of pore template and nickel precursor

Mesoporous templated NiO$_x$ films were deposited onto cleaned substrates (Ti, Si) via dipcoating performed at 25 °C and 40 % r.h. with 200 mm/min withdrawal rate. Dipcoating solutions contained a polymer template poly(ethylene oxide)-*b*-poly(butadiene)-*b*-poly(ethylene oxide) (PEO$_{213}$-PB$_{184}$-PEO$_{213}$),[65, 98] 0.2 mL water (milliQ) and 2.8 mL ethanol, to which 144.1 mg of citric acid and 436.0 mg of Ni(NO$_3$)$_2$·6 H$_2$O had been added. Freshly coated samples were dried for 10 minutes and further heat treated in air for (i) 1 hour at 250 °C and (ii) 1 hour at either 350, 400, 450 or 500 °C in a preheated muffle furnace (see experimental part for further details).

The synthesis method relies on the thermal transformation of the deposited mesophase of precursor complex and template polymer into the mesoporous carbonate and subsequent conversion into nickel oxide. Thermogravimetric analysis (TGA) was therefore employed to identify appropriate calcination conditions. Figure 14 shows the mass loss of a) template polymer PEO-PB-PEO and b) precursor complex formed from nickel nitrate and citric acid upon heating in air.
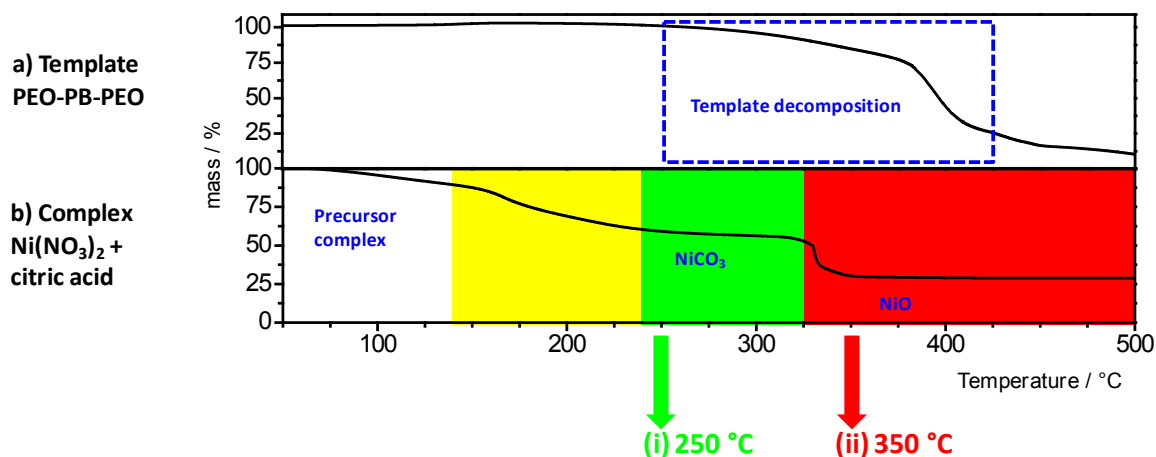
Figure 14: Thermogravimetric analysis (TGA) of a) template polymer PEO_{213}-PB_{184}-PEO_{213} and b) precursor complex formed from nickel nitrate and citric acid. a) Polymer starts to decompose at ca. 250 °C and rapidly decomposes between 350 °C and 425 °C. Nickel precursor complex shows a mass loss between 140 °C and 240 °C accompanied by release of CO_2 (online-MS), indicating the formation of $NiCO_3$. No significant mass loss is observed in the range between 240 and 325 °C, indicating the presence of a stable intermediate. Another rapid mass loss accompanied by the release of CO_2 occurs for temperatures above 325 °C, suggesting the transformation of $NiCO_3$ to NiO.

Thermal degradation of the pore template during calcination is a commonly observed and desirable feature of EISA based syntheses. The employed block copolymer PEO_{213}-PB_{184}-PEO_{213} starts to decompose at temperatures around ~250 °C and rapidly decomposes between 350 °C and 425 °C (Figure 14 a), indicating a better thermal stability than common Pluronic type polymers.[127] The observed thermal stability of PEO-PB-PEO is similar to the stability of poly(ethylene-co-butylene)-*b*-poly(ethylene oxide) (KLE), which is well-known for its templating capabilities.[128]

The chemical complex consisting of $Ni(NO_3)_2·6H_2O$ and citric acid shows a distinctly different thermal behaviour. A first mass loss occurs between 140 and 240 °C (Figure 14 b) accompanied by release of CO_2 as detected by online MS. In analogy to similar observation reported for citric acid complexes of other metal nitrates [103, 119] the mass loss is interpreted as a decomposition of the precursor complex into nickel carbonate.

The sample mass then remains constant between 240 °C and 325 °C indicating the presence of a stable intermediate, i.e. nickel carbonate (Figure 14 b). Above 325 °C another rapid mass loss of 25 % accompanied by CO_2 release is observed. The formation of CO_2 along with the mass loss suggest in analogy to other systems [103, 119] that $NiCO_3$ converts into nickel oxide above 325 °C. Based on the obtained information, temperatures of (i) 250 °C and (ii) 350 °C were selected to synthesize nickel carbonate and porous nickel oxide samples for further analysis as presented in the next section.

4.1.2 Physicochemical properties of coatings calcined at 250 °C and at 350 °C

Deposited Ni-based films calcined (i) for one hour at 250 °C and (ii) for one hour at 250 °C and one more hour at 350 °C were investigated with respect to sample morphology, crystalline phases and surface composition. Figure 15 presents results of the analysis by scanning electron microscopy (SEM), transmission electron microscopy (TEM), small angle X-ray scattering (SAXS) and selected area electron diffraction (SAED). Figure 16 displays corresponding data obtained by a) X-ray diffraction analysis (XRD) and b) surface composition from X-ray photoelectron spectroscopy (XPS).
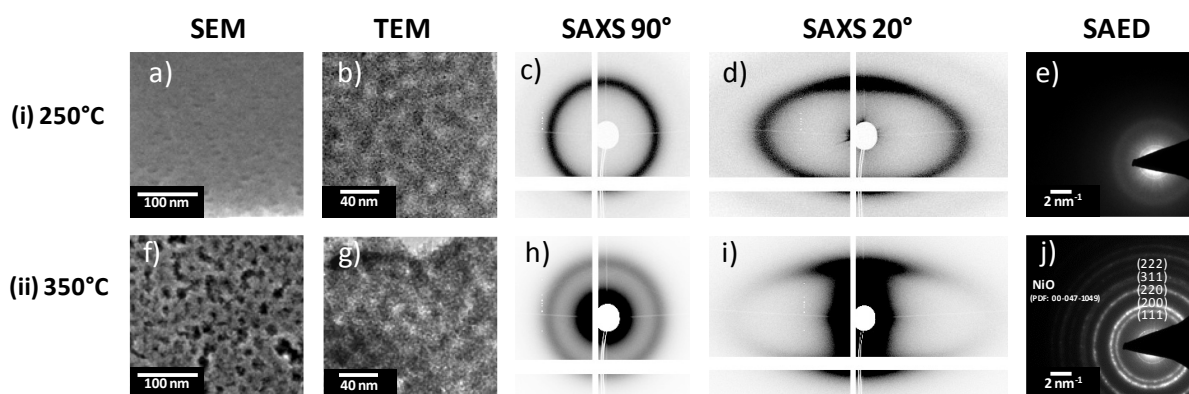

Figure 15: Analysis of samples heat treated (i) for 1 h at 250 °C and (ii) for another hour at 350 °C by SEM (a, f), TEM (b, g), SAXS at beam incident angles relative to the substrate of 90° (c, h) and 20° (d, i) as well as SAED (e, j). Samples heat treated at 250 °C show complete penetration with templated mesopores throughout the whole film volume (a, b) locally ordered parallel (c) and perpendicular (d) to the substrate surface. SAED does not provide evidence for crystalline phase (e). Samples (ii) calcined at 350 °C possess templated mesopores throughout the whole film volume (f, g) locally ordered parallel ((h) and perpendicular (i) relative to the substrate orientation. SAXS obtained at 20 ° show a less defined pattern indicating the onset of partial degradation of the ordered mesoporosity (i). SAED indicates crystallization of the material into a NiO phase with rock salt structure (PDF: 00-047-1049).

Morphology. SEM images recorded for the cross section of sample (i) calcined at 250 °C indicate the presence of mesopores in the materials cross section (Figure 15 a). The abundant presence of mesopores throughout the bulk of the material is confirmed by TEM images (Figure 15 b). SAXS recorded perpendicular to the substrate produces circular diffraction patterns (Figure 15 c, β = 90°) indicative of local pore order with a d-spacing of 27.0 nm in the in-plane direction. Additional SAXS recorded at smaller angles relative to the substrate (β = 20°) show an elliptically formed diffraction pattern with d-spacings corresponding to 27.0 nm (in-plane) and 9.5 nm (out-of-plane, Figure 15 d). Such small-angle diffraction patterns are typically observed for metal oxide films synthesized via EISA. The elliptical rings can be attributed to a uniaxial and homogeneous shrinkage of film and their

mesostructure in the direction perpendicular to the substrate during calcination,[98, 104, 129] whereas no shrinkage occurs in the in-plane direction.

SAED patterns recorded for material (i) do not show any diffraction rings or spots, suggesting the absence of crystalline phases (Figure 15 e). This observation is consistent with the presence of an amorphous carbonate phase as previously observed for other metal oxides and carbonates synthesized by a similar route.[103, 119]

Samples calcined by procedure (ii) for one hour at 250 °C and subsequently for one more hour at 350 °C were analyzed in a similar fashion (Figure 15 f-j). SEM images recorded in top-view mode show that the complete surface of the material is penetrated by mesopores with a pore diameter of ca. 13.7 nm (Figure 15 f). The porosity extends throughout the complete volume of the film (TEM, Figure 15 g). SAXS patterns recorded at β=90° still show a circular shape with a d-spacing of 26.3 nm, which is almost identical to sample (i). Also the SAXS patterns recorded at β=20° look similar to sample (i) with d-spacings corresponding to 26.3 nm (in-plane) and 6.8 nm (out-of-plane). The decrease from 9.5 nm (250 °C) to 6.8 nm (350 °C) indicates further shrinkage of the film in the direction perpendicular to the substrate. The less defined pattern of the ellipse (Figure 15 i) suggests also the onset of partial degradation of the ordered mesopore system due to calcination at 350 °C. At the same time SAED begins to evidence a crystalline phase (Figure 15 j). All of the observed diffraction rings can be assigned to a Nickel(II) oxide with rock-salt structure (PDF: 00-047-1049). The data suggest that an amorphous nickel carbonate formed during calcination (i) at 250 °C is transformed into mesoporous nickel oxide during subsequent calcination (ii) at 350 °C.

Composition. Further evidence for this transformation can be obtained from analysis of the bulk composition (XRD, Figure 16 a) and surface composition (XPS, Figure 16 b) of the Ni containing films deposited on Si wafers.

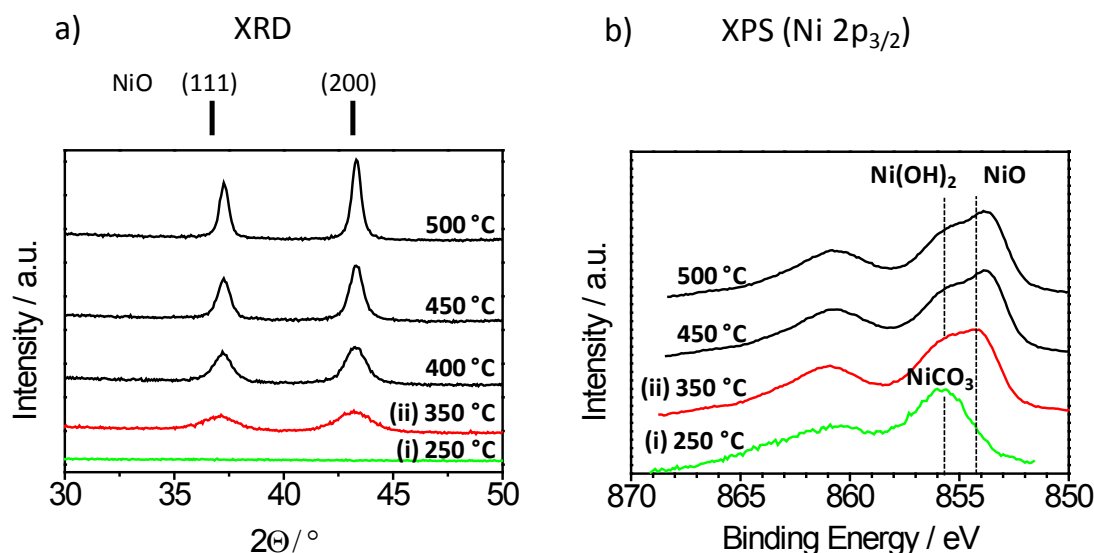a)   XRD   b)   XPS (Ni 2p$_{3/2}$)

Figure 16: Influence of calcination temperature on a) crystallinity and b) surface species. a) Samples calcined at (i) 250 °C show no evidence for crystallinity, whereas a subsequent calcination (ii) at 350 °C leads to appearance of signals at 37.5° and 43.0°, which can be attributed to (111) and (200) reflections of crystalline NiO in rock salt structure (PDF: 00-047-1049) with crystallite sizes of ca. 5-6 nm (Debye-Scherrer). The crystallite size increases from 6 to 11 to 17 to 27 nm (for 111 reflection) as a function of calcination temperature. b) XPS shows a clear signal at a binding energy of 855.7 eV for samples (i) calcined at 250 °C, which is assigned to NiCO$_3$. Subsequent calcination at (ii) 350 °C results in a signal at a binding energy of 855.7 eV as well as 854.4 eV. The signal at 854.4 eV is assigned to NiO, whereas the signal at 855.7 eV is either related to surface NiCO$_3$ or Ni(OH)$_2$.

X-ray diffraction confirms that calcination (i) at 250 °C does not result in crystalline phases (Figure 16 a, i). Samples calcined at 350 °C show clear diffraction signals at positions of 2θ equal to 37.5° (111) and 43.0° (200), which can be assigned to crystalline NiO with rock salt structure (PDF: 00-047-1049, Figure 16 a, ii). Applying the Debye-Scherrer equation to the (111) and (200) reflection reveals crystallite sizes of ca. 6 nm and 5 nm, respectively. The crystallites grow further with increasing calcination temperature up to about 27 nm for calcination at 500 °C. X-ray diffraction analysis thus supports the interpretation of initial formation of an amorphous nickel carbonate and its subsequent transformation into crystalline nickel oxide.

The surface composition of samples was analysed by XPS in the Ni 2p region (Figure 16 b). Sample (i) calcined at 250 °C show one clear signal at a binding energy of 855.7 eV. Further heating to 350 °C results in a spectrum that can be deconvoluted into two signals with binding energies of 855.7 eV and 854.4 eV, respectively. The signal at 854.4 eV arising at 350 °C can be assigned to NiO[130] , which is consistent with results from XRD and SAED analysis. Unfortunately, interpretation of the signal at 855.7 eV is complicated by the fact that two different Ni species can contribute at this binding energy, i.e. NiCO$_3$[131] and Ni(OH)$_2$-

phase.[132] However, TGA (Figure 14) indicated the presence of a carbonate bulk phase up to 325 °C and the decomposition of the nickel carbonate accompanied by a mass loss and release of CO_2 at higher temperatures. It is therefore likely, that for sample (i) calcined at 250 °C the signal at 855.7 eV corresponds to $NiCO_3$. For sample (ii) calcined at 350 °C, the signal at 855.7 eV could be interpreted either as a surface carbonate or nickel hydroxide. However, the fact that the carbonate decomposes already at 325 °C makes the assignment to a surface hydroxide more likely. A further increase in calcination temperature to 450 and 500 °C show similar curves as for 350 °C but provide less pronounced signals at binding energies of 855.7 eV ($Ni(OH)_2$). The decrease in intensity is possibly related to a lower content of $Ni(OH)_2$ within NiO obtained for as prepared samples that were heat treated at higher temperatures.

The combined data therefore suggest that calcination (i) of the deposited films at 250 °C forms an amorphous Nickel carbonate phase structured by the locally ordered micelles. Further calcination (ii) at 350 °C and above transforms this phase into crystalline nickel oxide with templated mesopore structure. The content of $Ni(OH)_2$ in NiO of as prepared samples seems to lower as a function of calcination temperature. The specific surface area of the Nickel oxide corresponds to approximately 300 m^2/g as derived from Kr Physisorption (surface area) and ICP-OES (mass).

4.1.3 OER activity vs. catalyst surface area

The OER activity of NiO_x samples calcined at different temperatures was studied under alkaline conditions and compared with the surface area of the respective catalysts as obtained from Kr-physisorption experiments. Samples were calcined for 1 h at 250 °C followed by 1 h at either 250, 350, 400, 450 or 500 °C to obtain NiO_x with different crystallinity and surface area. OER activity was assessed by cyclic voltammetric RDE measurements in 0.1 M KOH. Figure 17 presents a) the recorded cyclic voltammograms, b) pre-oxidation waves prior to OER onset, c) the influence of calcination temperature on the OER current density recorded at a potential of 1.85 V_{RHE} and d) the influence of calcination temperature on the surface area as derived from Kr-physisorption data in m^2 of film per m^2 of the substrates planar dimensions.
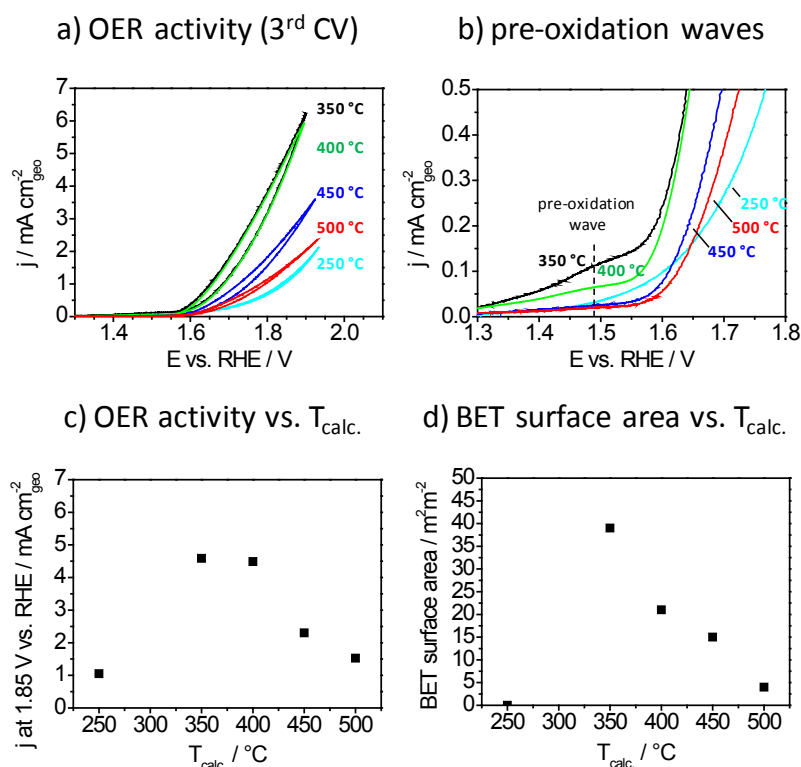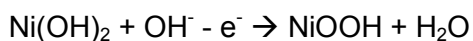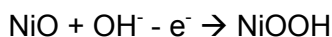
Figure 17: Influence of calcination temperature of mesoporous templated NiO and NiCO₃ on a) OER cyclic voltammograms, b) pre-oxidation waves c) OER current density and d) BET surface area in m² of film per m² of the substrates planar dimensions. OER activity was assessed in a RDE setup (n=1600 rpm) in 0.1 M KOH electrolyte sweeping the potential between 1.20 - 1.95 V_{RHE} at a scan rate of 6 mV/s. a) All catalysts are active in OER. b) Samples heat treated at 350 and 400 °C show weak pre-oxidation characteristics prior OER onset, usually assigned to the reversible reactions of NiO to NiOOH and Ni(OH)₂ to NiOOH. c) Geometric current density compared at 1.85 V_{RHE} as a function of calcination temperature reveals a drastic increase in OER activity when going from 250 to 300 °C, whereas higher calcination temperature lead to continuous decrease of OER activity. This trend in OER activity closely correlates with d) BET surface area presented in m² film surface per m² substrate. The correlation suggests that the accessible surface is one of the most important activity determining parameters.

All catalysts show significant OER currents (Figure 17 a). However, the applied calcination temperature has a severe influence on the achieved catalytic performance. Catalytic activity drastically increases when going from 250 to 350 °C, whereas higher calcination temperatures of 400, 450 and 500 °C lead to continuous decrease in activity (Figure 17 c). The highest geometric current density is reached by the sample calcined at 350 °C with 4.3 mA/cm² observed at a potential of 1.85 V_{RHE}.

Also the shape of the recorded CVs change with calcination temperature. The most active films, i.e. samples calcined at 350 °C and at 400 °C, show a distinct oxidation wave at about 1.50 V_{RHE} prior to the onset of the OER (Figure 17 b). This wave is not evident for samples calcined at temperatures of 250, 450 and 500 °C. The signals can be assigned to the following possible electrochemical reactions. [133]

$$NiO + OH^- - e^- \rightarrow NiOOH$$

$$Ni(OH)_2 + OH^- - e^- \rightarrow NiOOH + H_2O$$

The impact of calcination temperature on the surface area of NiO_x films is presented in Figure 17 d in terms of m^2 of internal pore surface area of NiO_x film per m^2 of geometric surface area of the planar substrate. Films calcined at 250 °C possess a very low surface area, suggesting that this temperature is not sufficient to remove the template polymer. Calcination at 350 °C produces the highest specific surface area, with a continuous decline at further increased calcination temperatures. This trend in surface area as a function of calcination temperature follows very closely the OER activity trend shown in Figure 17 c. It can be concluded that within the range of studied synthesis parameters the accessible surface area has a dominating impact on the resulting OER performance.

4.1.4 Electrochemical activation treatment

The overpotential observed in the present study in 1.0 M KOH at 1 mA/cm^2 amounts to about 425 mV. This value is ca. 150 mV higher than the best reported Ni based catalysts based on e.g. nanoparticle immobilization[26, 134] or nickel nitrate decomposition.[27] The lower performance could be related to the fact that the synthesis in its present form produces crystalline nickel oxide instead of the more active oxyhydroxides or hydroxides. According to literature NiO is less active in the OER than nickel hydroxides or oxyhydroxides. However, different reports suggest that nickel oxide can be transformed into a more active hydroxide species by prolonged electrochemical treatments.[27, 135] Trotochaud et al.[27] performed a galvanostatically anodic treatment of NiO at current densities of 10 mA/cm². After every hour a CV was recorded to assess the resulting OER activity. The anodic treatment resulted in an increase in OER activity from 0.2 mA/cm² to 1.0 mA/cm² (at 1.51 V_{RHE}) after 6 hours of treatment. Moreover, with extended treatments also the pre-oxidation wave at 1.40 V_{RHE} became more pronounced. Trotochaud[27] attributed the pre-oxidation/reduction wave to a redox process of $Ni(OH)_2$/NiOOH. The increased OER activity was rationalized by the better ability of $Ni(OH)_2$/NiOOH to intercalate water and anions. Furthermore, Klaus et al.[29] reported in-situ Raman studies on electrodeposited $Ni(OH)_2$. They observed a clear Raman signal shift in the same potential region as the pre-oxidation waves reported by Trotochaud et al.[27]. The Raman signals were assigned to $Ni(OH)_2$ at lower potentials and NiOOH at higher potentials, providing further evidence for a potential dependent transformation of $Ni(OH)_2$ to NiOOH.

We performed for the mesoporous NiO catalyst calcined at 350 °C a similar electrochemical treatment as reported by Trotochaud et al. in order to increase the OER activity. The treatment was performed with mesoporous templated NiO coated on titanium substrates with 5 mm in diameter and consisted of repeated potentiostatic treatments in 1.0 M KOH (n=1600 rpm) at a potential of 1.75 V_{RHE} for 5 hours. After every hour of potentiostatic treatment an intermediate CV was recorded in the OER range by sweeping the potential with 20 mV/s from 1.75 V_{RHE} to 1.20 V_{RHE} and back to 1.75 V_{RHE} in order to assess OER performance as well as pre-oxidation and corresponding reduction waves. Alternating potentiostatic treatments and CV measurement were repeated 5 times to follow the catalyst activation. In order to assess also the subsequent OER activity 20 consecutive CVs in the OER region were performed after 10 hours of potentiostatic treatment at 1.75 V_{RHE}. Figure 18 displays a, b) the CVs recorded initially as well as after 1, 3 and 5 h of potentiostatic treatment, c) the OER-related current density observed at 1.70 V_{RHE} during the CV sweeps and d) the 2nd, 5th, 10th and 20th CV after 10 hours of potentiostatic treatment.
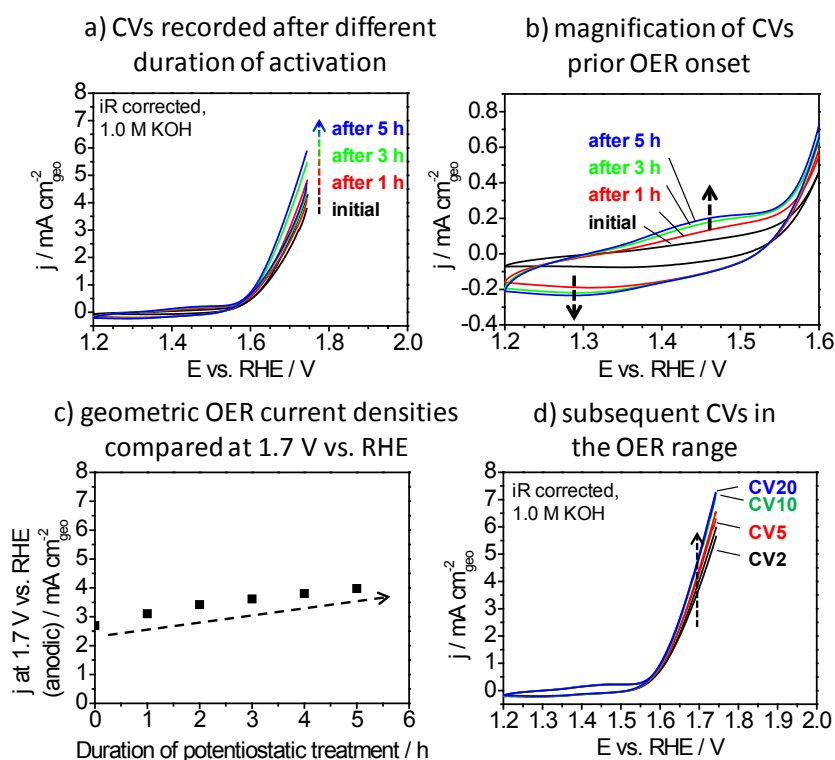

Figure 18: Influence of potentiostatic activation treatment at 1.75 V_{RHE} for NiO calcined at 350 °C on a,b) CV shape and c) OER activity. Subsequent OER performance of modified NiO is investigated with d) 20 consecutive CVs after 10 hours of potentiostatic treatment. a, b) CVs in the OER range recorded with a sweep rate of 20 mV/s from 1.75 V_{RHE} to 1.20 V_{RHE} before and after several electrochemical potentiostatic treatments at a potential of 1.75 V_{RHE} for 1 hour each. With each treatment OER activity increases (a) and the pre-oxidation wave at 1.47 V_{RHE} as well as the corresponding reduction wave at 1.28 V_{RHE} become more pronounced (b). c) Quantification of the activation in terms of observed geometric current density at 1.7 V_{RHE} after repeated activation treatments. d) OER performance is further enhanced also by conducting another 20 consecutive CVs after 10 hours of potentiostatic activation treatment.

The potentiostatic treatment resulted in two major changes of the catalyst's electrochemical behaviour. With each hour of treatment the pre-oxidation wave observed at about 1.47 V_{RHE} and the corresponding reduction wave at 1.28 V_{RHE} became more pronounced (Figure 18 b), indicating an improved redox ability. Moreover, also the current density observed in each subsequent CV became higher, indicating an increased OER performance (Figure 18 a).

Figure 18 c shows a quantitative evaluation of the increased activity by showing CVs conducted between 1 and 5 h of potentiostatic treatment. The OER-related current density obtained at a potential of 1.70 V_{RHE} steadily increases from initially 2.7 mA/cm² to about 4.0 mA/cm² after 5 h of potentiostatic treatment. Figure 18 d depicts the OER activity during subsequent repeated CVs. The measured OER activity at 1.70 V_{RHE} further increases up to 5.1 mA/cm² accompanied by a small increase of the pre-oxidation wave, indicating the opportunity for a further enhancement of OER activity. Both observed effects, the increase in pre-oxidation wave currents as well as the increased OER activity, are in full agreement with the report of Trotochaud et al.[27] It can be concluded, that the activity of the synthesized mesoporous nickel oxide can be further increased by extended anodic treatments that convert parts of the near-surface region of the catalyst into $Ni(OH)_2$ or NiOOH

4.1.5 OER activity comparison with reported catalysts

The overpotential is often used as a measure of catalytic activity and was quantified for the most active catalysts at 1 mA/cm² planar geometrical current density. The derived overpotential is then related to values obtained in previous studies reported in literature.

Yu et al.[23] prepared a nickel-based thin film (NiO_x) on multi walled carbon nanotubes deposited on ITO and observed an OER overpotential of 523 mV. Singh et al.[24] electrodeposited layers of nickel oxide from $[Ni(en)_3]Cl_2$ (en= 1,2-diaminoethane) on glassy carbon and reported 510 mV overpotential. Nardi et al.[25] deposited thin films of NiO $Ni(Cp)_2$ (cp=cyclopentadienyl) on fluorine doped tin oxide (FTO) via atomic layer deposition and achieved an overpotential of 400 mV. Lyons et al.[37] investigated the electrocatalytic activity of polycrystalline nickel foils and reported an overpotential of 379 mV. Fominykh et al.[26] prepared NiO nanoparticles using a solvothermal reaction in *tert*-butanol. Subsequently, NiO nanoparticles were deposited on Au-coated QCM electrodes in order to access the OER overpotential (280 mV). Trotochaud et al.[27] obtained a thin film of NiO_x by spincoating a solution containing $Ni(NO_3)_2 \cdot 6H_2O$ on Au-coated QCM electrodes. Subsequent electrocatalytic investigation in the OER regime revealed an overpotential of 279 mV.

Figure 19 shows reported overpotentials for nickel based catalysts at 1 mA/cm² and corresponding electron micrographs.
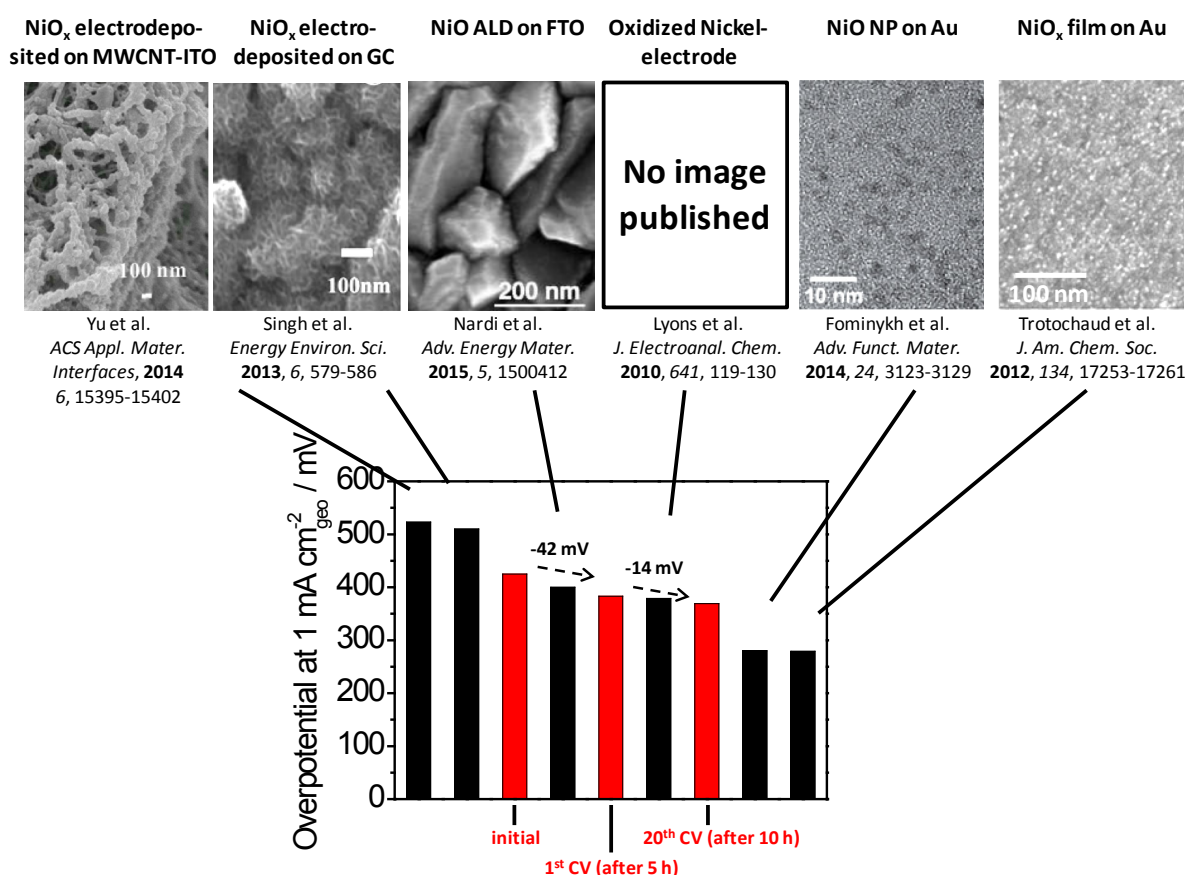
Figure 19: Comparison of OER overpotentials at 1 mA/cm² for mesoporous templated NiO (red columns) with previous reported literature data (black columns), and electron micrographs of the corresponding samples. The observed overpotential for mesoporous templated films of NiO (350 °C) decreases from 425 mV to 383 mV after 5 h of potentiostatic treatment. Subsequent CVs recorded after 10 h of potentiostatic treatment result in further decrease of the observed overpotential (369 mV).

The literature reports for different nickel based catalysts show OER overpotentials in the range between 523 mV and 279 mV to achieve a geometrical current density of 1 mA/cm². PEO-PB-PEO templated films of NiO calcined at 350 °C subsequently treated by an electrochemical activation procedure (chapter 4.1.4) show a fairly high OER overpotential of 369 mV. The observed overpotential is ca. 90 mV higher than the best reported Ni based catalysts based nanoparticle immobilization[26] or nickel nitrate decomposition.[27] The depicted lower activity could be related to the fact that the synthesis in its present form produces crystalline nickel oxide and that a total conversion to the more active oxyhydroxides or hydroxides by electrochemical treatment was not achieved. However, OER overpotentials reported by Fominykh et al. (280 mV)[26] and Trotochaud et al. (279 mV)[27] were both tested for nickel oxide based catalysts deposited on gold substrate. According to Pourbaix[136] the thermodynamic equilibrium potential of the Au/Au^{+III} redox couple is found to be 1.50 V$_{RHE}$. The observed OER overpotentials for nickel oxide catalysts on gold (1.51 V$_{RHE}$) and the thermodynamic equilibrium potential of the Au/Au^{+III} redox couple (1.50 V$_{RHE}$) are so close to

each other that the observed higher activity of such catalysts is probably attributed to oxidation of gold rather than oxygen evolution.

In summary it is shown that for the first time NiO films with ordered mesopore structure can be synthesized via soft-templating and proof to be active in OER catalysis. The synthesis succeeds by employing a metal complex formed from citric acid and nickel nitrate along with a polymer template PEO_{213}-PB_{184}-PEO_{213} to perform deposition via evaporation-induced self assembly. Calcination at 250 °C converts the deposited film into an amorphous carbonate, whereas higher calcination temperatures transform the carbonate into NiO while retaining the templated mesopore structure. All catalysts obtained by this synthesis possess significant OER activity, with samples calcined at 350 °C exhibiting the highest OER performance and the highest surface area. A further increase in OER activity for mesoporous NiO layers can be achieved by potentiostatic treatments at 1.75 V_{RHE}. This observation is in line with reports in literature[27] and is explained by an in-situ transformation from NiO to $Ni(OH)_2$/NiOOH,[29] assuming that NiOOH is most likely the active phase for OER.

Chapter 4.1 focused solely on oxides of one metal only, i.e Ni. Since mixed metal oxides of Ni with e.g. Fe, Co were reported to show higher intrinsic activities than nickel oxide, a further increase in OER performance can probably be achieved if the synthesis of corresponding mixed metal oxide film with micelle-controlled mesopore structure succeeds. However, the next chapter illustrates the synthesis pathway for the production of highly active OER catalysts operating under acidic conditions.

4.2 Mesoporous templated IrO$_2$ synthesized from Ir(OAc)$_3$

Electrolysers operating in acidic media provide several advantages compared to electrolysers in alkaline media, such as high current density (> 2 A/cm²), lower gas crossover rate, lower operational costs and high pressure output (also see chapter 2.1 for detailed description). Typical electrolysers are limited by the OER due to the fact that four electrons are needed to produce one molecule of oxygen and that the OER proceeds by a complex reaction mechanism.[13, 45-46] Electrocatalytic water splitting performed in acidic media therefore appears to be an attractive approach for a more efficient generation of molecular hydrogen. A major roadblock is to find materials that withstand corrosive conditions and provide significant electron conductivity. The oxides of ruthenium and iridium show the lowest OER overpotential in acidic media.[13, 52-53] Although ruthenium oxide shows higher activity, it typically corrodes during OER potential cycles. iridium oxide is therefore the best compromise for an active and stable OER catalyst.[13] However, limited abundance and competition with applications such as supercapacitors,[66-67] stimulating neural electrodes[68-69] and microelectrodes for pH sensing[70-71] require the most efficient utilization of IrO$_2$ that is possible.

Chapter 4.2 presents the potential of pore templating with polymer micelles in order to produce model-type porous catalysts for the investigation of structure-activity relationships in gas evolution reactions and for the optimization of the performance of IrO$_2$-based OER catalysts. The presented synthesis approach is based on pore templating with micelles of amphiphilic block copolymers PEO-PB-PEO (chapter 4.2.1) and further improved to produce iridium oxide films with controlled pore size, film thickness and crystallinity (chapter 4.2.2). The model systems are used to study the influence of porosity and crystallinity on electrochemically accessible surface area (ECSA), OER performance, gas transport and faradaic efficiency (chapters 4.2.3 - 4.2.4). A controlled variation in thickness of the porous catalysts explores, which parts of the catalyst can be utilized without transport limitations during high-current OER (chapter 4.2.5). The combined knowledge is used to design a multilayer-IrO$_2$ catalyst that shows the lowest OER overpotential reported so far for monometallic oxide compounds of Ir.

4.2.1 Physicochemical properties of PEO-PB-PEO templated mesoporous IrO$_2$

A dipcoating solution was prepared by dissolving PEO-b-PB-b-PEO triblockcopolymer and Ir(OAc)$_3$ in ethanol. Subsequently, dipcoating was performed on silicon substrate at a temperature of 25 °C and a relative humidity of 40 %. The as synthesized films were thermally treated at 375 °C in a preheated muffle furnace under air atmosphere. The obtained layers were physicochemical characterized in order to investigate morphology, layer thickness, crystallinity and locally pore ordering.

Figure 20 shows for mesoporous templated IrO$_2$ a) SEM, b) cross section SEM, c) TEM, d) SAED, SAXS at e) 90° and f) 20° with respect to the film surface normal and g) Kr-physisorption.

a) SEM   b) cross section SEM   c) TEM   d) SAED

e) SAXS 90°   f) SAXS 20°   g) Kr-physisorption
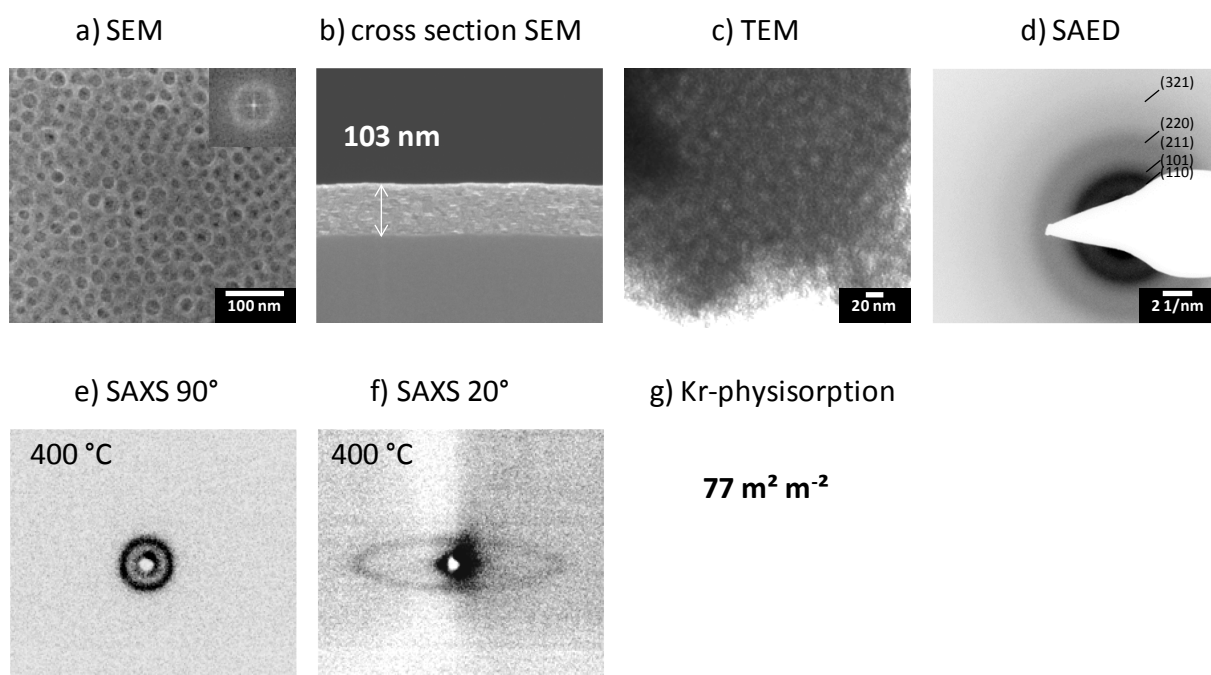
77 m^2 m^{-2}

Figure 20: Physicochemical properties of mesoporous PEO-PB-PEO templated IrO$_2$ dipcoated on silicon wafers and subsequently heat treated under air atmosphere. All samples were calcined at 375 °C, except for samples investigated by SAXS (400 °C). a) Templated mesoporosity is visible on the outer surface plane area. b) Layer thickness was revealed by cross section SEM and amounts to 103 nm. c) TEM micrographs were recorded from samples scratched off from silicon substrate and subsequently deposited on a TEM grid. d) Selected area electron diffraction images were recorded for investigating crystallinity. Pore ordering was determined by SAXS with an incident beam e) parallel (90°) and d) perpendicular (20°) to the film normal. g) BET surface area derived by Kr-physisorption is presented in m^2 film surface per m^2 substrate.

SEM images were recorded in top view mode in order to provide information about the morphology of the outer surface plane area. Figure 20 a shows a PEO-PB-PEO templated film calcined at 375 °C exhibiting pores that are uniform in shape and size. The diameter of the mesopores amounts to 21±4 nm. The corresponding FFT of the top view SEM image (inset Figure 20 a) shows an isotropic ring revealing the presence of an ordered pore

arrangement at the outer surface plane area with a periodic pore distance of 18 nm. The observed pore walls show a thickness of 11±1 nm as well as additional pores that appear to be smaller than 2 nm in size. The textural porosity is also present for untemplated samples[65] indicating that the presence of the template polymer does not introduce textural porosity. A possible explanation for that behaviour would be the formation of CO_2 during thermal decomposition of the acetate precursor.

The layer thickness was investigated by breaking a substrate coated with a mesoporous layer of IrO_2 into half and viewing it from the side by SEM. Figure 20 b presents for a sample heat treated at 375 °C a SEM micrograph recorded in cross section mode. The layer thickness amounts to 103 nm which is a typical value reported in literature for similar synthesized IrO_2. (ca. 100 nm - 150 nm)[65]

Figure 20 c depicts TEM micrographs revealing spherical mesopores with a diameter of ca. 20 nm, indicating that pores penetrate the sample throughout the whole film volume area. The local crystallinity of mesopore walls was studied by electron diffraction analysis on IrO_2 samples removed from substrate and placed on TEM grids. Figure 20 d shows SAED measurements of for a sample calcined at 375 °C. The sample shows very broad diffraction rings, indicating the onset of crystallization. The observed diffraction rings correspond with the lattice parameters of crystalline IrO_2 rutile (PDF 150870). The presence of broad reflection rings lead to the assumption that the synthesis produces films with small crystallites.

Insight of pore ordering is granted by SAXS and is shown for samples heat treated at 400 °C with the silicon substrate positioned perpendicular and parallel to the incident beam. Measurements with the substrate in transmission mode (90 °, Figure 20 e) display isotropic rings indicating well ordered porosity parallel to the substrate, whereas the out-of-plane measurement (10°, Figure 20 f) shows an elliptically distorted ring, indicating contraction of the pore system perpendicular to the substrate.

The surface area of layers coated on silicon substrate was investigated with krypton physisorption and is shown in Figure 20 g. The calculated BET surface area amounts to 91 m² film surface area per m² substrate geometric surface area indicating that most of the containing polymer template was removed and that an accessible mesopore system is produced. The surface area is in good agreement with reports in literature for mesoporous templated IrO_2 thermally treated at 400 °C (130 m²/m²).[65]

The combined physicochemical techniques thus suggest that the synthesis in its present form successfully introduces an accessible (Figure 20 g) open mesoporous system (Figure 20 a, c) into a metal oxide with low crystallinity (Figure 20 d). The established mesoporosity appears locally ordered parallel and perpendicular (Figure 20 e, f) to the film surface normal.

4.2.2 Influence of calcination temperature on morphology, ECSA and OER

The calcination temperature of micelle-templated oxide films can strongly influence the precursor decomposition, template removal and the obtained film morphology and surface area.[65] In order to relate the morphology of templated iridium oxide to its accessible surface area and catalytic activity dip-coated films were calcined at temperatures of 325, 350, 375, 400, 475, 550 and 625 °C and analyzed by SEM, ECSA measurements and OER testing. Figure 21 presents for selected calcination temperatures (a) top-view SEM images, (b) CVs in the ECSA range[55, 125-126] and (c) CVs recorded in the OER potential range.
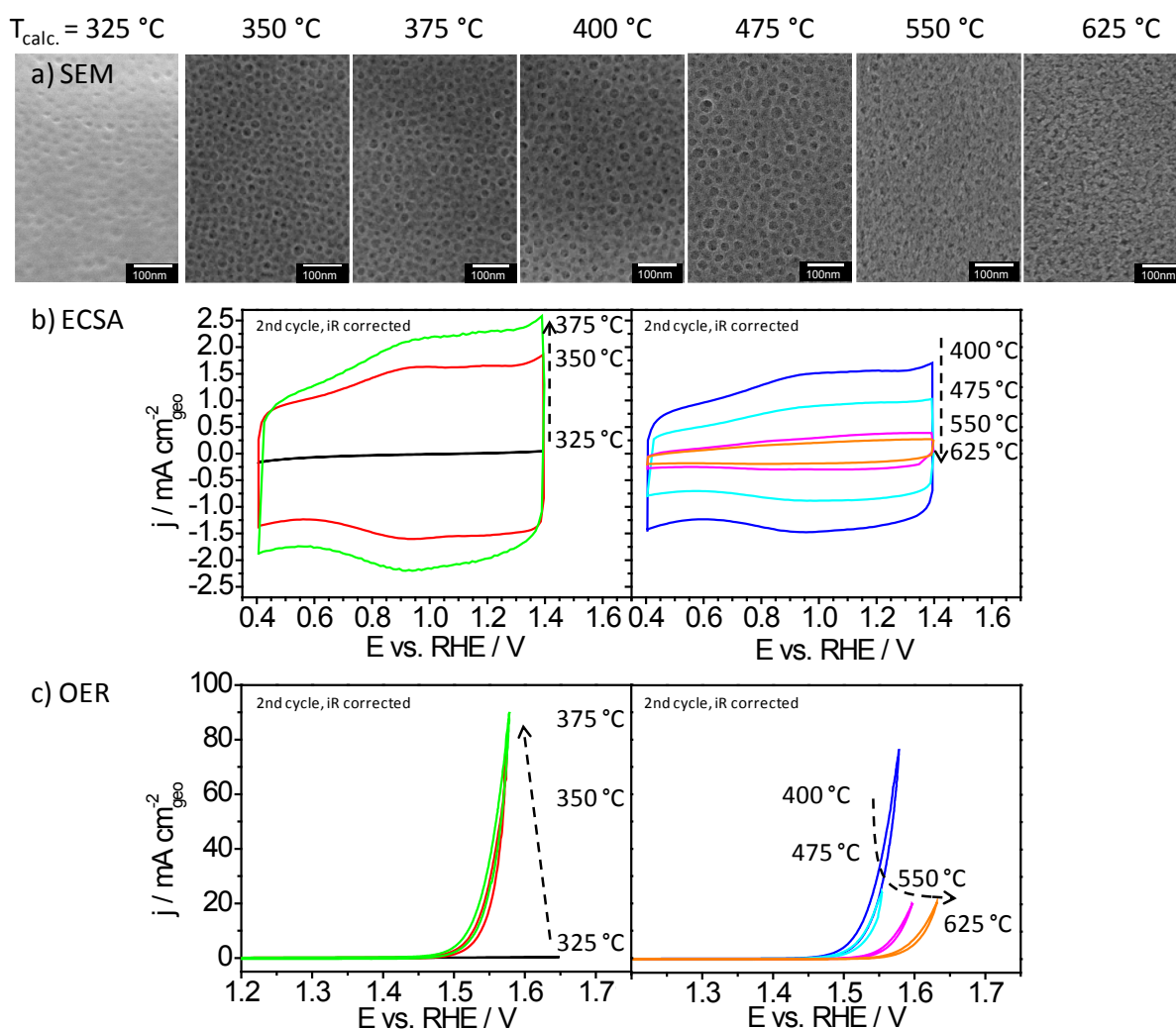

Figure 21: Influence of calcination temperature of micelle-templated iridium oxide films on a) film morphology, b) electrochemically accessible surface area and c) OER performance. a) top-view SEM images, b) CVs recorded in the ECSA range between 0.40 and 1.40 V_{RHE} at 50 mV/s and c) CVs recorded in the OER range between 1.20 and 1.65 V_{RHE} at 6 mV/s. All samples were coated on Ti cylinders and calcined for 5 min at the indicated temperature. All electrocatalytic data were recorded in 0.5 M H_2SO_4 electrolyte with rotating working electrode, RHE reference and Pt gauze counter electrode.

SEM images of the sample calcined at 325 °C (Figure 21 a - 325 °C) show charging, which indicates that the polymer template is not fully removed at this temperature and still blocks

the pore system. Films treated at higher temperatures of 350, 375, 400 and 475 °C feature a fully developed system of locally ordered mesopores (see e.g. SAXS data for calcination at 400 °C as presented in Figure 20 e and f) with pore diameters of ca. 21±4 nm and a wall thickness of 11±1 nm (values derived from Figure 21 a, 350 - 475 °C). The obtained mesoporosity agrees well with the pore morphology typically observed for oxide films templated by micelles of the pore template PEO-PB-PEO (TiO$_2$,[98] MgO,[103] ZnO,[119] Co$_3$O$_4$[119]). Moreover, SEM images of films calcined at 550 and 625 °C indicate the beginning deformation of the circular mesopore shape, which can be attributed to the onset of sintering.

The ECSA corresponding to each sample can be derived from the current response (normalized to the substrate geometric surface area) in the potential range between 0.40 and 1.40 V$_{RHE}$ as plotted in Figure 21 b. Samples calcined at 325 °C show a very small surface area (Figure 21 b). This observation is in good agreement with the SEM analysis where significant charging was observed. If charging is caused by incomplete removal of the pore template then the pore system is still blocked and not electrochemically accessible. For samples calcined at intermediate temperatures (Figure 21 b, 350 °C, 375 °C) a rapid increase in current density and accessible surface is observed. Temperature treatments at 400 °C and above progressively decrease the ECSA, yielding lowest ECSA values for samples heat treated at 625 °C.

OER performance was measured on the same catalysts by CVs in the potential range of 1.20 to 1.65 V$_{RHE}$. Figure 21 c shows the current response normalized to the Ti cylinders geometrical surface area. The OER activity strongly depends on the applied calcination temperature. All catalysts except for the sample calcined at 325 °C show significant OER activity. The OER activity increases up to 375 °C, whereas higher calcination temperatures lead to a progressing decrease in OER activity. Similar trends in ECSA and OER performance are also observed under alkaline conditions (see Figure A1 a, b).

The electrocatalytic OER performance of mesoporous templated IrO$_2$ calcined at 375 °C is further correlated to fundamental model type catalysts, e.g. cylinders of polycrystalline[56] and single crystalline Ir.[137] The electrocatalytic performance was investigated by cyclic voltammetry and the current response was normalized to the substrates planar geometrical surface area.
Figure 22 shows the OER activity measured for a bulk Ir-cylinder, an Ir(110) single crystal and a mesoporous templated IrO$_2$ heat treated at 375 °C.
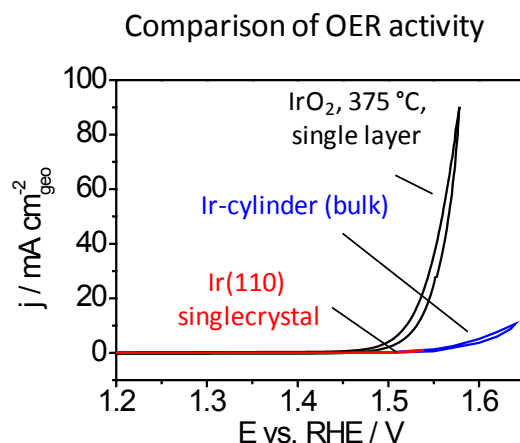
Comparison of OER activity

Figure 22: Comparison of OER activity for mesoporous templated IrO$_2$, Ir(110) single crystal[137] and Ir-cylinder (bulk).[56] At a potential of 1.53 V$_{RHE}$ the mesoporous templated IrO$_2$ films (375 °C) exhibit an approximately 20 times higher current density compared to Ir(110) single crystal and Ir-cylinder.

The observed OER activity strongly depends on the utilized system. However, the Ir (110) single crystal and the Ir-cylinder (bulk) show a very low current response in the OER potential window, whereas mesoporous templated IrO$_2$ calcined at 375 °C depict a significant higher OER activity. The mesoporous catalyst calcined at 375 °C is about 20 times more active than a single crystal Ir(110) or an Ir-cylinder (bulk).

The overpotential can be used as a measure of catalytic activity. Under standard conditions the thermodynamic minimum potential in the OER amounts to 1.23 V$_{RHE}$. Table 1 lists the respective overpotentials recorded at a current density of 0.5 mA/cm². The lowest overpotential (0.212 V) is observed for a sample calcined at 375 °C. Calcination at temperatures of 475 °C and above result in significantly increased overpotential values. Table 1 also lists overpotentials obtained by Reier et al.[64] on similarly prepared catalysts without templated mesoporosity, which results in e.g. 32 mV and 72 mV higher overpotentials for calcination at 350 and 550 °C, respectively. Summarizing, mesoporous templated IrO$_2$ shows a significant higher electrocatalytic OER activity than untemplated IrO$_2$.[64] The higher geometrical OER activity is related to the fully accessible porous system introduced by PEO-PB-PEO polymer template. The control in size, distance and connection of the templated mesopores allows the design of highly active OER catalysts.

Table 1: Influence of calcination temperature on OER overpotential (at 0.5 mA/cm²) and comparison to IrO₂ without templated mesopores (from [64]). Mesoporous IrO₂ heat-treated at 375 °C (highlighted in bold type) show the lowest overpotential.

Applied $T_{calc.}$ / °C	Overpotential / V at 0.5 mA cm^{-2} (IrO₂, this work)	Overpotential / V at 0.5 mA cm^{-2} (untemplated IrO₂ [64])
325	No significant activity	
350	0.228	0.26
375	**0.212**	
400	0.218	
475	0.228	
550	0.278	0.35
625	0.307	

4.2.3 Faradaic efficiency

The production of H_2O_2 and dissolution of the catalyst are common side reactions of the OER. Both effects were tested for. Titration with 0.001 mol/l $KMnO_4$ solution was performed on fresh electrolyte and after 50 OER cycles with the most active catalyst ($T_{calc.}$ = 375 °C) to test for H_2O_2. No significant differences were observed between the two electrolytes, suggesting that negligible amounts of H_2O_2 were formed. Moreover, ICP-OES analysis of the used electrolyte did not detect dissolved iridium species within the limits of experimental accuracy. Both tests suggest a high faradaic efficiency of the IrO_x catalysts.

In order to test further if residual carbon that could potentially remain after catalyst synthesis affects the OER current, additional tests were conducted by differential electrochemical mass spectrometry (DEMS) performed during OER while measuring the formed CO_2 and O_2 via MS. The detected product gases were O_2 and CO_2. The observed O_2 concentration for the 1st applied CV amounts to 98.7 %, the rest being CO_2. The O_2 selectivity further increases to 98.8 % for the 2nd CV and 99.9 % for the 10th applied cycle (see Figure A2). Hence, the current resulting from the removal of residual carbon during OER is rather small.

4.2.4 Relationship between OER activity, ECSA and sample crystallinity

The relation between the catalysts accessible surface area and the respective OER performance was further analyzed by quantification of the respective electrochemical data. Figure 23 plots as a function of calcination temperature (a) the total charge obtained by the mean value of the integrated anodic and cathodic currents in the ECSA range as a measure of the catalysts total surface area, (b) BET surface area presented in m^2 film surface per m^2 substrate (c) the current density normalized to the geometric electrode surface area recorded at 1.55 V_{RHE} during OER potential scans as a measure of OER activity, and (d) the current density at 1.55 V_{RHE} normalized to the ECSA charge as an indicator of each catalysts intrinsic activity.
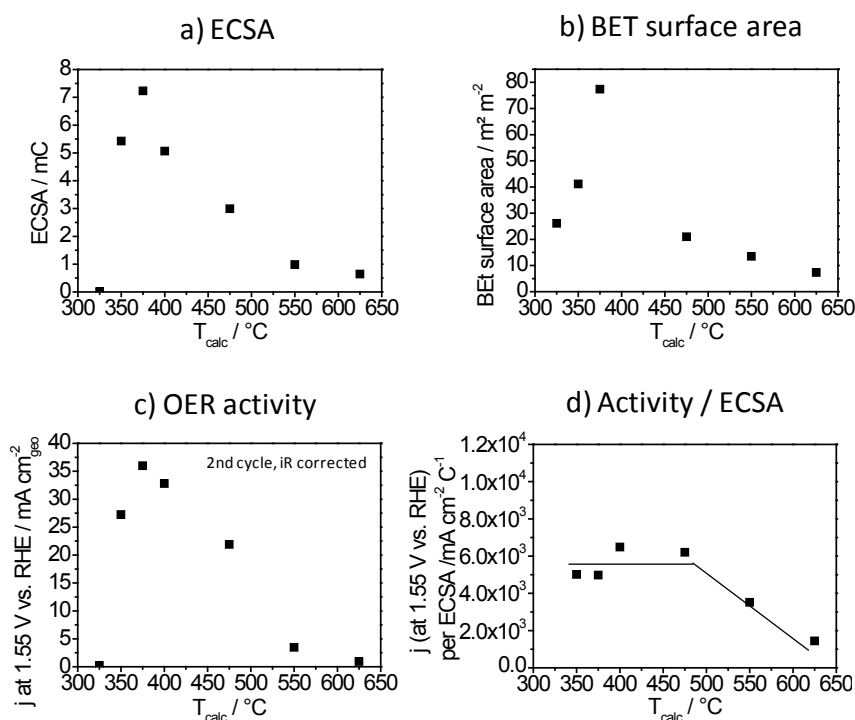
Figure 23: ECSA, BET surface area, OER activity and ECSA-normalized activity of mesoporous iridium oxide as a function of calcination temperature. a) ECSA as total charge obtained as a mean value of the integrated anodic and cathodic currents between 0.40 and 1.40 V_{RHE}, b) BET surface area in m² film surface normalized with respect to the substrates planar geometrical surface area c) current density recorded at 1.55 V_{RHE} normalized to the geometric electrode surface area, and d) geometric current density at 1.55 V_{RHE} normalized to the ECSA charge as an indicator of each catalysts intrinsic activity.

The ECSA increases from 325 °C to 375 °C with increasing calcination temperature (Figure 23 a) and then rapidly decreases between 400 and 625 °C. The catalysts surface area measured by Kr physisorption shows a very similar behavior and peaks at the same calcination temperature of 375 °C (Figure 23 b). Also the observed OER activity follows this trend (Figure 23 c). The OER activity increases rapidly with increasing calcination temperature reaching a maximum for 375 °C and steadily declines with further temperature increase. Figure 23 d relates for each calcination temperature higher than 325 °C the measured OER activity to the respective ECSA. It can be seen that this surface-area normalized activity stays almost constant for calcination between 350 and 475 °C, but steadily decreases for higher calcination temperatures. It is therefore evident that at least two major factors contribute to the overall OER activity, i.e. the accessible surface area as well as the intrinsic activity of each accessible site.

In order to relate the observed ECSA and activity trends to structural and compositional properties of the porous IrO_2 catalysts the respective samples were studied by XRD, SAED and TEM. Figure 24 presents a) diffractograms for the catalyst calcined at different

temperatures, b) selected area electron diffraction images and c) bright-field TEM images for representative samples calcined at 350, 375, 475, 550 and 625 °C.
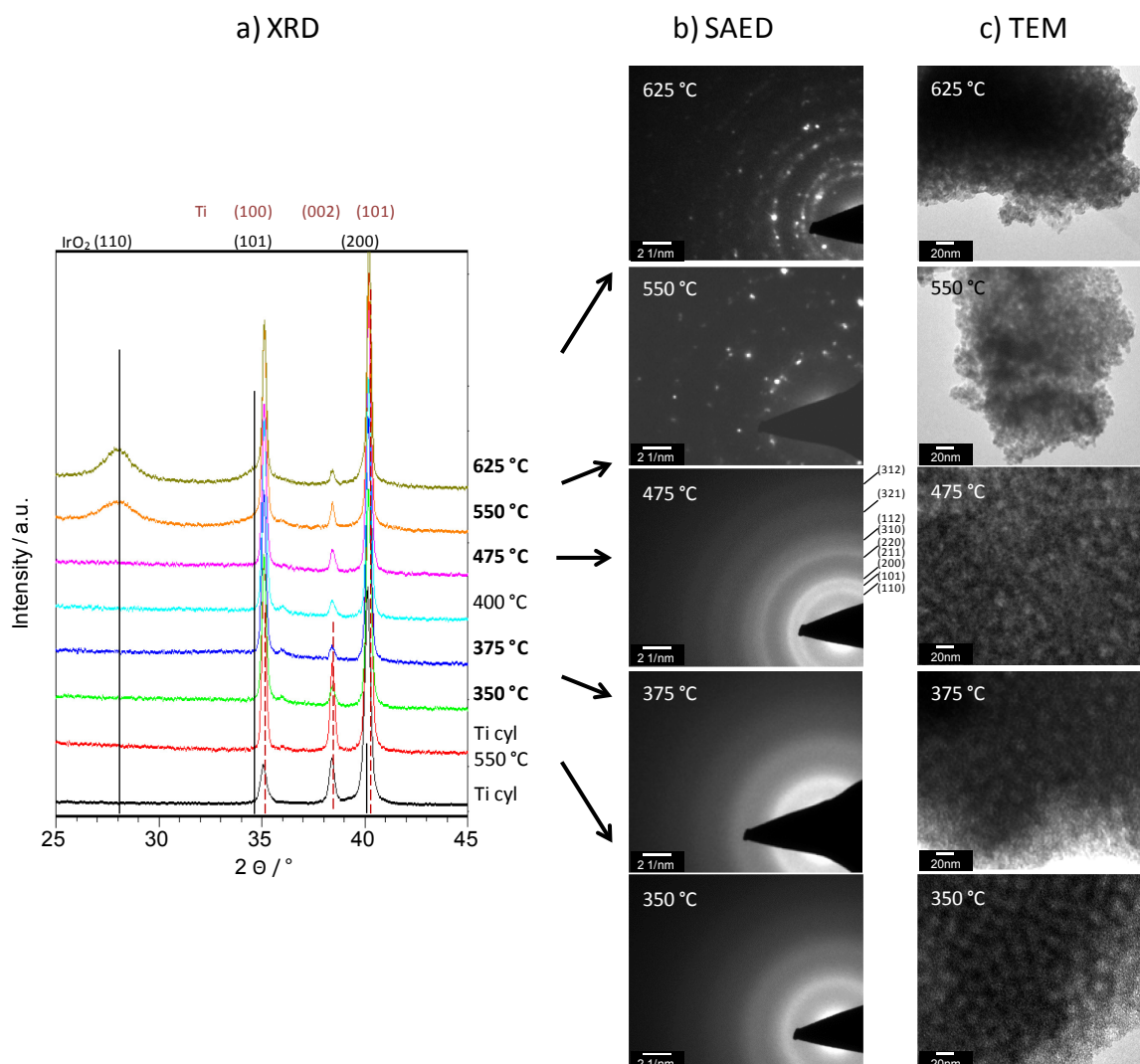

Figure 24: Analysis of crystallinity (XRD, SAED) and morphology (TEM) for mesoporous iridium oxide calcined at different temperatures between 350 and 625 °C. a) diffractograms for a polished titanium cylinder, the Ti cylinder calcined at 550 °C and for IrO$_x$-coated Ti-cylinders (350 – 625 °C). b) SAED analysis for IrO$_x$ samples calcined at 350, 375, 475, 550 and 625 °C. Indexing corresponds to IrO$_2$ rutile (PDF 150870), c) analysis of the pore structure of the samples by TEM.

The Ti substrate shows after polishing only the expected reflections that correspond to metallic Ti (PDF 00-044-1294) (Figure 24 a, "Ti cyl"). Heat treatment of the substrate under typical calcination conditions of this study (5 min, 550 °C) does not lead to a measurable formation of crystalline titanium oxides anatase or rutile (Figure 24 a, "Ti cyl 550 °C").

Coating the substrates with mesoporous iridium oxide and calcining at temperatures between 350 and 475 °C does not produce any additional reflections (Figure 24 a, 350 - 475 °C). Hence, the corresponding catalytic layers are X-ray amorphous: IrO$_2$ has either not crystallized yet or crystallites are too small to provide sufficiently intense diffraction signals. However, calcination at temperatures of either 550 °C or 625 °C result in broad reflections at

2-theta positions of 28.1 and 34.7° (Figure 24 a, 550 °C, 625 °C). The signals correspond well with the (110) and (101) reflections of crystalline IrO_2. An estimate by Scherrer equation provides a crystallite size of about 4 nm (550 °C). Increasing the calcination temperature to 625 °C increases the IrO_2 crystallite size to ca. 5 nm. X-ray diffraction analysis therefore suggests that calcination at 550 °C and higher temperatures forms crystalline IrO_2, which is absent at lower calcination temperatures.

The local crystallinity of mesopore walls was studied by electron diffraction analysis on IrO_2 samples removed from the Ti substrate and placed on TEM grids. Figure 24 b presents SAED images of samples calcined in air at 350, 375, 475, 550 and 625 °C, respectively. Films calcined at 350 and 375 °C show very broad diffraction rings, indicating the onset of crystallization. Samples calcined at 475 °C feature narrow diffraction rings. The respective hkl-indices (Figure 24 b, 475 °C) correspond well with the lattice parameters of crystalline IrO_2 rutile (PDF 150870). Calcination at 550 and 625 °C produces sharp diffraction rings with clearly distinguishable diffraction spots indicative of higher material crystallinity. SAED analysis of film samples removed from the substrate thus confirms the phase assignment to IrO_2 rutile. Crystallinity increases with increasing calcination temperature, with significant amounts of crystalline iridium oxide being present already at 475 °C.

TEM analysis for the same samples (Figure 24 c) confirm that calcination at 350 °C, 375 °C and 475 °C yields spherical mesopores origination from the pore template. However, the progressing crystallization at 550 and 625 °C leads to sintering, which results in deformation of the initially spherical pore shape (Figure 24 c, 550 °C, 625 °C). The combined XRD, SAED and TEM data thus suggests that catalyst films calcined between 350 and 475 °C are composed of iridium oxide with low crystallinity, whereas calcination at 550 or 625 °C produces a mesoporous well-crystallized IrO_2 rutile phase with slightly degraded pore structure.

Morphology and phase composition (Figure 24) can now be related to the ECSA and activity data (Figure 23). The lowest studied calcination temperature (325 °C) is too low to decompose template polymer. Hence pores are blocked and neither significant ECSA (Figure 23 a) nor OER activity (Figure 23 c) can be observed. Calcination at 350 °C or 375 °C removes the template polymer and forms an iridium oxide with very low crystallinity (Figure 24 b) but highly accessible pore structure (Figure 23 a, b). The accessible pore structure consists of highly active sites (Figure 23 c), which results in optimal OER performance (Figure 23 b).

Calcination at 400 or 475 °C produces a porous iridium oxide composed of sites with similar intrinsic activity (Figure 23 d). However, the ECSA decreases significantly with increasing calcination temperature (Figure 23 a) resulting in lower OER performance (Figure 23 c).

A further increase in calcination temperature to 550 and 625 °C forms a well crystallized IrO_2 (Figure 24 a, b) with a pore structure degraded by sintering (Figure 24 c). The sintering results in a further decreasing ECSA (Figure 23 a). Moreover, also the activity per accessible site decreases clearly with increasing material crystallinity (Figure 23 d). In consequence, overall OER performance decreases even further.

The activity of pore-templated iridium oxide films is therefore determined by at least two major factors, i.e. the accessible surface area which reaches an optimum at 375 °C, and the intrinsic activity of the accessible sites, which is high between 350 and 475 °C. The best overall performance is thus obtained for calcination at 375 °C.

Similar trends for the intrinsic OER activity were found by Reier et al. on untemplated iridium oxide thin-film catalysts.[64] They observed that the intrinsic OER activity remained independent of the calcination temperature between 250 and 350 °C, but decreased with calcination at   450 °C and at higher temperatures. High activity was assigned to an amorphous low temperature iridium oxide, whereas crystalline high-temperature oxide was reported to be less active. However, they did not observe an increase in ECSA and geometric OER activity between 325 and 375 °C suggesting that this effect is related to the removal of the pore template.

4.2.5 Single layer and Multilayer dipcoating - Influence of withdrawal rate on layer thickness, ECSA, OER and discussion of transport limitation

The transport of evolved gases can be limiting at high current densities. Zeradjanin et al. [138-140] studied the influence of the catalysts structure on the detachment of gas bubbles. Cracked surfaces, i.e. surfaces with added transport pores, showed a higher frequency of bubble detachment in oxygen and chlorine evolution than crack-free samples. Adding sufficiently large pores to OER catalysts could therefore provide a large and accessible active surface area and facilitate the transport of evolved gases. Moreover, quantitative studies of transport effects in gas evolution reactions would benefit from the availability of catalysts with defined and tuneable pore size.

The number of potentially active sites of a homogeneous catalytic coating is expected to scale linear with the amount of coating (i.e. film thickness) and its specific surface area. By increasing the withdrawal rate of the Ti substrates mesoporous single-layer iridium oxide coatings were prepared with higher film thickness in order to increase the catalysts overall

OER performance. However, the thickness of crack-free single layers of oxides that can be produced by EISA is limited.[111] Therefore, thicker films were produced by a new multilayer dipcoating procedure with intermediate calcination steps. The films were employed as scalable model systems with defined porosity to test if the transport of electrons to the active sites and/or the pore transport of produced oxygen gas to the outer film surface becomes limiting for thicker films at higher current density. Figure 25 shows a) SEM cross-section images, b) ECSA analysis and c) OER performance for the respective films.
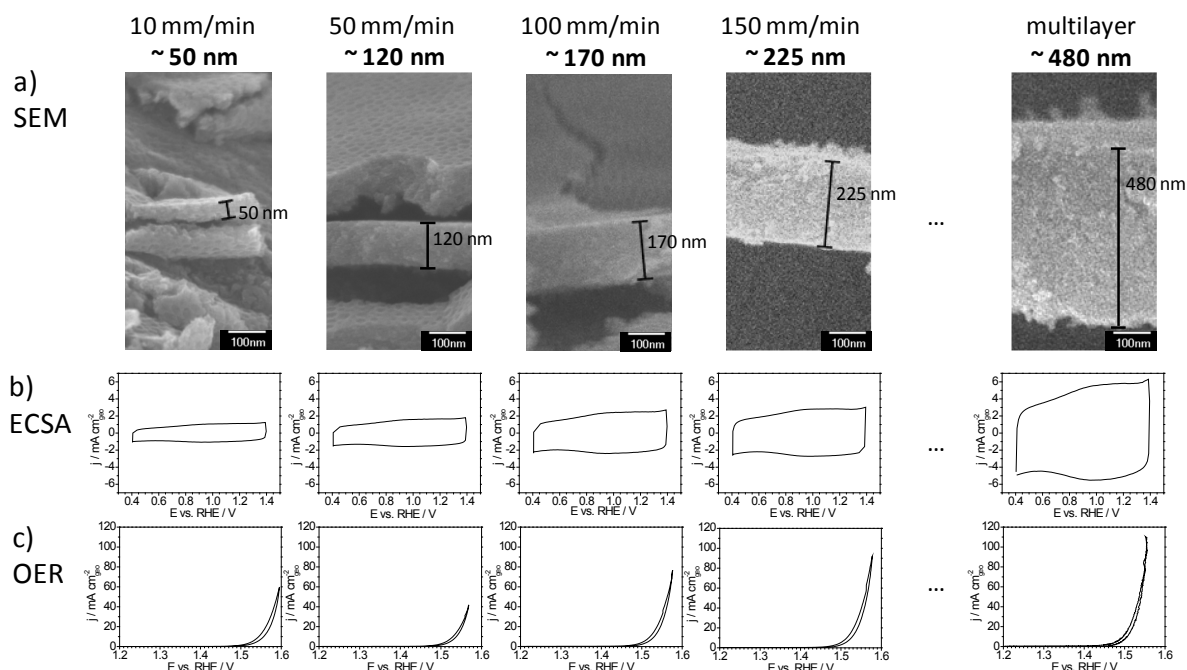

Figure 25 a) Cross section SEM images of mesoporous iridium oxide single- and multilayer films obtained by dipcoating. By adjusting withdrawal rate, controlled film thickness between ~50 and ~225 nm can be achieved in single layer regime. In order to obtain thicker layers multilayer films were synthesized. b) CVs measured in the ECSA potential region between 0.40 and 1.40 V vs. RHE. For thicker layers the current appears to be progressively larger, hence the multi layer sample obtains the highest ECSA. c) CVs measured in the OER range for different layer thicknesses. The OER activity increases with increasing layer thickness. The 480 nm thick multilayer catalyst achieves the lowest overpotential (0.20 V at 1.0 mA/cm²).

Mesoporous crack-free catalyst films were obtained for all single-layer coatings up to a withdrawal rate during dip-coating of 150 mm/min. (Note that the cracks visible in Figure 25 a are a result of sample preparation for film thickness analysis, not of the synthesis procedure.) The thickness of the produced mesoporous single-layer iridium oxide increases linear with increasing withdrawal rate of the substrate from 50 nm (10 mm/min) to 120 nm (50 mm/min), 170 nm (100 mm/min) and finally 225 nm (150 mm/min). A further increase in film thickness by faster substrate withdrawal resulted in cracking and peel-off of the films during calcination. However, significantly thicker films (480 nm) were produced by multilayer deposition

(30 mm/min, 4 layers) with intermediate stabilization steps at 200 °C and a final calcination at 375 °C (Figure 25 a, multilayer). ECSA recorded by cyclic voltammetry in the potential window between 0.40 and 1.40 V_{RHE} shows that the geometrical current response increases linearly with increasing film thickness (Figure 25 b). Moreover, also the respective OER scans shift towards lower overpotentials with increasing film thickness (Figure 25 c). The influence of film thickness on ECSA and OER activity was quantified by analysis of the respective electrocatalytic data. Figure 26 a plots the obtained total ECSA charge vs. film thickness, Figure 26 b shows geometric OER current densities at 1.50, 1.53 and 1.55 V_{RHE} plotted vs. the ECSA for each of the respective single-layer and multi-layer film.
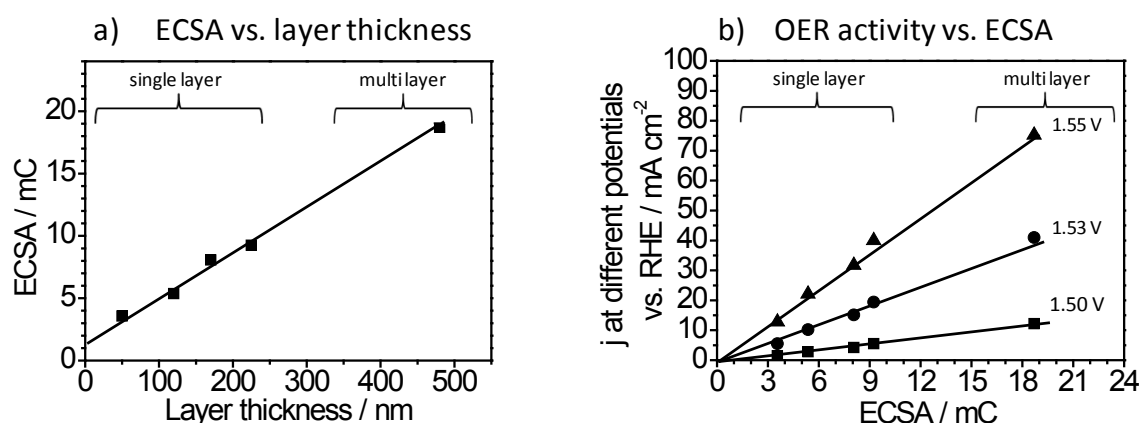

Figure 26: Influence of the thickness of mesoporous templated IrO$_2$ films on ECSA and on OER performance for single layer (50 – 225 nm) and multilayer catalysts (four layers, 480 nm). a) ECSA as total charge obtained as a mean value of the integrated anodic and cathodic currents between 0.40 and 1.40 V_{RHE} plotted vs. film thickness (from SEM), b) current density recorded at 1.50 V, 1.53 V and 1.55 V_{RHE} normalized to the geometric electrode surface area and plotted vs. ECSA. Layer thickness derived from cross section SEM (Figure 25 a). ECSA and OER cyclic voltammograms are shown in Figure 25 b and Figure 25 c.

The obtained ECSA scales clearly linear with film thickness for mesoporous IrO$_2$ films between 50 and 480 nm, indicating that for all films the complete film volume is accessible for ECSA analysis (Figure 26 a). Moreover, also the geometric current density obtained at a given potential in OER measurements scales linear with the employed ECSA area (Figure 26 b). This analysis suggests that independent of film thickness each surface site contributes equally to the OER reaction, even for the thicker films and higher current densities. If any other process than the surface reaction such as gas transport through the pore system or electron conduction to the active site was the limiting step a deviation from the linear behavior would be expected for thicker films at least for the higher potentials and current densities. Since this is not the case (Figure 26 b) transport limitation are absent in the case of iridium oxide catalyst films with templated mesopores at least up to 480 nm thickness, potentials of 1.55 V_{RHE} and current densities as high as 75 mA per cm^2 of planar electrode surface.

In order to relate the achieved catalytic performance to values obtained in previous studies the overpotentials can be compared at a given geometric current density. Johnson et al.[57] prepared thick IrO_2 layers by dropcasting and obtained OER overpotentials of about 0.240 V_{RHE} at 1 mA/cm². Hu et al.[58] synthesized macroporous IrO_2 with colloidal SiO_2 via hard templating and measured ca. 0.250 V overpotential at 1 mA/cm². Nakagawa et al.[141] used an electro-flocculation method to prepare 2 nm iridium oxide nanoparticles and reported 0.250 V overpotential at 0.5 mA/cm². Reier et al.[63] used spincoating to deposit a lay layer of Ir-Ni oxide onto titanium and showed an overpotential of 0.258 V at 1 mA/cm². Nong et al.[62] prepared Ir-Ni oxide nanoparticles with core-shell structure deposited on ATO support. Subsequently, performed electrocatalytic OER experiments revealed an overpotential of 0.260 V (at 1 mA/cm²). Kushner-Lenhoff et al.[59] synthesized iridium oxide layers via electrodeposition from $Cp*Ir(H_2O)_3]^{2+}$ ($Cp*$ =pentamethylcyclopentadienyl)] and reported 0.267 V at 0.5 mA/cm². A similar synthesis performed by Blakemore et al.[60] led to catalysts with approximately 0.270 mV overpotential (at 0.5 mA/cm²). Oh et al.[61] successfully deposited iridium nanodendrites on oxide supports (ATO) and observed an overpotential of approximately 0.270 V (at 1 mA/cm²). A polycrystalline iridium cylinder measured by Reier et al.[56] revealed an overpotential of 0.300 V (at 1 mA/cm²). However, investigations of the OER activity for single crystalline Ir(110) performed by Oezer et al.[137] revealed an overpotential of 0.340 V (at 1 mA/cm²). Ortel et al.[65] achieved 0.220 V (1 mA/cm²) overpotential for thinner single-layer IrO_2. The optimized catalyst of the present study (480 nm thick multilayer calcined at 375 °C) achieves overpotentials as low as 0.200 V (at 1 mA/cm²), i.e. significantly lower than previously reported values. A further increase in performance is likely if thicker films are obtained by further exploitation of the multilayer approach or dip-coating in the capillary regime.[111]

Table 2 Comparison of OER overpotentials at a given current density with previously reported literature data.

Material	Current density j / mA cm^{-2}	Overpotential / V	Reference
Mesoporous templated IrO$_2$ (multi layer)	1.0	0.200	This work
Mesoporous templated IrO$_2$ (single layer)	1.0	0.220	Ortel et al.[65]
IrO$_2$ layer	1.0	0.240	Johnson et al.[57]
Macroporous IrO$_2$	1.0	0.250	Hu et al.[58]
IrO$_2$ nanoparticles	0.5	0.250	Nakagawa et al.[141]
Ir-Ni oxide films	1.0	0.258	Reier et al.[63]
IrNiO$_x$ nanoparticles on ATO	1.0	0.260	Nong et al.[62]
Electrodeposited IrO$_2$ layer	0.5	0.267	Kushner-Lenhoff et al.[59]
Ir-Nanodendrites on ATO	1.0	0.270	Oh et al.[61]
Electrodeposited IrO$_2$ layer	0.5	0.270	Blakemore et al.[60]
Polycrystalline Ir	1.0	0.300	Reier et al.[56]
Single crystalline Ir (110)	1.0	0.340	Oezer et al.[137]

In summary, a new synthesis approach for model-type OER catalysts with controlled thickness, pore size and crystallinity is reported. In combination with the investigation of structure-activity relationships the best Ir-oxide based OER catalyst reported so far in literature is obtained. Mesopores introduced into the catalyst by templating with micelles of block copolymers enable a rapid transport of the produced oxygen at least up to current densities of 75 mA/cm^2. Thick mesoporous catalyst films are obtained by multilayer deposition. Even the most active catalyst did not show signs of limitation of electron transport, electrolyte access or gas transport. The catalyst films are chemically and mechanically stable also at current densities as high as 115 mA/cm^2. The investigation of structure-activity relationships revealed that the OER performance of mesoporous IrO$_2$ is controlled by at least two independent factors, i.e. the accessible surface area and the intrinsic activity per accessible site.

The next chapter will extend the concept to a more complex system, i.e. mixed metal oxides of iridium and titanium in order to possibly lower the required content of noble metal under the preservation of OER performance.

4.3 Mesoporous templated IrO$_2$/TiO$_2$ synthesized from Ir(OAc)$_3$ and TiCl$_4$

Limited availability of Ir, high prices and competition with other applications demand further improvement of iridium based electrocatalysts in terms of i) activity and ii) stability. In order to achieve this goal different concepts were reported in literature. i) Hu et al.[142] showed enhanced iridium mass based OER activities of catalysts consisting of IrO$_2$ deposited on Nb doped TiO$_2$ nanoparticles prepared by a sol-gel method. ii) Improving the catalytic stability is considered as another important approach to further increase the sustainability of iridium based OER catalysts for practical applications such as water splitting. Comninellis et al.[74] reported that the addition of non conducting oxides such as TiO$_2$, Ta$_2$O$_5$, ZrO$_2$ significantly decreases the dissolution rate of an active and conductive metal oxide (e.g. IrO$_2$) under acidic OER conditions. The lower dissolution rate of iridium oxide during OER is explained by the beginning formation of a solid solution of IrO$_2$ and TiO$_2$. McDaniel et al.[143] reported a complete formation of a solid solution of IrO$_2$ and TiO$_2$ which was obtained by firing a mixture of powders from IrO$_2$ and TiO$_2$ at 900 °C and 1000 °C, respectively.

The addition of TiO$_2$ to IrO$_2$ is considered an important approach to improve electrocatalytic properties of IrO$_2$ which is presented in this thesis. A detailed description of some existing synthesis routes for mesoporous TiO$_2$ is given in chapter 2.3.2 These pathways comprise titanium alkoxides and stabilizers,[120] titanium chloride,[105] preformed titanium oxide nanoparticles,[95] as well as TALH.[109] The synthesis route with titanium alkoxides requires the use of stabilizing agents. These agents, however, appear less practical during synthesis. The formation of a solid solution at comparable low temperature is unlikely for synthesis strategies using preformed TiO$_2$ nanoparticles. Thus, a synthesis route for PEO-PB-PEO polymer templated IrO$_2$/TiO$_2$ is presented with the use of TiCl$_4$ (chapter 4.3) and TALH (chapter 4.4), respectively.

Titanium chloride exhibits excellent sol-gel capabilities and is a well investigated precursor for the production of mesoporous TiO$_2$ via soft templating.[99] Catalytic coatings consisting of IrO$_2$ and TiO$_2$ were synthesized from Ir(OAc)$_3$ and TiCl$_4$, and physicochemically characterized (chapter 4.3.1). A controlled variation in calcination temperature was conducted in order to investigate changes in crystallinity, morphology, electrical conductivity (chapter 4.3.2), as well as electrochemical activity and surface area (chapter 4.3.3). The varying iridium oxide loading within titanium oxide is considered as another important synthesis paramater. Thus, iridium loading was selectively adjusted in order to investigate the influence on morphology, electrical conductivity (chapter 4.3.4), as well as electrochemical OER activity and surface area (chapter 4.3.5). The gained knowledge is then combined to identify the OER reaction controlling parameters that allow the production of highly active OER catalysts.

4.3.1 Physicochemical characterization: Ir(OAc)$_3$ and TiCl$_4$ calcined at 400 °C

Films of mesoporous templated IrO$_2$/TiO$_2$ were obtained via dipcoating at 25 °C, 40 % relative humidity and a withdrawal rate of 150 mm/min on polished substrates (Ti, Si). Dipcoating solutions were prepared by dissolving Ir(OAc)$_3$, TiCl$_4$ and PEO$_{213}$-PB$_{184}$-PEO$_{213}$ in ethanol and water. The as prepared samples were dried for 10 minutes in the dipcoating chamber under controlled atmosphere and subsequently transferred into a preheated muffle furnace at 400 °C. Physicochemical characterization of the obtained sample is shown in Figure 27 comprising a, b, c) SEM; d) TEM; e) SAED f, g) SAXS; and h) Kr-physisorption of a film containing 30 wt. % Ir in Ir/TiO$_2$.
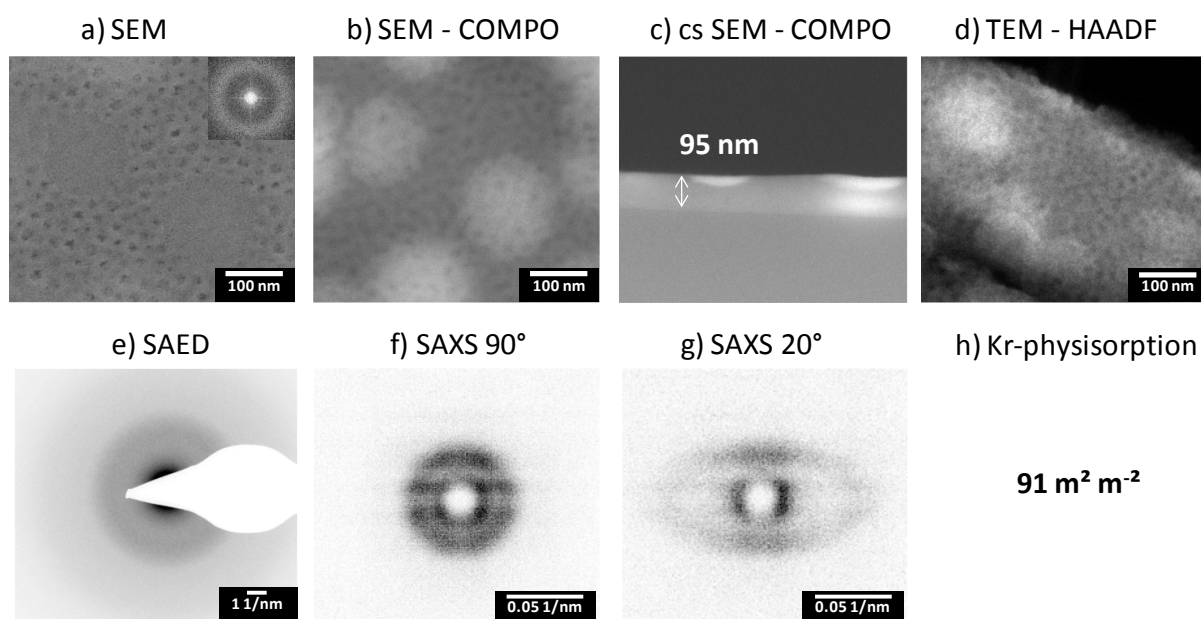

a) SEM   b) SEM - COMPO   c) cs SEM - COMPO   d) TEM - HAADF

95 nm   100 nm   100 nm   100 nm

e) SAED   f) SAXS 90°   g) SAXS 20°   h) Kr-physisorption

1 1/nm   0.05 1/nm   0.05 1/nm   91 m² m⁻²

Figure 27: Morphology, composition, crystallinity, pore ordering and surface area of PEO-PB-PEO templated 30 wt. % Ir in Ir/TiO$_2$ films calcined at 400 °C under air. a) Scanning electron microscopy show mesoporous templated and untemplated domains at the outer surface plane area. The difference in z-contrast of both domains is revealed b) for the outer surface plane area in the COMPO image of the corresponding SEM image as well as for the c) film volume. The emergence of segregated areas on the outer surface plane and in the film volume suggest titanium rich mesoporous templated and iridium rich untemplated domains. Segregation throughout the whole film volume is further confirmed by d) TEM in high angle annular darkfield mode. e) Selected area electron diffraction measurements show no pronounced rings suggesting that crystallites are too small to create distinct reflections. Templated mesoporosity appears to be locally ordered f) parallel (90°, in-plane) and g) perpendicular (20°, out-of-plane) to the substrate. h) Kr-physisorption reveals 91 m² film surface per m² substrate indicating a fully accessible pore system.

The SEM images recorded in top view mode (Figure 27 a) reveal two different types of domains, i.e. an untemplated, textural porous and a mesoporous templated domain comprising spherical pores with pore openings of 25 ± 4 nm in diameter. The corresponding

FFT of the top view SEM image (inset Figure 27 a) shows an isotropic ring revealing the presence of an ordered pore arrangement at the outer surface plane area. The periodic distance between pore centers amounts to approximately 27 nm.

In order to explore the composition of segregated domains, a COMPO image corresponding to the top view SEM image is shown (Figure 27 b) which indicates the presence of heavier elements for the untemplated (brighter areas, iridium rich) and lighter elements for the mesoporous templated (darker areas, titanium rich) domain.

A cross section SEM image in COMPO mode is shown (Figure 27 c) to provide insight into segregation throughout the whole film volume area. The image reveals a layer thickness of approximately 95 nm, as well as two domains with different concentration of heavier and lighter elements. This indicates that segregation of iridium and titanium, which was already observed in top view SEM (Figure 27 a and b), even occurs within the layer. The observation is further confirmed by coatings scratched off from the titanium substrate and subsequently investigated with TEM in high angle annular darkfield mode (Figure 27 d). The image reveals segregated areas with different brightness, underlining that separation between titanium and iridium occurs inside the film volume. Furthermore, TEM reveals spherical pores indicating complete penetration of the coating by templated mesoporosity. A performed electron diffraction measurement (Figure 27 e) features no pronounced rings which can be attributed to a crystallite size which is too low for the production of distinct reflections.

The pore ordering was investigated with 2D SAXS data recorded in transmission mode of layers deposited on titanium foil. The SAXS diffraction patterns of a layer recorded with an incident beam angle of 90° (Figure 27 f) and 10° (Figure 27 g) with respect to film surface normal is shown. The image recorded at 90° (in-plane) displays an isotropic ring suggesting that domains of PEO-PB-PEO micelles arrange locally ordered parallel to the substrate (d_{xy}=30 nm). Adjusting an angle of 20° between incident beam and surface normal by tilting the sample, features an elliptically distorted ring, suggesting locally ordered mesoporosity perpendicular to the substrate but with slight deformation of the mesopore structure (d_z=8.1 nm). As to the difference in distance of pore centres (*d*-spacing) parallel (30 nm) and perpendicular (8.1 nm) to the substrate, the synthesis in its present form produces an elliptically deformed pore morphology caused by solvent evaporation and film shrinkage during dip-coating.[101-102, 144]

The surface area of the layer coated on silicon substrate was investigated with krypton as an adsorbate. The BET surface area amounts to 91 m² film surface area per m² substrate geometric surface area indicating that most of the containing polymer template was removed and that an accessible mesopore system is produced. The surface area is in good agreement with literature reports for thermally prepared mesoporous templated IrO_2 synthesized from $Ir(OAc)_3$ and PEO-PB-PEO (130 m²/m²).[65]

4.3.2 Influence of calcination temperature on morphology, crystallinity and sheet conductivity: Ir(OAc)$_3$ and TiCl$_4$ calcined between 200 - 600 °C

Samples of mesoporous templated IrO$_2$/TiO$_2$ were obtained by dipcoating and subsequent calcination for 10 minutes at temperatures between 80 and 600 °C, respectively. The obtained samples were analyzed in terms of morphology (SEM, Figure 28 a), crystallinity (XRD, Figure 28 b, c) and electrical sheet conductivity (Figure 28 d) in order to identify the impact of calcination temperature.
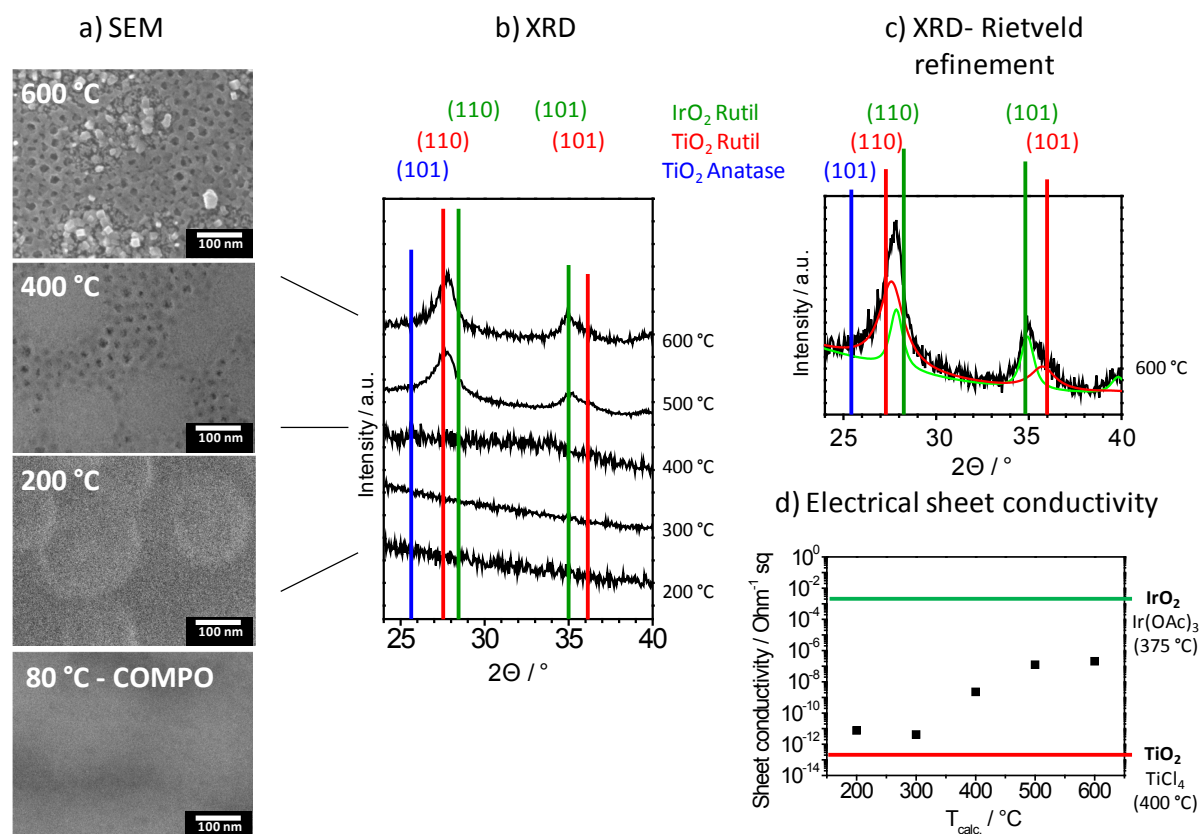

Figure 28: Influence of calcination temperature on a) morphology, b, c) crystallinity and d) sheet conductivity of PEO-PB-PEO templated IrO$_2$/TiO$_2$ derived from Ir(OAc)$_3$ and TiCl$_4$ (30 wt. % Ir in Ir/TiO$_2$). a) SEM micrographs feature segregated areas for samples calcined at different temperatures between 200 and 600 °C, respectively. b) Thermally treated samples at temperatures higher than 500 °C produce additional reflections that can be assigned to a rutile phase. c) Rietveld refinement was applied for diffractograms recorded for samples calcined at 600 °C in order to investigate phase composition. d) Electrical sheet conductivity increases as a function of calcination temperature.

SEM micrographs (Figure 28 a) for films thermally treated at 80 and 200 °C feature segregated domains and poor contrast. The presence of segregated domains for samples thermally treated below 200 °C rule out temperature as a driving force for demixing. The observed poor contrast is related to incomplete polymer template removal.[47] A vast majority of the polymer template is removed when applying higher calcination temperatures, e.g. 400 °C (Figure 28 a). The electron micrograph reveals two different type of domains, i.e. an

untemplated, textural porous and a mesoporous templated domain. The obtained titanium rich mesoporous regime shows spherical pores with a pore opening of 25 ± 4 nm in diameter, whereas the untemplated iridium rich area possesses textural porosity with pore openings smaller than 2 nm. (also see Figure 27). A further increase of calcination temperature to 600 °C still shows two separated areas. The mesoporous templated titanium rich domain exhibits smooth pore walls under preservation of mesoporosity, whereas the iridium rich domain features temperature induced crystal growth leading to loss of textural porosity.

Silicon wafers coated with IrO_2/TiO_2 and calcined at temperatures between 200 and 600 °C were investigated by XRD in order to assess the impact of calcination temperature on crystal properties (Figure 28 b). Samples calcined between 200 and 400 °C do not show distinct reflections within X-ray diffraction patterns. Hence, the corresponding films appear to be X-ray amorphous suggesting that the respective oxides of iridium and titanium are either not crystallized yet or too small to produce diffraction signals. An increase of calcination temperature to 500 or 600 °C leads to reflections at 2-theta positions of 37.8°, 34.9° and to an additional shoulder at 36.2°. The reflection pattern at 600 °C was further analyzed by Rietveld refinement (Figure 28 c). The deconvoluted signals correspond with a IrO_2-rutile phase containing a small fraction of titanium and a TiO_2-rutile phase with additional iridium content. Scherrer equation was applied on the deconvoluted curves in order to reveal the crystallite size. The obtained values for the respective phases amount to 12 nm (IrO_2-rutile containing Ti) and 6 nm (TiO_2-rutile containing Ir).

Figure 28 d presents the influence of calcination temperature for films of IrO_2/TiO_2 (30 wt. % Ir in Ir/TiO_2) on electrical sheet conductivity. For the purpose of comparison, the sheet conductivity for similar calcined, mesoporous templated IrO_2 and TiO_2 coated on glass substrate is provided by red and green bars (TiO_2 synthesized from $TiCl_4$ and calcined for 10 minutes at 400 °C: $2.2 \cdot 10^{-13}$ $(Ohm/sq)^{-1}$, and IrO_2 synthesized from $Ir(OAc)_3$ calcined for 5 minutes at 375 °C: $2.6 \cdot 10^{-3}$ $(Ohm/sq)^{-1}$). The observed sheet conductivity appears to be low for samples heat treated at 200 °C and 300 °C, respectively. This observation is in good agreement with SEM micrographs suggesting incomplete template removal for films calcined at 200 °C (Figure 28 a) and 300 °C (Figure 44). A further increase of the calcination temperature steadily increases the electrical sheet conductivity to $2 \cdot 10^{-7}$ $(Ohm/sq)^{-1}$, probably related to ongoing crystallite growth and an accompanying decrease in the amount of grain boundaries.

In summary, three effects are observed: i) a segregation of IrO_2 and TiO_2 on a lengthscale of roughly 100 nm, ii) the development of a mesoporous structure solely for titanium rich domains and iii) a higher degree of textural porosity for iridium rich domains. Based on these observations, a structural model is deduced and shown in Figure 29. We hypothesize that all

three effects can be explained by the different chemical properties of the utilized metal oxide precursors (e.g. $TiCl_4$ and $Ir(OAc)_3$):
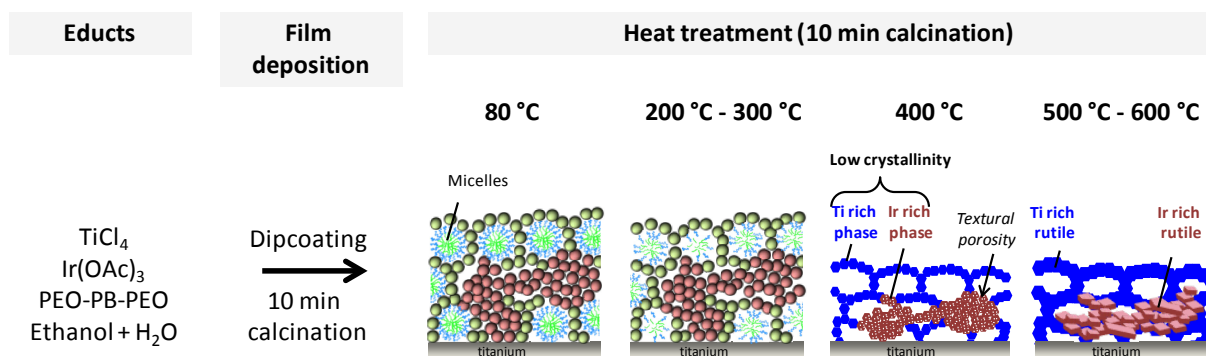

Figure 29: Structural modifications as a function of calcination temperature for 30 wt. % Ir in Ir/TiO_2 coatings on titanium synthesized from a solution comprising $TiCl_4$, $Ir(OAc)_3$, PEO-PB-PEO, EtOH and H_2O. Dipcoating was performed under a controlled atmosphere at 25 °C and 40 % relative humidity. The as prepared samples were dried for 10 minutes in the dipcoating machine and subsequently transferred to a preheated muffle furnace for calcination at temperatures between 80 and 600 °C, respectively. The structural models are deduced from observations of physicochemical measurements such as SEM (Figure 27, Figure 28), TEM (Figure 27), SAXS (Figure 27) and XRD (Figure 28).

Titanium tetrachloride ($TiCl_4$) is a well known precursor often used in syntheses of nanostructured TiO_2 (see chapter 2.2.6 for more detailed information). In literature, it is reported that $TiCl_4$ shows rather fast hydrolysis and condensation rates.[99, 102] The intrinsic production of HCl during hydrolysis and condensation prevents further polycondensation. The result is the formation of self stabilized titanium oligomers terminated by hydroxide groups with particle diameters in the range between 0.4 - 1.7 nm (reported in literature for $TiCl_4$ dissolved in EtOH+F127[107]). The presence of accessible hydroxide groups enables the interaction with hydrolytic regions of the block copolymer (e.g. PEO) through hydrogen bonding.[99]

iridium acetate is characterized by the presence of acetic acid as a chelat ligand. The precursor is stable against hydrolysis and condensation in water and ethanol at room temperature[145] thus forming no small oligomers. The absence of hydroxide groups at the central atom prevents the interaction of dissolved $Ir(OAc)_3$ and hydrolytic regions of the polymer template (e.g. PEO).

Based on these reports and the observations from physicochemical analysis within this work, the above mentioned effects (i-iii) are explained as followed:

i) The equilibrated dipcoating solution comprised small titanium oligomers ($TiCl_{4-x-y}(OEt)_x(OH)_y$, derived by $TiCl_4$), $Ir(OAc)_3$, PEO-PB-PEO, ethanol, and water. The colloidal suspension appeared clear and showed a light green colour. Tyndall effect usually occurs for particles dispersed in a liquid medium with a diameter of at least ~100 nm.[146-147] Thus, it can be concluded that no light is scattered by particles larger than ~100 nm

dispersed in the suspension. The absence of larger particles implies that the observed segregated domains in catalytic layers are not formed inside the solution. Hence, demixing very likely occurs after film deposition and is possibly related to different drying behaviours of iridium and titanium. Different drying behaviours can be associated with different mobilities of both metal oxide precursors within the dipcoating solution. We hypothesize that the different mobilities are caused by different interaction behaviours: $TiCl_4$ interacts with the polymer template, whereas $Ir(OAc)_3$ has no hydroxide groups that may interact with the polymer template.

Moreover, the different interaction behaviours of $TiCl_4$ and $Ir(OAc)_3$ with the polymer template are used to describe ii) the development of mesoporosity solely for titanium rich domains. It is likely to find an oxide precursor next to the polymer template for precursors possessing the capability to interact with the polymer template (e.g. $TiCl_4$). As a consequence, titanium rich domains appear to be mesoporous templated, whereas iridium rich domains show no sign of templated mesoporosity.

However, the iii) iridium rich domains depict a very high degree of textural porosity in contrast to templated titanium rich domains. This behaviour is associated with the different chemical structure of the respective precursors. The acetic acid surrounding iridium as a chelat ligand contains a higher degree of carbon than $TiCl_4$. Carbon containing precursors decompose to CO_2 during calcination which possibly introduces textural porosity to the iridium rich domains.[65, 148]

4.3.3 OER activity and electrochemical active surface area

Dipcoated films of a solution containing $Ir(OAc)_3$, $TiCl_4$, PEO-PB-PEO, ethanol and water were calcined in a preheated muffle furnace between 200 and 600 °C. The as received samples (IrO_2/TiO_2, 30 wt. % Ir in Ir/TiO_2) were subsequently mounted as a working electrode in a three electrode disc setup using a reversible hydrogen electrode (RHE) as a reference and a Pt-gauze as a counter electrode. All electrochemical experiments were conducted with a rotation speed of the working electrode of 1600 rpm, are corrected for iR drop and the current response is normalized to the substrates geomerical planar surface area. OER (oxygen evolution reaction) activity was determined by cyclic voltammetry in a potential window ranging between 1.20 - 1.65 V_{RHE} (6 mV/s, Figure 30 a). Furthermore, the OER performance is shown as a function of calcination temperature by measuring the corresponding current density at 1.60 V_{RHE} (Figure 30 b). The ECSA (electrochemical active surface area) was investigated by cyclic voltammetry in a lower potential window of 0.40 - 1.40 V_{RHE} (50 mV/s, Figure 30 c). The mean value of the integrated anodic and cathodic scan of each cyclic voltammogram was determined in order to derive a value for the electrochemical accessible surface area (Figure 30 d).

For IrO_2/TiO_2 synthesized from $Ir(OAc)_3$ and $TiCl_4$ (30 wt. % Ir in Ir/TiO_2) with different calcination temperatures Figure 30 shows a) the cyclic voltammograms (CVs) in the OER regime, b) the quantified OER performance as a function of $T_{calc.}$, c) the CVs in the ECSA region, as well as d) the quantified ECSA in a dependency of $T_{calc.}$.
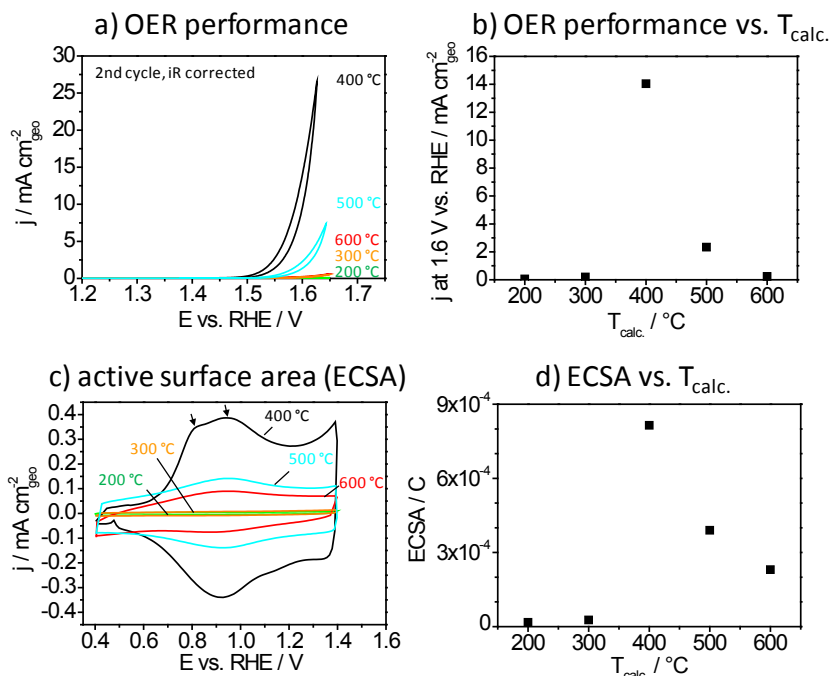

Figure 30: Influence of calcination temperature on a,b) OER performance and c,d) electrochemical accessible surface area (ECSA) of mesoporous templated IrO_2/TiO_2 (30 wt. % Ir in Ir/TiO_2) on titanium substrate. a) CVs recorded in the OER potential window between 1.20 and 1.65 V_{RHE} at a scanrate of 6 mV/s, b) current density measured at 1.60 V_{RHE} normalized to the geometric electrode surface area, c) CVs were recorded in a lower potential window between 0.40 and 1.40 V_{RHE} at 50 mV/s in order to access electrochemical accessible surface area, d) ECSA is derived as the total charge obtained as a mean value of the integrated anodic and cathodic currents between 0.40 and 1.40 V_{RHE}. Electrocatalytic data were accessed in 0.5 M H_2SO_4 electrolyte with rotating working electrode, RHE reference and Pt gauze counter electrode. Approximate layer thickness: 100 nm.

Figure 30 a depicts the current response normalized to the titanium sheet's geometrical surface area. The current response is directly related to the OER activity and appears to strongly depend on the applied calcination temperature. Catalysts calcined at 400 and 500 °C show the highest current densities among the studied samples. In order to visualize the impact of calcination temperature, the OER activity, quantified by measuring the current density at a potential of 1.60 V_{RHE}, was plotted as a function of calcination temperature (Figure 30 b). It is clearly visible that the OER activity increases between 200 and 400 °C but progressively declines with a further increase of calcination temperature.

The ECSA of each sample can be determined from the corresponding current density in the potential window between 0.40 - 1.40 V_{RHE} as shown in Figure 30 c. The recorded cyclic voltammograms appear symmetric with respect to the horizontal axis. Samples, heat treated

between 400 and 600 °C, depict a significant current response during the anodic and cathodic scan. Furthermore, the sample heat treated at 400 °C shows broad humps at potentials around 0.80 and 0.92 V_{RHE} (marked by arrows). The redox wave at a potential of ~0.92 V_{RHE} is related to the transformation of the Ir^{III}/Ir^{IV} redox couple.[125, 136] However, no clear explanation is found for the presence of the small shoulder at potentials of 0.80 V_{RHE}.

Figure 30 d plots the charge determined by the mean value of the integrated anodic and cathodic currents in the ECSA range as a function of calcination temperature. The derived charge is defined as a measure of electrochemical active surface area. Between 200 - 400 °C the ECSA increases with higher calcination temperature, but steadily declines between 400 and 600 °C for higher calcination temperatures.

The OER activity as well as the electrochemical active surface area show very similar trends. Electrochemical activity and surface area rapidly increase from 200 to 400 °C and progressively decrease with further increase of temperature. It is therefore evident that the accessible surface area contributes to the overall OER activity.

Morphology, crystallinity and electrical sheet conductivity (Figure 28) can now be correlated to the electrochemical active surface area and OER activity (Figure 30). The low surface area for samples calcined at 200 and 300 °C (Figure 30 d) is in good agreement with observations from SEM analysis (Figure 28 a) where poor contrast and brightness was observed. The appearance of poor contrast and brightness is possibly caused by incomplete polymer template removal. If the samples still contain remaining polymer residues, the pore system is still blocked. Thus, no electrochemically accessible surface area (Figure 30 d) as well as no OER activity (Figure 30 b) is observed. Enhancing the calcination temperature to to 400 °C forms a mixed metal oxide of iridium and titanium with very low crystallinity (Figure 28 b), higher electrical sheet conductivity (Figure 28 c) and a high number of accessible active sites (Figure 30 d). The good accessibilty of the porous structure and the higher electrical sheet conductivity consequently result in a high OER activity (Figure 30 b). A further increase of the calcination temperature to 500 and 600 °C forms a well crystallized mixed metal oxide of iridium and titanium (Figure 28 b) with a loss of textural porosity of the iridium rich domain (Figure 28 a). Furthermore, the electrical sheet conductivity is increasing, whereas the observed ECSA progressively decreases at temperatures higher than 500 °C (Figure 30 d). The strong decline in the ECSA is related to the sintering of the textural porosity induced by crystal gowth of oxides from iridium and titanium. The activity of polymer templated mixed oxide films of iridium and titanium is influenced by at least one major factor, i.e. the accessible surface area.

4.3.4 Influence of Ir-content on morphology and sheet conductivity

Mesoporous templated films of IrO_2/TiO_2 with varying iridium content (0 - 100 wt. % Ir in Ir/TiO_2) were dipcoated on titanium and microscope slides and subsequently calcined for 10 minutes at 400 °C under air. In order to reveal the impact of iridium loading on morphology and electrical sheet conductivity, the samples were investigated by SEM and sheet resistivity measurements. The findings of physicochemical characterizations are shown in Figure 31 for a) SEM and b) electrical sheet conductivity.

a) SEM
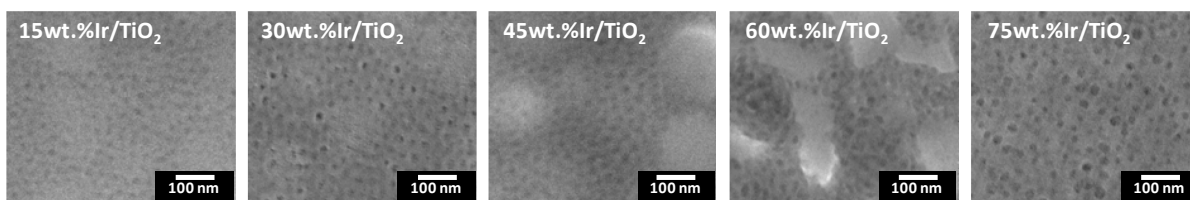
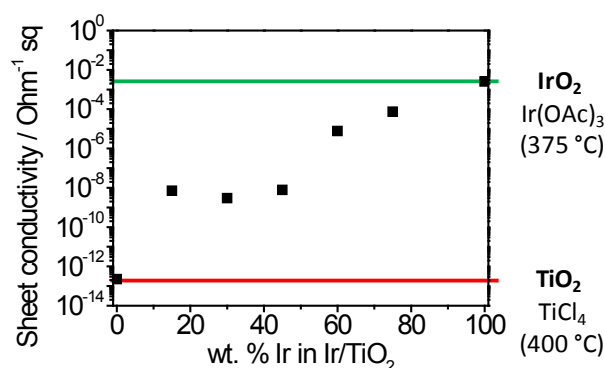
b) Electrical sheet conductivity

Figure 31: Influence of iridium content on the a) morphology and b) electrical sheet conductivity of mesoporous templated IrO₂/TiO₂ with different iridium loadings and a subsequent heat treatment at 400 °C under air. For comparison, the electrical conductivity values of similar prepared, mesoporous templated IrO₂ (Ir(OAc)₃, 5 min 375 °C) and TiO₂ (TiCl₄, 10 min 400 °C) are added as green and red lines, respectively.

SEM images recorded in top view mode (Figure 31 a) for samples with 15 wt. % Ir in Ir/TiO_2 and heat treated at 400 °C reveal two different type of domains, i.e. untemplated, textural porous and mesoporous templated domains with spherical pores. The elemental composition of both domains was investigated by COMPO (Figure 27 b) revealing the presence of heavier elements for the untemplated (brighter areas, iridium rich) and lighter elements for the mesoporous templated (darker areas, titanium rich) domains. The segregation between both metal oxides (Ir, Ti) is still present with increasing iridium content up to loadings of 75 wt. % Ir in TiO_2. Segregation of both metal oxides is explained by the distinct chemical properties of the utilized precursor systems, i.e. $Ir(OAc)_3$ and $TiCl_4$ (see chapter 4.3.2 for detailed explanation of demixing). However, the distance between iridium rich areas decreases as the iridium loading within TiO_2 increases.

The electrical sheet conductivity was determined for different loadings of IrO_2 within TiO_2 coated on insulating glass and subsequently heat treated at 400 °C under air. For the purpose of comparison, the sheet conductivity for similar calcined, mesoporous templated IrO_2 and TiO_2 coated on glass substrate is provided by red and green bars (TiO_2 synthesized from $TiCl_4$ and calcined for 10 minutes at 400 °C: $2.2 \cdot 10^{-13}$ $(Ohm/sq)^{-1}$ and (IrO_2 synthesized from $Ir(OAc)_3$ calcined for 5 minutes at 375 °C: $2.6 \cdot 10^{-3}$ $(Ohm/sq)^{-1}$). The iridium content has a severe impact on electrical sheet conductivity (Figure 31 b). It increases with higher iridium content which is related to the metallically conductive character of IrO_2.[54]

4.3.5 Influence of Ir-content on electrochemical OER activity and surface area

The effect of iridium content on morphology and sheet conductivity can now be correlated with OER activity and electrochemical accessible surface area. Films of mesoporous templated IrO_2/TiO_2 with different loadings of iridium were obtained via dipcoating on polished titanium sheet substrates. The OER activity was determined by cyclic voltammetry in a potential window ranging between 1.20 - 1.65 V_{RHE} (6 mV/s, 1600 rpm iR corrected, Figure 32 a). Furthermore, the OER performance at a potential of 1.60 V_{RHE} is shown as a function of iridium loading within TiO_2 (Figure 32 b). The ECSA (electrochemical active surface area) was investigated by cyclic voltammetry in a lower potential window between 0.40 - 1.40 V_{RHE} (50 mV/s, Figure 32 c). The mean value of the integrated anodic and cathodic scan of each cyclic voltammogram was determined in order to derive a value for the electrochemical accessible surface area. The ECSA is shown in dependency of iridium loading (Figure 32 d).

For IrO_2/TiO_2, derived from $Ir(OAc)_3$ and $TiCl_4$ (400 °C) with different iridium loadings in TiO_2, Figure 32 depicts a) the cyclic voltammograms in the OER regime, b) the quantified OER performance as a function of iridium content, c) CVs in the ECSA region, as well as d) the quantified ECSA as a function of iridium loading.
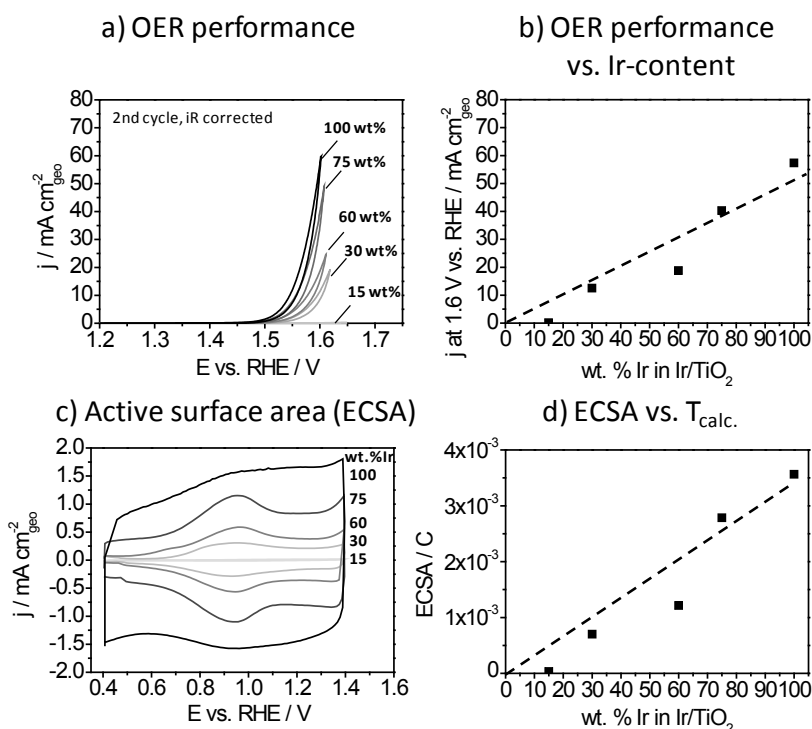
Figure 32: Influence of iridium content on a,b) OER performance and c,d) electrochemical accessible surface area. a) CVs recorded in the OER regime between 1.20 - 1.65 V_{RHE} (6 mV/s), b) current density recorded at 1.60 V_{RHE} with respect to geometrical surface area, c) cyclic voltammograms recorded in the ECSA range between 0.40 - 1.40 V_{RHE} (50 mV/s), d) ECSA derived as the total charge obtained as a mean value of integrated anodic and cathodic currents.

The OER performance of each catalyst (IrO_2/TiO_2, 400 °C) with different iridium loading was accessed by cyclic voltammetry. Figure 32 a shows the current response normalized with respect to the titanium sheet's geometrical surface area. All catalysts except for the sample with a loading of 15 wt. % Ir in Ir/TiO_2 depict a significant OER activity. However, increasing the loading to 30 wt. % Ir leads to a higher OER performance. The OER activity was quantified by measuring the current density at potentials of 1.60 V_{RHE}. In order to visualize the influence of the iridium loading on the electrocatalytic performance, Figure 32 b shows the quantified OER activity as a function of iridium loading. The OER activity steadily increases with higher iridium content.

The corresponding ECSA of each sample was investigated by cycling the potential between 0.40 - 1.40 V_{RHE} (50 mV/s) as depicted in Figure 32 c. The varying iridium content shows a severe impact on the current response. The recorded cyclic voltammograms feature a symmetric behaviour with respect to the horizontal axis. All samples show broad redox-waves at potentials of ca. 0.94 V_{RHE} indicating the presence of a Ir^{III}/Ir^{IV} redox couple.[125, 136] In order to quantify the impact of iridium loading on the active surface area, Figure 32 d shows the charge determined by the mean value of the integrated anodic and cathodic currents in the ECSA range as a function of iridium loading. The determined charge is understood as a measure of electrochemical active surface area. The ECSA steadily increases with higher

iridium content. It is clear to see that the OER activity and ECSA follow similar trends as they steadily increase with increasing iridium content. Thus, it is obvious that ECSA has a severe influence on the overall OER activity.

Morphology and electrical sheet conductivity (Figure 31) of IrO_2/TiO_2 calcined at an intermediate temperature (400 °C, low crystallinity, Figure 28) can now be correlated to the OER activity and ECSA. Samples with a loading of 15 wt. % Ir in Ir/TiO_2 exhibit a very low ECSA (Figure 32 d). The morphology is characterized by the presence of a mesoporous system (Figure 31 a). Furthermore, charging was absent as SEM images were recorded indicating that most of the polymer template was removed during heat treatment. The active surface area of a catalytic coating is expected to scale linear with the amount of active centres, e.g. iridium loading within TiO_2. An increase of the iridium loading from 15 wt. % (6.8 mol %) to 30 wt. % (15.1 mol %) Ir in Ir/TiO_2 enhances the amount of active centres by ca. 2.2. However, the electrochemical active surface area is enhanced by ca. 20 times (Figure 32 d). The discrepancy to the expected behaviour suggests that other effects than the amount of active centres influence the active surface area. Stoerzinger et al.[78] observed an enlarged distance of redox peaks for $LaCoO_3$ on different electrical conductive substrates. For low conductivity these redox peaks have the greatest distance to the equilibrium potential. Hence, samples with a low electrical conductivity suffer from a larger voltage drop over the layer. As a consequence, these samples suffer from a decreased electrocatalytic reactivity. In the case of IrO_2/TiO_2, the observed sheet conductivity, however, does not scale linearly with the amount of iridium (Figure 31 b). It is therefore required to further explore the exact impact of conductivity on the electron transport and the resulting effects on intrinsic reactivity. A more detailed discussion can be found in the chapters 4.4.4 - 4.4.6 for IrO_2/TiO_2 synthesized from $Ir(OAc)_3$ and TALH.

If electrons travelling through the catalytic layer are hindered by an insufficient degree of electrical conductivity the presence of two different reactivity regimes are expected, i.e. i) a high surface area with a high OER activity for samples with a sufficient degree of electrical conductivity and ii) a low surface area with a low OER activity for samples showing an insufficient electrical conductivity.

4.4 Mesoporous templated IrO$_2$/TiO$_2$ synthesized from Ir(OAc)$_3$ and TALH

Catalytic films of mesoporous templated IrO$_2$/TiO$_2$ derived by Ir(OAc)$_3$ and TiCl$_4$ show large segregated areas with diameters larger than approximately 100 nm. The process of demixing is associated with the different chemical behaviours of both metal oxide precursors in solution (see chapter 4.3.2). In order to obtain well mixed metal oxides of titanium and iridium, two possible pathways are imaginable.

The first route includes an IrO$_2$ precursor with the capability to undergo hydrolysis and condensation processes. As a consequence this may lead to the interaction with the polymer template and hydrolyzed titanium species. In the second pathway a TiO$_2$ precursor is incapable to interact with the polymer template, thus being chemical more similar to Ir(OAc)$_3$. However, dipcoated films, obtained by solutions prepared with IrCl$_3 \cdot$xH$_2$O instead of Ir(OAc)$_3$ and TiCl$_4$, exhibit small iridium rich domains even at low loadings (15 wt. % Ir in TiO$_2$) and low calcination temperatures (325 °C, Figure A3). The present demixing between both metal oxides suggest that the usage of IrCl$_3 \cdot$xH$_2$O and TiCl$_4$ is not suitable for the preparation of well mixed metal oxides of iridium and titanium.

Therefore, the second pathway must be taken into consideration. Titanium(IV) bis(ammonium lactato)dihydroxide (TALH) is well known to act as a suitable metal oxide precursor for the successful synthesis of mesoporous templated TiO$_2$ (see chapter 2.3.2).[109] TALH is characterized by a titanium cation (oxidation state +IV) complexed by lactic acid which functions as a chelat ligand, and two hydroxide groups. It was reported that TALH does not undergo hydrolysis and condensation when dissolved in water.[149] Iridium acetate shows a similar behaviour as it is complexed by acetic acid, thus stabilised against hydrolysis and condensation when dissolved in water and ethanol at room temperature.[145] The similarity of both metal oxide precursors is considered as an important factor for the synthesis of mixed metal oxides.

Chapter 4.4.1 illustrates the structure of IrO$_2$/TiO$_2$ dipcoated from a solution containing Ir(OAc)$_3$, TALH metal oxide precursors and PEO-PB-PEO polymer template and heat treated for 10 minutes at 400 °C. The influence of calcination temperature on morphology, crystallinity and electrical conductivity is investigated (4.4.2). Furthermore, the obtained information are then correlated with electrocatalytic OER activity and active surface area in order to deduce structure-activity relations (4.4.3). The amount of active iridium within TiO$_2$ is considered as another important synthesis parameter. Chapter 4.4.4 studies the impact of iridium loading on morphology and electrical conductivity. The electron transport processes within the catalytic layer (4.4.5) are investigated in detail and correlated with the electrocatalytic OER activity and intrinsic reactivity (4.4.6). The combined knowledge is used to elucidate the impact of electrical conductivity on the intrinsic reactivity.

4.4.1 Physicochemical characterization (Ir(OAc)$_3$ and TALH)

Catalytic coatings of mesoporous IrO$_2$/TiO$_2$ on polished silicon and titanium susbtrates were obtained by dipcoating a solution of PEO$_{213}$-PB$_{184}$-PEO$_{213}$ polymer template, Ir(OAc)$_3$, TALH, methanol and water. Dipcoating was performed at a withdrawal rate of 150 mm/min, an ambient temperature of 25 °C and a relative humidity of 40 %. Thereafter, the as prepared samples remained in the dipcoating chamber for 10 minutes to assure evaporation of volatile residues, such as ethanol. Subsequently, the samples were transferred into a preheated muffle furnace and calcined at 400 °C under air. The obtained samples contain a nominal iridium content of 30 wt. % Ir in Ir/TiO$_2$. Figure 33 shows the physicochemical characterization data obtained by a, b) SEM; c, d) TEM; e) SAED; f) integrated SAED; g, h) SAXS and i) Kr-physisorption.

a) SEM   b) cs SEM - COMPO   c) TEM   d) HR - TEM

e) SAED   f) SAED - integrated   g) SAXS 90°   h) SAXS 20°
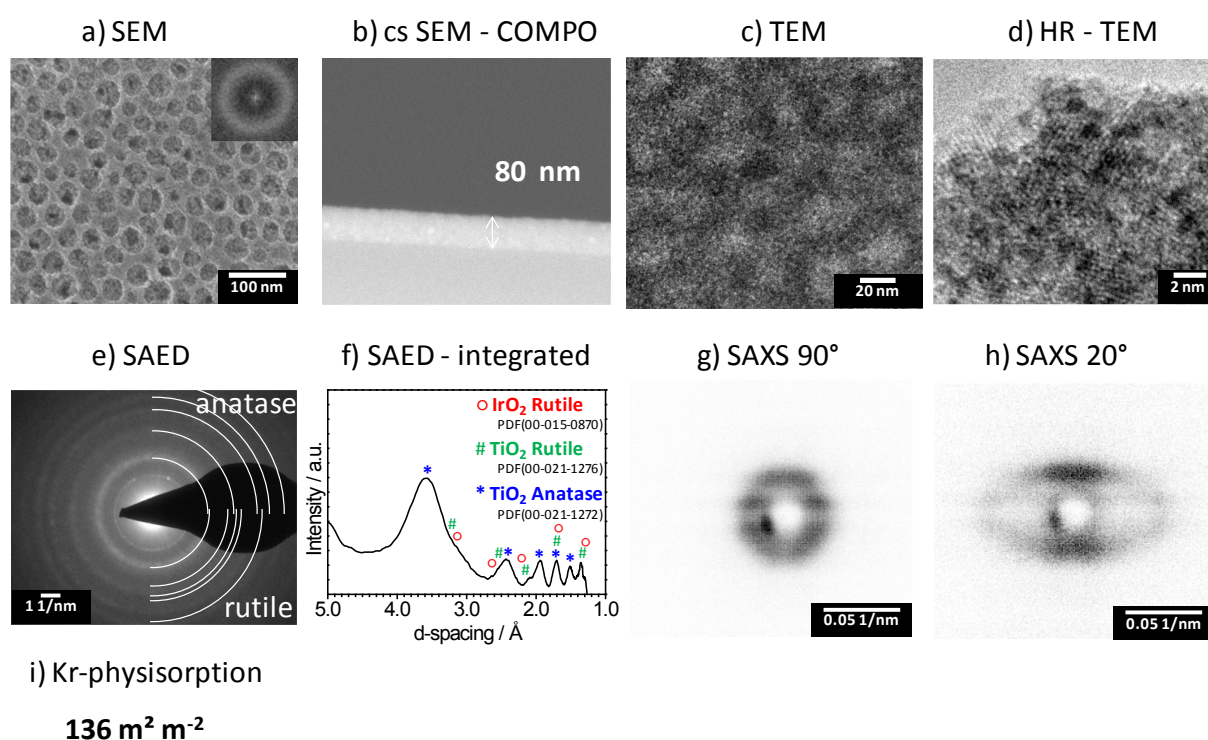
i) Kr-physisorption

136 m² m⁻²

Figure 33: Morphology, composition, pore ordering and surface area for samples dipcoated on silicon and titanium from a solution of PEO-PB-PEO, Ir(OAc)$_3$, TALH, methanol and water (30 wt. % Ir in Ir/TiO$_2$). Subsequently, heat treatment was conducted under air at 400 °C. a) SEM micrographs feature a fully developed pore system at the outer surface plane area as well as a homogenous distribution of IrO$_2$ and TiO$_2$. The film volume area was investigated by b) cross section SEM in COMPO mode, TEM at c) lower magnification and d) higher magnification. The obtained e) SAED diffraction pattern features broad isotropic rings indicating that the mesopore walls consist of nanocrystallites. f) The corresponding integrated SAED image was used to assign crystalline phases (see text for detailed explanation). SAXS measurements feature g) isotropic (90°) and h) ellipsoidal shaped (20°) rings suggesting the presence of locally ordered mesopores parallel and perpendicular to the substrate. i) Kr-physisorption provides a surface area of 136 m² film surface per m² substrate indicating a fully accessible pore system.

In order to assess the pore morphology and the distribution of iridium oxide in titanium oxide, a top view SEM image was recorded and is presented in Figure 33 a. The coating exhibits

spherical pores on the outer surface plane area with a diameter of 29 ± 6 nm. These pores are slightly larger than for PEO-PB-PEO templated IrO_2 synthesized from $Ir(OAc)_3$ (16 nm[65]), and for PEO-PB-PEO templated TiO_2 derived by $TiCl_4$ (21 nm[98]). The larger pore diameter is most likely induced by swelling of the polymer template due the high water content in the purchased TALH precursor solution (contains 50 wt. % H_2O). The FFT image (inset of Figure 33 a) of the corresponding SEM image features an isotropic ring, suggesting an ordered pore arrangement with a periodic distance of approximately 32 nm between pore centers. The film volume was investigated by cross section SEM in COMPO mode for samples coated on silicon substrate and is shown in Figure 33 b. The obtained micrograph depicts a layer thickness of 80 nm.

The mesoporous templated IrO_2/TiO_2 were further investigated by TEM in order to provide more detailed data regarding morphology (Figure 33 c, d) and crystallinity (Figure 33 e). The TEM micrograph at low magnification (Figure 33 c) shows spherical pores suggesting a complete penetration of the coating by templated mesoporosity. High resolution TEM image (Figure 33 d) features small dark spherical areas attributed to a higher content of iridium indicating segregation on a length scale of 1 - 2 nm. Furthermore, distinct lattice fringes are revealed suggesting the presence of nanocrystallites within the pore walls. In order to assess information about the crystal phases, selected area electron diffraction (SAED) measurements were performed. Figure 33 e depicts SAED data for films containing 30 wt. % Ir in TiO_2 as well as the reference data for IrO_2 rutile (PDF: 00-015-0870) and TiO_2 anatase (PDF: 00-021-1272). The resolution of the SAED measurement is too low to clearly distinguish between crystal phases of IrO_2 rutile and TiO_2 rutile. However, the obtained SAED pattern features isotropic rings leading to the conclusion that the pore wall is composed of randomly oriented nanocrystallites assigned to TiO_2 anatase as well as IrO_2 rutile and/or TiO_2 rutile (Figure 33 f), as well as an unknown amount of crystallites too small in size to produce distinct diffraction signals. Due to the broad appearance of the diffraction rings, caused by a very low crystallite size and by similar lattice parameters for IrO_2 rutile and TiO_2 rutile, the presence of either IrO_2 rutile, TiO_2 rutile or a mixture of both can not be distinguished.

The local pore arrangement of layers deposited on titanium foil was investigated with 2D-SAXS data recorded in transmission mode. SAXS pattern of IrO_2/TiO_2 films recorded with an incident beam angle of 90° (Figure 33 g) feature an isotropic ring indicating locally ordered mesoporosity parallel to the substrate. The scattering images for tilted samples at angles of 20° (Figure 33 h) show ellipsoidal shaped rings suggesting locally ordered mesoporosity perpendicular to the substrate. The film exhibits *d*-spacings of 40 nm (in-plane, 90°) and 10 nm (out of plane, 20°) representing an elliptically deformed pore morphology.

Kr-physisorption was used in order to assess the surface area of IrO_2/TiO_2 layers derived from $Ir(OAc)_3$ and TALH coated on silicon substrate. The BET surface area amounts to

136 m² film surface area per m² substrate geometric surface area (layer thickness: 80 nm). An almost fully removed polymer template as well as an accessible porous system (Figure 33 i) is formed. The surface area for mesoporous templated films synthesized from $Ir(OAc)_3$ and $TiCl_4$ amounts to 91 m²/m² (layer thickness: 95 nm). The significant higher surface area for TALH based films is most likely caused by the higher degree of textural porosity within the pore walls. The latter is probably induced by the formation of CO_2 from the decomposition of TALH and $Ir(OAc)_3$ during thermal treatment.[65]

4.4.2 Influence of calcination temperature on morphology, crystallinity and electrical conductivity

Calcination temperature can have a severe impact on morphology, crystallinity and electrical conductivity. Mesoporous templated films of IrO_2/TiO_2 were dipcoated from a solution containing $Ir(OAc)_3$ and TALH (30 wt. % Ir in Ir/TiO_2) and calcined at temperatures between 200 and 600 °C, respectively. The obtained films were characterized in terms of morphology, crystallinity and electrical sheet conductivity. For the differently heat treated samples Figure 34 shows the corresponding a) SEM micrographs, b) X-ray diffraction patterns, c) Rietveld refinement and d) electrical sheet conductivity.
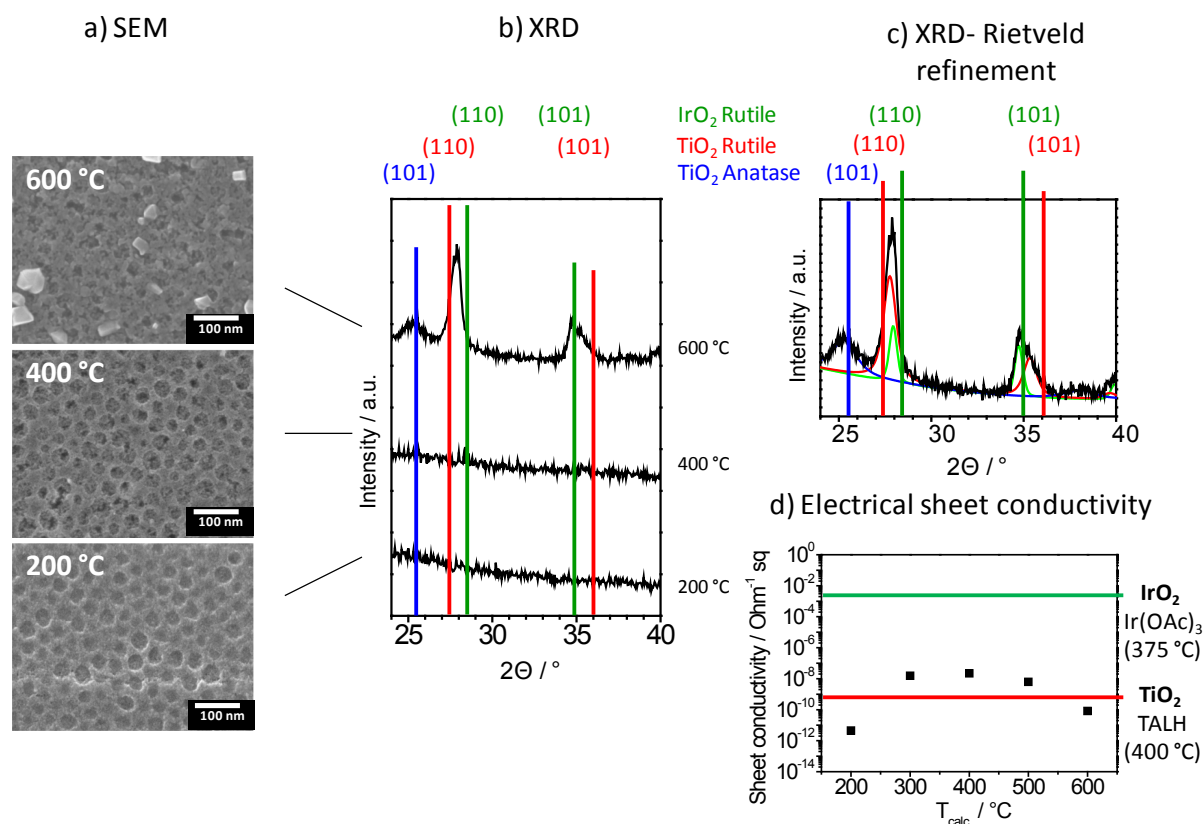

Figure 34: Impact of thermal treatment on a) morphology, b, c) crystallinity and d) electrical sheet conductivity for PEO-PB-PEO templated IrO_2/TiO_2 (30 wt. % Ir in Ir/TiO_2) synthesized from $Ir(OAc)_3$ and TALH. a) Samples calcined at 200 °C exhibit charging suggesting incomplete polymer template removal. An increase of the calcination temperature to 400 °C reveals a fully developed pore system, whereas

higher calcination (600 °C) induces crystal growth. b) The larger crystallite size for calcination at 600 °C is confirmed by XRD due to the additional reflections which appear in the corresponding diffractogram. c) Rietveld refinement was applied for diffractograms recorded for samples at 600 °C in order to investigate the phase composition. d) Sheet conductivity is shown for samples calcined at temperatures between 200 - 600 °C and for comparison, of IrO_2 synthesized from IrOAc (375 °C) and TiO_2 obtained by TALH (400 °C).

SEM micrographs for samples calcined at 200 °C (Figure 34 a) show a grainy texture and a bright horizontal line throughout the whole image. The grainy appearance of the image and the observed higher partial brightness may signify incomplete removal of the polymer template. Furthermore, no large segregated domains in the range of > 5 nm are observed suggesting a thorough mixture of IrO_2 and TiO_2. An increase in calcination temperature to 400 °C (Figure 34 a) feature a fine granulated SEM micrograph with good contrast and brightness. The presence of a fine grained SEM image is possibly related to the removal of most of the polymer template. Furthermore, the mesopore walls are characterized by textural porosity. However, calcination at 600 °C (Figure 34 a) causes a distortion of spherical mesopore shape and leads to a decreasing textural porosity associated with the onset of sintering. The SEM image further depicts small particles arising on the outer surface plane area. These particles are possibly related to temperature induced crystallite growth of an iridium rich oxide.

The corresponding films were further characterized by XRD (Figure 34 b) in order to relate the morphological changes to the crystal properties. Mesoporous layers heat treated between 200 and 400 °C do not provide reflection signals that can clearly be associated with crystalline phases. The derived samples are therefore either amorphous or possess crystallites too small in diameter for sufficient production of intense reflection signals. An increase in calcination temperature to 600 °C provides XRD patterns with reflections at 2-theta positions of 25.3°, 27.9°, 34.8° and a small shoulder at 35.0°. Rietveld refinement was conducted for further analysis of the crystal phases. The deconvoluted curves of the corresponding XRD pattern for samples calcined at 600 °C (Figure 34 c) are assigned to TiO_2 anatase, TiO_2-rutile (containing Ir) and IrO_2-rutile (containing Ti) indicating the formation of solid solutions. The respective crystallite sizes obtained by the Scherrer-equation amount to 5 nm (TiO_2-anatase), 12 nm (TiO_2-rutile containing Ir) and 21 nm (IrO_2-rutile containing Ti).

The electrical sheet conductivity was analyzed as a function of calcination temperature and is shown in Figure 34 d. For the purpose of comparison, the sheet conductivity of similar calcined, mesoporous templated IrO_2 and TiO_2 coated on glass substrate is provided by red and green bars, respectively (TiO_2 synthesized from TALH (400 °C): $7.1 \cdot 10^{-10}$ $(Ohm/sq)^{-1}$, IrO_2 synthesized from $Ir(OAc)_3$ (375 °C): $2.6 \cdot 10^{-3}$ $(Ohm/sq)^{-1}$). Samples calcined at 200 °C exhibit low sheet conductivity. This observation is in good agreement with SEM images that implied incomplete template removal. The electrical sheet conductivity strongly increases for samples thermally treated at temperatures between 300 and 400 °C. This behavior is

explained by the removal of most of the polymer template and the formation of nanocrystallites. The formation of nanocrystallites strongly decreases the amount of grain boundaries which is associated with a faster electron transport. However, a further increase of calcination temperature reduces sheet conductivity. We hypothesize, that the decrease in sheet conductivity at high calcination temperatures (600 °C) is possibly attributed to the aggregation of IrO_2 which in turn is caused by crystallite growth. As a consequence of enhanced crystallite growth, the preliminary connected and conductive IrO_2 network is interrupted. Thus, the electron transport through the catalytic layer is decelerated.

The obtained data from the physicochemical characterisation of Figure 33 and Figure 34 was used to derive a structural model which is shown in Figure 35. The model describes temperature induced changes in morphology and crystallinity of IrO_2/TiO_2 synthesized from a dipcoating solution containing TALH, $Ir(OAc)_3$, PEO-PB-PEO, methanol and water. In Figure 35 the samples show i) a thorough mixture of IrO_2/TiO_2 up to intermediate calcination temperatures (400 °C), ii) a textural porosity throughout the mesopore walls, iii-1) a temperature induced demixing and iii-2) the beginning formation of a solid solution for samples heat treated above ca. 500 °C.
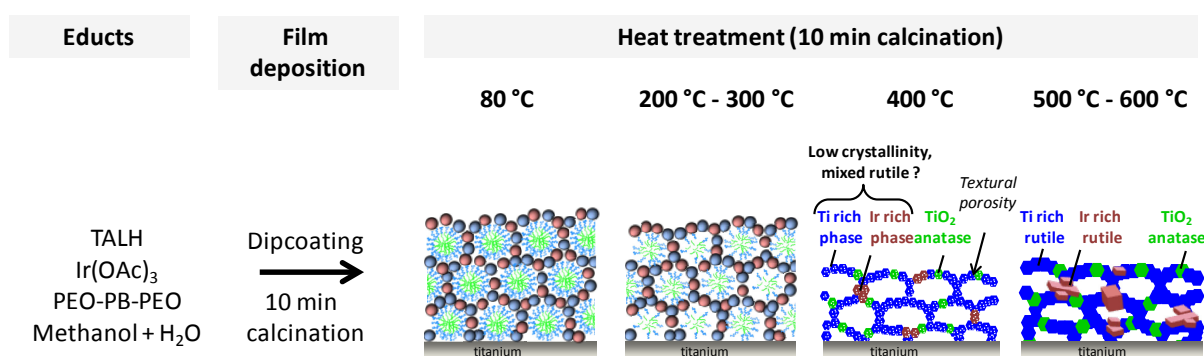

Figure 35: Structural changes as a function of calcination temperature for 30 wt. % Ir in Ir/TiO$_2$ coatings on titanium prepared from a solution containing TALH, Ir(OAc)$_3$, PEO-PB-PEO, MeOH and H$_2$O. Dipcoating was performed under a controlled atmosphere at 25 °C and 40 % relative humidity. The as prepared samples were dried for 10 minutes in the dipcoating chamber and subsequently transferred to a preheated muffle furnace for calcination at temperatures between 80 and 600 °C, respectively. The structural models are deduced from observations of physicochemical measurements such as SEM (Figure 33, Figure 34), TEM (Figure 33), SAXS (Figure 33) and XRD (Figure 34).

i) The utilized metal oxide precursors, i.e. $Ir(OAc)_3$ and TALH are characterized by sterically demanding chelat ligands, such as acetic acid and lactic acid, respectively. Reports from literature claim that both metal oxide precursors appear stable to hydrolysis and condensation when dissolved in water.[145, 149] The absence of hydrolysis and condensation prevents the formation of hydroxide groups which in turn prevents the interaction with

hydrolytic regions of the polymer template. Thus, Ir(OAc)$_3$ and TALH exhibit similar chemical reactivity in solution.

Film deposition on titanium substrate followed by a heat treatment at 200 °C reveals a thorough mixture of IrO$_2$ and TiO$_2$ (Figure 34 a), possibly due to a similar drying behavior of Ir(OAc)$_3$ and TALH. This behavior is associated with equal interaction properties with the polymer template. Both metal oxide precursors tend to show no attractive interaction with the polymer template as they lack of hydrolysis and condensation. Therefore, we hypothesize that a higher chemical similarity between the used metal oxide precursors such as Ir(OAc)$_3$ and TALH causes a more homogenously distributed mixed metal oxide, e.g. IrO$_2$ and TiO$_2$.

ii) An increase in calcination temperature to 400 °C features a fully developed pore system (Figure 34 a) with textural porosity in the mesopore walls. The textural porosity is possibly introduced by the combustion of carbon to CO$_2$ from both metal oxide precursors.[65] However, TEM studies (Figure 33 d) reveal small (ca. 2 nm), segregated areas which appear darker in brightfield mode suggesting an iridium rich domain. SAED images (Figure 33 e) of the corresponding samples show diffraction rings which can be assigned to a mixture of TiO$_2$-anatase and rutile. The broadness of the diffraction rings and the similar lattice parameters of TiO$_2$-rutile and IrO$_2$-rutile neither allow a clear distinction of both rutile phases (IrO$_2$ and TiO$_2$) nor a mixture thereof. The derived scheme (Figure 35) therefore shows TiO$_2$ anatase, small iridium rich phases, and titanium rich phases, from which the latter two possibly crystallized in a mixed rutile structure.

iii) Due to a further increase in calcination temperature, a distortion of the spherical mesopore shape can be observed. The arising crystallites appear iridium rich. XRD measurements (Figure 34 b) show distinct reflection signals which can be assigned to TiO$_2$ anatase, TiO$_2$ rutile containing Ir (Ti-rich rutile), and IrO$_2$ rutile containing Ti (Ir-rich rutile). Obviously, two effects occur when calcination temperatures higher than 500 °C are applied: iii-1) thermally induced demixing, and iii-2) the beginning formation of a solid solution. Tammann[150] reported that atoms can change places within crystallites or at the interface between two different crystallite species, if a sufficient degree of atom oscillation (temperature dependent) is reached. In honour of Tammann, this particular temperature is called the Tammann temperature. He further found[150] that metals must be heated to ca. 1/3 of their melting temperature in order to form a solid solution. In case of oxides from titanium and iridium, the Tammann temperature $T_{Tammann}$ has the followed values:

TiO$_2$: $T_{Tammann}$ = 791 °C[151]

IrO$_2$: $T_{Tammann}$ = 413 °C[152]

iii-1) The lower Tammann temperature of IrO$_2$ in comparison to TiO$_2$ allows mobility at much lower temperatures than required for TiO$_2$. Thus, thermally induced demixing of IrO$_2$/TiO$_2$ should start for samples calcined at temperatures above ca. 400 °C. In fact, samples heat

treated at 400 °C show only a very low degree of demixing between IrO_2 and TiO_2 (Figure 33). Samples heat treated at 500 °C, however, clearly depict larger areas with iridium rich crystallites. iii-2) A further increase in calcination temperature to 600 °C forms a demixed solid solution of IrO_2 and TiO_2. We assume, that an incorporation of TiO_2 by surrounding IrO_2 crystallites is initiated which results in fractions of iridium rich rutile and titanium rich rutile. In literature, the formation of a phase pure solid solution between IrO_2 and TiO_2 [143] was achieved by exceeding the Tammann temperature with a mixture of IrO_2-powder and TiO_2-powder (900 °C). However, simply enhancing the calcination temperature in the presented mesoporous templating synthesis approach would lead to excessive crystallite growth and, in consequence to a complete loss of textural porosity as well as mesoporosity. Furthermore, the underlying titanium substrate might oxidize to form a rather thick insulating layer of TiO_2. Thick layers of TiO_2 are known to cause an additional voltage drop over the layer, further inhibiting electrocatalytic reactivity.[153]

4.4.3 Influence of calcination temperature on electrochemical OER activity and surface

Mesoporous templated films of IrO_2/TiO_2 (30 wt. % Ir in Ir/TiO_2) were prepared on titanium sheet substrates by dipcoating and subsequent calcination for 10 minutes under air at temperatures between 200 - 600 °C, respectively. The obtained samples were mounted as a working electrode within a RDE setup. A reversible hydrogen electrode served as the reference and a platinum gauze as the counter electrode. All electrochemical experiments were conducted at a speed of rotation of 1600 rpm in 0.5 M H_2SO_4. During electrochemical investigations, the resulting current response was normalized to the substrate's geometrical planar surface area and the potential was corrected for iR drop. The OER (oxygen evolution reaction) activity was determined by cyclic voltammetry in a potential window ranging between 1.20 - 1.65 V_{RHE} (6 mV/s, Figure 36 a). Furthermore, the OER performance is shown as a function of calcination temperature by measuring the corresponding current density at 1.60 V_{RHE} (Figure 36 b). The ECSA (Electrochemical active surface area) was investigated by cyclic voltammetry in a lower potential window of 0.40 - 1.40 V_{RHE} (50 mV/s, Figure 36 c). The mean value of the integrated anodic and cathodic scan of each cyclic voltammogram was determined in order to derive a value for the electrochemical accessible surface area. The ECSA is shown in dependency of the calcination temperature (Figure 36 d).

For IrO_2/TiO_2 synthesized from $Ir(OAc)_3$ and TALH (30 wt. % Ir in Ir/TiO_2) with different calcination temperatures Figure 36 shows a) cyclic voltammograms recorded in the OER regime, b) the quantified OER performance as a function of calcination temperature, c) cyclic voltammograms in the ECSA region, and d) the calcination temperature dependent quantified ECSA.
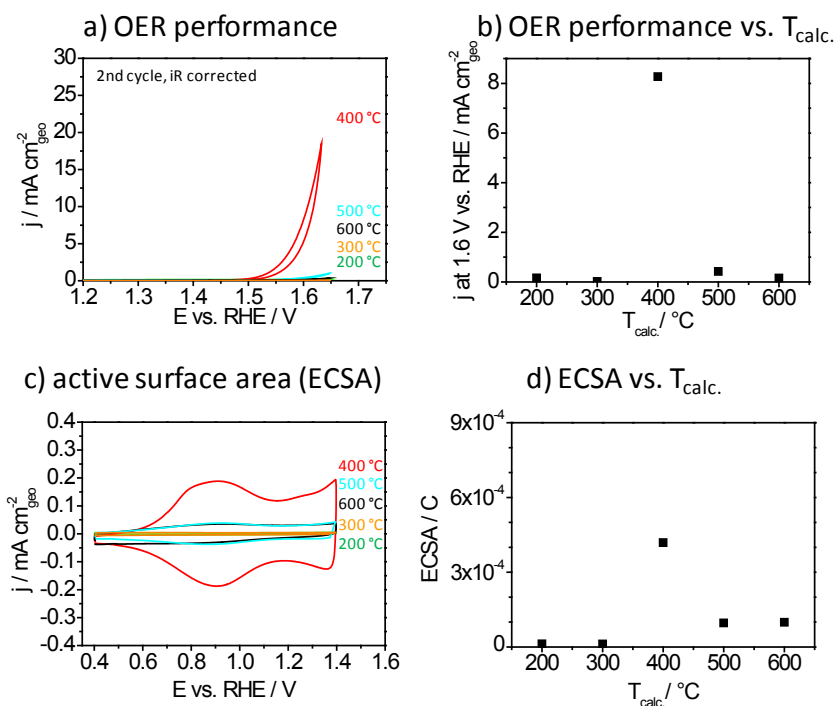
Figure 36: Impact of calcination temperature on a, b) OER performance and c, d) electrochemical accessible surface area (ECSA) for 30 wt. % Ir in Ir/TiO₂ synthesized from Ir(OAc)₃ and TALH. a) CVs recorded in the OER potential window between 1.20 and 1.65 V$_{RHE}$ at a scanrate of 6 mV/s, b) current density measured at 1.60 V$_{RHE}$ normalized to the geometric electrode surface area, c) CVs recorded in a lower potential window between 0.40 and 1.40 V$_{RHE}$ at 50 mV/s are used to access the electrochemical accessible surface area, d) ECSA is derived as the total charge obtained as a mean value of the integrated anodic and cathodic currents between 0.40 and 1.40 V$_{RHE}$. Electrocatalytic data were recorded in 0.5 M H₂SO₄ with a rotating working electrode, a RHE reference and a Pt gauze counter electrode.

The OER activity for samples of IrO₂/TiO₂ synthesized from Ir(OAc)₃ and TALH is shown in Figure 36 a. The observed current density is defined as a measure of OER activity and appears to be strongly dependent on the applied calcination temperature. However, only catalysts calcined at 400 °C show a significant OER activity. The corresponding cyclic voltammogram features a typical exponential relationship as stated by the Butler-Volmer equation. The impact of calcination temperature on the OER activity was quantified by measuring the OER activity at potentials of 1.60 V$_{RHE}$. Figure 36 b shows the OER activity as a function of calcination temperature. It is clearly visible that the OER activity increases within a temperature window of 200 - 400 °C, whereas a further increase to 500 and 600 °C strongly decreases the OER activity.

The corresponding electrochemical active surface area (ECSA) of each sample was accessed by measuring the current density in a lower potential window of 0.40 - 1.40 V$_{RHE}$ (Figure 36 c). The obtained "ECSA-CVs" are symmetrical with respect to the horizontal axis. The observed current density in the anodic and cathodic scan appear to be affected by the

applied calcination temperature. Samples calcined at 400 °C depict by far the largest current response, thus the highest ECSA. Furthermore, all CVs feature redox waves at a potential of ca. 0.92 V_{RHE} which are associated with the equilibrium potential of the Ir^{III}/Ir^{IV} redox couple.[125, 136] In order to further analyze the relationship between ECSA and OER activity, the total charge, obtained as a mean value of the integrated anodic and cathodic scans of CVs from the ECSA regime, is plotted as a function of calcination temperature (Figure 36 d). The derived charge is used as a measure for ECSA. Samples heat treated at 200 and 300 °C do not exhibit a significant ECSA. However, the ECSA shows the highest values at calcination temperatures of 400 °C but strongly decreases with further increasing the calcination temperature.

The OER activity as well as the electrochemical active surface area show very similar trends as a function of calcination temperature. Samples heat treated at intermediate temperatures (400 °C) show a high ECSA as well as a high electrochemical OER activity. Therefore, we conclude that the electrochemical accessible surface area is considered as an important oxygen evolution reaction controlling parameter and contributes to the overall OER activity.

The influence of morphology, crystallinity and sheet conductivity can now be related to the oxygen evolution reaction (OER) activity as well as to the electrochemical accessible surface area (ECSA) in order to deduce structure-activity relationships. Samples heat treated at 200 and 300 °C exhibit no significant ECSA (Figure 36 d) which is in line with SEM (Figure 34 a). Here, a grainy texture and partially charging was observed which indicates that the sample has an insufficient degree of electrical conductivity which in fact was observed with sheet resistivity measurement (Figure 34 c). If the sample still comprises remaining polymer template residues, it appears likely that the pore system is not accessible, thus neither ECSA (Figure 36 d) nor OER activity (Figure 36 b) is observed. An increase in calcination temperature to 400 °C forms a material with increased electrical conductivity (Figure 34 c), low crystallinity (Figure 34 b), and a throughout mixture of iridium oxide and titanium oxide (Figure 34 a). Furthermore, a strong increase is observed for the ECSA (Figure 36 d) and the OER activity (Figure 36 b). The tremendous increase in the ECSA is related to the removal of most of the polymer template which creates an accessible pore system, thus a higher overall OER activity. At calcination temperatures of 500 and 600 °C an induced crystallite growth (Figure 34 b) accompanied by the formation of not phase pure i) titanium rich rutile, ii) iridium rich rutile, and iii) anatase (Figure 35) is observed. Moreover, a decrease occurs in textural porosity (Figure 34 a) and electrical conductivity (Figure 34 c). Also, the ECSA strongly (Figure 36 d) decreases. The tremendous degradation of the ECSA is related to the loss of textural porosity by the onset of sintering which in turn is caused by the temperature induced crystallite growth of oxides from iridium and titanium. Due to the very similar trends of OER

activity and ECSA as a function of calcination temperature the assumption can be made that the activity of polymer templated mixed oxide films of iridium and titanium is influenced by at least one major factor, i.e. the accessible surface area.

4.4.4 Influence of Ir-content on morphology and sheet conductivity

Mesoporous templated layers of IrO_2/TiO_2 with different iridium loadings (0 - 100 wt. % Ir in Ir/TiO_2) were deposited on silicon and glass substrates by dipcoating and subsequent calcination for 10 minutes at 400 °C under air. The effects of iridium concentration on morphology and electrical conductivity of the catalytic IrO_2/TiO_2 films were analyzed by SEM and resistivity measurements. For samples with different iridium content Figure 37 shows a) SEM micrographs and b) electrical sheet conductivity of corresponding samples dipcoated on glass substrates.

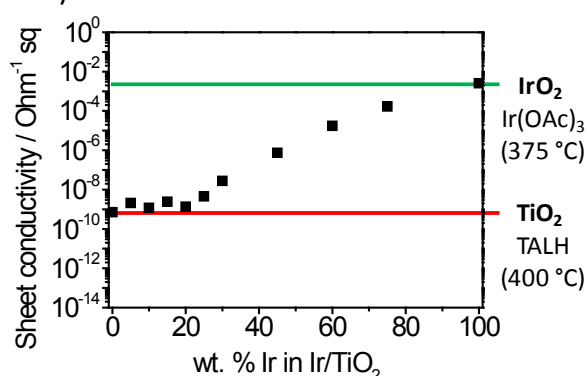a) SEM
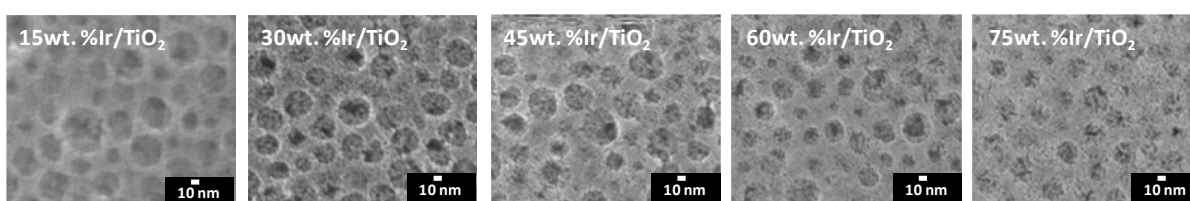
b) Electrical sheet conductivity

Figure 37: Impact of iridium content on a) morphology (on silicon) and b) sheet conductivity (on glass) for mesoporous templated IrO_2/TiO_2 systems synthesized from $Ir(OAc)_3$ and TALH and subsequently heat treated at 400 °C under air. a) SEM micrographs depict a homogenous dispersion of IrO_2 and TiO_2 b) Sheet conductivity remains constant for iridium loadings of 25 wt. % Ir in Ir/TiO_2. A further increase of the iridium content significantly enhances sheet conductivity.

Figure 37 a illustrates the morphology at the outer surface plane area for films of IrO_2/TiO_2 with a different amount of iridium. The SEM micrographs feature a homogenous mixture of IrO_2 and TiO_2 without large (ca. 100 nm) aggregated domains regardless of the iridium content. All samples exhibit spherical pore openings. However, pore openings increase in size with higher titanium content from 23.1 nm (75 wt. % Ir) to 30.3 nm (15 wt. % Ir). The effect of the water containing TALH-solution (50 wt. % H_2O) is a higher ratio of water to

polymer template within the dipcoating solution. This leads to a swelling of formed micelles, thus larger pore openings.

In Figure 37 b the influence of the iridium content on the electrical sheet conductivity is featured. For the purpose of comparison, the sheet conductivity of similar calcined, mesoporous templated IrO_2 and TiO_2 coated on glass substrate, is provided by green and red bars, respectively (TiO_2 (TALH, 10 min 400 °C): $7.1 \cdot 10^{-10}$ (Ohm/sq)$^{-1}$, IrO_2 (Ir(OAc)$_3$ 5 min 375 °C: $2.6 \cdot 10^{-3}$ (Ohm/sq)$^{-1}$). The electrical conductivity remains unaffected up to an iridium content of 20 wt. % Ir in TiO_2 and stays constant within a range of $0.7 \cdot 10^{-9}$ to $4 \cdot 10^{-9}$ (Ohm/sq)$^{-1}$. However, an increase of the iridium loading to 25 wt. % in TiO_2 enhances the electrical conductivity to $4.5 \cdot 10^{-9}$ (Ohm/sq)$^{-1}$. At iridium contents higher than 30 wt. % in TiO_2 a significant improvement of the electrical sheet conductivity with higher iridium content is observed. Pure, mesoporous templated IrO_2 shows the highest electrical sheet conductivity which equals to $2.6 \cdot 10^{-3}$ (Ohm/sq)$^{-1}$. Normalizing this value for a layer thickness of 50 nm results in a specific conductivity of $5.1 \cdot 10^4$ S/m ($5.1 \cdot 10^2$ S/cm) which is considered as metallically conductive[54] and is in good agreement with values reported in literature ranging from $4.3 \cdot 10^5$ S/m[154] to $2 \cdot 10^6$ S/m.[155]

The observed electrical sheet conductivity for IrO_2/TiO_2 coatings, synthesized from Ir(OAc)$_3$ and TALH on glass substrates, strongly depend on the added amount of iridium. The insignificant changes in the electrical conductivity for mesoporous templated TiO_2, with loadings ranging between 5 - 25 wt. % Ir in Ir/TiO_2, is potentially related to the incomplete connection of conductive IrO_2 chains. The insulating TiO_2 positioned between conductive domains of IrO_2 hinders fast electron transport through the layer. The electrical sheet conductivity significantly increases for samples with iridium loadings higher than 30 wt. % Ir in Ir/TiO_2. The addition of a sufficient amount of iridium oxide might connect conductive IrO_2 chains. The electrical conductivity is therefore enhanced as electrons must not longer travel through insulating TiO_2 domains. A further increase in iridium loading progressively increases the electrical sheet conductivity as there is a further amount of metallically conducting IrO_2 present. The observed behaviour is in good agreement with the percolation theory which describes the electrical conductivity of conductive materials (e.g. IrO_2) within an insulating matrix (e.g. TiO_2).[74, 77]

4.4.5 Influence of Ir-content on electron transport resistance and electrochemical active surface area

Electrochemical investigations for IrO_2/TiO_2 layers with different content of iridium on titanium substrates were conducted in order to determine the impact of iridium loading on the electron transport resistance through the film, on the electrochemical active surface area (ECSA) and also on the oxygen evolution reaction (OER) performance. The IrO_2/TiO_2 layer was coated on titanium substrate and employed as a working electrode in a rotating-disc electrode (RDE) setup. A Pt-mesh and a RHE were used as a counter and reference electrode, respectively. 0.5 M H_2SO_4 served as an electrolyte solution. ECSA[125] measurements were performed at a lower potential regime between 0.40 -1.40 V_{RHE} and a sweeprate of 50 mV/s. The applied potential was iR-corrected and the resulting current response was normalized to the electrode's planar geometric surface area. Every figure shows the 2nd cycle.

For mesoporous templated IrO_2/TiO_2 ($Ir(OAc)_3$+TALH) layers with different iridium loadings deposited on titanium sheets Figure 38 shows the a, b) cyclic voltammograms recorded in the ECSA regime (0.40 - 1.40 V_{RHE}). As a function of iridium loading, Figure 38 shows c) the redox peak position from the "ECSA-CVs" and the d) quantified ECSA.
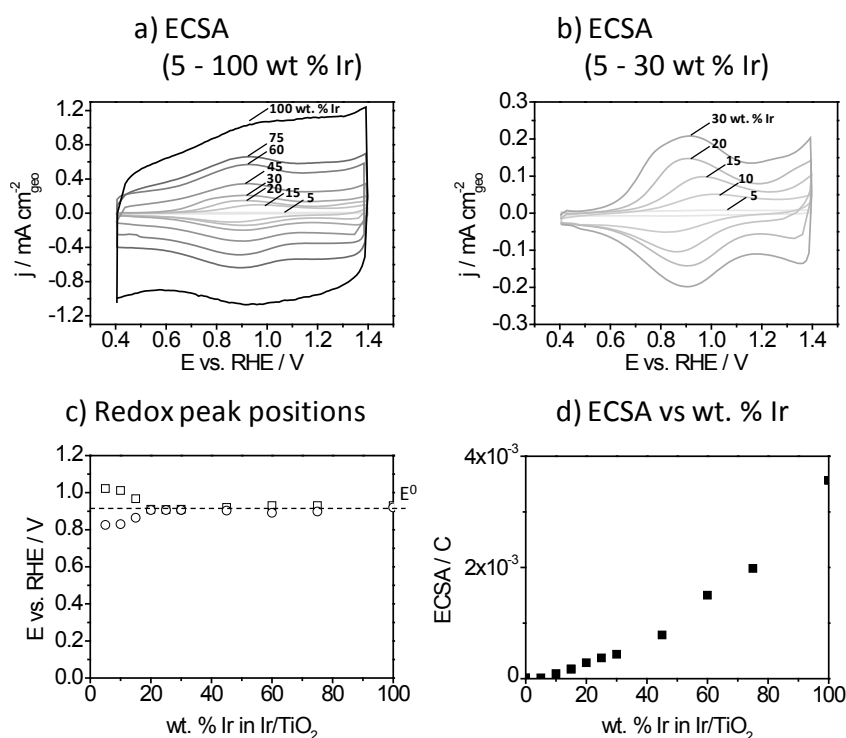

Figure 38: Influence of iridium loading on a, b) CVs recorded in the ECSA potential window between 0.40 - 1.40 V_{RHE} at a sweep rate of 50 mV/s, c) the redox peak positions E^0 for the (Ir^{III}/Ir^{IV}) couple obtained by the corresponding CVs recorded in the ECSA regime and d) the quantified ECSA. a, b) Enhanced current density and a drift in peak positions is observed as a function of iridium content. c) The redox peak potentials are plotted depending on the iridium content. A clear spreading of the redox peaks away from the equilibrium potential $E^0(Ir^{III}/Ir^{IV})$ is observed for samples with iridium loadings lower than 20 wt. % Ir in

Ir/TiO$_2$. This observation is associated with an insufficient degree of electrical conductivity. d) The mean value of the integrated anodic and cathodic charge of the recorded CVs shows a successive increase of ECSA as a function of iridium loading. All samples were coated on titanium substrates followed by thermally treatment at 400 °C under air.

Figure 38 a and b show the current response of IrO$_2$/TiO$_2$ layers on titanium substrates recorded in a lower potential window of 0.40 - 1.40 V$_{RHE}$. The current response is normalized to the electrode's geometrical surface area and is composed of contributions from the double layer capacitance and faradayic currents. Currents related to the double layer capacitance are recorded over the whole potential window, whereas faradayic currents show pronounced broad peaks at a specific equilibrium potential which is associated with a Ir^{+III}/Ir^{+IV} redox couple. Our thermally prepared mesoporous layers of IrO$_2$/TiO$_2$ coated on titanium substrates show a peak potential at 0.92 V$_{RHE}$ which is in good agreement with values found in literature (0.90 V$_{RHE}$[64] and 0.95 V$_{RHE}$[125]) for similar prepared IrO$_2$. Faradayic currents of highly hydrated IrO$_2$ are the result when reacting in terms of a proton-inclusion-mechanism which is described as followed[156]:

$$IrO_x(OH)_y + \delta\ H^+ + \delta\ e^- \rightarrow IrO_{x-\delta}(OH)_{y+\delta}$$
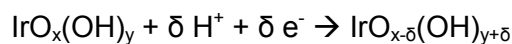
Considering this equation, a decrease in the iridium content leads to a reduced number of iridium centres, and hence a drop in the current density as noticeable in Figure 38 a. However, when lowering the iridium content, the peaks are still pronounced (Figure 38 b). Similar prepared mesoporous templated "iridium free" TiO$_2$ coatings on titanium substrate show no significant contribution to the current density. Therefore, we assume that for mixed IrO$_2$/TiO$_2$ systems with different loadings of iridium, the appearing peaks are caused by faradayic currents related to the Ir^{+III}/Ir^{+IV} redox couple. However, a clear shift of the peak position to higher (anodic scan) and lower (cathodic scan) potentials is visible for iridium loadings lower than 20 wt. % Ir in Ir/TiO$_2$ (Figure 38 c).

The quantification of peak positions as a function of iridium content in TiO$_2$ is shown in Figure 38 c. The redox peaks at approximately 0.92 ± 0.01 V$_{RHE}$ of pure mesoporous templated IrO$_2$ (100 wt. % Ir) are ascribed to the equilibrium voltage of the Ir^{+III}/Ir^{+IV} redox couple.[64, 125] Redox peaks are still located near the equilibrium voltage with an iridium content as low as 20 wt. % Ir in Ir/TiO$_2$. A further decrease of the iridium loading significantly spreads the redox peaks away from the equilibrium voltage (Figure 38 c). In the latter case, the electron transport is hindered through layers of IrO$_2$/TiO$_2$.

The electron transport through bulk materials, such as unporous LaCoO$_3$, has been investigated by Stoerzinger et al.[78]. LaCoO$_3$ was deposited on three substrates with different conductivity by pulsed laser epitaxy. To investigate, the influence of the electron transport through the layer as a function of conductivity, the peak positions of the [Fe(CN)$_6$]$^{3-/4-}$ redox

couple were analyzed. They observed an enlarged distance of the redox peaks from the equilibrium potential for samples with lower conductivity. Thus, the higher resistivity of these samples induces a voltage drop over the layer.

Samples with iridium loadings of at least 20 wt. % Ir in Ir/TiO$_2$ exhibit redox peaks positioned near the equilibrium potential, suggesting a sufficient degree of electrical conductivity. Additional ex-situ measurements for electrical resistivity (Figure 37 b) showed a significant increase of conductivity for samples with a slightly higher iridium loading of at least 30 wt. % Ir in Ir/TiO$_2$. Therefore, we hypothesize that the samples need to be at least conductive as approximately $3 \cdot 10^{-8}$ (Ohm/sq)$^{-1}$ (ca. 0.1 S/m) in order to provide a sufficient electron transport through the layer and perform as highly active OER catalysts.

In Figure 38 d the electrochemical accessible surface area (ECSA) is plotted as a function of iridium loading. The ECSA corresponds to the transferred charge in the cyclic voltammograms (CVs) of Figure 38 a and was obtained by the mean value of the integrated cathodic and anodic scan for each CV. The differing iridium content within TiO$_2$ has a severe impact on the ECSA. This observation is in good agreement with the expected proton-inclusion-mechanism of IrO$_2$. The faradayic current response within the ECSA-CVs is associated with the transformation of the Ir^{+III}/Ir^{+IV} redox couple. It is therefore plausible, that an increasing iridium amount within TiO$_2$, normalized with respect to the planar geometrical surface area, leads to a higher ECSA.

4.4.6 Influence of Ir-content on OER performance and intrinsic activity

Mesoporous templated IrO$_2$/TiO$_2$ with different iridium loadings were dipcoated on titanium sheet substrates from a solution of Ir(OAc)$_3$ and TALH. The as prepared samples were dried in the dipcoating chamber under controlled atmosphere and subsequently transferred into a preheated muffle furnace. All samples were calcined at 400 °C under air atmosphere. The obtained samples were employed as the working electrode within a rotating-disc electrode setup. The OER performance was investigated in a potential window of 1.20 - 1.65 V$_{RHE}$ with a scan rate of 6 mV/s. The applied potential was iR-corrected and the resulting current response was normalized with respect to the electrode's planar geometric surface area.

For different loadings of iridium within TiO$_2$ Figure 39 shows a) the 2nd iR-corrected cyclic voltammograms in the OER regime, b) the quantified OER activity at potentials of 1.60 V$_{RHE}$; c, d) the quantified charge as a measure of electrochemical active surface area (ECSA).
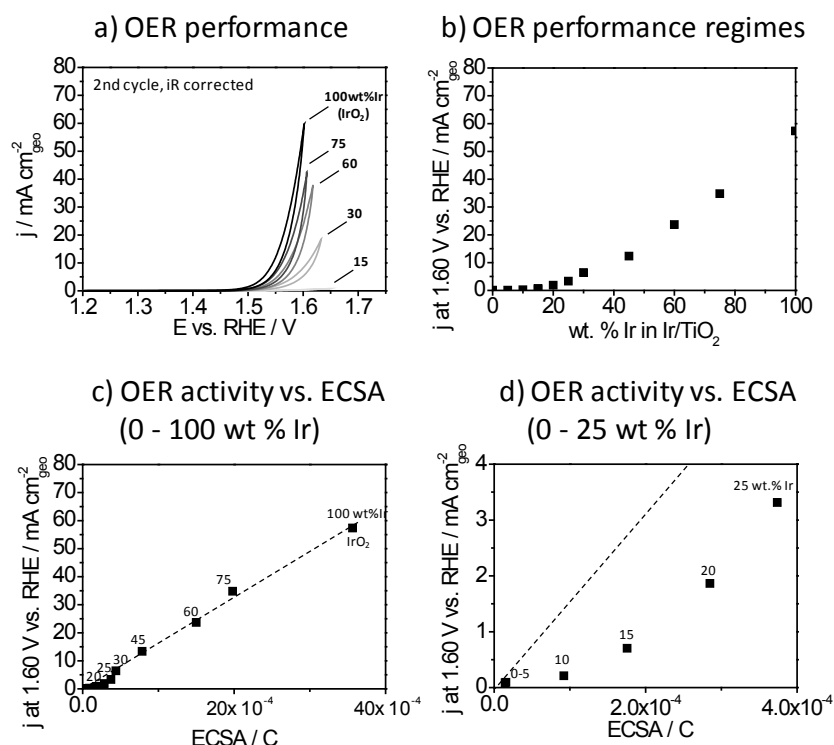
Figure 39: Impact of iridium content in IrO₂/TiO₂, synthesized from Ir(OAc)₃ + TALH, dipcoated on titanium sheets and subsequently heat treated at 400 °C on a) CVs recorded in the OER regime, b) OER activity at 1.60 V_RHE and c, d) relationship between OER activity and ECSA. a) CVs recorded in the OER regime in a potential window between 1.20 - 1.65 V_RHE. b) The OER activity increases as a function of iridium content. c) The Intrinsic activity is derived by a linear fit between OER activity and ECSA. d) The difference in OER activity and linear fit for samples with lower iridium content suggest a decrease in intrinsic activity.

The OER activity in Figure 39 a is measured for samples with iridium contents between 15 wt. % - 100 wt. % Ir (pure IrO_2). The current response was normalized to the substrate's planar geometric surface area (0.1965 cm²). Samples with iridium loadings higher than 20 wt. % Ir in Ir/TiO_2 are more active in the OER than samples with lower loadings of iridium. The OER performance increases for higher iridium loadings. In order to visualize the increase in the OER performance, the current density at 1.60 V_{RHE} was measured and is plotted as a function of the iridium content (Figure 39 b).

Figure 39 b shows the current density values at 1.60 V_{RHE} of equally prepared and measured samples with loadings between 0 - 100 wt. % Ir in Ir/TiO_2. A low current density is observed for samples with loadings below 20 wt. % Ir in Ir/TiO_2. However, at iridium loadings of 25 wt. % Ir in Ir/TiO_2 and higher, the observed OER activity successively increases.

In Figure 39 c the quantified OER activity of all samples is plotted as a function of ECSA. The OER activity of iridium loadings between 30 - 100 wt. % Ir in Ir/TiO_2 is linearly dependent on the ECSA (fixed intercept at 0). The OER performance is increased by 16.4 mA/cm² for every $1 \cdot 10^{-3}$ ECSA [C] (R²=0.998).

In Figure 39 d, only the current response for samples with loadings between 0 and 25 wt. % Ir is displayed. The dashed line is the extrapolated linear fit from the 30 -

100 wt. % Ir region (Figure 39 c). The current densities at a potential of 1.60 V_{RHE} are significantly lower than expected by the extrapolated linear fit from the 30 - 100 wt. % Ir region. This discrepancy between the observed and the expected current density suggest a different intrinsic electrocatalytic reactivity of IrO_2 dispersed within TiO_2.

Two different regimes are observed within the OER-ECSA plot (Figure 39 c and d) for IrO_2/TiO_2 synthesized from $Ir(OAc)_3$ and TALH: i) a linear relation for samples with loadings higher than ca. 30 wt. % Ir in Ir/TiO_2, and ii) a discrepancy from the expected linear behaviour for samples with loadings lower than ca. 30 wt. % Ir in Ir/TiO_2. In order to explain both regimes, a correlation with the electrocatalytic and physicochemical properties of the corresponding samples is provided.

i) Samples with iridium loadings higher than 20 wt. % Ir feature redox peaks associated with the Ir^{+III}/Ir^{+IV} redox couple located close to the thermodynamic equilibrium (Figure 38 c). Samples with loadings higher than 30 wt. % Ir show a significant increase in the electrical sheet conductivity (Figure 37 b) as a function of iridium loading. Both observations suggest a sufficient degree of the electrical conductivity. Thus, no additional voltage drop over the layer is expected that potentially might diminish electrocatalytical processes. In chapter 4.2.5 a linear dependency between the OER activity and ECSA up to current densities of ca. 80 mA/cm² was observed for mesoporous IrO_2 (Figure 26 b). Prior conducted investigations on the electrical conductivity (Figure 37 b, Figure 38 c) and the OER-ECSA scaling relation (Figure 26 b) are in good agreement with the linear dependency between the OER activity and the ECSA for IrO_2/TiO_2 samples with loadings higher than 30 wt. % Ir in TiO_2 (Figure 39 c). The combined data thus suggest that IrO_2 dispersed in TiO_2 has the same intrinsic electrocatalytic reactivity as mesoporous templated IrO_2.

ii) Samples with loadings lower than 20 wt. % Ir in Ir/TiO_2 show peak potentials in the ECSA regime spreading away from the equilibrium voltage of the Ir^{+III}/Ir^{+IV} redox couple (Figure 38 c). For samples with loadings less than or equal to 30 wt. % Ir the observed electrical sheet conductivity attains a value too small to provide a sufficient electron transport through the layer (Figure 37 b). The consequence is an additional voltage drop over the layer which in turn lowers the electrocatalytic reactivity. The higher overpotential appears as a discrepancy from the expected linear relationship between the OER and the ECSA (Figure 39 d). Therefore it is evident, that an iridium loading of at least 30 wt. % Ir in TiO_2 and/or a sheet conductivity higher than approximately $3 \cdot 10^{-8}$ (Ohm/sq)$^{-1}$ (ca. 0.1 S/m) must be provided in order to ensure a sufficient electron transport through the layer and to further avoid additional voltage drops.

In conclusion, active iridium centres in mixed IrO_2/TiO_2 systems exhibit the same intrinsic activity as in pure IrO_2, if a sufficient degree of conductivity is provided.

4.5 Reference catalysts

A detailed electrocatalytic investigation of commercial reference catalysts appears to be mandataroy in order to incorporate our new mesoporous systems into a more global context. Commercial available powders consisting of IrO_x/TiO_x and IrO_2 were considered as relevant systems for the sake of comparison. The powders were separately dispersed in ^{i}PrOH, milliQ H_2O and Nafion, (see 3.1.6 and 3.1.7 for detailed procedure) and subsequently ultrasonified for 15 minutes in order to obtain "inks". A defined volume from each of the inks was pipetted onto titanium cylinders, followed by a drying step at 60 °C. The obtained samples were analyzed physicochemically (SEM) and electrochemically (OER).

Chapter 4.5.1 shows SEM images of IrO_x/TiO_x and IrO_2 on titanium cylinders at different magnifications to identify the morphology of the dropcasted powders. The OER activity is discussed in chapter 4.5.2 and was derived in an acidic electrolyte solution. In addition, the iridium mass base related OER activity is determined in order to identify the commercial system with higher activity. Finally, chapter 4.5.3 shows the geometrical OER activity for the higher active system (e.g. IrO_x/TiO_x) as a function of iridium loading to investigate the reproducibility of the synthesis approach and to identify signs of transport limitations.

4.5.1 SEM

In order to investigate the morphology of commercial available catalysts, dispersions of IrO_x/TiO_x or IrO_2 were dropcasted onto titanium cylinders (A = 0.1963 cm²). The prepared samples were dried at 60 °C and finally investigated by SEM. Recorded electron micrographs are shown in Figure 40 for a) IrO_x/TiO_x ("Elyst") and b) IrO_2.
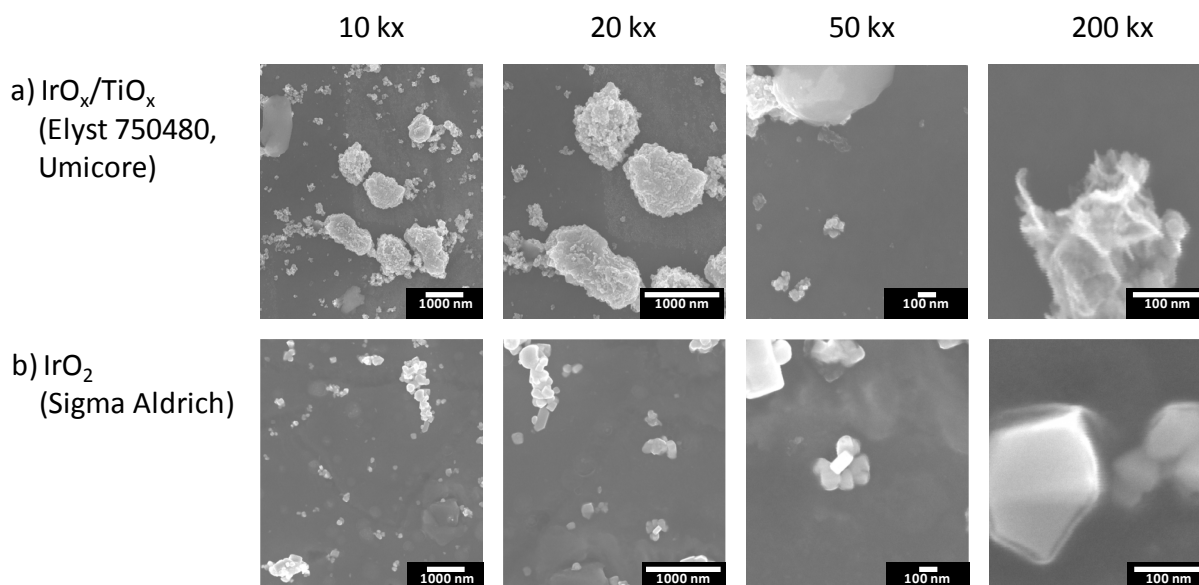

Figure 40: Morphology of different commercial available catalysts deposited by an "ink procedure" on titanium substrates. The used inks consisted of ^{i}PrOH, H_2O, Nafion and a) IrO_x/TiO_x ("Elyst") or b) IrO_2.

Figure 40 a depicts electron micrographs recorded for IrO_x/TiO_x "Elyst". It is clearly visible that particles with different sizes are present. A rough estimation of the particle size reveals a distribution between ca. 50 - 1000 nm. Furthermore, the particles appear to be randomly distributed onto the substrate's surface without any sign of ordering. An enhanced magnification shows that the surface of grains is characterized by stripes with brighter and darker appearance. It appears that a homogenous particle size distribution cannot be achieved by ultrasonification. The inhomogenous distribution of grains on the substrate might be a result of the drying behavior during dropcasting. The difference in contrast and brightness on the particle surface suggest textural roughening.

Scanning electron microscopy images shown in the bottom row feature the morphology of IrO_2 (Figure 40 b). A particle size distribution similar as for IrO_x/TiO_x is observed. It is visible that particles with a size roughly between 50 and 1000 nm are present. However, these particles appear to be randomly distributed on the surface indicating that the synthesis in its present form does not lead to the production of homogenous catalytic coatings. Images recorded with higher magnifications depict large areas of IrO_2 grains on the surface with comparable contrast and brightness. The smooth particle interface is often associated with a crystalline character.

Both commercial available catalysts feature a broad particle size distribution and appear to be inhomogenously distributed on the titanium substrate. However, powders of IrO_x/TiO_x (Figure 40 a) tend to show a higher degree of textural roughening, whereas IrO_2 (Figure 40 b) depicts a smooth outer surface area.

4.5.2 OER activity

Dropcasted layers of IrO_x/TiO_x and IrO_2 on titanium cylinders served as the working electrode in a rotating disc electrode setup. The OER activity was determined by cycling the potential between 1.20 – 1.65 V_{RHE} at 6 mV/s. Current responses were normalized with respect to the substrate's planar geometrical surface area and were corrected for iR drop. Figure 41 shows for commercial systems (IrO_x/TiO_x and IrO_2) the a) 2nd and 25th CV and the b) iridium mass based OER activity at potentials of 1.55 V_{RHE} during the anodic scan of the corresponding CVs
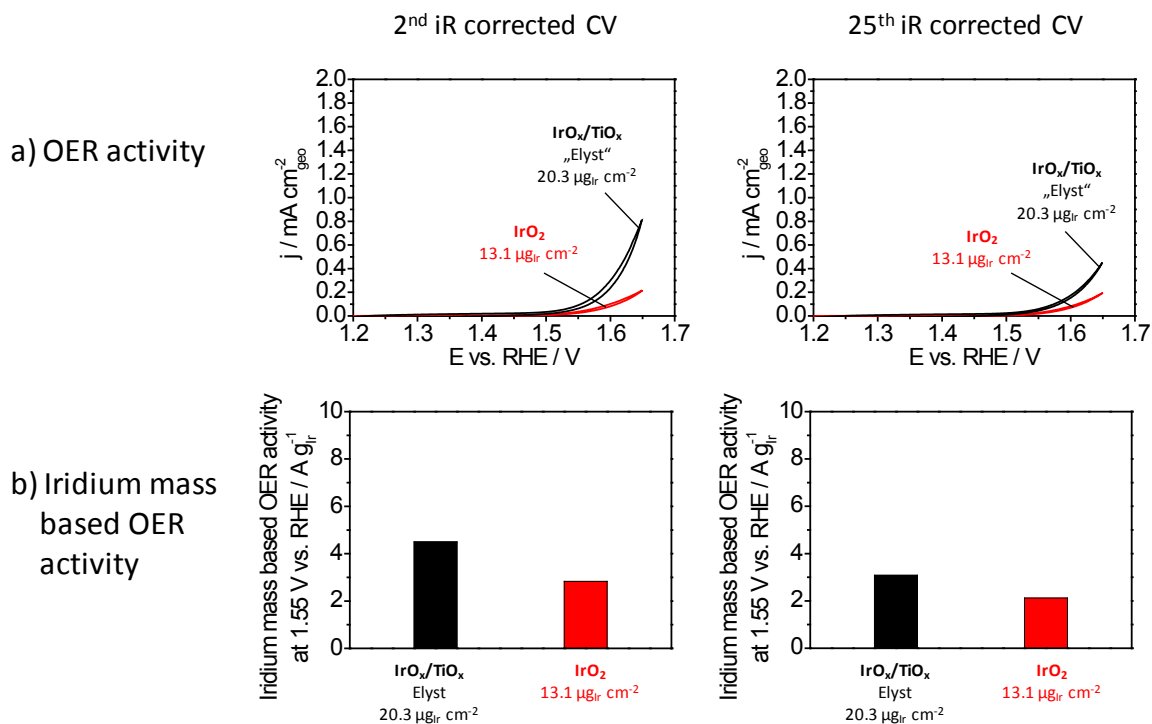
Figure 41: a) Geometrical and b) iridium mass based OER activity for commercial systems comprising IrO$_x$/TiO$_x$ and IrO$_2$. Commercial catalysts were dropcasted by an ink procedure onto titanium cylinders and subsequently investigated electrochemically. The resulting OER activity of the commercial catalysts is shown within the a) 2nd and 25th CV. By measuing the current at 1.55 V$_{RHE}$ during the anodic scan of the corresponding CVs, the b) nominal iridium mass based OER activity (unit: A/g$_{Ir}$) was derived. (1.20 - 1.65 V$_{RHE}$, 6 mV/s, 1600 rpm, 0.5 M H$_2$SO$_4$, nominal iridium mass)

For IrO$_x$/TiO$_x$ and IrO$_2$ coated on titanium cylinders Figure 41 a shows the 2nd and 25th iR corrected cyclic voltammograms. Both catalysts show a decrease in the OER related current density after 25 consecutive cycles. The observed current density of IrO$_x$/TiO$_x$ ("Elyst") is higher than for IrO$_2$ during the 2nd and 25th cyclic voltammogram. However, the nominal iridium loading on the substrate must be considered, which is 1.55 times higher for the IrO$_x$/TiO$_x$ catalyst than that of IrO$_2$. In order to identify the commercial system with the higher mass base related iridium activity and to quantify the decrease in current density, the current was measured at 1.55 V$_{RHE}$ during the anodic scan of the corresponding CVs and normalized with respect to the nominal iridium loading. Figure 41 b depicts the iridium mass based OER activity of IrO$_x$/TiO$_x$ and IrO$_2$. IrO$_x$/TiO$_x$ shows a decrease of 31 % in current density from 4.5 (2nd CV) to 3.1 (25th CV) A/g$_{Ir}$. The iridium mass based current of IrO$_2$, however, reduces it's activity by 25 % from 2.8 (2nd CV) to 2.1 (25th CV) A/g$_{Ir}$. A similar decrease in the mass related OER activity suggests that both catalysts are equally stable. However, IrO$_x$/TiO$_x$ shows a 1.6 times higher mass base related OER activity than IrO$_2$, and thus is identified as the more active commercial catalyst.

4.5.3 Influence of catalyst loading onto titanium substrate on OER activity

Chapter 4.5.2 revealed a higher mass base related OER activity for commercial catalysts of IrO_x/TiO_x ("Elyst") than IrO_2. To further investigate the reproducibility of the dropcasting synthesis approach and to identify any limitations, different loadings of IrO_x/TiO_x on titanium cylinders were produced. The amount of ink volume that can be pipetted on a titanium cylinder at once is limited by the size of the droplet which must not overflow along the borders of the substrate. Therefore, we multi-dropcasted only small volumes of an "IrO_x-TiO_x ink" accompanied by intermediate drying steps at 60 °C in order to vary the iridium loading within a wide range. The achieved loading range of iridium onto titanium cylinders (A = 0.1963 cm²) was about 4 - 800 μg_{Ir} (ca. 20 - 4075 μg_{Ir}/cm²).

The impact of the nominal iridium loading on the current density at 1.56 V_{RHE} during the anodic scan is shown for the a) 2nd CV and b) 25th CV (Figure 42).
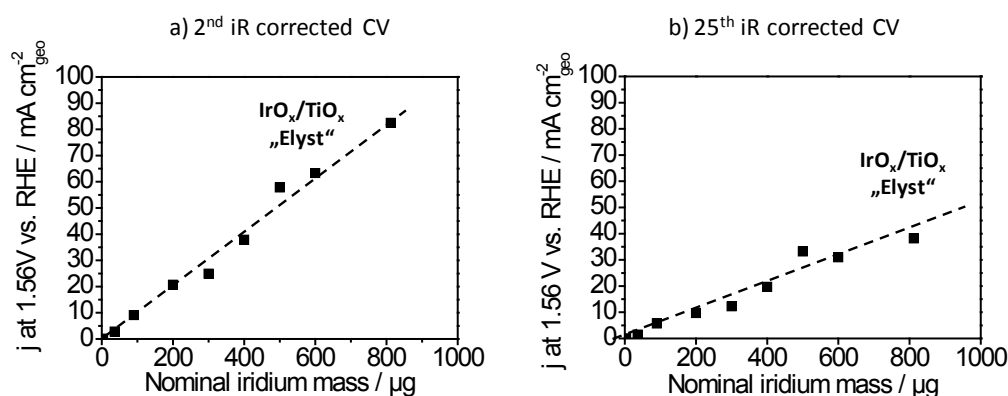

Figure 42: Influence of the nominal iridium mass of catalytic systems of IrO_x/TiO_x ("Elyst") on the geometrical current density in the OER regime. The current density at 1.56 V_{RHE} during the anodic scan is shown for the a) 2nd and b) 25th CV. Cyclic voltammograms were obtained by sweeping the potential between 1.20 - 1.65 V_{RHE} at 6 mV/s (1600 rpm, 0.5 M H_2SO_4, Pt-mesh).

Figure 42 a depicts the geometrical current response at 1.56 V_{RHE} during the anodic scan of the 2nd CV as a function of the nominal iridium mass. A clear linear relationship between the current density and the nominal iridium loading up to current densities as high as ca. 80 mA/cm² (1.56 V_{RHE}) and nominal iridium loadings of ca. 800 μg_{Ir} can be observed with a slope of 0.103 mA/cm² per 1 μg_{Ir} (R^2=0.994). The plot in Figure 42 b is equally derived for the 25th CV. The lower slope of 0.051 mA/cm² per 1 μg_{Ir} (R^2=0.978) indicates that these catalysts exhibit a lowered mass related performance. However, the clear presence of a linear relationship between the OER activity and the iridium mass at 2 and 25 consecutive CVs indicates the absence of transport limitation and reveals a good reproducibility of the synthesis approach. The obtained OER overpotential at 1 mA/cm² for a sample with a nominal iridium loading during the 2nd CV amounts to 0.248 V, which is in good agreement with values reported in literature, e.g. 220 mV.[65]

5 General discussion

The obtained knowledge from the chapters 4.2 and 4.5 are now used to establish a general discussion (chapter 5) in order to identify trends valid for all catalytic coatings operating under acidic conditions, i.e. IrO_2 and IrO_2/TiO_2. Synthesis parameters such as calcination temperature, crystallinity, electrical conductivity, electrochemical active surface area (ECSA) and layer thickness were identified as the most relevant OER-controlling parameters. Furthermore, the applied overpotential during electrocatalytic investigation showed to possess an impact on kinetical aspects, i.e. Tafel slope.

The general discussion shows the structure and morphology of TiO_2, IrO_2 and IrO_2/TiO_2 as a function of the applied precursors (e.g. $TiCl_4$, TALH, $Ir(OAc)_3$), mixtures thereof (chapter 5.1), and as a function of calcination temperature (5.2). The observed morphology is then used to develop a scheme (5.3) in which most of the relevant structural aspects of all systems are shown. In order to identify OER-controlling parameters, convenient plots are presented to demonstrate the influence of calcination temperature (5.4), crystallinity (5.5), electrical conductivity (5.6), and layer thickness (5.7) on OER activity. Moreover, Tafel slopes were determined and discussed for i) mesoporous templated IrO_2 as a function of layer thickness (5.7); and ii) IrO_2 and IrO_2/TiO_2 as a function of calcination temperature (5.8) and iridium loading (5.9). The data are then combined to deduce structure-activity relations (5.10). For the most relevant systems, according to the structure-activity relations, a comparison of the iridium mass based OER activity between the reference catalysts and the new catalysts from this work will be established (5.11).

Structural formula of precursor	$T_{calc.}$	SEM: top view	SEM: high resolution	SEM: cross section	TEM	SAED
TiO_2 ($TiCl_4$)	1 K/min 20 min at 475 °C	a)	b)	c) cs SEM 126 nm	d)	e) TiO_2-anatase
TiO_2 (TALH)	1 K/min 20 min at 400 °C	f)	g)	h) cs SEM 93 nm	i)	j) TiO_2-anatase
IrO_2 (Ir(OAc)$_3$)	5 min at 375 °C	k)	l)	m) cs SEM 68 nm	n)	o) IrO_2-rutile
IrO_2/TiO_2 (Ir(OAc)$_3$+$TiCl_4$) +	10 min at 400 °C (30wt. % Ir)	p)	q)	r) cs SEM - COMPO 95 nm	s)	t) low crystallinity/ amorphous
IrO_2/TiO_2 (Ir(OAc)$_3$+TALH) +	10 min at 400 °C (30wt. % Ir)	u)	v)	w) cs SEM - COMPO 80 nm	x) y)	z) TiO_2-anatase IrO_2+TiO_2 rutile?

Figure 43: Different precursor systems were used to derive different categories of mesoporous templated oxides, such as TiO_2 (1st and 2nd row), IrO_2 (3rd row) and IrO_2/TiO_2 (4th and 5th row). The precursors: $TiCl_4$, TALH and Ir(OAc)$_3$ have different chemical natures, thus highly affecting the appearance of mesopores as well as pore walls (SEM: top view and high resolution, see text for detail description). All samples show similar layer thicknesses (SEM: cross section) and templated mesoporosity within the film volume area (TEM). Crystallinity was investigated by SAED showing TiO_2-anatase (1st and 2nd row),[98, 109] IrO_2-rutile (3rd row), low crystalline/amorphous IrO_2/TiO_2 (4th row), and a mixture of TiO_2 anatase and rutiles of TiO_2 and IrO_2 (propably forming a solid solution) (5th row).

5.1 Influence of precursor on structure/morphology (TiO$_2$, IrO$_2$, IrO$_2$/TiO$_2$)

An overview on the structure of metal oxides of iridium and titanium and mixtures thereof are provided in Figure 43. The scheme illustrates the morphology and crystallinity of TiO$_2$ synthesized from TiCl$_4$ (a - e), TiO$_2$ synthesized from TALH (f - j), IrO$_2$ synthesized from Ir(OAc)$_3$ (k - o), IrO$_2$/TiO$_2$ synthesized from Ir(OAc)$_3$ and TiCl$_4$ (p - t), as well as IrO$_2$/TiO$_2$ synthesized from Ir(OAc)$_3$ and TALH (u - z).

TiO$_2$ synthesized from TiCl$_4$

The first row shows TiO$_2$ dried for 4 h at 80 °C and calcined at 475 °C (1 K/min). All images were published by Ortel et al.[98] and are reused with the permission of John Wiley. Templated mesopores with a spherical shape are visible at the outer surface plane area (Figure 43 a) suggesting the successful introduction of mesoporosity. SEM images with higher mangification (Figure 43 b) show a smooth appearance of the pore walls and no sign of textural porosity. SEM recorded in cross section shows a layer thickness of 126 nm (Figure 43 c). TEM indicates the presence of mesoporosity suggesting complete pore penetration of the film volume area (Figure 43 d). The corresponding SAED reveals diffraction rings and spots that are attributed to a crystalline TiO$_2$-anatase phase. The synthesis produces layers of mesoporous templated TiO$_2$-anatase with smooth pore walls

TiO$_2$ synthesized from TALH

The second row depicts mesoporous TiO$_2$ dipcoated from a solution of Titanium(IV) bis(ammonium lactato)dihydroxide (TALH) on silicon substrates and heat treated at 400 °C (1 K/min). SEM and SAED were published by Ortel et al.[109] and reused with the permission of ACS. The SEM shows mesoporosity at the outher surface plane area indicating the introduction of mesoporosity (Figure 43 f). The SEM image obtained in high resolution mode reveals textural porosity within the mesopore walls (Figure 43 g). Cross section SEM determines the layer thickness (93 nm, Figure 43 h). The presence of mesoporosity in the TEM image suggests a complete penetration of the film volume area by mesopores (Figure 43 i). The SAED measurements show diffraction rings associated with a crystalline TiO$_2$-anatase phase (Figure 43 j). The synthesis approach produces layers of mesoporous templated TiO$_2$-anatase with pore walls characterized by textural porosity

IrO$_2$ synthesized from Ir(OAc)$_3$ (data from chapter 4.2)

SEM images of templated IrO$_2$ synthesized from Ir(OAc)$_3$ and heat treated at 375 °C are shown in Figure 43 k. Templated mesoporosity is present at the outer surface plane area. Higher magnification in SEM reveals textural porosity within the mesopore walls (Figure 43 l). The layer thickness determined by SEM amounts to 68 nm (Figure 43 m). TEM reveals

mesoporosity suggesting that the pores completely penetrate the whole film volume area (Figure 43 n). Recorded SAED images show broad and weak diffraction rings indicating an IrO_2-rutile phase with a very low crystallite size (Figure 43 o). The synthesis produces layers of mesoporous templated IrO_2-rutile with low crystallinity and textural porosity.

IrO_2/TiO_2 synthesized from $Ir(OAc)_3$ and $TiCl_4$ (data from chapter 4.3)

The fourth row of Figure 43 shows the structural properties for mixed metal oxides of IrO_2/TiO_2 obtained by $Ir(OAc)_3$ and $TiCl_4$ heat treated in air at 400 °C. The SEM image shows templated and untemplated domains (ca. 100 nm in diameter) at the outer surface plane area (Figure 43 p). SEM micrographs recorded in COMPO mode (Figure 27 b) reveal a higher brightness for the untemplated than for the templated domain. Hence, the untemplated domains contain a higher content of iridium, whereas the templated domains contain more titanium. High resolution SEM reveals textural porosity in the untemplated domains (Figure 43 q), whereas textural porosity is less pronounced in the mesoporous templated titanium rich domains. The layer thickness was derived by SEM in COMPO mode (95 nm, Figure 43 r). The observed difference in z-contrast in cross section SEM in COMPO mode suggests a three-dimensional segregation of IrO_2 and TiO_2. TEM images show mesoporosity suggesting complete penetration of the film volume area by pores (Figure 43 s). The dark areas observed in Figure 43 s show a higher brightness for images recorded in HAADF mode (Figure 27 e) indicating that iridium rich phases are present within the film volume. Recorded SAED images show no diffraction rings (Figure 43 t) representative for samples with crystallites too small to produce signals sufficient enough to be detected in SAED. The synthesis produces layers of mesoporous templated titanium rich and untemplated iridium rich domains on a lengthscale of ca. 100 nm. Both domains are characterized by low crystallinity, wheras the iridium rich domain features a high degree of textural porosity.

IrO_2/TiO_2 synthesized from $Ir(OAc)_3$ and TALH (data from chapter 4.4)

The last row of Figure 43 shows the physicochemical analysis of IrO_2/TiO_2 synthesized from $Ir(OAc)_3$ and TALH calcined at 400 °C. The SEM image (Figure 43 u) reveals mesoporosity at the outer surface plane area. Furthermore, high resolution SEM reveals textural porosity at the mesopore walls (Figure 43 v). The layer thickness amounts to 80 nm (Figure 43 w). TEM images recorded in brightfield mode with high magnification (Figure 43 x) reveal small areas (ca. 2 nm) which appear darker than the surrounding which can be attributed to an iridium rich domain. The observed mesoporosity (Figure 43 y) suggests complete penetration of the layer by pores. Recorded SAED images (Figure 43 z) indicate pronounced diffraction rings attributed to a TiO_2-anatase and to a rutile phase. However, similar lattice parameters of IrO_2-rutile, TiO_2-rutile, as well as the broadness of reflection rings prevent a clear distinction between IrO_2-rutile, TiO_2-rutile, or a mixture thereof, which is noted as: "IrO_2+TiO_2 rutile?"
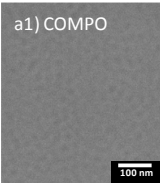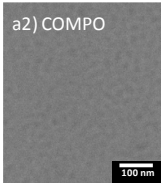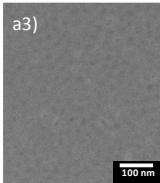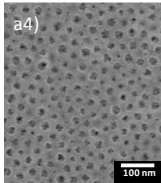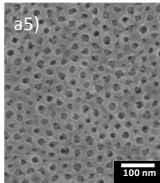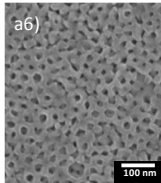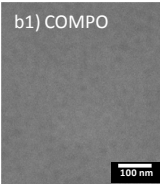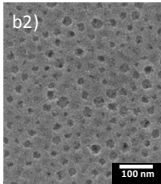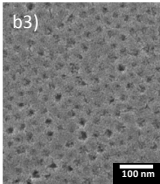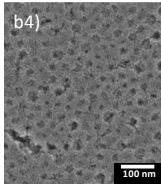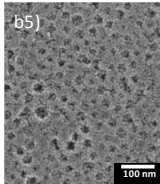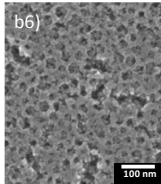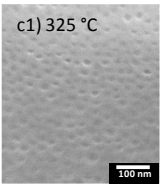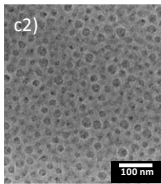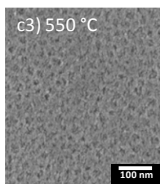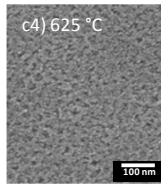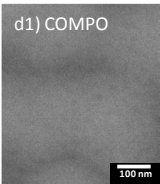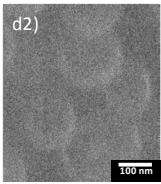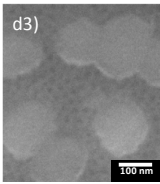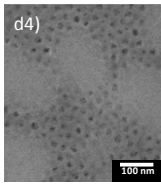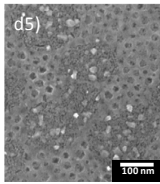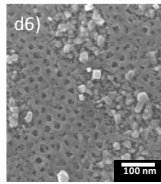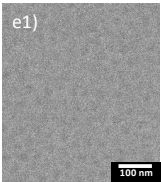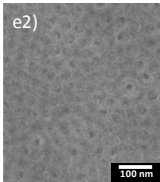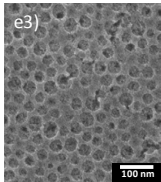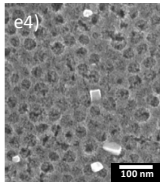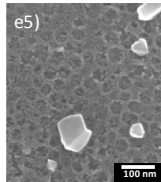
Structural formula of precursor	$T_{calc.}$	80 °C	200 °C	300 °C	400 °C	500 °C	600 °C
TiO$_2$ (TiCl$_4$)	1 K/min 20 min at $T_{calc.}$	a1) COMPO	a2) COMPO	a3)	a4)	a5)	a6)
TiO$_2$ (TALH)	1 K/min 20 min at $T_{calc.}$	b1) COMPO	b2)	b3)	b4)	b5)	b6)
IrO$_2$ (Ir(OAc)$_3$)	5 min at $T_{calc.}$			c1) 325 °C / c2)		c3) 550 °C	c4) 625 °C
IrO$_2$/TiO$_2$ (Ir(OAc)$_3$+TiCl$_4$) +	10 min at $T_{calc.}$ (30wt. % Ir)	d1) COMPO	d2)	d3)	d4)	d5)	d6)
IrO$_2$/TiO$_2$ (Ir(OAc)$_3$+TALH) +	10 min at $T_{calc.}$ (30wt. % Ir)	e1)	e2)	e3)	e4)	e5)	

Figure 44: Influence of calcination temperature ($T_{calc.}$) on the morphology of PEO-PB-PEO templated TiO$_2$ derived by TiCl$_4$ (1st row, silicon substrate, ramp: 1 K/min), and TALH (2nd row, silicon substrate, ramp: 1 K/min); IrO$_2$ derived by Ir(OAc)$_3$ (3rd row, titanium substrate, preheated furnace); as well as IrO$_2$/TiO$_2$ derived by Ir(OAc)$_3$ and TiCl$_4$ (4th row, titanium substrate, preheated furnace), as well as Ir(OAc)$_3$ and TALH (5th ro w, titanium substrate, preheated furnace).

5.2 Influence of calcination temperature on morphology (TiO$_2$, IrO$_2$, IrO$_2$/TiO$_2$)

Figure 44 shows the influence of calcination temperature on the morphology of TiO$_2$ synthesized from TiCl$_4$ (a1-a6), TiO$_2$ synthesized from TALH (b1 - b6), IrO$_2$ synthesized from Ir(OAc)$_3$ (c1 - c4), IrO$_2$/TiO$_2$ synthesized from Ir(OAc)$_3$ and TiCl$_4$ (d1 - d6), as well as IrO$_2$/TiO$_2$ synthesized from Ir(OAc)$_3$ and TALH (e1 - e5).

TiO$_2$ synthesized from TiCl$_4$

TiO$_2$ obtained by TiCl$_4$ on silicon was dried at 80 °C for 4 h and heat treated between 200 - 600 °C in air (ramp: 1 K/min). A calcination temperature between 80 and 300 °C show a poor contrast and brightness due to their insufficient electrical conductivity which is most likely related to an incomplete removal of the polymer template (Figure 44 a1 - a3). An increase in calcination temperature to 400 and 500 °C (Figure 44 a4 - a5) produces a fully developed pore system with a smooth appearance of the mesopore walls (see Figure 43 b for higher resolution). The beginning distortion of the mesopores observed for samples heat treated at 600 °C (Figure 44 a6) indicate ongoing sintering which is induced by crystallite growth.

TiO$_2$ synthesized from TALH

The 2nd row in Figure 44 shows layers of TiO$_2$ obtained by TALH thermally treated at temperatures between 80 and 600 °C in air (1 K/min). Samples dried at 80 °C show a poor contrast and brightness in SEM suggesting an incomplete template removal (Figure 44 b1). However, increasing the calcination temperature to 200 °C produces samples with a good contrast and brightness due to a developed mesoporous system (Figure 44 b2). The pore walls have textural porosity (note that textural porosity is more evident in images recorded at higher magnification, e.g. Figure 43 g). A further increase in calcination temperature to 300 and 400 °C show no significant change of the mesopore shape or textural porosity at the outer surface plane area (Figure 44 b3 - b4). Grains and a beginning distortion of the spherical mesoporous shape can be observed for samples heat treated at 500 °C (Figure 44 b5). In addition, textural porosity starts to decline. If the calcination temperature is further increased to 600 °C, not only a higher degree of distortion of the spherical mesoporous shape is occuring, but also an almost complete depletion of textural porosity (Figure 44 b6). Both observations are attributed to the ongoing sintering due to temperature induced crystallite growth.

IrO$_2$ synthesized from Ir(OAc)$_3$

Layers of mesoporous templated IrO$_2$ were obtained by Ir(OAc)$_3$ and a subsequent heat treatment at temperatures between 325 and 625 °C. Thermally prepared IrO$_2$ at 325 °C shows a poor contrast and brightness in SEM indicating incomplete polymer template

removal (Figure 44 c1). An increase in calcination temperature to 400 °C (Figure 44 c2) reveals a fully developed pore system with additional textural porosity in the mesopore walls (see Figure 43 l for SEM with higher magnification). Heat treated samples between 550 and 625 °C (Figure 44 c3 - c4) show a beginning distortion of mesopore walls and an almost fully depletion of textural porosity caused by temperature induced crystallite growth.

IrO$_2$/TiO$_2$ synthesized from Ir(OAc)$_3$ and TiCl$_4$

IrO$_2$/TiO$_2$ was coated on titanium and obtained by different metal oxide precursors, such as Ir(OAc)$_3$ and TiCl$_4$. The samples were heat treated at temperatures between 80 and 600 °C. Low calcination temperatures between 80 and 300 °C (Figure 44 d1 - d3) show largely segregated areas with a high content of iridium and titanium, respectively. Moreover, a poor contrast and brightness is observed suggesting incomplete polymer template removal. Enhancing the calcination temperature to 400 °C (Figure 44 d4) reveals a templated, titanium rich domain as well as an untemplated, iridium rich domain (suggested by COMPO Figure 27 b). The untemplated areas are rich in textural porosity, whereas templated areas show less degree of textural porosity (see Figure 43 q). A heat treatment of samples at 500 and 600 °C (Figure 44 d5 - d6) is accompanied by a depletion of textural porosity and a formation of bright particles suggesting temperature induced crystallite growth.

IrO$_2$/TiO$_2$ synthesized from Ir(OAc)$_3$ and TALH

Ir(OAc)$_3$ and TALH served as metal oxide precursors for the preparation of IrO$_2$/TiO$_2$ on titanium substrates. The samples were calcined at temperatures between 200 and 600 °C. Samples heat treated between 200 and 300 °C (Figure 44 e1 - e2) show a poor contrast and brightness suggesting an incomplete polymer template removal. A fully developed pore system with an additional content of textural porosity is observed for samples heat treated at 400 °C (Figure 44 e3 and Figure 43 v). A further increase in calcination temperature to 500 and 600 °C reveals particles arising on the outer surface plane area (Figure 44 e4 - e5). The temperature induced demixing is caused by the excessively crystallisation behaviour of IrO$_2$.
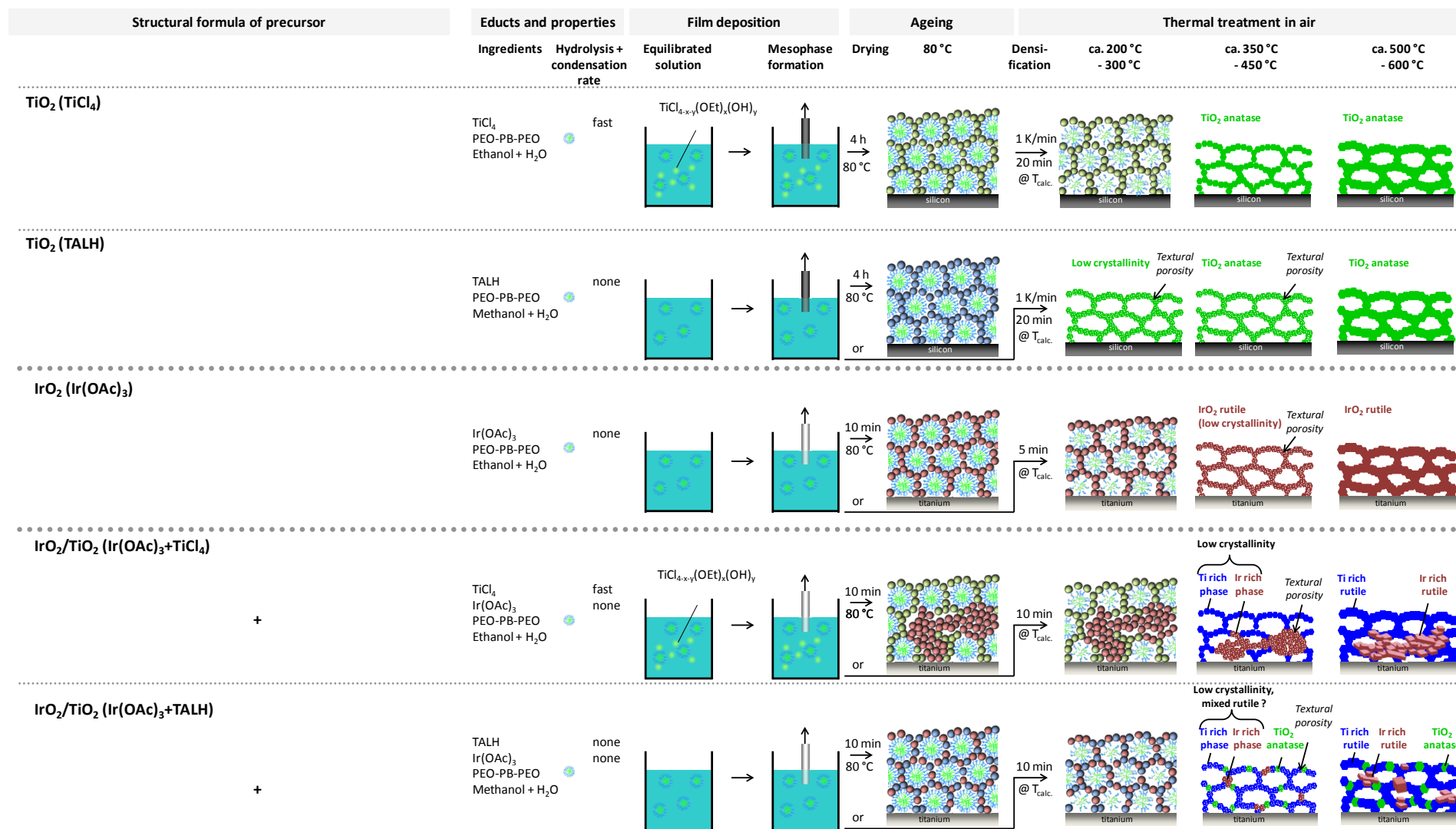
Figure 45: A general scheme based on the observations from Figure 44 (Influence of precursor on morphology) and Figure 43 (influence of calcination temperature on morphology/crystallinity). The figure depicts the structural formula of the utilized precursors; the corresponding equilibrated solutions; the morphology of films deposited on a substrate and dried at 80 °C; and the morphology/crystallinity after heat treatment at temperatures between 200 - 600 °C.

5.3 Processes during synthesis and the resulting morphology

Figure 45 combines the observations from chapter 5.1 and 5.2 in a general scheme in order to illustrate processes occuring during the preparation of dipcoating solutions, film deposition, and subsequent heat treatments for TiO_2 synthesized from $TiCl_4$ (1st row), TiO_2 synthesized from TALH (2nd row), IrO_2 synthesized from $Ir(OAc)_3$ (3rd row), IrO_2/TiO_2 synthesized from $Ir(OAc)_3$ and $TiCl_4$ (4th row), and IrO_2/TiO_2 synthesized from $Ir(OAc)_3$ and TALH (5th row).

TiO_2 synthesized from $TiCl_4$ (1st row)

Titanium tetrachloride is often used to obtain nanostructured TiO_2 (see chapter 2.2.6). In literature, it is reported that $TiCl_4$ shows fast hydrolysis and condensation rates.[99, 102] However, hydrolysis and condensation of $TiCl_4$ produces HCl which prevents further polycondensation and therefore leads to the formation of self stabilized titanium oligomers with particle diameters in the range of 0.4 - 1.7 nm.[107] Figure 45 (1st row) depicts the equilibrated solution of $TiCl_4$ dissolved in ethanol, water and PEO-PB-PEO. The obtained titanium oligomers are shown as small spherical particles well dispersed in the solvent. Moreover, these oligomers are typically terminated by hydroxide groups thus possessing the capability to interact with hydrolytic regions of the utilized polymer, e.g. PEO.[99, 102] Subsequent to dipcoating, the solvent evaporates together with HCl triggering two effects: i) the alignment of pre formed micelles and ii) a further polycondensation of the titanium oligomers.[157] The obtained samples are dried for 4 h at 80 °C (ensuring reproducibility[99]) and are further heat treated at temperatures above 400 °C in air to fully remove the polymer template and to convert the precursor into a crystalline TiO_2-anatase with smooth pore walls. This pore wall structure was already reported in literature[98] and is associated with highly crystalline materials. This assumption is in good agreement with XRD of the corresponding samples calcined at 400 °C. The Scherrer equation applied at the (101) reflection reveals a crystallite size of ~20 nm. An increase of calcination temperatures to 500 and 600 °C further enhances the crystallite size to 21 and 23 nm which distort the spherical mesopore shape.

TiO_2 synthesized from TALH (2nd row)

Titanium(IV) bis(ammonium lactato)dihydroxide (abbreviated as: TALH) is characterized by a Ti cation complexed by lactic acid (chelat ligand), and two hydroxide groups. Chelat groups show rather slow hydrolysis rates compared to alkoxy groups.[158] In fact, TALH does not undergo hydrolysis and condensation when dissolved in water.[149] The graphical illustration of the equilibrated solution (Figure 45; 2nd row) thus depicts a particle character only for PEO-PB-PEO polymer templates, whereas TALH does not form any particles (in contrast to $TiCl_4$). Calcination at 200 °C shows mesoporosity and textural porosity. The successful preparation of mesoporous TiO_2 by using TALH demonstrates, that precursors without hydrolysis and

condensation capabilities can be used along with polymer templates in order to successfully synthesize mesoporous samples. The occuring textural porosity for TiO_2 obtained by TALH and the presence of smooth pore walls for TiO_2 derived by $TiCl_4$ suggests that the carbon content of the precursor significantly changes the microstructure of the mesopore walls. The decomposition of carbon containing precursors forms CO_2 during calcination. Hence, a possible explanation for the textural porosity might be the departure of CO_2 during heat treatment. This observation is in line with reports of Schmack et al.[148] who observed a clear correlation between the carbon content in metal oxide precursors and degree of textural porosity in the mesopore walls of templated films. The corresponding XRD for samples calcined at 400 °C reveal a crystallite size of ca. 4 - 5 nm (Scherrer equation, (101) reflection, Figure A4 a). The lower crystallite size for TALH based TiO_2 films (4 - 5 nm, Figure A4 b) in comparison to $TiCl_4$ based TiO_2 films (20 nm) can be attributed to the higher carbon fraction of the TALH precursor which potentially inhibits temperature induced crystallite growth. The degree of textural porosity declines as a function of calcination temperature. Moreover, the distortion of the spherical mesopore shape depends on the applied temperature during heat treatment. A depletion of the textural porosity and distortion of the mesopore shape are due to sintering which is induced by ongoing crystallite growth.

IrO_2 synthesized from $Ir(OAc)_3$ (3rd row)

$Ir(OAc)_3$ is stable to hydrolysis and condensation in water and ethanol at room temperature,[145] forms no small oligomers and is therefore chemically similar to TALH. Dissolving PEO-PB-PEO and $Ir(OAc)_3$ in ethanol and water forms a clear greenish solution (Figure 45; 3rd row). Thermal treatment of deposited layers between 80 and 300 °C in air does not fully remove the polymer. However, a fully developed pore system is obtained when heat treating at 400 °C. The mesopore walls contain textural porosity (see Figure 43 l) as it was the case for TiO_2 obtained by TALH. As to the similar chemical behaviour of $Ir(OAc)_3$ and TALH comparable morphologies of the obtained mesoporous layers are obtained. The textural porosity might be explained by the formation of CO_2 as the metal oxide precursor decomposes during thermal treatment.[148] An increase in calcination temperature leads to a depletion of textural porosity and distortion of the spherical mesopore shape indicating ongoing sintering due temperature induced crystallite gowth.

IrO_2/TiO_2 synthesized from $Ir(OAc)_3$ and $TiCl_4$ (4th row)

In order to produce mixed metal oxides of Ti and Ir, $Ir(OAc)_3$ and $TiCl_4$ were immersed in ethanol and water. $Ir(OAc)_3$ was found to be stable against hydrolysis and condensation,[145] and thus showing a poor interaction with hydrolytic regions of the polymer template, whereas $TiCl_4$ shows fast hydrolysis and condensation rates and can interact with the polymer.

The equilibrated solution of $TiCl_4$, $Ir(OAc)_3$, PEO-PB-PEO, ethanol, and water (Figure 45; 4th row) is characterized by small titanium oligomers, PEO-PB-PEO micelles and $Ir(OAc)_3$ dissolved in ethanol and water. The solution was light green and clear indicating that no light is scattered by particles that are dispersed within the suspension. The Tyndall effect usually occurs for particles dispersed in a liquid medium with a diameter of at least ~100 nm.[146-147] As a consequence, the produced solution is not expected to contain particles exhibiting diameters larger than ca. 100 nm. However, dipcoating on titanium with a subsequent heat treatment at 80 °C reveals largely segregated domains with diameters of at least 100 nm. An increase in calcination temperature to 400 °C removes most of the polymer template and reveals an untemplated, iridium rich domain with textural porosity and a templated, titanium rich domain with less textural porosity. A further increase in calcination temperature diminishes the textural porosity, and forms particles, whereby the spherical mesoporous shape distorts under the development of an Ir rich and Ti rich rutile phase

Three important effects are observed: i) the segregation of IrO_2 and TiO_2 on a lengthscale of roughly 100 nm, ii) the development of a mesoporous structure solely for titanium rich domains and iii) a higher degree of textural porosity for iridium rich domains. i) The synthesized dipcoating solution contains PEO-PB-PEO, $TiCl_4$ and $Ir(OAc)_3$ in ethanol and water, was clear and showed a greenish colour. Therefore, as particles with a diameter of larger than ~100 nm are not present in the solution,[146-147] the observed segregated domains in the layers are not formed within the solution. Thus, demixing very likely occurs after film deposition and is possibly related to different drying behaviours of Ir and Ti precursors. The distinct behaviours might be associated with different mobilities of both metal oxide precursors within the solution. We hypothesize that the different mobilities are related to the different interaction behaviours: $TiCl_4$ interacts with the polymer template, whereas $Ir(OAc)_3$ does not. Moreover, the different interaction behaviours of $TiCl_4$ and $Ir(OAc)_3$ with the polymer template are used to describe ii) the development of mesoporosity solely for titanium rich domains. It appears likely to find a precursor molecule next to a polymer molecule if the precursor is able to interact with the polymer (e.g. $TiCl_4$). As a consequence, Ti rich domains appear to be mesoporous templated, whereas iridium rich domains show no sign of templated mesoporosity. However, the iii) iridium rich domains exhibit a high degree of textural porosity in contrast to the templated Ti rich domains. This behaviour is associated with the higher degree of carbon within $Ir(OAc)_3$ than $TiCl_4$. During calcination the carbon oxidizes to CO_2, whereby textural porosity is introduced to the iridium rich domains.[65, 148]

IrO_2/TiO_2 synthesized from $Ir(OAc)_3$ and TALH

Both, $Ir(OAc)_3$ and TALH are characterized by sterically demanding chelat ligands, such as acetic acid and lactic acid, respectively. Hence, no hydrolysis and condensation is observed

to form hydroxide groups which prevents the interaction with the polymer template. The obtained dipcoating solution of PEO-PB-PEO, $Ir(OAc)_3$ and TALH in methanol showed a green colour without turbidity.

A layer deposited on titanium substrate was heat treated at 200 °C and showed i) a poor contrast and brightness in SEM suggesting incomplete template removal and ii) no largely segregated areas with diameters of 100 nm as it was observed in the case of $TiCl_4$ and $Ir(OAc)_3$. A more even distribution of IrO_2 and TiO_2 after film deposition might be related to a similar drying behavior of $Ir(OAc)_3$ and TALH. Both metal oxide precursors therefore show similar, however no attractive, interactions with the polymer template. We hypothesize, that higher chemical similarity of the used metal oxide precursors result in a more homogenous distribution of IrO_2 and TiO_2 within films. An increase to 400 °C features a fully developed pore system (Figure 44) with textural porosity in the mesopore walls due to the combustion of carbon to CO_2 from both used metal oxide precursors. However, TEM studies show small (ca. 2 nm) segregated and dark areas in brightfield mode suggesting a higher amount of Ir than Ti. According to SAED images, TiO_2-anatase and rutile are present. Due to the broadness of the rings and the similar lattice parameters of TiO_2-rutile and IrO_2-rutile, a clear distinction between both rutile phases (IrO_2 and TiO_2) or a mixture thereof can not be given. Therefore, the presented scheme in Figure 45 (5th row) shows i) TiO_2 anatase, ii) small Ir rich domains, and iii) titanium rich domains, whereof, ii) and iii) are possibly crystallized in a rutile structure. Further increasing the calcination temperature, not only distort the spherical mesopore shape but also forms iridium rich crystallites (Figure 34 a). XRD (Figure 34 b, c) shows distinct reflection signals corresponding to TiO_2 anatase, TiO_2 rutile containing Ir (Ti-rich rutile), and IrO_2 rutile containing Ti (Ir-rich rutile). Obviously, two effects are observed: i) a thermally induced demixing, and ii) the beginning formation of a solid solution. Tammann[150] reported, that atoms can change places within crystallites or at the interface between two different crystallite species, if a sufficient degree of atomic oscillation (temperature dependent) is reached. In honour of Tammann, this temperature is called the Tammann temperature. The Tammann temperatures for TiO_2 and IrO_2 are as followed:

TiO_2: $T_{Tammann}$ = 791 °C[151]

IrO_2: $T_{Tammann}$ = 413 °C[152]

i) For IrO_2 the lower Tammann temperature implies mobility at much lower temperatures than required for TiO_2. Hence, thermally induced demixing of IrO_2/TiO_2 slowly begins for samples calcined above ca. 400 °C. In fact, for samples calcined at 400 °C a demixing between IrO_2 and TiO_2 is not very pronounced, whereas samples heat treated at 500 °C clearly depict larger areas with Ir rich crystallites. ii) A further increase in calcination temperature to 600 °C forms a solid solution of IrO_2 and TiO_2. We assume, that present IrO_2 crystallites starts to incorporate surrounded TiO_2 leading to fractions of Ir rich rutile and titanium rich rutile.

5.4 Influence of calcination temperature on OER activity and ECSA

In dependency of the calcination temperature, the following chapter shows the quantified electrochemical measurements of the oxygen evolution reaction (OER) activity and the electrochemical accessible surface area (ECSA) of mesoporous templated IrO_2 and IrO_2/TiO_2, respectively. The electrochemical data are then related to the morphology. Figure 46 shows for IrO_2 and IrO_2/TiO_2 (synthesized from $TiCl_4$ or TALH) the a) OER activity and b) corresponding ECSA as a function of calcination temperature, as well as the c) OER activity as a function of ECSA.
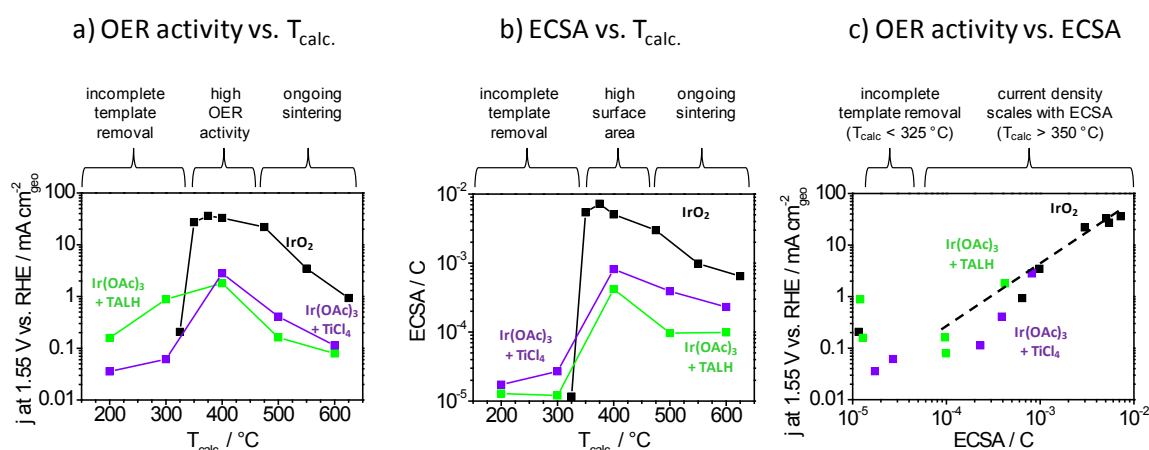
Figure 46: Influence of calcination temperature on a) OER activity and b) corresponding ECSA. Moreover the c) OER activity is plotted as a function of ECSA. IrO_2 (black) was synthesized from $Ir(OAc)_3$ and heat treated for 5 min at $T_{calc.}$; IrO_2/TiO_2 (purple) was synthesized from $Ir(OAc)_3$ and $TiCl_4$, exhibits a loading of 30 wt. % Ir in Ir/TiO_2 and was heat treated for 10 min at $T_{calc.}$; IrO_2/TiO_2 (green) synthesized from $Ir(OAc)_3$ and TALH with a loading of 30 wt. % Ir in Ir/TiO_2 and heat treatment for 10 min at $T_{calc.}$

A comparison of OER activities in dependence of the calcination temperature was established by measuring the current density at a potential of 1.55 V_{RHE} from the upscan of the 2nd iR corrected CV (Figure 46 a, note: y-axis is shown logarithmically). The OER activity is normalized to the substrate's planar geometrical surface area. Catalytic layers containing mesoporous IrO_2 depict an increase in OER activity in the temperature range of 325 – 375 °C. For higher calcination temperatures the OER activity steadily decreases. From $TiCl_4$ and TALH produced samples display a very similar trend. First, the OER activity is steadily enhanced in the temperature range between 200 to 400 °C, but successively decreases between 400 and 600 °C.

Figure 46 b shows the quantified ECSA measurements of the corresponding samples from Figure 46 a. The ECSA (in Coloumb) is obtained by the mean value of the integrated anodic and cathodic charge from CVs recorded in a lower potential window between 0.40 – 1.40 V_{RHE}. The ECSA follows a very similar trend as the OER activity in dependency of temperature. The IrO_2 ECSA successively increases up to temperatures as high as 375 °C

and progressively declines for higher calcination temperatures. The ECSA of IrO_2/TiO_2 either synthesized from $TiCl_4$ or TALH follow a very similar trend as a function of calcination temperature. An increase in ECSA is observed for both systems between 200 and 400 °C, but subsequently declines with respect to the calcination temperature. In Figure 46 c the influence of the ECSA on the OER activity is established for each system. Samples heat treated below 325 °C show a poor OER activity and a small ECSA, whereas samples calcined at temperatures higher than 350 °C depict a higher OER activity and a larger ECSA with a fairly linear relationship.

Based on the present data the following conclusion is drawn. All samples that were thermally treated between 200 and 325 °C show an incomplete removal of the polymer template (Figure 44) which blocks the mesopores and consequently causes a small ECSA. An increase of calcination temperature slightly higher than the combustion temperature of the polymer template (350 – 475 °C) produces low crystallinity (Figure 43) and a fully accessible pore system as indicated by Kr-physisorption (Figure 23 b). A high surface area is the consequence. The depletion of textural porosity and distortion of mesopores is induced by a further increase in calcination temperature (> 500 °C) and progressively decreases the ECSA. The loss in porosity related to an ongoing sintering is caused by thermally induced crystallite growth (Figure 44 (SEM of IrO_2 and IrO_2/TiO_2), Figure 24 (XRD of IrO_2), Figure 28 (XRD of IrO_2/TiO_2, $TiCl_4$), Figure 34 (XRD of IrO_2/TiO_2, TALH)). In conclusion, temperatures slightly higher than the decomposition temperature of the polymer template produce samples with a high surface area. Moreover, if the polymer is removed, a fairly linear relationship between the OER activity and ECSA is observed suggesting that ECSA contributes to the OER activity.

5.5 Influence of crystallinity on OER activity

The degree of crystallinity influences the intrinsic OER reactivity of mesoporous IrO_2 as described in chapter 4.2.4. It was observed that IrO_2 heat treated at or temperatures higher than 550 °C display crystallites large enough to produce distinct diffraction signals in XRD. At lower calcination temperatures, however, no XRD reflections are observed but very broad diffraction rings in SAED images due to low crystallinity (Figure 24). Furthermore, samples with a low crystallinity show higher intrinsic OER reactivity (Figure 23).

As thermally treated IrO_2/TiO_2 (synthesized from $Ir(OAc)_3$ and $TiCl_4$) at 400 °C show no significant diffraction rings in SAED (Figure 43, 4th row) the obtained layer is composed of crystallites too small in size to produce intense reflections. The reflections in XRD at 500 °C can be attributed to a Ti rich rutile and an Ir rich rutile phase (Figure 28).

A heat treatment at 400 °C of IrO_2/TiO_2 synthesized from $Ir(OAc)_3$ and TALH show rings in SAED images corresponding to TiO_2 anatase, and rutile (Figure 43). However, no distinct reflections have been observed in XRD diffraction patterns (Figure 34 b). At calcination temperatures higher than 500 °C diffraction patterns of a TiO_2 anatase, a Ti rich rutile, and a iridium rich rutile phase are observed (Figure 34 b).

In order to reveal the impact of crystallinity on the OER activity different criteria for crystallinity have to be defined. A sample is considered as i) low crystalline, if no distinct reflections are observed in XRD but diffraction rings in SAED. And it is considered as ii) high crystalline, if distinct reflections are shown in XRD. For samples with a removed template Figure 47 depicts the measured OER activity during the upscan of the 2nd iR corrected CV at a potential of 1.55 V_{RHE} as a function of crystallinity for a) IrO_2, b) IrO_2/TiO_2 (synthesized from $Ir(OAc)_3$ and $TiCl_4$), and c) IrO_2/TiO_2 (synthesized from $Ir(OAc)_3$ and TALH).
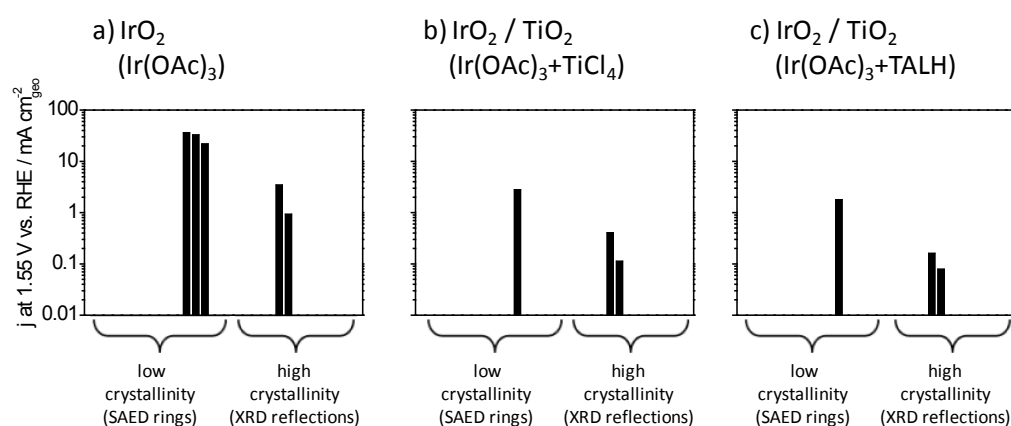
Figure 47: Influence of crystallinity on the OER activity from catalytic layers coated on titanium substrates. Three different systems are shown for comparison: a) IrO_2, b) IrO_2/TiO_2 synthesized from $Ir(OAc)_3$ and $TiCl_4$, as well as c) IrO_2/TiO_2 synthesized from $Ir(OAc)_3$ and TALH. The OER activity was accessed by measuring the current density (with respect to the planar geometrical surface area) in the upscan of the 2nd iR corrected CV at potentials of 1.55 V_{RHE} (1600 rpm, 6 mV/s, 0.5 M H_2SO_4).

Figure 47 a reveals the OER activity for IrO_2 with low crystallinity (3 bars on the left side, $T_{calc.}$ = 375, 400, 475 °C) and high crystallinity (2 bars on the right side, $T_{calc.}$ = 550, 625 °C). In Figure 47 b the OER activity of IrO_2/TiO_2 ($TiCl_4$) is shown for low cystallinity (1 bar on the left side, $T_{calc.}$ = 400 °C) and high crystallinity (2 bars on the right side, $T_{calc.}$ = 500, 600 °C). Finally, Figure 47 c depicts the OER activity of IrO_2/TiO_2 (TALH) with low crystallinity (1 bar on the left side, $T_{calc.}$ = 400 °C) and high crystallinity (2 bars on the right side, $T_{calc.}$ = 500, 600 °C).

It is obvious, that materials with a lower degree of crystallinity exhibit a higher OER activity which is in line with the observations made for mesoporous templated IrO_2 in chapter 4.2.4. A high calcination temperature leads to an increase in crystallite size and a decrease in ECSA. It was shown, that ECSA exhibits a severe impact on the OER activity (Figure 46 c). Therefore, the decrease in the OER activity shown in Figure 47 is not solely related to the

change of crystallinity as both, the crystallinity and the ECSA are strongly affected by the applied calcination temperature. Consequently, Figure 47 shows the overlapping influences of a decreasing surface area and an increasing crystallinity on the OER activity of IrO_2 and IrO_2/TiO_2.

For this reason, it appears difficult to investigate mesoporous IrO_2 and IrO_2/TiO_2 with the same active surface area but a different crystallinity. In order to study the influence of ECSA on the OER activity independent of crystallinity, chapter 5.6 shows a variation of the IrO_2 content in TiO_2 calcined at similar temperatures, whereas chapter 5.7 presents an equal heat treated IrO_2 with different layer thickness.

5.6 Influence of electrical conductivity on OER activity

The electrical conductivity can have a tremendous impact on electrons travelling through the catalytic layer, to or away, from active centres. The electron transport is hindered if, for instance, an insufficient degree of electrical conductivity is present, thus causing an additional overpotential in electro catalytic reactions such as the oxygen evolution reaction. The additional overpotential during electrochemical testing is shown for IrO_2/TiO_2 with low iridium loading produced from $Ir(OAc)_3$ and TALH (chapter 4.4). The electrical conductivity of IrO_2/TiO_2 showed a significant increase if a certain amount of conductive iridium is added. This behaviour is in fair good agreement with percolation theory[74, 77] describing the electrical conductivity of randomly packed conductive and insulation particles. A more comprehensive illustration across more systems on the impact of electrical conductivity on intrinsic reactivity is depicted in Figure 48.

Figure 48 shows the OER activity as a function of ECSA for IrO_2/TiO_2 ($Ir(OAc)_3$+TALH, 400 °C) with iridium loadings between a) 0 to 100 wt. % Ir in Ir/TiO_2 and b) 0 to 25 wt. % Ir in Ir/TiO_2. Furthermore, c) depicts the OER activity plotted as a function of electrical conductivity. In order to identify general trends d) shows the OER activity of IrO_2/TiO_2 (synthesized from $Ir(OAc)_3$, and $TiCl_4$ or TALH, respectively) for different iridium loadings calcined at 400 °C, for different calcination temperatures with an iridium loading of 30 wt. % Ir in Ir/TiO_2.
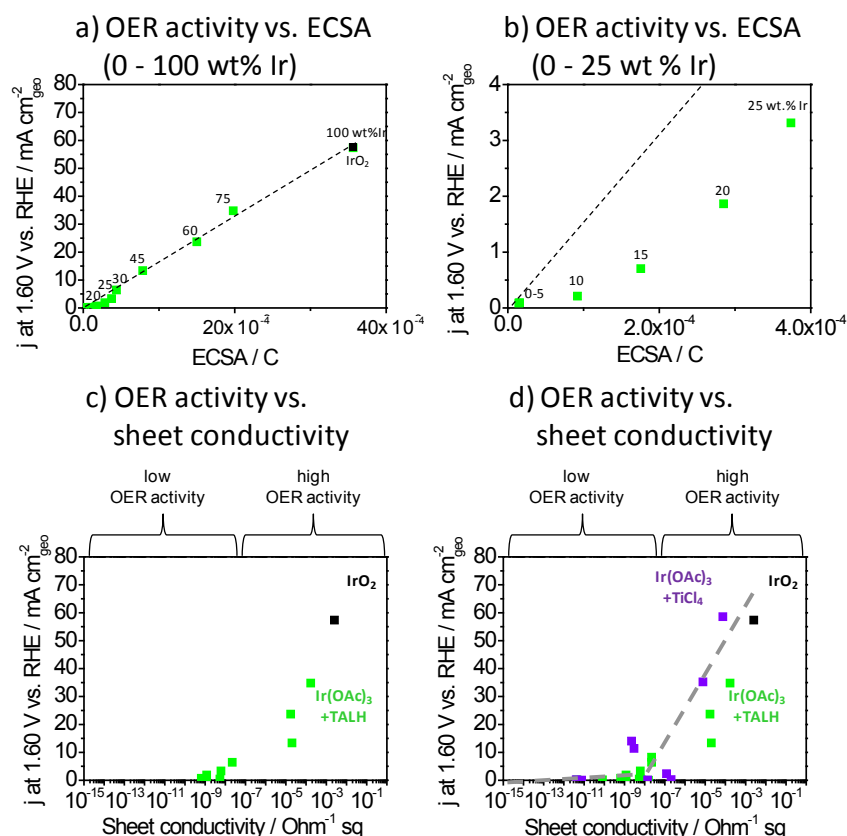
Figure 48: Infuence of a, b) ECSA and c, d) sheet conductivity on the OER activity. For IrO$_2$/TiO$_2$ (produced from Ir(OAc)$_3$ and TALH) the a) OER activity scales linearly in the region of 30 - 100 wt. % Ir. However, a discrepancy from the linear relationship is observed at b) lower loadings of Ir in Ir/TiO$_2$. c) The OER activity further seems to be affected by the electrical sheet conductivity. d) Two regimes are clearly identified if further data points of Ir(OAc)$_3$ + TiCl$_4$ are added.

Figure 48 a shows the OER activity at 1.60 V$_{RHE}$ as a function of ECSA. A linear dependency is present between the OER activity and ECSA for iridium loadings between 30 - 100 wt. % Ir in Ir/TiO$_2$. However, Figure 48 b reveals a discrepancy from the linear fit for samples with loadings between 5 - 25 wt. % Ir in Ir/TiO$_2$. The observed current density is smaller than suggested by the extrapolated linear fit of the 30 - 100 wt. % Ir region.

Figure 48 c depicts as a function of electrical sheet conductivity, the OER activity of IrO$_2$ calcined at 375 °C (50 nm, noted as 100 wt. % Ir in Ir/TiO$_2$), IrO$_2$/TiO$_2$ synthesized from Ir(OAc)$_3$ + TALH calcined at 400 °C with loadings between 0 - 75 wt. % Ir and loadings of 30 wt. % Ir calcined between 200 - 600 °C, respectively. The sheet conductivity was determined by a sheet resistivity measurement of IrO$_2$/TiO$_2$ on insulating glass substrates (microscope slides). The values are not corrected for layer thickness. However, systems obtained under these synthesis conditions typically exhibit layer thicknesses between 50 and 100 nm. Hence, the small difference in layer thickness does not affect the observed relationships as the x-axis is depicted logarithmically. It is clear to see that the observed OER

activity is low until the sheet conductivity reaches values of ca. 10^{-8} (Ohm/sq)$^{-1}$. For samples with higher values, the OER activity seems to be dependent on the electrical conductivity.

In order to provide a comprehensive comparison, Figure 48 d contains in addition to Figure 48 c data points from IrO_2/TiO_2 synthesized from $Ir(OAc)_3$ + $TiCl_4$ calcined at 400 °C with loadings between 15 - 75 wt. % Ir and loadings of 30 wt. % Ir calcined between 200 - 600 °C, respectively. These data points reveal the presence of two regimes i) a low OER activity for samples with a conductivity below ca. 10^{-8} (Ohm/sq)$^{-1}$, and ii) a high OER activity for samples with values exceeding ca. 10^{-8} (Ohm/sq)$^{-1}$.

The present data lead to the following thoughts. The iridium content is an important parameter that influences the electrical conductivity (Figure 31 b, Figure 37 b). Samples with a low amount of iridium oxide show a low electrical conductivity which might be insufficient, thus not providing a fast electron transport through the layer. In order to underline this assumption, measurements regarding the electron transport were conducted for IrO_2/TiO_2 with different iridium loadings in the ECSA regime between 0.40 - 1.40 V_{RHE} (Figure 38 c). The pronounced oxidation and reduction waves were assigned to the Ir^{III}/Ir^{IV} redox couple. The redox waves of samples with lower iridium loadings were far off the equilibrium potential (Figure 38 b), indicating an insufficient degree of electrical conductivity. Usually, an insufficient electrical conductivity causes an additional overpotential that most likely affects the intrinsic reactivity of active iridium centres. The number of active Ir centres (e.g. wt. % Ir in Ir/TiO_2) scale linear with the ECSA. Moreover, the ECSA should exhibit a linear relationship with the OER activity. If any other process than the surface reaction, such as gas transport through the pore system or electron conduction to the active site, was the limiting step, a deviation from the linear behavior would be expected. Samples of IrO_2/TiO_2 with high Ir loadings (> 30 wt. % Ir) show a linear dependency between the OER activity and ECSA at relatively high current densities (ca. 60 mA/cm²), thus excluding transport limitation effects (Figure 48 a). However, loadings lower than 30 wt. % Ir in Ir/TiO_2 show a discrepancy from the extrapolated linear fit for the higher iridium loading regime suggesting an insufficient degree of conductivity (Figure 48 b). A hindered electron transport through the layer can be assumed which causes the reduction of the intrinsic reactivity of active iridium centres.

An increase in Ir content leads to a higher sheet conductivity (Figure 31 b, Figure 37 b), higher ECSA (Figure 38 c, Figure 48 a), and higher OER activity (Figure 39 b, Figure 48 a). However, the linear dependency of OER activity and ECSA is still observed with increasing sheet conductivity (Figure 48 a and c). This suggests that samples with loadings of at least 30 wt. % Ir in Ir/TiO_2 and/or a sheet conductivity higher than approximately 10^{-8} (Ohm/sq)$^{-1}$ (ca. 0.1 S/m) do not suffer from an additional voltage drop over the layer. If a sufficient electrical conductivity is provided, the OER activity linearly scales with the ECSA and ensures the same intrinsic reactivity for active Ir centres dispersed in TiO_2 as for "pure" IrO_2.

5.7 Influence of layer thickness on gas removal rate

The active surface area is expected to scale linear with the amount of active sites, whereas the amount of active sites can be adjusted with, e.g. the iridium loading in TiO_2 (Figure 48 a) or the layer thickness of a homogenous prepared catalytic layer (this chapter). A deviation of the linear dependency between OER activity and ECSA at higher geometrical current densities is therefore associated with a sign of transport limitation of produced O_2 within the pore system. In order to investigate transport limitations mesoporous templated layers of IrO_2 coated on titanium cylinders were used as a model system. Different layer thicknesses between 50 - 225 nm were obtained by dipcoating at withdrawal rates between 10 and 150 mm/min, respectively. Thicker layers could not be obtained with single layer dipcoating since peeling off from the substrate occured. To solve this problem, multi-layer dipcoating was used. 4 single layers on titanium substrate were deposited at a withdrawal rate of 30 mm/min and intermediate calcination steps at 200 °C followed by a final heat treatment for 5 min at 375 °C. The layer thicknesses of the corresponding samples were obtained by SEM (Figure 25 a). Figure 49 shows as a function of layer thickness the a) OER activity and b) ECSA. In order to identify if transport limitation is present the c) OER activity is shown as a function of ECSA. For different layer thicknessses the d) Tafel plots, e) kink potentials and the f) corresponding Tafel slopes are evaluated.
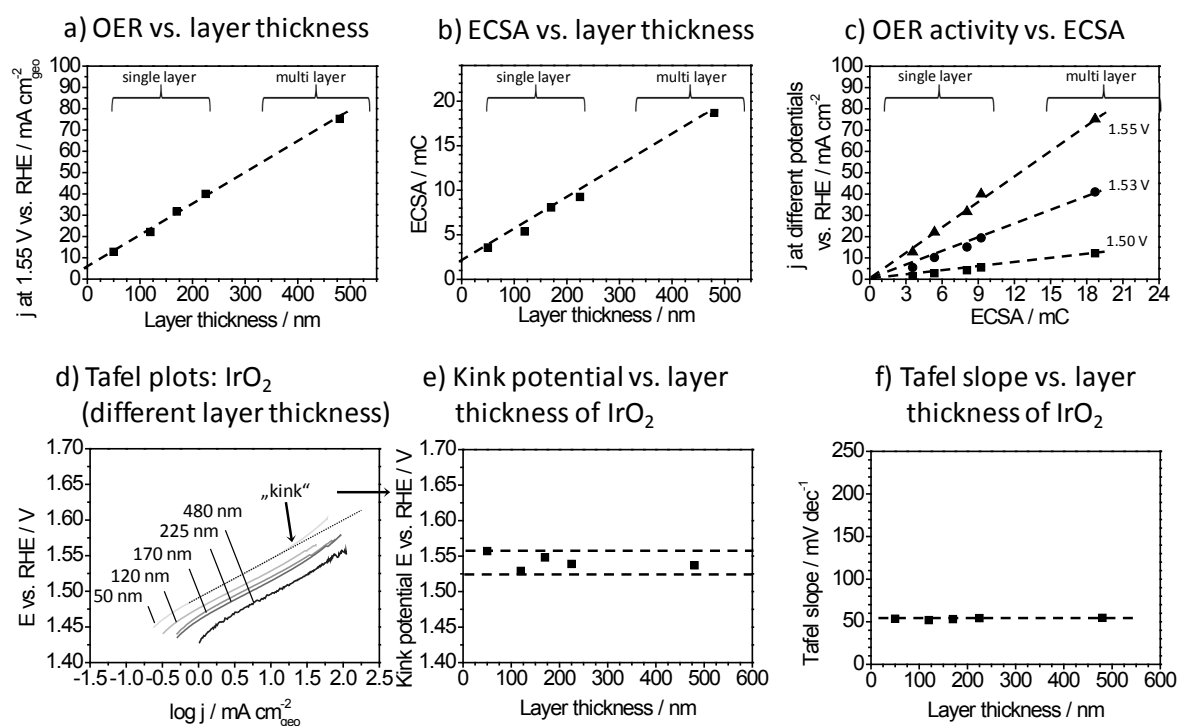
Figure 49: Single layer and multi layer dipcoating techniques were applied in order to obtain mesoporous IrO_2 with different layer thicknesses. The influence of layer thickness is depicted on a) OER activity and b) ECSA. To investigate the gas removal within the pore system c) the OER activity is plotted as a function of ECSA. Kinetical aspects are studied by interpreting the d) Tafel plots in terms of e) kink potential and f) Tafel slopes.

The OER activity of IrO_2 coated on titanium was quantified by measuring the normalized geometrical current density at potentials of 1.55 V_{RHE}. The determined OER activity as a function of layer thickness in Figure 49 a depicts a clear linear correlation. The influence of layer thickness on ECSA is shown in Figure 49 b. Both, OER activity and ECSA show a linear behaviour strongly suggesting that the complete film volume is available as the active surface area contributes to the electrocatalytic oxygen evolution. In order to underline this assumption, the OER activity is shown as a function of ECSA in Figure 49 c. The derived OER activity at 1.55 V_{RHE} scales linearly with the determined ECSA. Regardless of film thickness each surface site thus contributes equally to the OER reaction, even for thicker films and higher current densities. If any other process than the surface reaction such as gas transport through the pore system, was the limiting step, a deviation from the linear behavior would be expected for thicker films at least for higher potentials and current densities. As this is not the case, transport limitations are absent in the case of iridium oxide catalyst films with templated mesopores of at least up to 480 nm in thickness, at potentials of 1.55 V_{RHE} and current densities as high as 75 mA per cm^2 of the planar electrode surface.

The Tafel plot is often used to investigate catalytic properties such as the i) rate determining step of a postulated OER mechanism, ii) appearance of transport limitation of produced O_2 gas, as well as iii) limited electron transport through catalytic layers. Figure 49 d show Tafel plots for IrO_2 with different layer thicknesses. The natural logarithm of the current density from the respective 2nd iR corrected CV recorded in the OER potential window between 1.20 - 1.65 V_{RHE} (Figure 25 c) has been used. However, only the corresponding current densities at potentials higher than ca. 1.43 V_{RHE} are shown (Figure 49 d), to only include potentials that are causing currents attributed to the oxygen evolution reaction. The cyclic voltammograms (Figure 25 c) and the derived Tafel plots (Figure 49 d) show a shift to lower overpotentials for samples with higher layer thicknesses. The observed Tafel plots exhibit an almost linear behaviour between E and log j at lower potentials (ca. 1.47 - 1.52 V_{RHE}). However, higher overpotentials strongly increase the Tafel slopes and produce "kinks" in the Tafel plot. In order to investigate the potential and the current density at which the kink appears, a formal criterion is defined: If the slope exceeds values greater than 1.1 times the Tafel slope, a kink occurs (the first derivative of the Tafel plot was used for quantification, Figure A5 a)

Figure 49 e shows the determined kink potentials with respect to the layer thickness of IrO_2. The kinks occur independently of the layer thickness between 1.53 - 1.56 V_{RHE}. It is unlikely that the increase in Tafel slope is related to a limited electron transport through the layer since IrO_2 shows metallic conductivity. When considering the linear relationship between OER activity and ECSA even at high current densities (75 mA/cm²), the increase in Tafel slope can also not be due to the transport limitation of produced O_2 within the pore system. The determined corresponding current densities at the kinks underline this assumption, as

they appear to scatter around comparable low and high current densities (kink current densities: 50 nm: 12.8 mA/cm²; 480 nm: 75.2 mA/cm²).

If the Tafel slope in the linear region is plotted as a function of layer thickness (Figure 49 f), it attains a value of 52 - 55 mV/dec regardless of layer thickness and current density. If mass transport limitation within the mesopore system is present, an increase in Tafel slope is expected as the gas removal becomes the rate determining step. However, this is not the case for IrO_2 with different layer thicknesses at high current densities. The derived Tafel slopes are in good agreement with reports in literature for thermally prepared iridium oxide: 40 - 60 mV/dec.[64, 126, 159] Moreover, it was reported that metallic iridium oxidized under acidic OER conditions and exhibits similar Tafel slopes as thermally prepared iridium oxide: 40 - 60 mV/dec. [153, 160] Recently, Oezer et al.[137] published Tafel slopes for oxidized Ir(111)/(110) single crystals. At lower potentials (1.52 - 1.58 V_{RHE}) the Tafel slope amounts to 60 mV/dec and 64 mV/dec for Ir(111) and Ir(110), respectively. However, sweeping to potentials higher than 1.58 V_{RHE} strongly increases the Tafel slope for both oxidized iridium single crystals (Ir(111): 89 mV/dec, Ir(110): 83 mV/dec). The current densities measured at kinks are too low (1 mA/cm²) for mass transport limitations.

In order to explain the increase in Tafel slopes at higher potentials McCrory et al.[38] has stated the following: i) potential-dependent changes in the rate-determining step of the catalytic mechanism, ii) repulsion of between adsorbed intermediates (which can be more distinct at larger overpotentials due to a larger coverage of intermediates), and iii) blocking of active sites by unreactive species.

These assumptions might be related, in the case of IrO_2, to structural changes during OER. Minguzzi et al.[161-162] reported, that Ir^{IV} slowly starts to transform to Ir^{V} at potentials around 1.30 V_{RHE}. The transformation is accelerated with higher potentials, whereas a significant amount of Ir^{V} is present at potentials around 1.50 V_{RHE}. The transformation of Ir^{IV} to Ir^{V} at higher potentials was further observed by the group of Nilsson.[163-164]

Based on the availability of data, we hypothesize that the transformation to higher oxidative states of iridium at higher potentials leads to structural modifications which possibly affect the rate determining step within the OER mechanism and strongly increases the Tafel slope.

In the current chapter (5.7) a linear relationship between OER activity and ECSA as a function of layer thickness was established. Therefore, mass transport limitations were excluded even at high layer thickness (480 nm) and high current density (75 mA/cm²). The derived Tafel slopes were not only independent of the layer thickness and current densities, with values as high as 52 - 55 mV/dec, but further excluded the presence of transport limitations. However, applying high electrical potentials progressively increased the Tafel slope possibly due to the transformation of Ir^{IV} to Ir^{V}, along with structural modifications changing the rate determining step within the OER mechanism.

5.8 Tafel slope as a function of calcination temperature and potential

Changes in morphology and electrical conductivity as a function of calcination temperature can now be related to electrochemical properties. Therefore, the Tafel plots of IrO_2 and IrO_2/TiO_2 were derived. Figure 50 presents the Tafel plots for different calcined samples containing a) IrO_2, b) IrO_2/TiO_2 ($Ir(OAc)_3+TiCl_4$) and c) IrO_2/TiO_2 ($Ir(OAc)_3+TALH$). A further evaluation of the Tafel plots reveal for all samples, the d) kink potentials and e) Tafel slopes as a function of calcination temperature.
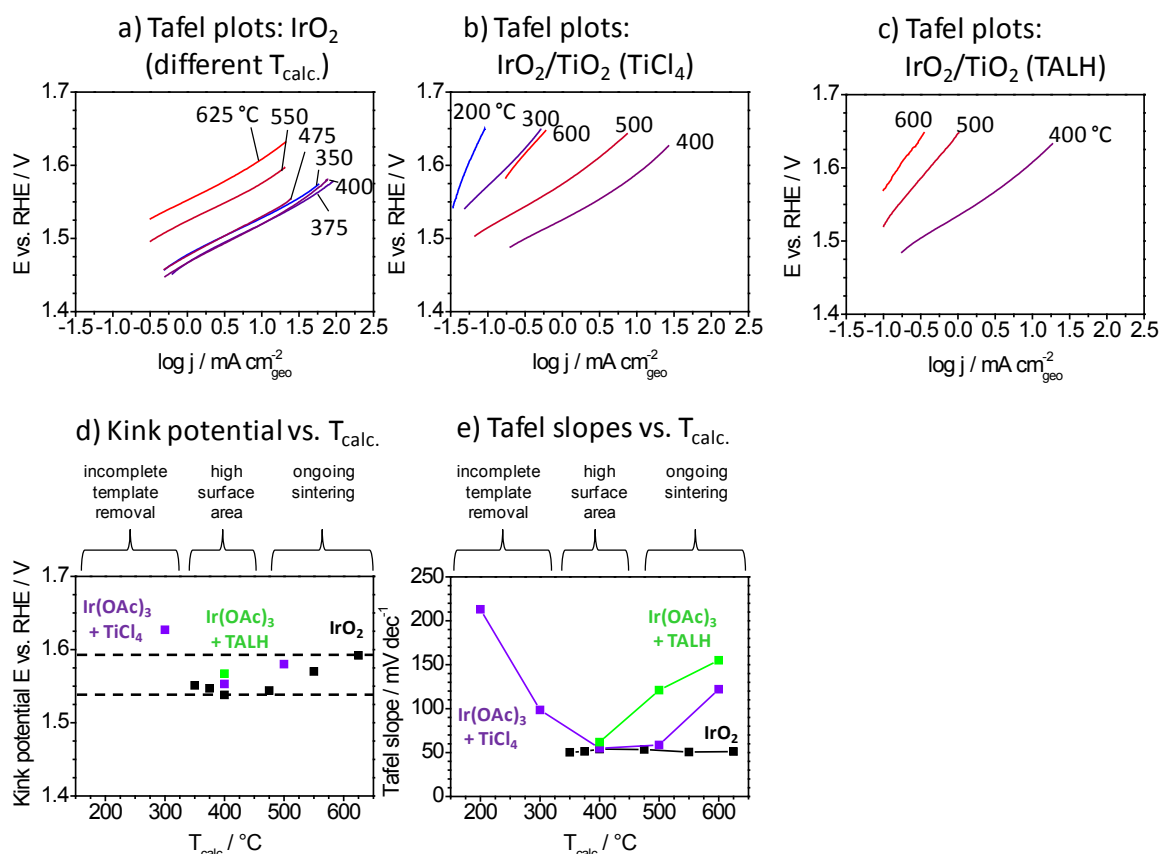
Figure 50: Tafel plots are presented for different calcined a) IrO_2, b) IrO_2/TiO_2 produced from $TiCl_4$ (30 wt. % Ir) and c) IrO_2/TiO_2 derived by TALH (30 wt. % Ir). For all investigated systems the observed d) kink potentials and e) Tafel slopes with respect to the applied calcination temperature are shown. All Tafel plots were derived from the upscan of the 2nd iR corrected CV (6 mV/s, 0.5 M H_2SO_4, 1600 rpm).

Figure 50 a shows that different heat treated IrO_2 exhibit similar Tafel slopes in the range between 50 - 54 mV/dec being in line with slopes reported for thermally prepared IrO_x (40 - 60 mV/dec).[64, 126, 159] A steady increase of the Tafel slope is observed at higher potentials producing kinks. The kinks were quantified (according to a procedure described in chapter 5.7) and show the following values: 1.55 V_{RHE} (350 °C), 1.55 V_{RHE} (375 °C), 1.54 V_{RHE} (400 °C), 1.54 V_{RHE} (475 °C), 1.57 V_{RHE} (550 °C), 1.59 V_{RHE} (625 °C).

Figure 50 b depicts the Tafel plots of IrO_2/TiO_2 synthesized from $Ir(OAc)_3$ and $TiCl_4$ which were thermally treated at different temperatures. The overpotential decreases with respect to

the calcination temperature between 200 to 400 °C. A further increase of calcination temperature to values exceeding 500 °C reveals a progressive increase in overpotential. The Tafel slope follows a very similar trend as observed for the overpotential. A steady decline is noted for increasing temperatures of 200 °C (213 mV/dec) over 300 °C (98.5 mV/dec) to 400 °C (54.8 mV/dec). A successive increase is observed for higher calcination temperatures such as 500 °C (58.6 mV/dec) and 600 °C (122 mV/dec). Moreover, only samples heat treated at 300 °C (1.63 V_{RHE}), 400 °C (1.55 V_{RHE}) and 500 °C (1.58 V_{RHE}) depict a kink potential according to the previously defined criterion.

Figure 50 c shows Tafel plots for different heat treated IrO_2/TiO_2 ($Ir(OAc)_3$ + TALH). Samples calcined between 200 and 300 °C reveal Tafel slopes exceeding 2000 mV/dec. Therefore, the respective samples are not considered in the discussion as the occuring current most likely is not related to the oxygen evolution reaction. The lowest overpotential is observed for samples heat treated at 400 °C and steadily increases when moving to higher temperatures: 400 °C (62 mV/dec), 500 °C (121 mV/dec) and 600 °C (155 mV/dec). However, only samples calcined at 400 °C depict a kink potential as high as 1.57 V_{RHE}.

In order to deduce global trends, Figure 50 d presents the observed kink potentials of all systems with respect to the calcination temperature. The kink potentials of all systems occur between 1.54 - 1.59 V_{RHE} (Note: $Ir(OAc)_3$+$TiCl_4$ calcined at 300 °C still contains polymer template and is not considered in the discussion). The respective kink potentials of IrO_2 show a slight increase as the calcination temperature is increased. A similar trend is observed for IrO_2/TiO_2 derived by $Ir(OAc)_3$ + $TiCl_4$ as the kink potential increases from 400 to 500 °C. The kink potential of $Ir(OAc)_3$ + TALH calcined at 400 °C is found in similar regions such as for similar calcined IrO_2. The combined data of all systems reveal a slight increase in the kink potential as a consequence of increasing calcination temperatures. The behaviour of the kink potentials might be associated with the higher degree of crystallinity. If the kink is somehow related to the transformation of Ir^{IV} to Ir^{V},[161-164] possibly more crystalline materials are in need of more energy (thus a higher potential) to undergo that transformation and cause a strong increase in the Tafel slope. However, no other data were derived in order to underline this theory. The observed kink potentials for IrO_2 and IrO_2/TiO_2 as a function of applied calcination temperature are reasonable in line with reports from literature for single crystals of Ir(111) and Ir(110) (both ca. 1.58 V_{RHE}).[137]

In Figure 50 e the Tafel slopes are plotted as a function of calcination temperature. Interestingly, the Tafel slope of IrO_2 seems to be independent of the applied calcination temperature suggesting that structural modifications such as crystallinity are not sufficient enough to change the rate determining step within the OER mechanism. Scheuermann et al.[153] deposited different layer thicknesses of TiO_2 by ALD on oxidized silicon substrates and subsequently applied iridium as a catalyst onto TiO_2 by PVD. The investigated

electrocatalytic performance in the OER regime as a function of TiO_2 layer thickness revealed an increase in Tafel slope for samples with a TiO_2 layer thickness greater than 2 nm. The increase in Tafel slope is related to a hindered electron transport process through the layer as a consequence of a lowered electrical conductivity. Therefore, we assume that the constant slope of IrO_2 as a function of calcination temperature indicates the absence of a significant oxidation of the underlying titanium substrate. This behaviour is in line with reports from the literature claiming that titanium covered by "thick" layers of IrO_2 is shielded towards oxidation.[57]

In the case of IrO_2/TiO_2 either produced from $Ir(OAc)_3$ + $TiCl_4$ or $Ir(OAc)_3$ + TALH, the Tafel slope remains high at calcination temperatures below 400 °C (Figure 50 e). In addition, the ECSA (Figure 46 b), OER activity (Figure 46 a), and electrical conductivity (Figure 28 d, Figure 34 d) of the corresponding samples appear low indicating incomplete template removal. If the calcination temperature is increased to 400 °C, the polymer template seems to be fully removed. Hence, an accessible pore system is observed with the capability to provide a high OER activity (Figure 46 a). The observed Tafel slopes of such systems are comparable to slopes determined for "pure" mesoporous templated IrO_2. A further increase in calcination temperature steadily increases the Tafel slope of IrO_2/TiO_2. For IrO_2 it was found that different calcination temperature, thus crystallinity does not significantly affect the Tafel slopes (Figure 50 e). Under the assumption that this finding is valid for systems with mixed metal oxides, the increase in Tafel slope is possibly related to the interaction between iridium oxide and titanium oxide which form solid solutions at higher calcination temperatures (Figure 28, Figure 34). This behaviour possibly changes the catalytic reactivity of iridium centres in a way that an increase in the Tafel slope is the consequence.

5.9 Investigation of Tafel slopes as a function of iridium loading and potential

In order to evaluate the influence of iridium loading on the Tafel slopes, and kink potentials Figure 51 shows Tafel plots of samples with different iridium loadings, such as IrO_2/TiO_2 produced by a) $Ir(OAc)_3$ + $TiCl_4$ and b) $Ir(OAc)_3$ + TALH (Note: 100 wt. % Ir in Ir/TiO_2 describes "pure, titanium free" IrO_2). In addition, for all systems the observed c) kink potentials and d) quantified Tafel slopes are shown.
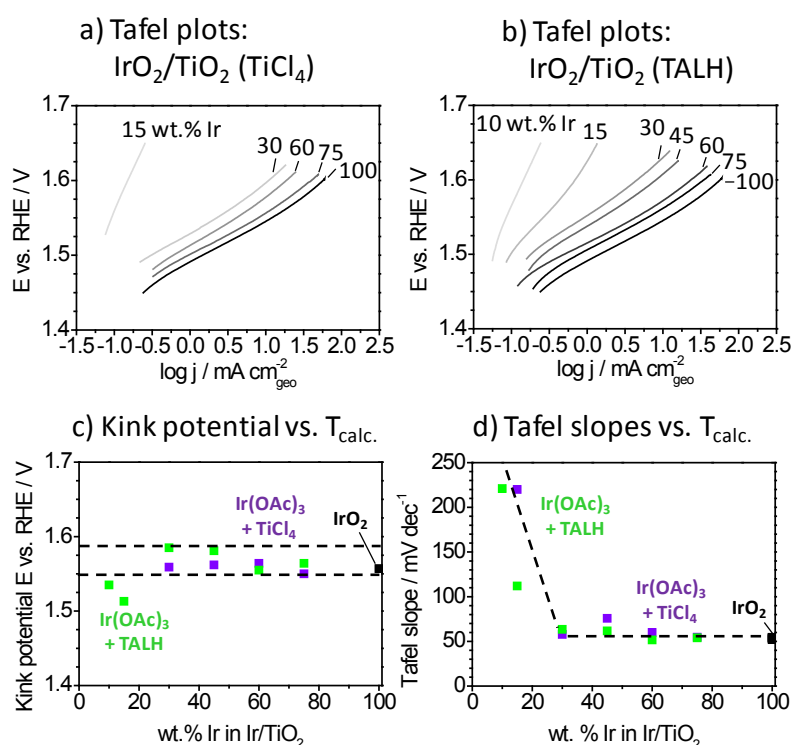
Figure 51: The anodic scan of the 2nd iR corrected CVs are illustrated as Tafel plots for thermally prepared (400 °C) a) IrO_2/TiO_2 from $Ir(OAc)_3$ + $TiCl_4$ and b) IrO_2/TiO_2 obtained with $Ir(OAc)_3$ + TALH. Moreover, the quantification of observed c) kink potentials and d) Tafel slopes are shown. (1.20 - 1.65 V_{RHE}, iR corrected, 0.5 M H_2SO_4, 6 mV/s, 1600 rpm)

For IrO_2/TiO_2 ($Ir(OAc)_3$ + $TiCl_4$) Figure 51 a shows that the Tafel slopes drastically decrease from 220 mV/dec (15 wt. % Ir in Ir/TiO_2) to 58 mV/dec (30 wt. % Ir) and remain constant against a further increase in iridium content: 60 mV/dec (60 wt. % Ir), 55 mV/dec (75 wt. % Ir), 53 mV/dec (100 wt. % Ir equals to 50 nm IrO_2). Moreover, a steady increase of the Tafel slope with higher applied potentials is observed as a kink. The kinks occur at defined potentials which were quantified according to a criterion introduced in chapter 5.7. The observed kink potentials are as followed: 1.56 V_{RHE} (30 wt. % Ir), 1.56 V_{RHE} (60 wt. % Ir), 1.55 V_{RHE} (75 wt. % Ir), 1.58 V_{RHE} (100 wt. % Ir).

In analogy, Figure 51 b presents the Tafel plots of IrO_2/TiO_2 obtained from $Ir(OAc)_3$ + TALH. A similar trend is shown with the Tafel slope which strongly decreases from 211 mV/dec (10 wt. % Ir in Ir/TiO_2) over 112 mV/dec (15 wt. % Ir) to 63 mV/dec (30 wt. % Ir). A further

increase in the iridium content reveals no significant influence on the Tafel slope: 62 mV/dec (45 wt. % Ir), 52 mV/dec (60 wt. % Ir), 54 mV/dec (75 wt. % Ir) and 53 mV/dec (100 wt. % Ir). The observed kinks in the Tafel plots were quantified (criterion from 5.7) and occur at the following potentials: 1.54 V_{RHE} (10 wt. % Ir in Ir/TiO$_2$), 1.51 V_{RHE} (15 wt. % Ir), 1.59 V_{RHE} (30 wt. % Ir), 1.58 V_{RHE} (45 wt. % Ir), 1.56 V_{RHE} (60 wt. % Ir), 1.56 V_{RHE} (75 wt. % Ir) and 1.58 V_{RHE} (100 wt. % Ir).

In order to deduce general trends Figure 51 c shows all observed kink potentials for IrO$_2$/TiO$_2$, either derived by Ir(OAc)$_3$ + TiCl$_4$ or Ir(OAc)$_3$ + TALH, as a function of iridium loading. It is clearly visible that kink potentials for samples with loadings of 10 and 15 wt. % Ir in Ir/TiO$_2$ appear to be significantly lower than for higher loadings. As suggested by Figure 48, samples with low iridium loadings suffer from a hindered electron transport processes through the layer which possibly affects the kink potential. However, if the iridium content exceeds 30 wt. % Ir, the kink potentials are located in the same region as they are for 100 wt. % Ir ("pure" IrO$_2$) and are related to changes in the rate determining step of the OER mechanism affected by the transformation of Ir^{IV} to Ir^{V}.[38, 161-163]

Interestingly, the Tafel slopes depict a complementary behaviour (Figure 51 d) as they steadily decrease with increasing iridium loadings from 10 to 30 wt. % Ir, but do not change significantly with further increasing iridium. The higher Tafel slope for layers with low iridium loadings is related to an insufficient degree of electrical conductivity as electrons travelling through the layer away from the catalytic centre are delayed.[153] Moreover, the Tafel slope of IrO$_2$/TiO$_2$ appears to be independent of morphological aspects as it is not changing with different TiO$_2$ precursors as long as a sufficient degree of conductivity is provided. Layers of IrO$_2$/TiO$_2$ derived by Ir(OAc)$_3$ + TiCl$_4$ show largely segregated areas with ca. 100 nm in diameter (Figure 43 p), whereas IrO$_2$/TiO$_2$ obtained with Ir(OAc)$_3$ + TALH only depict small segregated domains of IrO$_2$ with ~2 nm (Figure 43 u), thus providing a more homogenous morphology.

5.10 Deduced structure-activity relations

In the upcoming chapter all findings of this thesis are summarized in one scheme. It reflects all investigated OER-controlling parameters (Figure 52 a), which were identified by a controlled variation of different paramaters within the synthesis procedures (Figure 52 b), and all electrocatalytic investigations (Figure 52, right column). The structure is affected by these parameters leading to two possible conditions (Figure 52 c and d). By investigating the OER activity of both conditions, structure-activity relations are deduced (Figure 52 e).

Deduced structure-activity relations

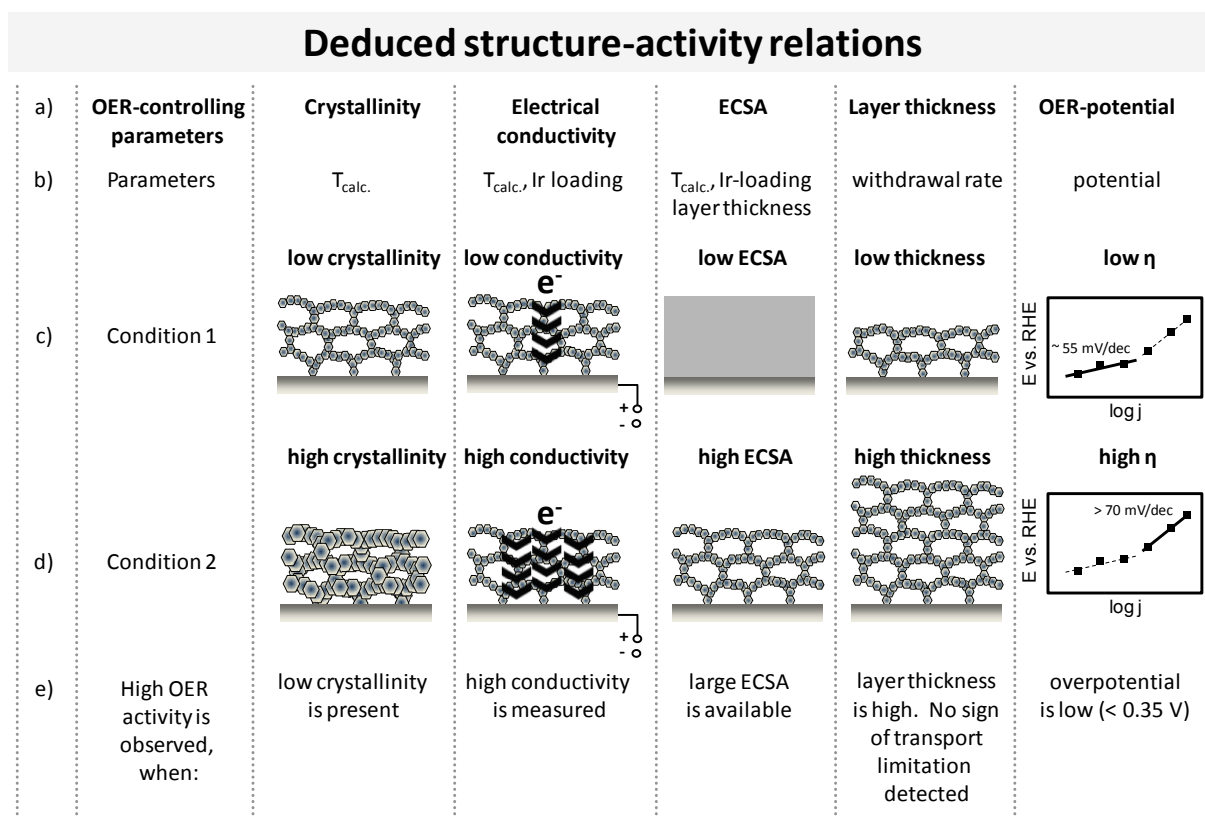| a)	OER-controlling parameters	Crystallinity	Electrical conductivity	ECSA	Layer thickness	OER-potential
b)	Parameters	$T_{calc.}$	$T_{calc.}$, Ir loading	$T_{calc.}$, Ir-loading layer thickness	withdrawal rate	potential
c)	Condition 1	low crystallinity	low conductivity	low ECSA	low thickness	low η
d)	Condition 2	high crystallinity	high conductivity	high ECSA	high thickness	high η
e)	High OER activity is observed, when:	low crystallinity is present	high conductivity is measured	large ECSA is available	layer thickness is high. No sign of transport limitation detected	overpotential is low (< 0.35 V)

Figure 52: Different OER-controlling parameters were identified in the thesis (Figure 51 a). The OER-controlling parameters are affected by parameters (Figure 51 b) varied during synthesis ($T_{calc.}$, Ir-loading, withdrawal rate) or electrocatalytic testing (applied potential). The parameters affect the resulting structure and lead to two possible conditions (Figure 51 c, Figure 51 d). The electrocatalytic performance of both conditions was correlated in order to deduce structure-activity relations (Figure 51 e).

Calcination temperature highly affects crystallinity ($Ir(OAc)_3$: Figure 24, $Ir(OAc)_3$ + $TiCl_4$: Figure 28, $Ir(OAc)_3$+TALH: Figure 34). The degree of crystallinity within a sample is either characterized as low (XRD amorphous) or high (XRD reflections). An increase of calcination temperature leads to enhanced crystallinity (Figure 24, Figure 28, Figure 34) and lowers the ECSA (Figure 46 b). It was observed that samples with a low crystallinity exhibit a higher overall OER activity than crystalline materials (Figure 46). However, a material with low crystallinity is also characterized by a high ECSA. The observation in Figure 46 thus shows the overlapping effects of crystallinity and ECSA on OER activity.

The electrical conductivity of layers coated on substrates is affected by two independent synthesis parameters: the applied calcination temperature ($IrOAc)_3$ + $TiCl_4$: Figure 28, $Ir(OAc)_3$ + TALH: Figure 34) and the Ir loading ($IrOAc)_3$ + $TiCl_4$: Figure 31, $Ir(OAc)_3$ + TALH: Figure 37). A controlled variation of the calcination temperature simultaneously modified crystallinity, electrical conductivity and accessible active surface area. Therefore, a variation of the calcination temperature appears inappropriate in order to investigate the influence of electrical conductivity on intrinsic reactivity separately. Therefore, the Ir content within TiO_2 was varied, producing a lower intrinsic reactivity (Figure 48) as well as higher Tafel slopes

(Figure 51) for samples with loadings lower than 30 wt. % Ir in Ir/TiO_2. Layers with Ir loadings higher than 30 wt. % Ir in Ir/TiO_2 exhibit the same intrinsic reactivity and Tafel slopes as for "pure" mesoporous templated IrO_2. The combined data suggest that a distinct electron transport mechanism is present for samples with an insufficient electrical conductivity.

The active surface area is affected by the i) calcination temperature (Figure 46), ii) layer thickness (Figure 49), and iii) iridium loading within TiO_2 (Figure 48). All synthesis parameters were varied and the resulting OER activities and active surface areas were investigated. The combination of all obtained data suggests that if a sufficient degree of conductivity is provided (> 30 wt. % Ir/TiO_2, 0.1 S/m) the OER activity scales with the ECSA suggesting that the ECSA must be one of the most relevant OER-controlling parameter.

The O_2 evolution was investigated for layers consisting of mesoporous templated IrO_2. The ECSA and OER activity scaled linear with the layer thickness. In order to obtain samples with different layer thicknesses, a controlled variation of the withdrawal rate during dipcoating was carried out. If any other process than the surface reaction, such as gas transport through the pore system, was the limiting step, a deviation from the linear behavior between OER activity and ECSA would be expected. As this is not the case (Figure 49), the transport is not limited in the case of iridium oxide catalyst films with templated mesopores of at least 480 nm in thickness, at potentials of 1.55 V_{RHE} and current densities of 75 mA/cm².

The influence of the OER-controlling parameters on observed Tafel slopes were investigated for layers consisting of IrO_2 and IrO_2/TiO_2. Within the investigated paramater range, the Tafel slopes of IrO_2 are unaffected by layer thickness (Figure 49), and calcination temperature (Figure 50). The constant Tafel slopes as a function of layer thickness confirm the absence of mass transport limitations. The steadiness of the slopes as a function of calcination temperature can be related to the prevented oxidation from the underlying Ti substrate and that crystallinity seems not to change the rate determining step in the OER kinetics.

The Tafel slope of mixed metal oxides such as IrO_2/TiO_2 shows very similar values as for IrO_2 with a loading of at least 30 wt. % Ir in Ir/TiO_2 (Figure 51). The higher Tafel slope for lower loadings is associated with a different electron transport mechanism most likely induced by an insufficient degree of electrical conductivity. If the calcination temperature is lower than 300 °C, the samples suffer from incomplete template removal thus causing a higher Tafel slope as for samples calcined at 400 °C. Calcination at temperatures higher than 500 °C results in an increased Tafel slope and is related to crystallisation and the beginning formation of solid solutions containing IrO_2 and TiO_2. The formation of a solid solution seems to be unfavorable for the preparation of highly active OER electrocatalysts. At higher potentials of ca. 1.55 - 1.60 V_{RHE}, the Tafel plots exhibit an increased Tafel slope which is related to a change in the rate determining step of the OER kinetics. We associate the increase to the beginning transformation of Ir^{IV} to Ir^{V}.

5.11 Comparison of iridium-mass based OER activity

Chapter 5.11 presents a comparison of the iridium mass base related OER activity between a) commercial catalysts and b) new mesoporous catalysts of this work. a) The reference catalysts were deposited on titanium via an "ink"-procedure (chapter 4.5). The iridium mass was determined by the volume drop-casted onto the substrate and the powder concentration within the ink. b) IrO_2 and IrO_2/TiO_2 with a high expected activity according to Figure 52 (low crystallite size, sufficient electrical conductivity, high ECSA) were synthesized by dipcoating a solution containing PEO-PB-PEO and different metal oxide precursors (e.g. $Ir(OAc)_3$, $TiCl_4$, TALH) onto titanium sheets. The final catalysts were obtained by a subsequent heat treatment at temperatures between 375 and 400 °C. In order to determine the OER activity and the iridium mass before catalytic testing, each coated titanium sheet was blanked out twice. For each catalytic system this technique provides two identical specimen with equal geometrical iridium loading. The first specimen was dispersed in aqua regia and subsequently treated in the micro wave to dissolve iridium oxide. The iridium mass was finally quantified by ICP-OES. The second specimen and the commercial catalysts were used as working electrodes.

Figure 53 shows SEM images of a) dropcasted inks of commercial catalysts onto titanium cylinders and b) new mesoporous templated catalytic coatings of IrO_2 and IrO_2/TiO_2. The iridium mass based OER activity is included for the 50th and 100th CVs. On top of each column the factors denote the relative iridium mass based OER activity of IrO_2 powder, IrO_2/TiO_2 ($Ir(OAc)_3$+$TiCl_4$), IrO_2/TiO_2 ($Ir(OAc)_3$+TALH) and IrO_2 ($Ir(OAc)_3$) with respect to commercial available IrO_x/TiO_x powder.
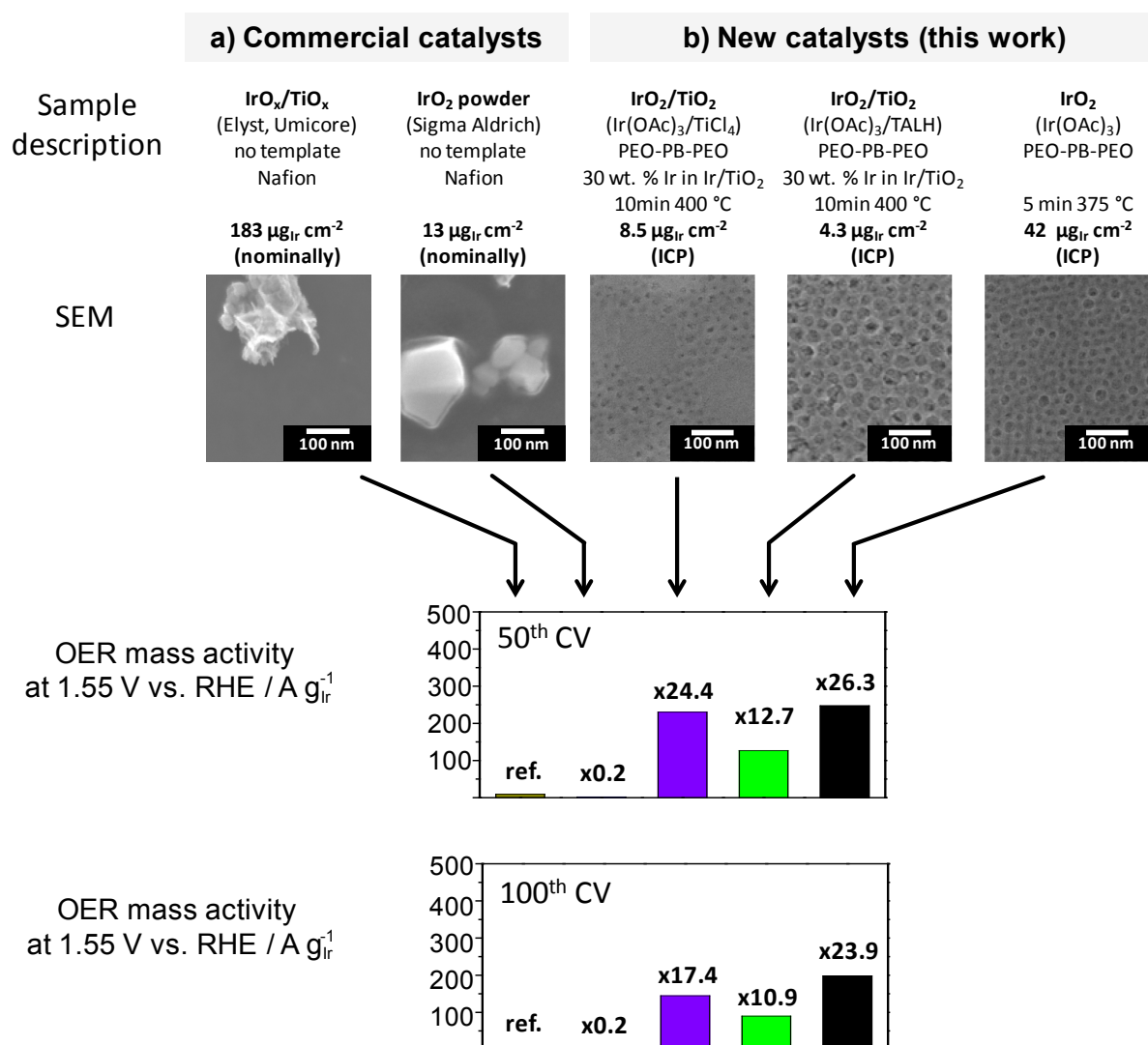
Figure 53: Investigation of morphology and iridium mass based OER activity for a) commercial catalysts (IrO$_x$/TiO$_x$ and IrO$_2$ powder) and b) new catalysts with templated mesoporous structure (IrO$_2$/TiO$_2$ (Ir(OAc)$_3$ + TiCl$_4$), IrO$_2$/TiO$_2$ (Ir(OAc)$_3$ + TALH) and IrO$_2$ (Ir(OAc)$_3$)). SEM images were obtained for inks dropcasted on titanium cylinders and for mesoporous coatings on titanium sheets subsequent to heat treatment at 400 °C and 375 °C, respectively. The morphology of commercial systems and mesoporous catalytic coatings appear to be different in terms of porosity and homogeneity. The iridium mass before catalytic testing was derived a) nominal and b) by ICP-OES. The OER activity was accessed by cyclic voltammetric measurements in 0.5 M H$_2$SO$_4$ and 1600 rpm within a potential window of 1.20 - 1.65 V$_{RHE}$ (6 mV/s). The current measured at 1.55 V$_{RHE}$ during the anodic scans of the 50th and 100th CVs were normalized to the derived iridium mass. The factors on top of each column respresent the relative activity with respect the reference system (ref.: IrO$_x$/TiO$_x$).

The stripes with brighter and darker appearance in the derived SEM images of dropcasted inks for commercial IrO$_x$/TiO$_x$ powders can be related to edge effects suggesting textural roughness on the outer surface area (Figure 53 a). In contrast, IrO$_2$ powders depict larger areas with similar brightness. The absence of brightness variations is often related to a smooth surface area appearing for materials with a higher degree of crystallinity. However,

PEO-PB-PEO templated samples clearly (Figure 53 b) reveal homogenous and crack free layers with a film volume completely penetrated by mesopores.

During the 50th CV the iridium mass based OER activity of purchased IrO_2 powder appears to be 5 times smaller (x 0.2) than for IrO_x/TiO_x powder. In contrast, new mesoporous templated catalysts from this work show a 24 (IrO_2/TiO_2: $Ir(OAc)_3$+$TiCl_4$), 13 (IrO_2/TiO_2: $Ir(OAc)_3$+TALH) and even 26 times (IrO_2: $Ir(OAc)_3$) higher iridium mass related OER activity. Similar relative mass activities are observed for each system even after 100 CVs. The deduced structure-activity relations can be used to explain the enhanced OER activity of new catalysts from this work (see Figure 52). A high OER activity was observed for samples with i) a sufficient degree of electrical conductivity, ii) a fast removal of produced O_2 gas, iii) a low crystallinity as well as iv) a high accessible active surface area.

The accessible surface area (ECSA) was determined by the mean value of the integrated anodic and cathodic scans for CVs recorded within a potential window of 0.40 - 1.40 V_{RHE} (50 mV/s). The ECSA, iridium mass and ECSA normalized to the iridium mass is shown for different catalytic systems in Table 3.

Table 3. ECSA and iridium normalized ECSA for commercial catalysts and new catalysts from this work.

Catalytic system	ECSA / mC	Ir mass / µg	ECSA per Ir mass / C g^{-1}
Commercial: IrO_x/TiO_x (Umicore)	1.610	36	45
Commercial: IrO_2 (Sigma)	0.070	2.6	27
This work: IrO_2/TiO_2 ($Ir(OAc)_3$+$TiCl_4$)	0.918	1.7	108
This work: IrO_2/TiO_2 ($Ir(OAc)_3$+TALH)	0.572	0.9	133
This work: IrO_2 ($Ir(OAc)_3$)	3.560	8.3	660

All catalytic systems show different ECSA thus complicating the identification of a clear trend. The difference in surface area is related to the different amount of iridium which is expected to scale with the number of active sites. In order to correct the ECSA for the iridium mass, a "specific surface area" is defined and expressed as ECSA per mass of iridium (C/g_{Ir}). It is clearly visible that new catalytic systems of this work provide an at least 2 times higher specific surface area. Our mesoporous templated coatings therefore further exploit the performance of scarce iridium. The lower iridium mass related OER activity for commercial systems can also be due the use of Nafion®. Nafion® is often added as a binder to attach the catalyst on the surface of the substrate. However, reports in literature show a significant decrease of electro catalytic performance when adding Nafion® as a binder.[165]

6 Conclusions and Outlook

The electrocatalytic splitting of water by using renewable energy sources such as wind and solar power is regarded as a possible route for a sustainable energy economy. However, the efficiency of water electrolyzer devices is limited by the complex reaction mechanism of the oxygen evolution reaction (OER) resulting in a high anodic overpotential. The goal of this work was the preparation of films with higher electrocatalytic oxygen evolution reaction activity compared to commercial available catalyst powders and to understand structure-activity relations. To achieve this goal a controlled variation of synthesis parameters during the preparation of catalytic layers (i.e. NiO, IrO_2 and IrO_2/TiO_2) was performed.

NiO films with an ordered mesopore structure were synthesized via soft-templating by employing a metal complex formed from citric acid and nickel nitrate along with a polymer template PEO_{213}-PB_{184}-PEO_{213}. At calcination of 250 °C an amorphous carbonate is formed which transforms into NiO at higher calcination temperature while retaining the templated mesopore structure. All catalysts show a significant OER activity, whereby samples calcined at 350 °C exhibit the highest OER performance and the highest surface area. A further increase in OER activity for mesoporous NiO layers can be achieved by potentiostatic treatments at 1.75 V_{RHE} which is in line with reports in literature[27] and is explained by an in-situ transformation from NiO to $Ni(OH)_2$/NiOOH, with NiOOH being the active phase for OER.

Films of mesoporous IrO_2 were obtained via a soft-templating approch based on micelles of amphiphilic block copolymers PEO_{213}-PB_{184}-PEO_{213} and iridium acetate. The samples show significant OER activity when calcined at temperatures higher than 350 °C. Heat treatment at 375 °C produces samples with ordered pores, low crystallinity, highest OER activity and highest surface area. Thick mesoporous catalyst films were obtained by multilayer deposition and show no signs of gas transport limitations even at current densities of 115 mA/cm^2.

The synthesis of mixed metal oxides was performed by an amphiphilic triblock copolymer PEO_{213}-PB_{184}-PEO_{213}, iridium acetate and either $TiCl_4$ or TALH. Different iridium loadings and calcination temperatures between 200 - 600 °C were studied to convert deposited films into mixed metal oxides of IrO_2/TiO_2 with tunable iridium loading and crystallinity. Samples of IrO_2/TiO_2 obtained by iridium acetate and $TiCl_4$ show largely segregated domains (ca. 100 nm) of IrO_2 and TiO_2 independently of the calcination temperature. Layers of IrO_2/TiO_2 produced by iridium acetate and TALH (400 °C), however, only show a small segregation of ca. 2 nm. The highest OER activity and highest active surface area was observed for samples calcined at 400 °C. The observed electrical conductivity significantly increases for iridium loadings higher than 30 wt. % thus following percolation theory.

The investigation of structure-activity relationships revealed that the OER performance of mesoporous IrO_2 and IrO_2/TiO_2 is controlled by at least three independent factors, i.e. i) the intrinsic reactivity per accessible site, ii) the electrical conductivity and iii) the accessible surface area (ECSA).

i) At low calcination temperatures, the pore system is still partially blocked by the remaining polymer template. High calcination temperatures decrease the ECSA due to sintering and crystallite growth. Two different regimes of reactivity were identified for mesoporous IrO_2. At calcination between 350 and 475 °C iridium oxide with low crystallinity and high activity is produced. However, at higher calcination temperatures a progressive crystallization and decreasing OER activity is observed. Calcination at 375 °C thus produces the highest ECSA and the highest reactivity. ii) The synthesis of mixed metal oxides of IrO_2/TiO_2 provided a high ECSA and an optimal electron transport through the layer for samples with an iridium content of at least 30 wt. % Ir in Ir/TiO_2. At lower iridium content, the electrical conductivity is insufficient thus causing an additional overpotential and a lowering of the intrinsic reactivity per accessible active site. Higher iridium loadings successively increase electrical conductivity as well as ECSA. However, the provided ECSA clearly depict a linear relationship with the OER activity. Therefore we conclude that, if a sufficient degree of electrical conductivity is achieved, the intrinsic reactivity of active iridium centres dispersed in TiO_2 is the same as for "pure" IrO_2. iii) The produced monometallic Ir-oxide based OER catalysts show the lowest overpotential reported so far in literature. Mesopores, introduced into the catalyst by templating with micelles of block copolymers, allow a rapid transport of the produced oxygen up to current densities of 75 mA/cm^2. Thick mesoporous catalyst films are obtained by multilayer deposition and did not show signs of gas transport limitations. The catalyst films were mechanically stable even at current densities of 115 mA/cm^2.

The developed films represent an example for homogeneous and scalable model systems to investigate the influence of crystallinity, electrical conductivity and gas production rate on intrinsic and overall OER activity. The films provide a narrow pore size distribution, a tunable pore size, a controlled layer thickness and a high activity. The concept enables optimal use of precious iridium. Moreover, the model system paves the way for quantitative investigations of structure-activity relationships and transport properties in other gas evolution reactions.

Further work will extend the concept of highly conducting catalysts with a high active surface area by focusing on more complex systems, e.g. niobium doped TiO_2 with an additional content of IrO_2. Niobium is well known for its capabilities to enhance electron conductivity of titanium oxide. By synergy of TiO_2 and niobium sufficient conductivity is achieved even at low iridium loadings, potentially leading to a higher iridium mass based OER activity.

References

[1]   M. Hirscher, *Angew. Chem., Int. Ed.* **2011**, *50*, 581-582.
[2]   S. Authayanun, K. Im-Orb, A. Arpornwichanop, *Chinese Journal of Catalysis* **2015**, *36*, 473-483.
[3]   M. Hook, X. Tang, *Energy Policy* **2013**, *52*, 797-809.
[4]   F. Haber, G. van Oordt, *Z. Anorg. Allg. Chem.* **1905**, *44*, 341-378.
[5]   T. Inagawa, O. Okada, S. Misawa, *JP57017403-A Chloric acid production by hydrogen and chlorine combustion - in column connected to absorbing-cooling column prepared from impermeable graphite tube,* **1982**
[6]   M. Radovic, E. Lara-Curzio, *Acta Mater.* **2004**, *52*, 5747-5756.
[7]   F. H. Bruner, *Industrial and Engineering Chemistry* **1949**, *41*, 2511-2515.
[8]   L. J. Cheng, J. S. Ma, *Synth. Commun.* **1994**, *24*, 2771-2775.
[9]   S. Sa, H. Silva, L. Brandao, J. M. Sousa, A. Mendes, *Applied Catalysis B-Environmental* **2010**, *99*, 43-57.
[10]   J. A. Velasco, C. Fernandez, L. Lopez, S. Cabrera, M. Boutonnet, S. Jaras, *Fuel* **2015**, *153*, 192-201.
[11]   M. Ni, M. K. H. Leung, D. Y. C. Leung, K. Sumathy, *Renewable & Sustainable Energy Reviews* **2007**, *11*, 401-425.
[12]   C. Perkins, A. W. Weimer, *Int. J. Hydrogen Energy* **2004**, *29*, 1587-1599.
[13]   M. Carmo, D. L. Fritz, J. Mergel, D. Stolten, *Int. J. Hydrogen Energy* **2013**, *38*, 4901-4934.
[14]   A. T. Marshall, S. Sunde, A. Tsypkin, R. Tunold, *Int. J. Hydrogen Energy* **2007**, *32*, 2320-2324.
[15]   E. Zoulias, E. Varkaraki, N. Lymberopoulos, C. Christodoulou, G. Karagiorgis, *TCJST* **2004**, *4*, 41-71.
[16]   M. D. Merrill, R. C. Dougherty, *J. Phys. Chem. C* **2008**, *112*, 3655-3666.
[17]   M. W. Kanan, D. G. Nocera, *Science* **2008**, *321*, 1072-1075.
[18]   Y. Surendranath, M. Dincă, D. G. Nocera, *J. Am. Chem. Soc.* **2009**, *131*, 2615-2620.
[19]   A. Bergmann, E. Martinez-Moreno, D. Teschner, P. Chernev, M. Gliech, J. F. de Araujo, T. Reier, H. Dau, P. Strasser, *Nature Communications* **2015**, *6*, 1-9.
[20]   A. Indra, P. W. Menezes, N. R. Sahraie, A. Bergmann, C. Das, M. Tallarida, D. Schmeisser, P. Strasser, M. Driess, *J. Am. Chem. Soc.* **2014**, *136*, 17530-17536.
[21]   W. Y. Bian, Z. R. Yang, P. Strasser, R. Z. Yang, *J. Power Sources* **2014**, *250*, 196-203.
[22]   D. A. Corrigan, R. M. Bendert, *J. Electrochem. Soc.* **1989**, *136*, 723-728.
[23]   X. X. Yu, T. Y. Hua, X. Liu, Z. P. Yan, P. Xu, P. W. Du, *ACS Appl. Mater. Interfaces* **2014**, *6*, 15395-15402.
[24]   A. Singh, S. L. Y. Chang, R. K. Hocking, U. Bach, L. Spiccia, *Energy Environ. Sci.* **2013**, *6*, 579-586.
[25]   K. L. Nardi, N. Y. Yang, C. F. Dickens, A. L. Strickler, S. F. Bent, *Advanced Energy Materials* **2015**, *5*.
[26]   K. Fominykh, J. M. Feckl, J. Sicklinger, M. Doblinger, S. Bocklein, J. Ziegler, L. Peter, J. Rathousky, E. W. Scheidt, T. Bein, D. Fattakhova-Rohlfing, *Adv. Funct. Mater.* **2014**, *24*, 3123-3129.
[27]   L. Trotochaud, J. K. Ranney, K. N. Williams, S. W. Boettcher, *J. Am. Chem. Soc.* **2012**, *134*, 17253-17261.
[28]   J. C. K. Ho, D. L. Piron, *J. Appl. Electrochem.* **1996**, *26*, 515-521.
[29]   S. Klaus, Y. Cai, M. W. Louie, L. Trotochaud, A. T. Bell, *J. Phys. Chem. C* **2015**, *119*, 7243-7254.
[30]   M. Gorlin, M. Gliech, J. F. de Araujo, S. Dresp, A. Bergmann, P. Strasser, *Catal. Today* **2016**, *262*, 65-73.
[31]   F. Dionigi, T. Reier, Z. Pawolek, M. Gliech, P. Strasser, *ChemSusChem* **2016**, *9*, 962-972.

[32]   M. Gong, Y. G. Li, H. L. Wang, Y. Y. Liang, J. Z. Wu, J. G. Zhou, J. Wang, T. Regier, F. Wei, H. J. Dai, *J. Am. Chem. Soc.* **2013**, *135*, 8452-8455.

[33]   L. Trotochaud, S. L. Young, J. K. Ranney, S. W. Boettcher, *J. Am. Chem. Soc.* **2014**, *136*, 6744-6753.

[34]   A. Bergmann, I. Zaharieva, H. Dau, P. Strasser, *Energy Environ. Sci.* **2013**, *6*, 2745-2755.

[35]   K. Mette, A. Bergmann, J. P. Tessonnier, M. Havecker, L. D. Yao, T. Ressler, R. Schlogl, P. Strasser, M. Behrens, *Chemcatchem* **2012**, *4*, 851-862.

[36]   M. Gliech, A. Bergmann, C. Spori, P. Strasser, *Journal of Energy Chemistry* **2016**, *25*, 278-281.

[37]   M. E. G. Lyons, M. P. Brandon, *J. Electroanal. Chem.* **2010**, *641*, 119-130.

[38]   C. C. L. McCrory, S. H. Jung, J. C. Peters, T. F. Jaramillo, *J. Am. Chem. Soc.* **2013**, *135*, 16977-16987.

[39]   X. Y. Lu, C. A. Zhao, *Nature Communications* **2015**, *6*, 1-7.

[40]   W. Grot, *Chem. Ing. Tech.* **1978**, *50*, 299-301.

[41]   W. Grot, *Chem. Ing. Tech.* **1972**, *44*, 167-169.

[42]   S. Slade, S. A. Campbell, T. R. Ralph, F. C. Walsh, *J. Electrochem. Soc.* **2002**, *149*, 1556-1564.

[43]   P. Medina, M. Santarelli, *Int. J. Hydrogen Energy* **2010**, *35*, 5173-5186.

[44]   B. Bensmann, R. Hanke-Rauschenbach, I. K. P. Arias, K. Sundmacher, *Electrochim. Acta* **2013**, *110*, 570-580.

[45]   A. Goni-Urtiaga, D. Presvytes, K. Scott, *Int. J. Hydrogen Energy* **2012**, *37*, 3358-3372.

[46]   M. Y. Wang, Z. Wang, X. Z. Gong, Z. C. Guo, *Renew. Sust. Energ. Rev.* **2014**, *29*, 573-588.

[47]   M. Bernicke, E. Ortel, T. Reier, A. Bergmann, J. Ferreira de Araujo, P. Strasser, R. Kraehnert, *ChemSusChem* **2015**, *8*, 1908-1915.

[48]   S. Ferro, D. Rosestolato, C. A. Martinez-Huitle, A. De Battisti, *Electrochim. Acta* **2014**, *146*, 257-261.

[49]   M. Morimitsu, R. Otogawa, M. Matsunaga, *Electrochim. Acta* **2000**, *46*, 401-406.

[50]   M. H. P. Santana, L. A. De Faria, J. F. C. Boodts, *Electrochim. Acta* **2004**, *49*, 1925-1935.

[51]   P. Hong Hanh, N. Ngoc Phong, D. Chi Linh, L. Ba Thang, *Advances in Natural Sciences: Nanoscience & Nanotechnology* **2015**, *6*, 1-5.

[52]   M. Vukovic, D. Cukman, M. Milun, L. D. Atanasoska, R. T. Atanasoski, *J. Electroanal. Chem.* **1992**, *330*, 663-673.

[53]   R. Kotz, S. Stucki, *Electrochim. Acta* **1986**, *31*, 1311-1316.

[54]   Y. Matsumoto, E. Sato, *Mater. Chem. Phys.* **1986**, *14*, 397-426.

[55]   H. Over, *Chem. Rev. (Washington, DC, U. S.)* **2012**, *112*, 3356-3426.

[56]   T. Reier, M. Oezaslan, P. Strasser, *Acs Catalysis* **2012**, *2*, 1765-1772.

[57]   B. Johnson, F. Girgsdies, G. Weinberg, D. Rosenthal, A. Knop-Gericke, R. Schlogl, T. Reier, P. Strasser, *J. Phys. Chem. C* **2013**, *117*, 25443-25450.

[58]   W. Hu, Y. Q. Wang, X. H. Hu, Y. Q. Zhou, S. L. Chen, *J. Mater. Chem.* **2012**, *22*, 6010-6016.

[59]   M. N. Kushner-Lenhoff, J. D. Blakemore, N. D. Schley, R. H. Crabtree, G. W. Brudvig, *Dalton Trans.* **2013**, *42*, 3617-3622.

[60]   J. D. Blakemore, N. D. Schley, G. W. Olack, C. D. Incarvito, G. W. Brudvig, R. H. Crabtree, *Chem. Sci.* **2011**, *2*, 94-98.

[61]   H. S. Oh, H. N. Nong, T. Reier, M. Gliech, P. Strasser, *Chemical Science* **2015**, *6*, 3321-3328.

[62]   H. N. Nong, H. S. Oh, T. Reier, E. Willinger, M. G. Willinger, V. Petkov, D. Teschner, P. Strasser, *Angew. Chem., Int. Ed.* **2015**, *54*, 2975-2979.

[63]   T. Reier, Z. Pawolek, S. Cherevko, M. Bruns, T. Jones, D. Teschner, S. Selve, A. Bergmann, H. N. Nong, R. Schlogl, K. J. J. Mayrhofer, P. Strasser, *J. Am. Chem. Soc.* **2015**, *137*, 13031-13040.

[64]   T. Reier, I. Weidinger, P. Hildebrandt, R. Kraehnert, P. Strasser, *ECS Trans.* **2013**, *58*, 39-51.

[65]   E. Ortel, T. Reier, P. Strasser, R. Kraehnert, *Chem. Mat.* **2011**, *23*, 3201-3209.

[66]   C. Yi-Min, C. Jhen-Hong, H. Ying-Sheng, L. Kuei-Yi, T. Dah-Shyang, T. Kwong-Kau, *Nanotechnol.* **2011**, *22*, 355708 -355708.

[67]   S. C. Raghu, M. Ulaganathan, T. M. Lim, M. S. Kazacos, *J. Power Sources* **2013**, *238*, 103-108.

[68]   I. S. Lee, J. M. Park, H. J. Son, J. C. Park, G. H. Lee, Y. H. Lee, F. Z. Ciu, in *Key Eng. Mat., Vol. 288-289*, **2005**, pp. 307-310.

[69]   Y. Lu, Z. X. Cai, Y. L. Cao, H. X. Yang, Y. Y. Duan, *Electrochem. Commun.* **2008**, *10*, 778-782.

[70]   I. A. Ges, B. L. Ivanov, A. A. Werdich, F. J. Baudenbacher, *Biosens. Bioelectron.* **2007**, *22*, 1303-1310.

[71]   L. M. Kuo, K. N. Chen, Y. L. Chuang, S. C. Chao, *Ecs Solid State Letters* **2013**, *2*, 28-30.

[72]   A. Marshall, B. Borresen, G. Hagen, M. Tsypkin, R. Tunold, *Electrochim. Acta* **2006**, *51*, 3161-3167.

[73]   G. H. Chen, X. M. Chen, P. L. Yue, *J. Phys. Chem. B* **2002**, *106*, 4364-4369.

[74]   C. Comninellis, G. P. Vercesi, *J. Appl. Electrochem.* **1991**, *21*, 335-345.

[75]   Galizzio.D, Tantardi.F, S. Trasatti, *J. Appl. Electrochem.* **1974**, *4*, 57-67.

[76]   S. Trasatti, G. Buzzanca, *J. Electroanal. Chem.* **1971**, *29*, 1-5.

[77]   E. Oakton, D. Lebedev, A. Fedorov, F. Krumeich, J. Tittier, O. Sereda, T. J. Schmidt, C. Coperet, *New J. Chem.* **2016**, *40*, 1834-1838.

[78]   K. A. Stoerzinger, W. S. Choi, H. Jeen, H. N. Lee, Y. Shao-Horn, *J. Phys. Chem. Lett.* **2015**, *6*, 487-492.

[79]   K. S. W. Sing, D. H. Everett, R. A. W. Haul, L. Moscou, R. A. Pierotti, J. Rouquerol, T. Siemieniewska, *Pure Appl. Chem.* **1985**, *57*, 603-619.

[80]   F. Schüth, *Chem. Ing. Tech.* **2010**, *82*, 769-777.

[81]   E. Ortel, Ph.D. thesis, Technische Universität Berlin (Berlin), **2012**.

[82]   F. Schüth, *Angew. Chem.* **2003**, *115*, 3730-3750.

[83]   G. Riess, *Prog. Polym. Sci.* **2003**, *28*, 1107-1170.

[84]   Y. J. Cheng, J. S. Gutmann, *J. Am. Chem. Soc.* **2006**, *128*, 4658-4674.

[85]   Z. C. Sun, D. H. Kim, M. Wolkenhauer, G. G. Bumbu, W. Knoll, J. S. Gutmann, *ChemPhysChem* **2006**, *7*, 370-378.

[86]   B. Ma, J. Ma, G. K. L. Goh, *J. Mater. Sci.* **2008**, *43*, 4297-4302.

[87]   B. Smarsly, G. Xomeritakis, K. Yu, N. G. Liu, H. Y. Fan, R. A. Assink, C. A. Drewien, W. Ruland, C. J. Brinker, *Langmuir* **2003**, *19*, 7295-7301.

[88]   E. Bloch, P. L. Llewellyn, T. Phan, D. Bertin, V. Hornebecq, *Chem. Mat.* **2009**, *21*, 48-55.

[89]   J. Lee, M. C. Orilall, S. C. Warren, M. Kamperman, F. J. Disalvo, U. Wiesner, *Nat. Mater.* **2008**, *7*, 222-228.

[90]   S. Guldin, S. Huttner, P. Tiwana, M. C. Orilall, B. Ulgut, M. Stefik, P. Docampo, M. Kolle, G. Divitini, C. Ducati, S. A. T. Redfern, H. J. Snaith, U. Wiesner, D. Eder, U. Steiner, *Energy Environ. Sci.* **2011**, *4*, 225-233.

[91]   J. Joo, J. Shim, H. Seo, N. Jug, U. Wiesner, J. Lee, S. Jeon, *Anal. Chem.* **2010**, *82*, 3032-3037.

[92]   A. H. Yuwono, Y. Zhang, J. Wang, X. H. Zhang, H. M. Fan, W. Ji, *Chem. Mat.* **2006**, *18*, 5876-5889.

[93]   D. Grosso, C. Boissiere, B. Smarsly, T. Brezesinski, N. Pinna, P. A. Albouy, H. Amenitsch, M. Antonietti, C. Sanchez, *Nat. Mater.* **2004**, *3*, 787-792.

[94]   B. Smarsly, D. Grosso, T. Brezesinski, N. Pinna, C. Boissiere, M. Antonietti, C. Sanchez, *Chem. Mat.* **2004**, *16*, 2948-2952.

[95]   T. Brezesinski, J. Wang, J. Polleux, B. Dunn, S. H. Tolbert, *J. Am. Chem. Soc.* **2009**, *131*, 1802-1809.

[96]   M. Groenewolt, T. Brezesinski, H. Schlaad, M. Antonietti, P. W. Groh, B. Ivan, *Adv. Mater.* **2005**, *17*, 1158-1162.

[97]   T. Brezesinski, M. Groenewolt, M. Antonietti, B. Smarsly, *Angew. Chem., Int. Ed.* **2006**, *45*, 781-784.

[98]   E. Ortel, A. Fischer, L. Chuenchom, J. Polte, F. Emmerling, B. Smarsly, R. Kraehnert, *Small* **2012**, *8*, 298-309.

[99]   J. H. Pan, X. S. Zhao, W. I. Lee, *Chem. Eng. J. (Lausanne)* **2011**, *170*, 363-380.

[100] D. G. Bucknall, H. L. Anderson, *Science* **2003**, *302*, 1904-1905.

[101] T. Brezesinski, A. Fischer, K. Iimura, C. Sanchez, D. Grosso, M. Antonietti, B. M. Smarsly, *Adv. Funct. Mater.* **2006**, *16*, 1433-1440.

[102] D. Grosso, G. Soler-Illia, F. Babonneau, C. Sanchez, P. A. Albouy, A. Brunet-Bruneau, A. R. Balkenende, *Adv. Mater.* **2001**, *13*, 1085-1090.

[103] B. Eckhardt, E. Ortel, J. Polte, D. Bernsmeier, O. Gorke, P. Strasser, R. Kraehnert, *Adv. Mater.* **2012**, *24*, 3115-3119.

[104] D. Grosso, G. Soler-Illia, E. L. Crepaldi, F. Cagnol, C. Sinturel, A. Bourgeois, A. Brunet-Bruneau, H. Amenitsch, P. A. Albouy, C. Sanchez, *Chem. Mat.* **2003**, *15*, 4562-4570.

[105] P. D. Yang, D. Y. Zhao, D. I. Margolese, B. F. Chmelka, G. D. Stucky, *Nature* **1998**, *396*, 152-155.

[106] J. Guilment, O. Poncelet, J. Rigola, S. Truchet, *Vib. Spectrosc.* **1996**, *11*, 37-49.

[107] V. Luca, W. K. Bertram, G. D. Sizgek, B. Yang, D. Cookson, *Langmuir* **2008**, *24*, 10737-10745.

[108] G. J. D. Soler-illia, C. Sanchez, B. Lebeau, J. Patarin, *Chem. Rev. (Washington, DC, U. S.)* **2002**, *102*, 4093-4138.

[109] E. Ortel, S. Sokolov, C. Zielke, I. Lauermann, S. Selve, K. Weh, B. Paul, J. Polte, R. Kraehnert, *Chem. Mat.* **2012**, *24*, 3828-3838.

[110] D. Grosso, F. Cagnol, G. Soler-Illia, E. L. Crepaldi, H. Amenitsch, A. Brunet-Bruneau, A. Bourgeois, C. Sanchez, *Adv. Funct. Mater.* **2004**, *14*, 309-322.

[111] D. Grosso, *J. Mater. Chem.* **2011**, *21*, 17033-17038.

[112] H. J. Chung, D. H. Go, J. W. Bae, I. K. Jung, J. W. Lee, K. D. Park, *Current Applied Physics* **2005**, *5*, 485-488.

[113] H. M. Kao, C. L. Chen, S. W. Chiao, *J. Chin. Chem. Soc. (Taipei, Taiwan)* **2005**, *52*, 693-699.

[114] P. Innocenzi, L. Malfatti, T. Kidchob, S. Enzo, G. Della Ventura, U. Schade, A. Marcelli, *J. Phys. Chem. C* **2010**, *114*, 22385-22391.

[115] J. D. Bass, D. Grosso, C. Boissiere, C. Sanchez, *J. Am. Chem. Soc.* **2008**, *130*, 7882-7897.

[116] Y. Zhang, J. Li, J. Wang, *Chem. Mat.* **2006**, *18*, 2917-2923.

[117] W. Xing, F. Li, Z. F. Yan, G. Q. Lu, *J. Power Sources* **2004**, *134*, 324-330.

[118] V. Subramanian, S. C. Hall, P. H. Smith, B. Rambabu, *Solid State Ionics* **2004**, *175*, 511-515.

[119] B. Eckhardt, E. Ortel, D. Bernsmeier, J. Polte, P. Strasser, U. Vainio, F. Emmerling, R. Kraehnert, *Chem. Mat.* **2013**, *25*, 2749-2758.

[120] D. M. Antonelli, J. Y. Ying, *Angew. Chem., Int. Ed. Engl.* **1995**, *34*, 2014-2017.

[121] D. Chandra, N. Abe, D. Takama, K. Saito, T. Yui, M. Yagi, *Chemsuschem* **2015**, *8*, 795-799.

[122] M. Bernicke, B. Eckhardt, A. Lippitz, E. Ortel, D. Bernsmeier, R. Schmack, R. Kraehnert, *ChemistrySelect* **2016**, *3*, 1-9.

[123] W. S. Rasband, *National Institutes of Health, Bethesda, Maryland, USA* **1997-2014**, *http://imagej.nih.gov/ij/*.

[124] Z. Jusys, H. Massong, H. Baltruschat, *J. Electrochem. Soc.* **1999**, *146*, 1093-1098.

[125] S. Ardizzone, A. Carugati, S. Trasatti, *J. Electroanal. Chem.* **1981**, *126*, 287-292.

[126] C. P. De Pauli, S. Trasatti, *J. Electroanal. Chem.* **2002**, *538*, 145-151.

[127] D. Grosso, C. Boissiere, L. Nicole, C. Sanchez, *J. Sol-Gel Sci. Technol.* **2006**, *40*, 141-154.

[128] T. Brezesinski, B. Smarsly, K. Iimura, D. Grosso, C. Boissiere, H. Amenitsch, M. Antonietti, C. Sanchez, *Small* **2005**, *1*, 889-898.

[129] C. Sanchez, C. Boissiere, D. Grosso, C. Laberty, L. Nicole, *Chem. Mat.* **2008**, *20*, 682-737.
[130] K. Kishi, *J. Electron Spectrosc. Relat. Phenom.* **1988**, *46*, 237-247.
[131] L. J. Matienzo, L. I. Yin, S. O. Grim, W. E. Swartz, *Inorg. Chem.* **1973**, *12*, 2762-2769.
[132] K. K. Lian, D. W. Kirk, S. J. Thorpe, *J. Electrochem. Soc.* **1995**, *142*, 3704-3712.
[133] Y. Q. Miao, L. Ouyang, S. L. Zhou, L. Xu, Z. Y. Yang, M. S. Xiao, R. Z. Ouyang, *Biosens. Bioelectron.* **2014**, *53*, 428-439.
[134] L. A. Stern, X. L. Hu, *Faraday Discuss.* **2014**, *176*, 363-379.
[135] C. Bocca, A. Barbucci, G. Cerisola, *Int. J. Hydrogen Energy* **1998**, *23*, 247-252.
[136] M. Pourbaix, *Atlas of electrochemical equilibria in aqueous solutions*, Pergamon Press, New York, **1966**.
[137] E. Özer, C. Spoeri, T. Reier, P. Strasser, *ChemCatChem* **2016**, DOI: 10.1002/cctc.201600423R201600421
[138] A. R. Zeradjanin, F. La Mantia, J. Masa, W. Schuhmann, *Electrochim. Acta* **2012**, *82*, 408-414.
[139] A. R. Zeradjanin, E. Ventosa, A. S. Bondarenko, W. Schuhmann, *ChemSusChem* **2012**, *5*, 1905-1911.
[140] A. R. Zeradjanin, A. A. Topalov, Q. Van Overmeere, S. Cherevko, X. X. Chen, E. Ventosa, W. Schuhmann, K. J. J. Mayrhofer, *Rsc Advances* **2014**, *4*, 9579-9587.
[141] T. Nakagawa, C. A. Beasley, R. W. Murray, *J. Phys. Chem. C* **2009**, *113*, 12958-12961.
[142] W. Hu, S. L. Chen, Q. H. Xia, *Int. J. Hydrogen Energy* **2014**, *39*, 6967-6976.
[143] C. L. McDaniel, S. J. Schneider, *Journal of Research of the National Bureau of Standards Section a-Physics and Chemistry* **1967**, *A 71*, 119-123.
[144] D. Grosso, A. R. Balkenende, P. A. Albouy, M. Lavergne, L. Mazerolles, F. Babonneau, *J. Mater. Chem.* **2000**, *10*, 2085-2089.
[145] J. R. Osman, J. A. Crayston, A. Pratt, D. T. Richens, *J. Sol-Gel Sci. Technol.* **2008**, *46*, 126-132.
[146] W. Kaiser, *Physical Review* **1957**, *105*, 1751-1756.
[147] W. Kaiser, H. L. Frisch, H. Reiss, *Physical Review* **1958**, *112*, 1546-1554.
[148] R. Schmack, B. Eckhardt, G. Koch, E. Ortel, R. Kraehnert, *Materials Science-Medziagotyra* **2016**, *22*, 74-81.
[149] V. G. Kessler, *J. Sol-Gel Sci. Technol.* **2013**, *68*, 464-470.
[150] G. Tammann, *Z. Anorg. Allg. Chem.* **1926**, *157*, 321-325.
[151] M. A. Carreon, V. V. Guliants, *Eur. J. Inorg. Chem.* **2005**, 27-43.
[152] H. Shi, X. B. Li, G. L. Haller, O. Y. Gutierrez, J. A. Lercher, *J. Catal.* **2012**, *295*, 133-145.
[153] A. G. Scheuermann, J. D. Prange, M. Gunji, C. E. D. Chidsey, P. C. McIntyre, *Energy Environ. Sci.* **2013**, *6*, 2487-2496.
[154] W. D. Ryden, A. W. Lawson, *Physical Review B* **1970**, *1*, 1494-1500.
[155] Y. X. Liu, H. Masumoto, T. Goto, *Mater. Trans.* **2004**, *45*, 3023-3027.
[156] S. Fierro, L. Ouattara, E. H. Calderon, C. Comninellis, *Electrochem. Commun.* **2008**, *10*, 955-959.
[157] D. Grosso, F. Babonneau, C. Sanchez, G. Soler-Illia, E. L. Crepaldi, P. A. Albouy, H. Amenitsch, A. R. Balkenende, A. Brunet-Bruneau, *J. Sol-Gel Sci. Technol.* **2003**, *26*, 561-565.
[158] D. M. Pickup, G. Mountjoy, G. W. Wallidge, R. Anderson, J. M. Cole, R. J. Newport, M. E. Smith, *J. Mater. Chem.* **1999**, *9*, 1299-1305.
[159] A. de Oliveira-Sousa, M. A. S. da Silva, S. A. S. Machado, L. A. Avaca, P. de Lima-Neto, *Electrochim. Acta* **2000**, *45*, 4467-4473.
[160] H. Takenaka, E. Torikai, Y. Kawami, N. Wakabayashi, *Int. J. Hydrogen Energy* **1982**, *7*, 397-403.
[161] A. Minguzzi, O. Lugaresi, C. Locatelli, S. Rondinini, F. D'Acapito, E. Achilli, P. Ghigna, *Anal. Chem.* **2013**, *85*, 7009-7013.

[162]   A. Minguzzi, C. Locatelli, O. Lugaresi, E. Achilli, G. Cappelletti, M. Scavini, M. Coduri, P. Masala, B. Sacchi, A. Vertova, P. Ghigna, S. Rondinini, *Acs Catalysis* **2015**, *5*, 5104-5115.

[163]   H. G. S. Casalongue, M. L. Ng, S. Kaya, D. Friebel, H. Ogasawara, A. Nilsson, *Angew. Chem., Int. Ed.* **2014**, *53*, 7169-7172.

[164]   H. Ogasawara, S. Kaya, A. Nilsson, *Top. Catal.* **2016**, *59*, 439-447.

[165]   M. Eguchi, K. Baba, T. Onuma, K. Yoshida, K. Iwasawa, Y. Kobayashi, K. Uno, K. Komatsu, M. Kobori, M. Nishitani-Gamo, T. Ando, *Polymers* **2012**, *4*, 1645-1656.

Appendix

A1: Electro-catalysis in alkaline media (OER and ECSA)

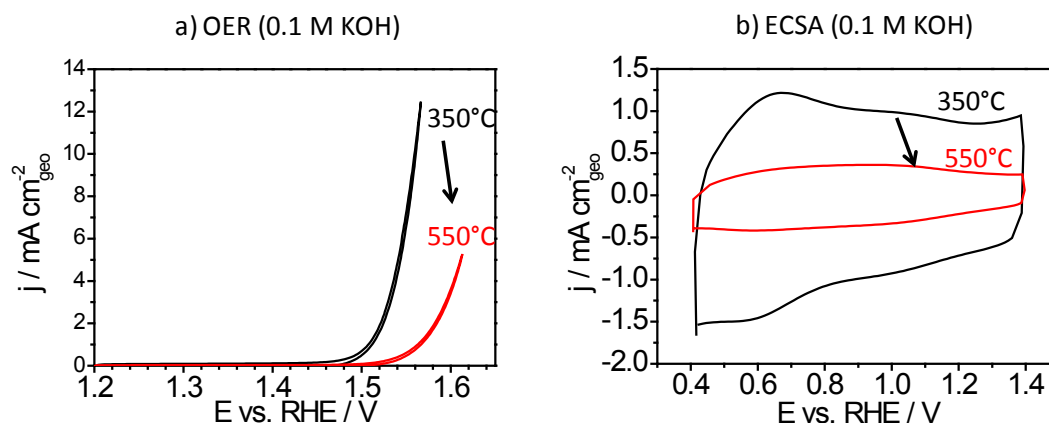a) OER (0.1 M KOH)   b) ECSA (0.1 M KOH)

Figure A1: a) Impact of calcination temperature of mesoporous templated IrO_2 films on oxygen evolution performance in alkaline media (0.1 M KOH). Samples calcined at 350 °C possess a higher activity than samples calcined at 550 °C. The same behavior for OER activity was observed for samples measured in acidic media. b) ECSA analysis recorded for potentials between 0.4 - 1.4 V_{RHE}. Samples calcined at 350 °C show a higher area, indicating that more charge has been transferred due to reversible proton inclusion mechanism. Hence, samples calcined at 350 °C possess a significantly higher ECSA than samples calcined at 550 °C. Experiments conducted in acidic media (0.5 M H_2SO_4) exhibit the same trend.

A2: Faraday efficiency
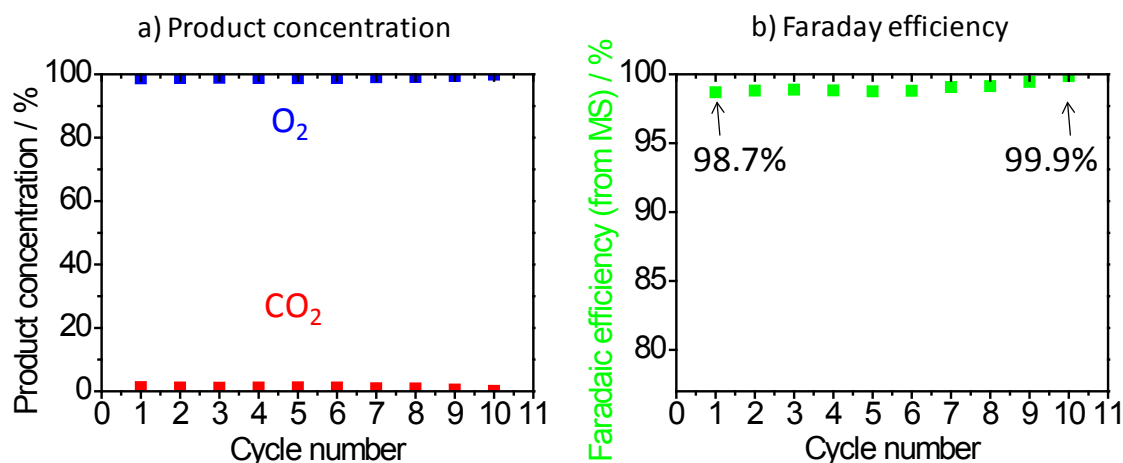

a) Product concentration   b) Faraday efficiency

Figure A2: a) Product concentration of CO_2 and O_2 is shown against applied cycle number. Evolving amount of O_2 appears to be high for the first 10 cycles in OER regime (1.2-1.65 V_{RHE}). b) Faraday efficiency is shown against cycle number. Mesoporous templated IrO_2 shows faraday efficiency of 98.7 % for the 1st and 99.9 % for the 10th cycle in OER regime (1.2 - 1.65 V_{RHE}).

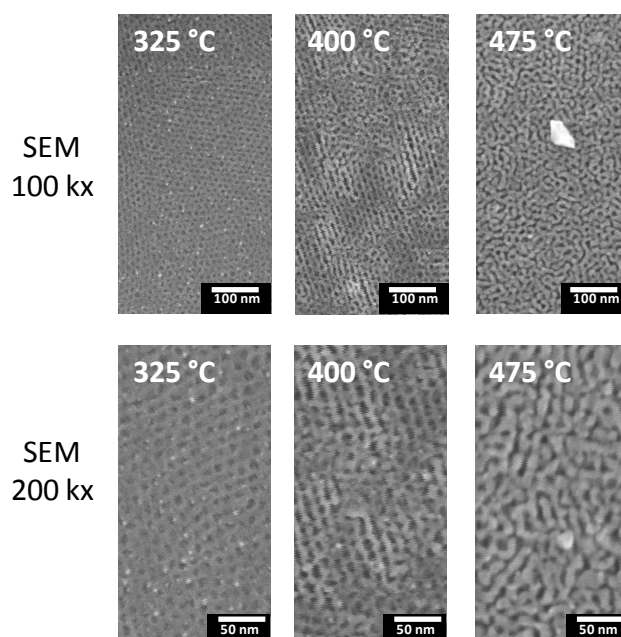## A3: IrO$_2$/TiO$_2$ (IrCl$_3$ + TiCl$_4$): Morphology

Figure A3: Illustrating morphology at different magnifications for 15 wt. % Ir in Ir/TiO$_2$ obtained by IrCl$_3$·xH$_2$O and TiCl$_4$ with subsequent heat treatment at different temperatures, respectively. Pronounced iridium rich particles are present within the studied temperature regime related to poor solubility of IrCl$_3$·xH$_2$O in the dip-coating solution. Thus, underlining that iridium chloride precursor are inappropriate for the formation of phase pure IrO$_2$/TiO$_2$ at low calcination temperatures.

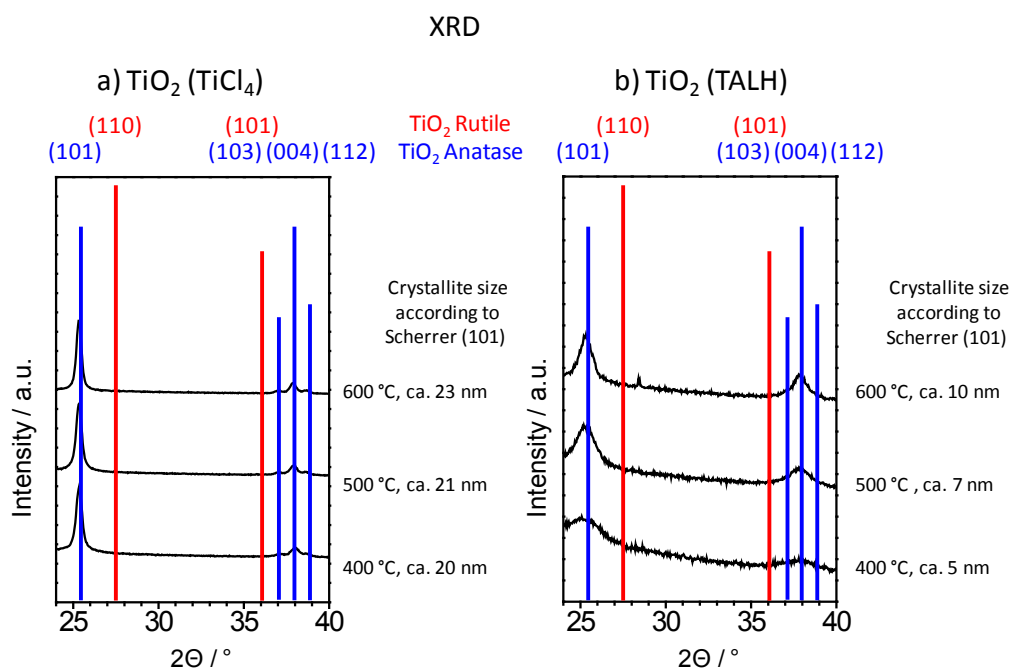## A4: Crystallinity of TiO$_2$ synthesized from TiCl$_4$ and TALH

Figure A4: X-ray diffraction patterns of TiO$_2$ heat treated at temperatures between 400 - 600 °C (ramp: 1 K/min, silicon substrate). The patterns were obtained for heat treated samples dipcoated from solutions containing PEO-PB-PEO and a) TiCl$_4$ or b) TALH.

A5: Determination of kink potentials for IrO_2

Tafelplots: IrO_2 ($T_{calc.}$: 375 °C)
(different layer thickness)

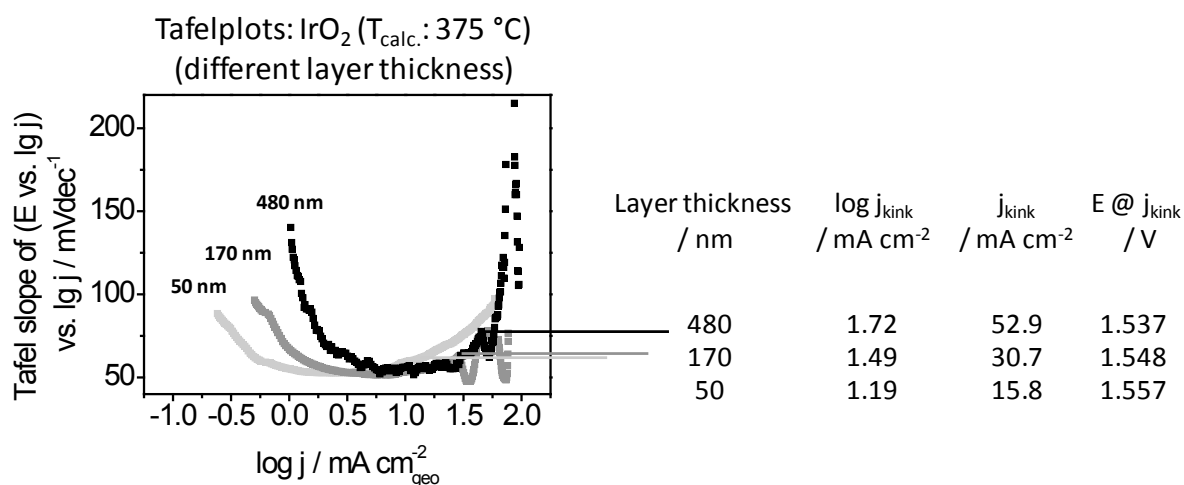| Layer thickness / nm	log j_{kink} / mA cm^{-2}	j_{kink} / mA cm^{-2}	E @ j_{kink} / V
480	1.72	52.9	1.537
170	1.49	30.7	1.548
50	1.19	15.8	1.557

Figure A5: Determination of kinks within Tafel plots derived from cyclic voltammograms in the OER regime of IrO_2 synthesized from $Ir(OAc)_3$ and PEO-PB-PEO ($T_{calc.}$: 375 °C). The image shows the first derivative of the Tafel plot as a function of log j. Turning points of the Tafel plots are represented as minima. The Tafel slope of the sample was determined with a linear fit in the Tafel plot (see Figure 49 d). A formal criterion was defined in order to quantify the kink. If the Tafel slope (represented at the y-axis) increases by another 10 % a "kink" occurs. The image further provides for different layerthicknesses, i) logj, j and the corresponding potential at which the kinks occur. Electrochemical testing was conducted on titanium substrates in 0.5 M H_2SO_4, CV: 1.2 - 1.65 V_{RHE} with 6 mV/s at 1600 rpm.

Acronyms

ALD	Atomic layer deposition
ATO	Antimony doped tin oxide
BET	Brunauer-Emmett-Teller
CLCT	Cooperative liquid crystal template
CLER	Chlorine evolution reaction
CMC	Critical micelle concentration
CV	Cyclic voltammogram
CVD	Chemical vapour deposition
DEMS	Differential electrochemical mass spectrometry
DSA	Dimensional stable anodes (e.g. RuO_2 coated on TiO_2 used for ClER)
E^0	Standard electrode potential
ECSA	Electrochemical accessible surface area
EISA	Evaporation induced self assembly
EtOH	Ethanol
F	Faraday constant (96 485 C/mol)
F127	PEO_{106}-PPO_{70}-PEO_{106}
ΔG^0	Standard Gibbs free energy
ΔH^0	Standard reaction enthalpy
HCl	Hydrochloric acid
HER	Hydrogen evolution reaction
ICP-OES	Inductively coupled plasma - optical emission spectrometry
KLE	PHB-b-PEO
n	Transferred electrons (during an electrochemical reaction)
NBB	Nano building blocks
OAc	Acetate
OER	Oxygen evolution reaction
P123	PEO_{20}-PPO_{70}-PEO_{20}
PB	Polybutadiene
PEM	Proton exchange membrane (e.g. Nafion[®])
PEO	Polyethylene oxide
PHB	Polyhydroxybutyrate
PIB	Polyisobutylene
PMMA	Poly(methyl methacrylate)
PPO	Polypropylene oxide
PS	Polystyrene
PTFE	Polytetrafluoroethylene

QCM	Quartz crystal microbalance
RHE	Reversible hydrogen electrode
ΔS^0	Standard molar entropy
SAXS	Small angle X-ray scattering
SAED	Selected area electron diffraction
SEM	Scanning electron microscopy
T	Temperature (K)
$T_{calc.}$	Calcination temperature (also: T_c)
TALH	Titanium(IV) bis(ammonium lactato)dihydroxide
TEM	Transmission electron microscopy
TGA	Thermogravimetric analysis
TLCT	True liquid crystal template
TTAB	Tetradecyltrimethylammonium bromide
XPS	X-ray photoelectron spectroscopy
XRD	X-ray diffraction